MODELLING, SIMULATION AND CONTROL OF AN ISOLATED PUMPING SYSTEM POWERED BY RENEWABLE ENERGY SOURCES

A Thesis Submitted for obtaining
the Scientific Title of PhD in Engineering
from
Politehnica University Timișoara
in the Field of SYSTEMS ENGINEERING
by

Eng. Dorin BORDEAȘU

PhD Committee Chair:	Prof.Phd.Eng. Radu-Emil PRECUP
PhD Supervisor:	Prof.Phd.Eng. Octavian PROȘTEAN
Scientific Reviewers:	Prof.Phd.Eng. Mihail ABRUDEAN
	Prof.Phd.Eng. Vlad MUREȘAN
	Prof.Phd.Eng. Ioan FILIP

Date of the PhD Thesis Defense: 10.03.2023

The PhD thesis series of UPT are:

1.Automation
2.Chemistry
3.Energetics
4.Chemical Engineering
5.Civil Engineering
6.Electrical Engineering
7.Electronic Engineering and Telecommunications
8.Industrial Engineering
9.Mechanical Engineering
10.Computer Science and
Information Technology
11.Science and Material Engineering
12.Systems Engineering
13.Energy Engineering
14.Computers and Information Technology
15.Materials Engineering
16.Engineering and Management
17.Architecture
18.Civil Engineering and Installations
19.Electronics, Telecommunications
and Information Technologies

Politehnica University Timișoara, Romania, initiated the above series to disseminate the expertise, knowledge and results of the research carried out within the doctoral school of the university. According to the Decision of the Executive Office of the University Senate No. 14/14.07.2006, the series includes the doctoral theses defended in the university since October 1, 2006.

Romania, 300223 Timișoara, Bd. Vasile Pârvan no. 2B
Tel./fax +40-(0)256 404677
e-mail: editura@upt.ro

Foreword

This doctoral thesis entitled "**Modelling, simulation and control of an isolated pumping system powered by renewable energy sources**" is a synthesis of the theoretical and experimental research activity started by the author at **Aalborg University (Denmark)**, developed at **Bombeatec (Spain)** and completed within the **Department of Automation and Applied Informatics of the Politehnica University Timişoara, Romania.**

The scope of the thesis is to reduce the operating expenses of the pumping systems, by powering them with photovoltaic or wind energy conversion systems, increasing their energy efficiency, reliability and robustness.

In this sense, the major objectives achieved by this thesis are: the development and validation of models that describe as precisely as possible the operation of a high-power pumping system; development and validation of models of photovoltaic, respectively, energy conversion systems; the integration of these models for the synthesis, implementation and validation of control strategies for the correct operation of a high-power isolated pumping system powered by photovoltaic or wind energy conversion systems.

In this thesis are addressed the issues specific to the field of pumping systems powered by renewable energy sources.

After a brief review of the state-of-the-art of the research in the field, is addressed the modelling of an isolated pumping system powered by photovoltaic or wind energy conversion systems. It has been developed, implemented and validated the customized control structures for driving the induction motor of a centrifugal pump at fixed (nominal) speed using a soft starter, and at variable speed, flow, pressure (pumping head) or power absorption using a variable frequency drive. Based on these customized control structures, the control strategies of a pumping system powered by photovoltaic or wind energy conversion systems were developed and implemented regulating the pumping system power absorption to track the power produced by the conversion energy system at partial load, and regulating the pressure (pumping head) according to its reference at full load it. A monitoring campaign is proposed and implemented to determine the performance of a pumping system powered by a photovoltaic energy conversion system by recording the values of the main parameters using a non-intrusive acquisition and storage system. At the end of the thesis are presented the performances and contributions brought by the proposed control structures based on the simulations results and experimental data.

The present work contributes to the European Union strategy regarding the reduction of greenhouse gas emissions, increase of the renewable energy consumption share and increase of the energy efficiency.

On this occasion, I address the first thanks with deep gratitude to the Phd supervisor **Prof.Phd.Eng. Octavian PROȘTEAN**, for accepting me as a PhD student and for the permanently support, effort, patience and competent guidance offered during the entire period of the thesis elaboration.

I express my full consideration towards the members of the doctoral committee, Mr. President **Prof.Phd.Eng. Radu-Emil PRECUP** from **Politehnica University of Timișoara, Prof.Phd.Eng. Mihail ABRUDEAN** from **Technical University of Cluj-Napoca, Prof.Phd.Eng. Vlad MUREȘAN** from **Technical University of Cluj-Napoca** and **Prof.Phd.Eng. Ioan FILIP** from **Politehnica University of Timișoara** who honored my invitation to be part of the thesis analysis committee and for their assessments about the thesis.

Thanks and gratitude to the **General Director** of **Kintech-Engineering Eng. Tirso VÁZQUEZ**, the **General Director** of **Bombeatec Eng. Alejandro SERRANO** and to the colleagues from these companies, for their support provided in the research activity and for their permission granted in the use of their research platforms and the data necessary for the experimental validation of the proposed approaches, without which the thesis could not have this scientific consistency.

I would like to express my warm thanks to the members of the guidance committee, from the Politehnica University of Timișoara who participated in the exams, presentations and presented reports, bringing useful observations and suggestions for the thesis improvement: **Assoc.Prof.Phd.Eng. Iosif SZEIDERT**, **Assoc.Prof.Phd.Eng. Cristian VAȘAR** and **Assoc.Prof.Phd.Eng. Sorin NANU**.

I address my respectful thanks to the Rector **Assoc.Prof.Phd.Eng. Florin DRĂGAN** and to the entire **Department of Automation and Applied Informatics from the Politehnica University of Timisoara**, for their warm welcoming in the team.

I express special considerations to the professors **Assoc.Prof.Phd.Eng. Mohsen SOLTANI** and **Assoc.Prof.Phd.Eng. Zhenyu YANG** for introducing and sharing their knowledge in power system engineering during my studies at Aalborg University in Denmark.

Last but not least, I would like to thank my family for their understanding, patience, constant encouragement and unconditional support offered during the entire period of the doctoral research program.

The best thoughts of gratitude and thanks go to my father **Prof.Phd.Eng. Ilare BORDEAȘU** for whom there are not enough words to express my gratitude. I only hope that my actions and professional development confirm the trust and support given.

Finally, I consider that the current work is of real use for research in the pumping system industry.

Timişoara, February 2023 **Eng. Dorin BORDEAȘU**

Bordeașu, Dorin

MODELLING, SIMULATING AND CONTROL OF AN ISOLATED PUMPING SYSTEM POWERED BY RENEWABLE ENERGY SOURCES

PhD theses of UPT, Series X, No. YY, Editura Politehnica, 2023, 267 pages, 233 figures, 24 tables.

ISSN:
ISBN:

Keywords
Wind energy; Photovoltaic energy; Wind energy conversion system; Photovoltaic energy conversion system; Pumping system; Monitoring system, Modelling, simulation and controlling.

Abstract
In this thesis are addressed the issues specific to the field of pumping systems (PS) powered by renewable energy sources (RES). After a brief review of the state-of-the-art of the research in the field, it is addressed the modelling of an isolated PS powered by photovoltaic or wind energy conversion systems (PECS or WECS). It has been developed, implemented and validated the customized control structures for driving the induction motor of a centrifugal pump at fixed (nominal) speed using a soft starter, and at variable speed, variable discharge (flow rate), variable pressure (pumping head) or variable power absorption using a variable frequency drive. Based on these customized control structures, the control strategies of a PS powered by PECS or WECS were developed and implemented for driving the PS so that its absorbed power tracks the power produced by the PECS or WECS at partial load and controls the pressure (pumping head) of the PS according to its reference at full load. A monitoring system is developed and implemented to determine the performance of a PS powered by a PECS that measures and stores the transducers values using a non-intrusive acquisition and logging system. At the end of the thesis, the performances and contributions brought by the proposed control structures and strategies are determined based on the simulations results and the data collected with the proposed monitoring system.

TABLE OF CONTENTS

ACRONYMS, SYMBOLS AND ABBREVIATIONS

Short form	**Full form**
PVG	Photovoltaic generator
WEG	Wind electrical generator
VFD	Variable frequency drive
MASLOWATEN	Market uptake of an innovative irrigation Solution based on LOW WATer-Energy consumption
UPM	Polytechnic University of Madrid
PECS	Photovoltaic Energy Conversion System
WECS	Wind Energy Conversion System
WPHG	Wind-Photovoltaic Hybrid Generator
PSPPECS	Pumping Systems Powered by Photovoltaic Energy Conversion Systems
PSPWECS	Pumping Systems Powered by Wind Energy Conversion Systems
PSPWPHG	Pumping Systems Powered by a Wind-Photovoltaic Hybrid Generator
PSPWPHECS	Pumping Systems Powered by a Wind-Photovoltaic Hybrid Energy Conversion Systems
H_2O	Water
DC	Direct Current
AC	Alternate current
V–f	Variable-frequency
V–I	Variable-current
VSD	Variable-speed drives
V/Hz	The ratio voltage over frequency
IGBT	Insulated-gate bipolar transistor
PS	Pumping System
LPG	Liquefied petroleum gas
PI	Proportional Integral
PWM	pulse-width modulation
NPSH	Net Positive Suction Head
PV	Photovoltaic
NOCT	Nominal Operating Cell Temperature
N	North
S	South
N-S	North-South
E	East
W	West
E-W	East-West
DU	Drive Unit
PLC	Programable Logic Controller
ISC	Short-Circuit Current
VOC	Open Circuit Voltage
PMAX	Maximum Power
P–V	Power-Voltage
I-V	Current-Voltage
MPP	Maximum Power Point

MPPT	Maximum Power Point Tracking
P&O	Perturb and observed
VMP	Maximum Power Voltage
PPT	Power Point Tracking
HSAT	Horizontal single-axis trackers
NREL	National renewable energy laboratory
DFIG	Doubly-fed induction generator
WT	Wind turbine
LHP	Left half plane
CP	Power coefficient
CT	Thrust coefficient
SISO	Single input - single output
MIMO	Multiple input - multiple output
SS	State-space
DFIM	Doubly fed induction machine
WRIM	Wound rotor induction machine
GVOVC	Grid voltage-oriented vector control
PLL	Phase locked loop
P	Proportional
I	Integral
HMI	Human Machine Interface
PS	Pumping system
PVS	Photovoltaic system
IM	Induction motor
RES	Renewable energy sources

VARIABLES NOTATIONS, DESCRIPTION AND UNITS

Variable notation	**Variable description**	**Unit**
T_{pump}	Pump (motor load) torque	[Nm]
T_{IM}	Induction motor torque	[Nm]
$P_{drivenominal}$	Induction motor drive nominal power	[W]
$P_{driveoutput}$	Induction motor drive output power	[W]
$P_{driveinput}$	Induction motor drive input power	[W]
I_{ps}	pumping system moment of inertia	[Kg m^2]
ω_{ps}	Angular velocity of the shaft connecting the motor and pump	[rad/s]
η_{drive}	Induction motor drive efficiency	[%]
η_{filter}	DV/DT filter efficiency	[%]
η_{cables}	The efficiency after the loss due to the voltage drop in the cables (typically between 1-3%)	[%]
x_a, x_b, x_c	Three phases corresponding to the complex space vector	[-]
x_α	The real component of the space vector	[-]
x_β	The imaginary component of the space vector	[-]
ω_{IM}	Electrical angular velocity of the induction motor	[rad/s]
v_{as}, v_{bs}, v_{cs}	The stator actual voltages for each phase winding	[V]
i_{as}, i_{bs}, i_{cs}	The stator actual currents for each phase winding	[A]
Ψ_{as}, Ψ_{bs}, Ψ_{cs}	The stator actual fluxes for each phase winding	[Vm]
R_r	The stator resistance	[Ω]
v_{ar}, v_{br}, v_{cr}	The rotor actual voltages for each phase winding	[V]
i_{ar}, i_{br}, i_{cr}	The rotor actual currents for each phase winding	[A]
Ψ_{ar}, Ψ_{br}, Ψ_{cr}	The rotor actual fluxes for each phase winding	[Vm]
R_r	Rotor resistance	[Ω]
L_h	Self-inductance of the stator windings	[H]
$L_{\sigma s}$	Leakage inductance of the stator windings	[H]
$L_{\sigma r}$	Leakage inductance of the rotor windings	[H]
$\overrightarrow{v_s}^s$	The stator voltage vector reference to the stator	[V]
$\overrightarrow{i_s}^s$	The stator current vector reference to the stator	[A]
$\overrightarrow{\psi_s}^s$	The stator flux vector reference to the stator	[Vm]
$v_{\alpha s}$	Stator voltage vector α component	[V]
$v_{\beta s}$	Stator voltage vector β component	[V]
$i_{\alpha s}$	Stator current vector α component	[A]

$i_{\beta s}$	Stator current vector β component	[A]
$\psi_{\alpha s}$	Stator flux vector α component	[Vm]
$\psi_{\beta s}$	Stator flux vector β component	[Vm]
$\overrightarrow{i_r}^{s}$	The rotor current vector reference to the stator	[A]
$\overrightarrow{\psi_r}^{s}$	The rotor flux vector reference to the stator	[Vm]
$i_{\alpha r}$	Rotor current vector α component	[A]
$i_{\beta r}$	Rotor current vector β component	[A]
$\psi_{\alpha r}$	Rotor flux vector α component	[Vm]
$\psi_{\beta r}$	Rotor flux vector β component	[Vm]
L_m	Mutual inductance	[H]
L_s	Stator inductance	[H]
L_r	Rotor inductance	[H]
ω_{ss}	Generator stator synchronous speed	[rad/s]
f_s	Grid frequency of the balanced three phases	[Hz]
p_{IM}	Generator pairs of poles	[-]
P_{IM}	Induction motor active power	[W]
v_α	Voltage vector α component	[V]
v_β	Voltage vector β component	[V]
i_α	Current vector α component	[A]
i_β	Current vector β component	[A]
Q_{IM}	Induction motor reactive power	[W]
σ	The leakage coefficient	[-]
$\overrightarrow{v_s}^{a}$	The stator voltage vector reference to synchronously rotating frame	[V]
$\overrightarrow{i_s}^{a}$	The stator current vector reference to synchronously rotating frame	[A]
$\overrightarrow{\psi_s}^{a}$	The stator flux vector reference to synchronously rotating frame	[Vm]
ψ_{ds}	Stator flux d component	[Vm]
ψ_{as}	Stator flux q component	[Vm]
v_d	Voltage vector d component	[V]
v_q	Voltage vector q component	[V]
i_{ds}	Stator current d component	[A]
i_{qs}	Stator current q component	[A]
$\overrightarrow{i_r}^{a}$	The rotor current vector reference to synchronously rotating frame	[A]
$\overrightarrow{\psi_r}^{a}$	The rotor flux vector reference to synchronously rotating frame	[Vm]
ψ_{dr}	The d component of the rotor flux	[Vm]
ψ_{ar}	The q component of the rotor flux	[Vm]
i_{dr}	Rotor current d component	[A]
i_{qr}	Rotor current q component	[A]
$Q*$	Pump service flow rate	[m^3/h]
$H*$	Submersible pump service head	[m]
$H*$	Pump rated efficiency	[%]
P_{pump}	Pump rated hydraulic power	[kW]

Q_{max}	Pump maximum flow rate	[m^3/h]
H_{max}	Pump head at theoretical 0 flow rate	[m]
H_{min}	Pump minimum head (at maximum flow rate)	[m]
$H*$	Pump efficiency at maximum flow rate	[%]
P_{PSmax}	Pump hydraulic power at maximum flow rate	[m^3/h]
Hg_{cons}	Consumer pressure	[bar]
Hg_{well}	Well Dynamic head	[mca]
ΔHg	Water level variation	[mca]
D_{pipe}	Pipe diameter	[m]
A	Head–flow 1st coefficient	[m]
B	Head–flow 2nd coefficient	[h/m^2]
C	Head–flow 3rd coefficient	[h/m^5]
D	Efficiency-flow 1st coefficient	[1/m^2]
E	Efficiency-flow 2nd coefficient	[1/m^5]
ρ_w	Water density	[Kg/m^3]
G	Pump geometry	[m^3]
$P_{ps}*$	Shaft pump power	[W]
$\omega_{ps}*$	Pump shaft angular velocity	[rad/s]
P_{pump}	Pump shaft power	[W]
$P_{hydraulic}$	Hydraulic power of the water at the pump outlet	[W]
g	Gravitational acceleration	[m/s^2]
Sa, Sb, Sc	The PWM switching commands (orders)	[-]
v_{ds} and v_{qs}	The stator three-phase AC voltage commands transformed in synchronous (dq) reference frame	[V]
$v_{\alpha s}$ and $v_{\beta s}$	The stator three-phase AC voltage commands transformed in stationary (αβ) reference frame	[V]
v_{as}, v_{bs}, v_{cs}	The stator three-phase AC voltages	[V]
i_{as}, i_{bs}, i_{cs}	The stator three-phase AC currents	[A]
i_α and i_β	The stator three-phase AC currents expressed in stationary (αβ) reference frame	[A]
$i_{ds}*$	Reference of the d-axis current loop	[A]
i_{ds}	The output of the d-axis current loop	[A]
$i_{qs}*$	The reference of the q-axis current loop	[A]
i_{qs}	The output of the q-axis current loop	[A]
$T_{dq.\alpha\beta}$	Transformation from synchronous (dq) reference frame into stationary (αβ) reference frame	[-]
$T_{\alpha\beta.dq}$	Transformation from stationary (αβ) into synchronous (dq) reference frame	[-]
$T_{abc.\alpha\beta}$	Transformation from three-phase (abc) complex space vector into stationary (αβ) reference frame	[-]
$T_{\alpha\beta.abc}$	Transformation from stationary (αβ) reference frame into three-phase (abc) complex space vector	[-]
k_{i1}	Integral time constant of the d and q axis currents systems	[-]
ω_{n1}	The first natural frequency of the d and q axis currents systems	[Hz]

k_{p1}	Proportional gain of the d and q axis currents systems	[-]
k_{i1}	Integral time constant of the d and q axis currents systems	[-]
Tem	Electromechanical torque of the induction motor	[Nm]
$Tem*$	Reference of the induction motor electromechanical torque	[Nm]
fm	Electrical frequency of the induction motor	[Hz]
$Fm*$	Reference of the induction motor electrical frequency	[Hz]
ω_{n2}	The first natural frequency of the driving shaft system	[Hz]
ξ_2	The damping factor of the driving shaft system	[Ns/m]
k_{p2}	Proportional gain of the driving shaft speed controller	[-]
k_{i2}	Integral time constant of the driving shaft speed controller	[-]
τ_r	Induction motor’s rotor time constant	[s]
ω_{n3}	The first natural frequency of the rotor flux estimator	[Hz]
ξ_3	The damping factor of the rotor flux estimator	[Ns/m]
k_{p3}	Proportional gain of the rotor flux controller	[-]
k_{i3}	Integral time constant of the driving rotor flux controller	[-]
P_{MAX}	Peak Power Watts	[Wp]
V_{MPP}	Maximum Power Voltage	[V]
I_{MPP}	Maximum Power Current	[A]
V_{OC}	Open Circuit Voltage	[V]
I_{SC}	Short Circuit Current	[A]
η_m	Module Efficiency	[%]
T	Nominal Operating Cell Temperature (NOCT)	[°C]
K_P	Temperature Coefficient of PMAX	[%/K]
K_V	Temperature Coefficient of VOC	[%/K]
K_I	Temperature Coefficient of ISC	[%/K]
η_{PPV}	Initial PV module power loss	[%]
$\eta_{PPVyear}$	Yearly PV module power loss	[%]
L_{EO}	Separation between trackers in E-W direction	[m]
θ_{MAX}	Maximum Rotation	[º]
Dev	Deviation of the rotating axis regarding the South (axis azimuth)	[º]
β_{AXIS}	Axis inclination	[º]
LNS	LNS: Separation between tracker rows in N-S direction	[m]
βG	Module inclination	[º]
G_{global}	Global irradiation	[W/m2]
G_{diff}	Diffuse irradiation	[W/m2]
$G_{clearsky}$	Clear sky irradiation	[W/m2]
T_{env}	Environment temperature	[ºC]
G_{direct}	Direct irradiation	[W/m2]
H	Solar time	[hh:mm]
γ_S	Solar elevation	[-]

θ	Angle of incidence of the PV generator	[^{0}]
$\%S$	Multiplier Factor for direct irradiance according to generator position	[-]
η_{sky}	Sky losses	[-]
G_{diff0}	Diffuse irradiation from the circumsolar region (equivalent to direct) in the plane of the generator	[W/m2]
C_{F1}	Correction factor for losses in Direct Irradiance and Diffuse Circumsolar Irradiance, due to angle of incidence and dirt	[-]
G_{dir0}	Correction into the direct irradiation in the generator plane	[W/m2]
G_{idiff}	The isotropic diffuse irradiation in the plane of the PV generator	[W/m2]
C	The correction factor for losses in Diffuse Isotropic, by angle of incidence and dirt	[-]
CF_{idiff}	The correction factor for losses in Diffuse Isotropic, by angle of incidence and dirt	[-]
G_{albedo}	Albedo irradiance in the plane of the generator	[W/m2]
CF_{albedo}	The correction factor for losses in Albedo, due to angle of incidence and dirt	[-]
C_{adj}	Adjustment coefficient based on the solar elevation	[-]
$G_{D\theta}$	The global irradiance in the plane of the generator after considering losses due to dirt and angle of incidence	[W/m2]
LNS_2	The distance between closest points of consecutive tracker panels	[m]
HPV	PV module height	[m]
H_{fence}	Height of the fence surrounding the PV generator	[m]
ω_{ID}	Ideal tracking angle	[^{0}]
S_{EW1}	Consecutive tracker's shadow length projection on the ground	[m]
S_{EW2}	The equivalent length favorable for not shading, favorable by elevation to the ground of the consecutive tracker	[m]
S_{EW3}	Length between trackers to avoid shadowing	[m]
S_{EW}	Valid distance for not generating shadows between the N-S axis	[m]
FS_{EW}	The shading factor between the 1-axis trackers (N-S) and the shadows	[-]
S_{fence}	The length of the shadow generated by the fence	[m]
FS_{fence}	The shadow Factor generated by the fence	[-]
$G_{\beta G}$	The global irradiance in the plane of the generator after considering losses due to dirt, the angle of incidence and the shadows between the trackers and from the fence	[W/m2]
T_{cell}	Actual temperature of the p-n junction (cell temperature)	[^{0}K]

P_{PVG}	The PV generator produced power	[W]
I_{PV}	The photovoltaic current that is generated by one PV module	[A]
V_{PV}	The photovoltaic voltage that is generated by one PV module	[V]
I_L	The light generated current at nominal condition (25ºC and 1000 W/ m2) by a PV module	[A]
I_0	The equivalent Diode saturation current of a PV module	[A]
R_s	The equivalent resistance of the PV cells connected in series in a PV module	[Ω]
R_{sh}	The shunt resistance representing the irradiance and temperature dependent I-V characteristics of a PV module	[Ω]
N_{cells}	number of cells connected in series in a PV module	[-]
k_B	The Boltzmann constant	[J/ºK]
q	The electron charge	[C]
n_I	The ideality factor of the equivalent diode of the p-n junction	[-]
T_N	Standard PV cell temperature	[ºK]
G_N	1000 standard irradiation	[W/m2]
I_{scN}	Short circuit current of a single cell of the PV module	[A]
K_I	The linear coefficient of the short circuit current according to the operating temperature	[%/ºK]
V_{ocN}	Open circuit voltage of a single cell of the PV module under the standard conditions	[V]
K_V	The linear coefficient of the voltage of the open circuit according to the operating temperature	[%/ºK]
v	Wind speed;	[m/s]
v_{rot}	Average wind speed over the wind turbine rotor;	[m/s]
λ	Wind turbine tip speed ratio;	[rad]
R	Wind turbine rotor radius;	[m]
Ω	Wind turbine rotor angular velocity;	[rad/s]
P_{rot}	Wind turbine rotor power;	[w]
ρ	Air density;	[kg/m3]
CP	Wind turbine power coefficient;	[-]
β	Wind turbine blade-pitch angle;	[°]
M_{rot}	Wind turbine rotor torque;	[N·m]
$CP(\lambda,\beta)$	Wind turbine power coefficient look up table;	[-]
F_{rot}	Wind turbine rotor thrust force;	[N]
$CT(\lambda,\beta)$	Wind turbine thrust coefficient look up table;	[-]
Ω_0	Wind turbine rated angular velocity of the rotor;	[rad/s]
v_{rot0}	Rated wind speed at wind turbine rotor;	[m/s]
λ_0	Wind turbine tip speed ratio at rated wind speed;	[-]
λ_l	Linear wind turbine tip speed ratio;	[-]

$\Delta\lambda$	Change in wind turbine tip speed ratio;	[-]
$\Delta\Omega$	Change in wind turbine rotor angular velocity;	[rad/s]
Δv_{rot}	Change in wind speed at wind turbine rotor;	[m/s]
cpp_{xy}	Wind turbine power coefficient polynomial coefficient indexed xy;	[-]
β_0	Initial wind turbine blade-pitch angle;	[°]
CP_0	Wind turbine power coefficient at rated wind speed;	[-]
ΔCP	Change in wind turbine power coefficient;	[-]
$\Delta\beta$	Change in wind turbine blade-pitch angle;	[°]
ctp_{xy}	Wind turbine thrust coefficient polynomial coefficient indexed xy;	[-]
ΔCT	Change in wind turbine thrust coefficient;	[-]
CT_0	Wind turbine thrust coefficient at rated wind speed;	[-]
CP_l	Linear wind turbine power coefficient;	[-]
CT_l	Linear wind turbine thurst coefficient;	[-]
M_{rot0}	Wind turbine rotor torque at rated wind speed;	[N·m]
ΔM_{rot}	Change in wind turbine rotor torque;	[N·m]
a_{mrot}	Wind turbine rotor torque sensitivity in respect to change in wind speed at rotor;	[-]
b_{mrot}	Wind turbine rotor torque sensitivity in respect to change in rotor angular velocity;	[-]
c_{mrot}	Wind turbine rotor torque sensitivity in respect to change in blade-pitch angle;	[-]
F_{rot0}	Wind turbine rotor thurst at rated wind speed;	[N·m]
ΔF_{rot}	Change in wind turbine rotor thrust;	[N·m]
a_{frot}	Wind turbine rotor thrust sensitivity in respect to change in wind speed at rotor;	[-]
b_{frot}	Wind turbine rotor thrust sensitivity in respect to change in rotor angular velocity;	[-]
c_{frot}	Wind turbine rotor thrust sensitivity in respect to change in blade-pitch angle;	[-]
I_{rot}	Wind turbine rotor moment of intertia;	[kg·m^2]
K_{shaft}	Wind turbine low-speed shaft torsion spring constant;	[N·m/rad]
B_{shaft}	Wind turbine low-speed shaft viscous friction constant;	[N·m·s]
$\dot{\Omega}$	Change in wind turbine rotor angular velocity;	[rad/s^2]
Φ	Wind turbine low-speed main shaft torsion;	[rad]
$\dot{\Phi}$	Change in wind turbine low-speed main shaft torsion;	[rad/s]
M_{gen}	Wind turbine generator torque;	[N·m]
I_{gen}	Wind turbine generator moment of intertia;	[kg·m^2]
ω	Wind turbine generator angular velocity;	[rad/s]
$\dot{\omega}$	Change in wind turbine generator angular velocity;	[rad/s^2]
N	Wind turbine gearbox ratio;	[-]
P_{out}	Wind turbine generator net output power;	[w]
η_{gen}	Wind turbine generator efficiency	[%]
M_{genref}	Wind turbine generator torque reference;	[N·m]

$\dot{M}_{gen}$	Change in wind turbine generator torque;	[N·m/s]
T_{gen}	Wind turbine generator time constant;	[s]
P_{ref}	Wind turbine generator output power reference;	[w]
ΔM_{gen}	Change in wind turbine generator torque;	[N·m/s]
$P_{out.gross}$	Wind turbine generator gross output power;	[w]
$P_{out.gross0}$	Wind turbine rated generator gross output power;	[w]
$P_{out.grossl}$	Wind turbine generator linear gross output power;	[w]
$\Delta\omega$	Change in wind turbine generator angular velocity;	[rad/s^2]
$M_{genref0}$	Rated wind turbine generator torque reference;	[N·m]
$M_{genrefl}$	Linear wind turbine generator torque reference;	[N·m]
ΔM_{genref}	Change in wind turbine generator torque reference;	[N·m/s]
m_{tow}	Wind turbine tower mass;	[kg]
K_{tow}	Spring constant of the wind turbine tower;	[N/m]
B_{tow}	Damping constant of the wind turbine tower;	[N·s/m]
z	Wind turbine nacelle position;	[m]
$\dot{z}$	Wind turbine nacelle velocity;	[m/s]
$\ddot{z}$	Wind turbine nacelle acceleration;	[m/s^2]
M_{blade}	Bending moment of the wind turbine blade	[N·m]
$\dot{\beta}$	Change in wind turbine blade-pitch angle;	[°/s] or [rad/s]
$\ddot{\beta}$	Sensitivity of the wind turbine blade-pitch angle;	[°/s^2] or [rad/s^2]
τ_{β}	Wind turbine pitch actuator time constant;	[s]
$u\beta$	Wind turbine pitch actuator input pitch angle;	[°]
$\lambda\beta$	Wind turbine pitch actuator time delay;	[s]
K_{β}	Wind turbine pitch actuator proportional regulator constant	[-]
β_m	Measured wind turbine blade-pitch angle;	[°]
β_{ref}	Reference wind turbine blade-pitch angle;	[°]
M_{brake}	Wind turbine brake torque;	[N·m]
$\dot{M}_{brake}$	Change in wind turbine brake torque;	[N·m/s]
T_{Mbrake}	Wind turbine brake time constant;	[s]
λ_{brake}	Wind turbine brake time delay;	[s]
M_{gen0}	Rated wind turbine generator torque;	[N·m]
$e\omega_{gen}$	Error between the step response of the nonlinear and linear models of the wind turbine generator angular velocity;	[rad/s]
eP_{out}	Error between the step response of the nonlinear and linear models of the wind turbine generator output power;	[w]
$y[n]$	Filtered generator angular velocity of the wind turbine control-measurment filter;	[rad/s]
$y[n-1]$	Previous filtered generator angular velocity of the wind turbine control-measurment filter;	[rad/s]
$u[n]$	Measured generator angular velocity of the	[rad/s]

	wind turbine control-measurment filter;	
n	Discrete-time-step counter of the wind turbine control-measurment filter;	[-]
T_s	Discrete-time-step of the wind turbine control-measurment filter;	[s]
F_c	Corner frequency of the wind turbine control-measurment low-pass filter;	[Hz]
a	Wind turbine control-measurment low-pass filter coefficient;	[-]
A_d	Wind turbine control-measurment low-pass filter discrete-time state matrix	[-]
B_d	Wind turbine control-measurment low-pass filter discrete-time input matrix;	[-]
C_d	Wind turbine control-measurment low-pass filter discrete-time output state matrix;	[-]
D_d	Wind turbine control-measurment low-pass filter discrete-time input transmission matrix;	[-]
$H_{filter}(z)$	Discrete transfer function of the wind turbine control-measurment low-pass filter;	[-]
$\Omega_{cut.in}$	Wind turbine rotor angular velocity at cut-in wind speed;	[rad/s]
$\omega_{cut.in}$	Wind turbine generator angular velocity at cut-in wind speed;	[rad/s]
v_{cutout}	Wind turbine cut-out wind speed;	[m/s]
$M_{gen.reagion1}$	Wind turbine generator torque in region 1;	[N·m]
$\omega_{reagion1}$	Wind turbine generator angular velocity in region 1;	[rad/s]
$\Omega_{optimal}$	Wind turbine rotor angular velocity at peak tip speed ratio;	[rad/s]
$\omega_{optimal}$	Wind turbine generator angular velocity at peak tip speed ratio;	[rad/s]
$v_{rot.optimal}$	Average wind speed over the rotor at peak tip speed ratio;	[m/s]
λ_{preak}	Wind turbine peak tip speed ratio;	[-]
$M_{gen.optimal}$	Wind turbine optimal generator torque;	[N·m]
k	Wind turbine optimal constant	[s^2/rad^2]
Cp_{peak}	Wind turbine power coefficient peak value at initial blade-pitch angle $\beta_0=0°$;	[-]
$M_{gen.region2}$	Wind turbine generator torque in region 2;	[N·m]
$\omega_{region2}$	Wind turbine generator angular velocity in region 2;	[rad/s]
P_{dem}	Demanded power from the wind turbine;	[w]
$P_{gen.rated}$	Rated net power of the wind turbine generator;	[w]
Ω_{rated}	Rated wind turbine rotor angular velocity;	[rad/s]
ω_{rated}	Rated wind turbine generator angular velocity;	[rad/s]
$M_{gen.rated}$	Rated wind turbine generator torque;	[N·m]
$M_{gen.region3}$	Wind turbine generator torque in region 3;	[N·m]
$\omega_{region3}$	Wind turbine generator angular velocity in region 3;	[rad/s]
$M_{gen.region1.1/2}$	Wind turbine generator torque in region 1½;	[N·m]
$\omega_{region1.1/2}$	Wind turbine generator angular velocity in	[rad/s]

	region 1½;	
$a_{1.1/2}$	Slope for region 1½ linear equation of the wind turbine torque controller;	[-]
$b_{1.1/2}$	Y-intercept for region 1½ linear equation of the wind turbine torque controller;	[-]
ω_{ss}	Wind turbine generator stator synchronous speed;	[rad/s]
f_s	Grid frequency of the balanced three phases;	[Hz]
$p_{wtgenerator}$	Wind turbine generator pairs of poles;	[-]
ω_{ms}	Wind turbine generator rotor mechanical speed at synchronous stator speed;	[rad/s]
$s_{wtgenerator}$	Wind turbine generator slip in region 2½;	[%]
$M_{gen.region2.1/2}$	Wind turbine generator torque in region 2½;	[N·m]
$\omega_{region2.1/2}$	Wind turbine generator angular velocity in region 1½;	[rad/s]
$a_{2.1/2}$	Slope for region 2½ linear equation of the wind turbine torque controller;	[-]
$b_{2.1/2}$	Y-intercept for region 2½ linear equation of the wind turbine torque controller;	[-]
$H_{wt}(z)$	Transfer function of the wind turbine linear model;	[-]
$u_{wt}(z)$	Input of the wind turbine linear model transfer function (blade pitch angle);	[°]
$y_{wt}(z)$	Output of the wind turbine linear model transfer function (blade pitch angle);	[rad/s]
β_{ref}	Wind turbine blade pitch controller reference angle;	
Kp_{rated}	Wind turbine blade pitch controller proportional gain at initial blade-pitch angle $\beta=0°$;	[s]
Ki_{rated}	Wind turbine blade pitch controller integral time constant at initial blade-pitch angle $\beta=0°$;	[-]
ω_{err}	Difference between rated ω_{rated} and actual ω wind turbine generator angular velocity;	[rad/s]
$Kp(\beta)$	Wind turbine blade pitch controller proportional gain at β blade-pitch angle;	[s]
$Ki(\beta)$	Wind turbine blade pitch controller integral time constant at β blade-pitch angle;	[-]
$GK(\beta)$	Wind turbine blade pitch controller linear gain correction factor, based on the blade-pitch angle;	[-]
β_k	Wind turbine blade pitch angle where the rotor torque sensitivity to blade pitch angle has doubled.	[rad]
k_{cp1}	Power coefficient regression coefficient 1	[-]
k_{cp2}	Power coefficient regression coefficient 2	[-]
k_{cp3}	Power coefficient regression coefficient 3	[-]
k_{cp4}	Power coefficient regression coefficient 4	[-]
k_{cp5}	Power coefficient regression coefficient 5	[-]
k_{cp6}	Power coefficient regression coefficient 6	[-]
k_{cp7}	Power coefficient regression coefficient 7	[-]
k_{cp8}	Power coefficient regression coefficient 8	[-]

k_{ct1}	Thrust coefficient regression coefficient 1	[-]
k_{ct2}	Thrust coefficient regression coefficient 2	[-]
k_{ct3}	Thrust coefficient regression coefficient 3	[-]
k_{ct4}	Thrust coefficient regression coefficient 4	[-]
k_{ct5}	Thrust coefficient regression coefficient 5	[-]
k_{ct6}	Thrust coefficient regression coefficient 6	[-]
k_{ct7}	Thrust coefficient regression coefficient 7	[-]
k_{ct8}	Thrust coefficient regression coefficient 8	[-]
$\overrightarrow{v_s}^{s}$	Stator voltage vector reference to the stator	[V]
R_s	Stator resistance	[Ω]
$\overrightarrow{i_s}^{s}$	Stator current vector reference to the stator	[A]
$\overrightarrow{v_r}^{r}$	Rotor voltage vector reference to the rotor	[V]
R_r	Rotor resistance	[Ω]
$\overrightarrow{i_r}^{r}$	Rotor current vector reference to the rotor	[A]
$\overrightarrow{\psi_s}^{s}$	Stator flux vector reference to the stator	[Vm]
$\overrightarrow{\psi_r}^{r}$	Rotor flux vector reference to the rotor	[Vm]
ω	High-speed shaft angular velocity	[rad/s]
$p_{wtgenerator}$	Electrical machine pole pairs	[-]
ω_{el}	Generator electrical speed	[rad/s]
$v_{\alpha s}$	Stator voltage vector a component	[V]
$v_{\beta s}$	Stator voltage vector β component	[V]
$i_{\alpha s}$	Stator current vector a component	[A]
$i_{\beta s}$	Stator current vector β component	[A]
$\psi_{\alpha s}$	Stator flux vector a component	[Vm]
$\psi_{\beta s}$	Stator flux vector β component	[Vm]
$v_{\alpha r}$	Rotor voltage vector a component	[V]
$v_{\beta r}$	Rotor voltage vector β component	[V]
$i_{\alpha r}$	Rotor current vector a component	[A]
$i_{\beta r}$	Rotor current vector β component	[A]
$\psi_{\alpha r}$	Rotor flux vector a component	[Vm]
$\psi_{\beta r}$	Rotor flux vector β component	[Vm]
$L_{\sigma s}$	Stator leakage inductance	[H]
$L_{\sigma r}$	Rotor leakage inductance	[H]
L_m	Mutual inductance	[H]
L_s	Stator inductance	[H]
L_r	Rotor inductance	[H]
ω_{ss}	Generator stator synchronous speed	[rad/s]
f_s	Grid frequency of the balanced three phases	[Hz]
Q_s	Stator reactive power	[w]
Q_r	Rotor reactive power	[w]
σ	Substituent check equation 2.61	[-]
v_{ds}	The d component of the stator voltage	[V]
v_{qs}	The q component of the stator voltage	[V]
v_{dr}	The d component of the rotor voltage	[V]
v_{qr}	The q component of the rotor voltage	[V]

i_{ds}	Stator current vector d component	[A]
i_{qs}	Stator current vector q component	[A]
i_{dr}	Rotor current vector d component	[A]
i_{qr}	Rotor current vector q component	[A]
ψ_{ds}	The d component of the stator flux	[Vm]
ψ_{as}	The q component of the stator flux	[Vm]
ψ_{dr}	The d component of the rotor flux	[Vm]
ψ_{ar}	The q component of the rotor flux	[Vm]
P_s	Stator active power	[w]
P_r	Rotor active power	[w]
η_{IM}	Induction motor efficiency	[%]
f_{IM}	Induction motor rated frequency	[Hz]
v_{IM}	Induction motor rated voltage	[V]
i_{IM}	Induction motor rated current	[A]
ω_{ps}	Induction motor nominal speed	[rpm]
pf_{IM}	Induction power factor (cos φ)	[-]
P_{vfd}	Variable frequency drive rated power	[kW]
V_{vfd}	Variable frequency drive rated voltage	[V_{ac}]
I_{vfd}	Variable frequency drive maximum continuous current	[A]

* Together with the subscript “0” represents the nominal value, and with “s” the current value.

LIST OF FIGURES

LIST OF TABLES

1. INTRODUCTION

1.1. Motivations and objectives of the thesis

At the end of 2019, the total installed renewable energy power was 2 533 GW, with 7% (177 GW) being installed in 2019 [1]. In the European Union, the total installed renewable energy power was 497 GW, with 6% (31 GW) installed only in 2019 [1]. Of the total global renewable energy capacity, 650 GW represents wind energy, with 9.3% (60.4 GW) installed in 2019 [2], and 579 GW represents photovoltaic energy, with 20% (115 GW) installed in 2019 [1]. Of the total renewable energy capacity of the European Union, 204.6 GW represents wind energy, with 7.5% (15.4 GW) installed in 2019 [2],[3], and 130 GW represents photovoltaic energy, with 12.3% (16 GW) installed in 2019 [1].

Taking into account the European Union "2030 climate and energy framework" [4], which aims to reduce greenhouse gas emissions by at least 40%, increase the share of renewable energy to at least 32% of the total consumption and improve the energy efficiency by 32.5% or more until 2030 [4], it is necessary to upgrade and integrate the renewable energy plants besides for to the main consumers, also for the secondary consumers of fossil and electrical energy. A significant share of these consumers, which can be domestic or industrial consumers [5], is represented by pumping systems from irrigation or water supply and distribution plants.

Currently, the pumping systems (PS) used in irrigation of agricultural fields are powered by electricity from the national grid in areas where this grid is found, and by diesel or gasoline generators, where it is missing. Because most of these systems are used during the summer, with maximum demand on the hottest and sunniest days of the year, the solution for powering an irrigation PS may consist in PVGs (Photovoltaic generators) leading to an excellent integration of the PVGs into such systems.

Another solution for powering the pumping systems is the wind electrical generator (WEG), which, depending on the characteristics of the wind, can ensure, at the pumping site, the availability of energy during the night and on cloudy days.

Irrigation installations have evolved significantly in recent years through progressive modernization, reaching more efficient irrigation methods in terms of water exploitation and usage. This has been achieved by integrating various solutions that have replaced traditional gravity irrigation systems such as sprinkler or drip irrigation systems, which significantly improve water usage efficiency. The payback of those methods represents the drastic increase in the energy consumption of the installations.

The investments in upgrading the irrigation systems were made based on an economic profitability study considering a price for powering the pumping system, that has drastically increased in the last years.

The current favorable legislation combined with the price decrease of photovoltaic panels makes the agricultural sector consider upgrading their pumping systems with photovoltaic, wind or wind-photovoltaic hybrid generators to ensure the energy necessary for operating the pumping system. However, despite the economic profitability offered by pumping installations powered by photovoltaic, wind or by wind-photovoltaic hybrid generators and the fact that their market demand is constantly increasing, those types of systems still require a technological maturation for becoming more robust, durable, reliable and efficient.

Currently, the existing irrigation systems powered by photovoltaic, wind or wind-photovoltaic hybrid generators have low reliability, not ensuring the correct operation of the system throughout the designed lifetime. Although there are various solutions on the market, such as photovoltaic pump kits, they are generally only valid for low power installations [6], [7], [8], [9].

Taking into account the aforementioned, this doctoral thesis "MODELLING, SIMULATING AND CONTROLLING AN ISOLATED PUMPING SYSTEM, POWERED BY RENEWABLE ENERGY GENERATORS" presents the development and implementation of a reliable and robust solution for powering a pumping system by a photovoltaic or wind energy conversion systems. This doctoral thesis contributes to the objective of the European Union regarding the reduction of greenhouse gas emissions, increase of the renewable energy consumption share and increase the energy efficiency.

1.2. State of the art

Analyzing the existing solutions offered by specialized literature (quite poor in such information), can be observed a high degree of difficulty in integrating renewable energy generators into the existing pumping system, due to the appearance of several technical problems, due to the lack of an appropriate technology [10], [11]. In recent years, there has even been a reluctance of possible customers to power their pumping systems with renewable energy generators.

The companies that started installing pumping systems powered by renewable energy can be classified into 3 groups:

a) Companies operating in the irrigation industry: Those companies, taking advantage of the already existing customer portfolio, offered them to integrate photovoltaic generators into their pumping system, without mastering the electrical protection part and electronic tuning. As a result, as can be seen in the pictures below (Figure 1.1.), many installations caught fire. Example: RiegoSolar from Spain [12].

b) Companies operating in the renewable energy (photovoltaic) sector: Those companies possessing extensive experience in the field of photovoltaic energy production have expanded their market by offering photovoltaic generators to existing pumping systems. Because these companies did not possess any expertise in the hydraulics sector, they treated these projects like a consumer that needed to be powered, ignoring the effects of hydraulic shock, water hammer, and cavitation [13-15]. Because of this, the lifetime of the pumps powered by photovoltaic energy has decreased considerably in the installations made by these companies (if a pump in the same installation lasted between 5 and 7 years before the installation of the photovoltaic generator, after its installation, the same pump model lasted a maximum one year). Example: Solenersa from Spain [16].

c) International enterprises with extensive experience in sectors like irrigation, pumps, power electronics and renewable energies. Those enterprises, due to their business model, cannot adapt to the pumping system market that needs to be powered by renewable energy due to the uniqueness of each project (at the moment, no standard solution can be implemented in all projects because of the complexity and uniqueness of each hydraulic system); those companies can only offer solar kits with powers up to 10 kW. Example: Grundfos [17].

Figure 1.1. a) A variable frequency drive (VFD), from a pumping system powered by a photovoltaic generator, that caught fire due to electric shocks (picture taken by the author during the visit of a pumping system powered by a photovoltaic generator from Frutas to Rinconada [18]).

Figure 1.1. b) Dv/Dt filter [19] from a pumping system powered by a photovoltaic generator, that caught fire due to improper use. The DV/Dt filter is used for cables up to 50 m long. For cables longer than 50 m, sinusoidal filters are recommended (picture taken by the author during the visit to a pumping system powered by a photovoltaic generator from Frutas to Rinconada [18]).

Figure 1. 1. The components of a pumping system powered by photovoltaic generator that caught fire

A high-performance pumping system powered by renewable energy has a particular complexity as it requires a perfect integration in a single integrated system of 4 subsystems from different technical fields:

1. Renewable energy generator (photovoltaic generator, wind generator or wind-photovoltaic hybrid generator);
2. Electrical system;
3. Hydraulic system;
4. Control system.

1.2.1. *State of the art of pumping systems powered by photovoltaic energy conversion systems*

In recent years, due to the continuous decrease in the price of photovoltaic panels, irrigation with photovoltaic energy has become increasingly tempting and represents the type of system that draws the greatest research effort among pumping systems powered by renewable energies. The only drawback for the possible customers remains the lack of the technology necessary for robust and reliable installations. The payback of the investment in irrigation with a photovoltaic generator is about 6 or 7 years, assuming a reliable system.

According to studies on the size of the potential market for photovoltaic pumping systems, the market is huge. Some significant data on the market size of the pumping systems powered by renewable energy generators is given in Table 1.1. [20]:

Table 1. 1. Data about the market size of the pumping systems powered by renewable energy generators [20]:

Country	Irrigated area (ha)	Irrigated area using underground water (ha)	Market size of the pumping systems powered by renewable energy generators	Value of the market size of the pumping systems powered by renewable energy generators
China	61.899.940	18.658.742	43.691	6.554
USA	28.375.752	18.384.053	32.612	4.892
Bangladesh	5.049.400	3.786.322	6.462	1.292
Turkey	5.215.144	1.621.546	3.744	749
Brazil	4.463.691	969.527	2.669	534
Australia	4.068.965	940.612	2.506	627
Peru	1.729.069	489.950	1.180	295
Algeria	569.418	368.489	654	163
South Africa	1.498.000	127.330	642	161

Photovoltaic powered pumping systems become particularly complex when the installed power increases, when they are directly connected to the irrigation system (without a water storage), when they are isolated (without support from a power grid) and when the hydraulic systems are very complex.

From a technological point of view, the characteristics of pumping systems can be divided into two categories:

1. Characteristics of a technologically simple system
    - Installed power < 25KW;
    - Pumping in a water storage at variable pressure and flow;
    - Hybridized with the power grid;
    - Hybridization with inverter (the pumps operate at a nominal frequency of 50 Hz);
    - Pumping systems with a single pump;
    - Fixed structure photovoltaic generator
    - Irrigation through drip irrigation system

2. Characteristics of a technologically complex system
    - Installed power >> 25KW;
    - Pumping directly into the irrigation system at constant pressure and flow;
    - Isolated from the power grid;
    - Hybridization with variable frequency drive (the pumps operate at variable frequency);
    - Pumping system with pumps in parallel and series, connected to a complex hydraulic network,
    - Photovoltaic generator with one or two axis trackers
    - Irrigation through sprinklers.

By the delimitation made previously, it can be understood that a pumping system is considered simple from a technological point of view when, by the typology type of the system, the effects of the intermittency and fluctuations of the power source are partially or totally reduced, and when the flow rate and pressure variations can be correlated with the variation (fluctuations and intermittency) of the power produced by the photovoltaic generator. For example, the effect of fluctuations in the power available from the photovoltaic generator can be partially reduced by oversizing the photovoltaic generator at a relatively acceptable cost, in the case of pumping systems with low nominal power (below 25 kW), or completely reduced in the case of its hybridization with the power grid, because the problem is solved by compensating the lack of energy from the photovoltaic generator with the energy available from the power grid. Pumping at variable flow and pressure can be correlated to a large extent with the variation (fluctuations and intermittency) of the energy available from the photovoltaic generator in the case of pumping into a water storage at variable flow and pressure, and to an acceptable extent in the case of drip or flood irrigation, due to the wide range of admissible flow and pressure variation.

A system is technologically complex when the effects of fluctuations and intermittency of the power supply cannot be reduced through the system typology and/ or when the pumping systems operate at constant pressure and/ or flow. For example, technologically complex systems are both an isolated pumping system powered only by a photovoltaic generator (there is no connection with the power grid) and a high-power pumping system, because oversizing the photovoltaic generator is not economically feasible, and the problems caused by photovoltaic generator powers intermittency and fluctuations must be overcome by technological means (highly efficient control systems). Direct sprinkler irrigation represents also a complex system from a technological point of view because the pumping into the hydraulic network is done at a high and constant pressure and can be correlated to the variation (fluctuations and intermittency) of the energy available in the photovoltaic generator only through highly efficient technological means.

Some of the technological problems of the pumping systems powered by photovoltaic generators highlighted previously, were tried to be solved by the implementation of an European research project called Market uptake of an innovative irrigation Solution based on LOW WATer-Energy consumption (MASLOWATEN), coordinated by the Polytechnic University of Madrid (UPM) and supported by the 2020 European Horizon program, with a budget of 5 million euros.

Through this project, some of the presented problems were researched, by implementing 5 high power pumping systems powered by photovoltaic generators [21], from which, the most significant ones are:

1. **Alter do Chão**, Portugal, 140 kW – isolated pumping system powered by a hybrid photovoltaic and diesel generator;
2. **Uri**, Sardinia, Italy, 40 kW - isolated sprinkle irrigation system powered by a photovoltaic generator hybridized with the power grid;
3. **Tamelalt**, Morocco, 120 kW – isolated pumping system powered by a photovoltaic generator hybridized with the power grid.

From the European Maslowaten project resulted the simulation tool developed to design a high-power pumping system powered by a photovoltaic generator called Sisifo [22]. The limitations of this tool consist of the fact that only relatively simple pumping systems, from the hydraulic point of view, and only systems powered by a photovoltaic generator can be simulated.

The typology of the pumping systems that can be simulated in Sisifo [22] consists of a single pump that can pump water into water storage at variable flow and pressure, or directly into an irrigation network at constant pressure and flow (see Figure 1.2.)

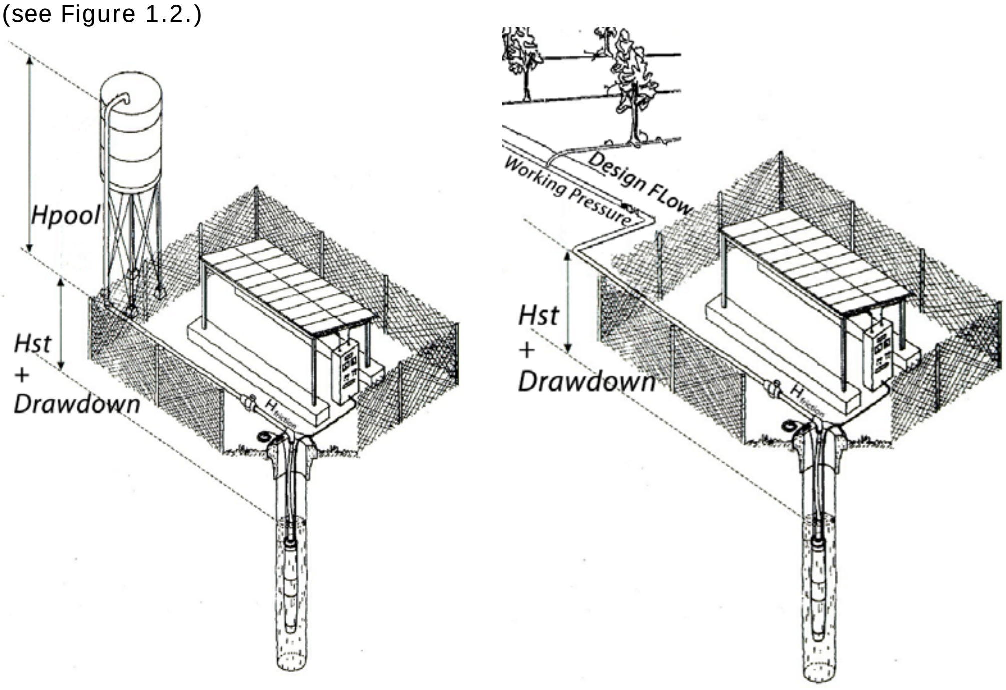

Single pump that can pump water into a water storage at variable flow and pressure.

Single pump that can pump water directly into the irrigation network at constant pressure.

Figure 1. 2. Pumping systems typology that can be simulated in Sisifo [22]

The **Sisifo** simulation and design tool is developed to simulate only pumping systems powered by photovoltaic generators, not by wind generators. This tool also presents little capabilities in designing and simulating complex hydraulic typologies with several pumps in parallel and/or series.

1.2.2. State of the art of pumping systems powered by wind energy conversion systems

The pumping systems powered by wind generators have lagged behind those powered by photovoltaic generators, although, as the price of photovoltaic energy, the price of wind energy has dropped substantially in recent years. Without mentioning that there are irrigation sites where wind energy resources are superior to photovoltaic ones. It should be noted that there is currently no reliable technology for pumping systems powered by wind energy.

The weak development of pumping systems powered by wind energy can also be due to the low supply of wind turbines with small and medium powers (powers between 5kW and 1 MW) and the difficulty raised by the impossibility of offering a varied range of powers, compared to the modularity offered by photovoltaic generators.

Taking into account that in many areas a pumping system powered by photovoltaic energy can operate for about 1700 hours per year, while one powered by wind energy can operate for 3500 or even 4000 hours, the operating period limitation offered by the pumping systems powered by photovoltaic generators can be overcome at specific sites by the ones powered by (or hybridized) with wind generators.

This doctoral thesis solves exactly this need by evaluating the possibility of integrating wind generators within isolated pumping systems.

Advantages and disadvantages of the pumping systems powered by a wind generator compared to those powered by a photovoltaic generator

Advantages:

1. The irrigating period using wind energy can be longer than the one using photovoltaic energy.
   Even if the price of a wind electrical generator is higher than that of a photovoltaic generator with the same nominal power, after a certain number of operating hours with wind energy, the irrigation with it becomes more profitable.

2. Wind energy irrigation can provide 100% of the energy demanded by the pumping system, in sites where there are more wind energy resources than photovoltaic energy.
   Photovoltaic powered pumping systems are not always able to pump the required water volume when the solar hours are less than the minimum operating hours. Therefore, these systems need the support of a diesel generator or a power grid during the night.

3. The area occupied by a wind generator is smaller than that occupied by a photovoltaic generator.
   The area occupied by a photovoltaic generator increases directly proportionally with its installed power, a fact that is not applicable to a wind generator.

4. The wind generator maintains its electrical efficiency throughout its lifetime
The wind generator maintains its electrical output throughout the lifetime of the project, while the photovoltaic generator decreases its electrical output over its lifetime, so that after 20 years of production, the output is approximately 20% lower, a feature that is not always taken into account when sizing the photovoltaic generator to power the pumping system.

5. A wind energy conversion system has already integrated the complex power electronics systems.
Due to this fact, the main parameters can be controlled without additional costs, while, in pumping systems powered by a photovoltaic generator, the power electronics must be integrated at an additional cost.

6. The possibility of exporting a larger amount of electrical energy increases the economic profitability of the system.
A wind generator can produce twice as much electrical energy as a photovoltaic generator with the same nominal power, and a higher excess of electrical energy can be exported, increasing the economic profitability of the system.

7. Fewer and smaller power fluctuations.
In isolated pumping systems powered by a photovoltaic generator, cloud passing is a serious problem. The photovoltaic generator can be covered by the shadow of a cloud in a few second, and the generator power will suddenly drop (for example, from 700 W/m2 to 150 W/m2). This sudden drop in power can cause hydraulic shock (cavitation and water hammer in the hydraulic system) and electrical shock (which also affects power semiconductors, due to the large voltage variation after the drop). Although the wind exhibits turbulence and varies more frequently, due to the inertia of the wind turbine rotor and generator, these drops cannot be as sudden, avoiding most hydraulic and electrical shocks.

Disadvantages:

1. The lack of correlation between the available wind energy and the volume of water needed to irrigate the crops.
Between a crop irrigation system and a photovoltaic generator, there is a correlation because the crops need to be irrigated especially during periods of high solar irradiation due to evapotranspiration.

2. The pumping systems, pumping directly into a hydraulic network with high volume and pressure variations, need water storage for pressure and flow regulation.
Due to fluctuations in wind speed and turbulences, direct pumping into a hydraulic network at constant pressure becomes problematic. The problem is that, depending on the weekly or monthly wind regime and the lack of correlation with the volume required to irrigate the crops, the required water storage size to maintain the flow and pressure constant can be very large.

3. The Pumping systems powered by a wind generator require more maintenance.
   Wind generators are more complex than photovoltaic generators and therefore require more maintenance. However, the availability provided by modern wind turbines is greater than 97% [23].
4. The wind resources are more difficult to evaluate and vary a lot with site location and orography.
   Photovoltaic resource evaluation is much simpler and has less uncertainty than wind resource evaluation, which also varies a lot from one area to another. However, modern assessment methods and the available virtual data to assess photovoltaic and wind energy resources have increased their accuracy in recent years.
5. A wind generator has a lower modularity (scalability) than a photovoltaic one.
   In a photovoltaic powered pumping system, the photovoltaic generator is easily scalable to obtain the desired power by increasing the number of strings (a string consists of photovoltaic panels connected in series to ensure the desired voltage). Wind generators can be scalable by placing more wind turbines, but the huge differences between wind turbine powers make it very difficult to avoid oversizing the wind generator.
6. Lack of manufacturers of small, medium-sized wind generators (10 kW – 500 kW)
   Currently, on the international market, this type of wind generator is not in high demand, which is why companies have abandoned their production [24].
7. The lack of wind generators adapted to pumping systems.
   Controlling a wind generator connected to a pumping system must be done exactly for this purpose, and currently there is no option commercially available on the market [25].

Taking into account the potential of the international market, the current work researched a solution capable of generating wind energy for an isolated pumping system without photovoltaic hybridization.

1.3. Thesis objectives and purpose

Considering the current state of the pumping systems powered by renewable energy research, which is almost non-existent and because the few installations carried out internationally are unreliable, this Ph.D. thesis entitled "Modelling, simulation and management of an isolated pumping system, powered by renewable energy sources" contributes to their development and implementation.

The main objectives addressed and solved in this Ph.D. thesis are:

- Advanced dynamic modelling, controlling and simulating of a photovoltaic generator, respectively, of a wind generator modified for powering a pumping system;
- Advanced dynamic modelling, controlling and simulating the operation of a complex pumping system (several centrifugal pumps in parallel and/ or in series);
- Analysis, synthesis and implementation of control structures of a pumping system powered by a photovoltaic or wind energy conversion system.

1.4. Thesis structure

In summary, ***Chapter 1*** - ***INTRODUCTION*** - presents the research topic, the purpose, the state of the art of the research and the objectives of the thesis. The proposed research topic consists of modelling, control and simulation the operation of a complex (pumps connected in series and/or parallel) and isolated pumping system, powered by a wind-photovoltaic hybrid generator.

Chapter 2, called ***PUMPING SYSTEMS***, presents, through adequate modelling and simulation, the proposed controlled strategies for the operation of a complex pumping system, consisting of several pumps in series and in parallel, powered by a fluctuating and intermittent power source.

Chapter 3, entitled ***PHOTOVOLTAIC ENERGY CONVERSION SYSTEMS (PECS)***, presents, through adequate modelling and simulation, the proposed controlled strategies for the operation of a PECS.

Chapter 4 – ***WIND ENERGY CONVERSION SYSTEMS (WECS)***, presents, through adequate modelling and simulation, the proposed controlled strategies for the operation of a WECS.

Chapter 5, called ***PUMPING SYSTEMS POWERED BY PHOTOVOLTAIC ENERGY CONVERSION SYSTEMS (PSPPECS)***, presents, through adequate modelling and simulation, the proposed control strategies for the operation of a pumping system powered by a photovoltaic energy conversion system. In partial operation, the power absorbed by the pumping system tracks the power generated by the photovoltaic energy conversion system and, at full load, the irrigation pressure is controlled.

Chapter 6, entitled ***PUMPING SYSTEMS POWERED BY WIND ENERGY CONVERSION SYSTEMS (PSPWECS)***, presents, through adequate modelling and simulation, the proposed control strategies for operation at partial load (the power absorbed by the pumping system tracks the power generated by the wind energy conversion system), and at nominal load (the power generated by the wind energy conversion system is limited according to the power required by the pumping system nominal operation).

In ***chapter 7***, ***FINAL CONCLUSIONS, PERSONAL CONTRIBUTIONS AND DEVELOPMENT PERSPECTIVES*** are pointed out the author's contributions along with possible directions for further research development. The overall research contribution brought by this thesis consists of the proposal of advanced models and control strategies for operating a complex and isolated pumping system powered by a wind or photovoltaic energy conversion system.

2. PUMPING SYSTEM

The current chapter presents the modelling, controlling and simulation of a pumping system. The first subchapter (***2.1. Pumping system description***) presents a short description of a general pumping system and its components together with the most common layouts of such a system. The second subchapter (***2.2. Pumping system modelling***) consists of a nonlinear mathematical model of a general pumping system, and the third subchapter (***2.3. Controlling a pumping system***) presents the proposed control strategy. In the fourth subchapter (***2.4. Pumping system simulations***), the performance of the proposed control strategy is determined by analyzing several performance indicators during five simulations. One simulation in which the pumping system operates at a fixed (nominal) speed. And four simulations where the pumping system operates at desired variable speed, flow, pressure and power. Finally, in the last subchapter (***2.5. Conclusions***) are presented the chapter conclusions.

2.1. Pumping system description

The main components and operating conditions of a complex pumping system will be described in detail in this subchapter.

2.1.1. Water source

The working fluid of the pumping systems considered in the presented work is fresh water (H_2O in liquid state) at standard ambient temperature and pressure. Fresh water is usually intended for irrigation and/or water supply and distribution. The water can be collected from a river, channel or aquifer.

The water can be extracted from a river, channel, damp and/or deposit with the help of a pumping system that is generally placed above the water level.

The aquifer (ground) water can be extracted through a well or borehole that is drilled into the ground until it reaches the water level. Normally inside a borehole, a steel tube is placed that acts as a sleeve for protecting the electric motor, pump and pipes. The electric motor converts the electric power into mechanical power, which is transmitted to the pump by a driving shaft. The pump converts the mechanical power into hydraulic power by pumping the water into the pipes with the help of a propeller. The water is pumped and distributed to the consumer through a hydraulic grid.

The water depth of the borehole when there is no water extraction from the borehole is called the static level and depends on the groundwater level. When the water starts being extracted from the borehole, the water level decreases and based on the extracted water flow, the new water depth stabilizes at a certain depth called dynamic level. Due to the reason that the dynamic level increases over time, the borehole has to be drilled greater than the water level, in order to install the pump at a depth ensuring it is submerged during the entire lifetime operation (taking into consideration the increase of the dynamic level over the lifetime of the borehole).

When the dynamic level increases, the power consumption of the pump increases proportionally because the pumping head depends on the dynamic level and not on the depth at which the pump is installed, a phenomenon that changes the optimal operation point of the pump. Every borehole has a specific volume flow (m^3/h) directly proportional to the increase in the dynamic level. Depending on the water needs, each borehole can be exploited in order to obtain the lowest increase in the dynamic level. The lower the increase in the dynamic level, the lower the pump head loss. The term used for a significant increase in dynamic level during extensive exploitation of a borehole is excessive pumping [26].

2.1.2. Hydraulic pumps

Pumps are machines (turbomachines) that deliver liquids. There are two main types of pumps: positive displacement and dynamic pumps. Positive displacement pumps force the fluid along by volume changes, while dynamic pumps add momentum to the fluid through fast-moving blades or vanes. Dynamic pumps can be rotary pumps (centrifugal) or special design pumps [27]. Dynamic pumps can provide high flow rates (69 000 m^3/h) with moderate pressure rise (few atm), while positive displacement pumps can provide low flow rates (23 m^3/h) at high pressures (300 atm) [27].

Due to the reason that irrigation, water supply and distribution require high flow rates at moderate pressure rise, in the current work only the centrifugal dynamic pumps will be considered. In centrifugal dynamic pumps, the fluid increases momentum while moving through openings and when it exits the diffuser section, the high velocity is converted into a pressure increase [27].

The centrifugal pumps can be submersible or surface pumps, depending on whether they are installed below (submersible) or above (surface) the dynamic water level.

Centrifugal pumps consist of an impeller rotating within a casing. The fluid that enters through the eye of the pump casing, is caught up in the impeller blades, and swirls outward into the diffuser part of the casing. The fluid gains both velocity and pressure while passing through the impeller [27].

2.1.3. Motors

The mechanical power required by a pump is delivered by a motor. The motor converts electrical power to mechanical power and transmits the mechanical power through a shaft to the pump. Although some manufacturers offer DC (Direct Current) motors for small power pumps, today most pumps are powered by an AC (Alternate current) asynchronous three-phase motor, because the cage induction motor is simpler, much cheaper and more robust than the DC motor [28].

2.1.4. Motor drives

Induction motor drives can be variable-speed drives that are based on the steady-state equivalent circuit of the motor or on vector-controlled drives that are based on dynamic models. Variable-speed drives (VSD) use stator voltage, slip power, variable-voltage, variable-frequency (V–f) or variable-current (V–I) as control methods, while vector-controlled drives use the indirect rotor flux-oriented vector or the direct vector control with airgap flux sensing as control methods [28].

Because most pumps use AC asynchronous three-phase motors, the current work focusses on soft starters for pumps operating at nominal grid frequency (50 Hz) or variable frequency drives (VFD) for pumps operating at variable frequency.
Both soft starters and VFDs can control the ramp-up and ramp-down of a motor during start-up and shut down operations.

In the case that the AC motor of the pump is intended to be powered up by a DC generator (for example, a photovoltaic generator), the VFD works also as an inverter, converting the voltage from DC to AC, while in the case of a soft starter, an additional inverter for converting the voltage from DC to AC has to be used.

2.1.4.1. Soft starter

Soft starters limit the starting torque and current by gradually increasing the voltage over a specific period. A similar procedure is applied to stopping the motor by gradually decreasing the voltage over a specific period.

The soft starters that drive the centrifugal pump induction motor limit the power absorption to the necessary one during the start and reduce the possibility of water hammer occurrence due to quick stopping [29].

Figure 2.1. presents the electrical diagram of a three-phase soft-starter based on a three-phase thyristor converter (controlled rectifier). Thyristors distort the voltage and current waveforms, generating harmonic torques until the induction motor has gained sufficient speed to connect the induction motor directly to the power line. Various starting programs can be implemented, such as maintaining a constant current or increasing the voltage [29]. As expected, the only drawback of soft starters is that the main currents during operation are not sinusoidal, leading to interference with other equipment on the same supply [30].

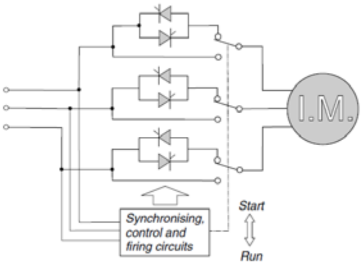

Figure 2.1. Soft starter electrical diagram [30]

2.1.4.2. Variable frequency drive (VFD)

The variable frequency drives (VFD) control the speed of an AC induction motor by varying the frequency of the input voltage that supplies to the motor.
In induction motors, the air gap flux is directly proportional to the ratio between the motor voltage and the frequency. If an induction motor is operating at constant speed, the flux remains constant because its voltage and frequency are constant. The torque is proportional to the flux. By changing the induction motor frequency, the speed and torque will also change. To maintain the torque constant while changing the speed, the voltage-frequency ratio (V/Hz) must be kept constant. The input voltage and the frequency of the VFD are constant and vary through a control strategy that kept the V/Hz ratio constant while changing the speed of the motor. This control method is also called the scalar control method because the VFD controls the frequency and magnitude of the voltage.

A VFD reduces the high starting current as the motor is accelerated to the operating speed because it is started at reduced voltage and frequency. The VFD increases the voltage and frequency while keeping the V/Hz ratio constant. A VFD can operate in open-loop or closed-loop mode. In the case of open-loop regulation, the reaction to sudden changes in load can be poor [31].

Figure 2.2. presents the electrical diagram of a Variable frequency drive. The VFD contains a three-phase diode converter and a three-phase inverter using insulated-gate bipolar transistors (IGBTs).

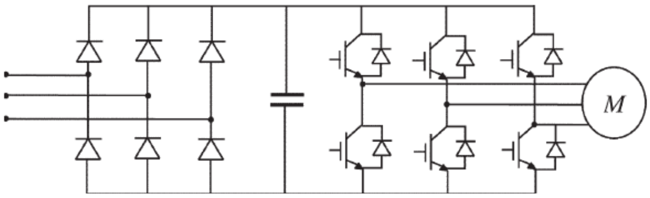

Figure 2.2. Variable frequency drive (VFD) electrical diagram [32]

2.1.5. Hydraulic network

The water is transported between two points with the help of a hydraulic network (pipeline). The hydraulic network can have an open channel flow if the pressure distribution within the flow is hydrostatic, since it has a free surface (boundary exposed to the atmosphere), or a pressurized flow if the flow pressure is above the atmospheric [26, 33]. Hydraulic networks are called pipe irrigation networks if they are destined for irrigation and water supply networks if they are destined to transport water for household or industrial use.

In general, a hydraulic network is mainly built from a pumping station that pumps the water through pipes that are interconnected with the help of some fittings. The flow is controlled by valves. Because hydraulic networks can be characterized with the pipe characteristic, a complete network can hydraulically be represented by a single pipe with hydraulic features equivalent to the entire network, called the network characteristic [34].

2.1.5.1. Hydraulic network design

In order to analyze a hydraulic network, first it has to be designed. This process consists in identifying the diameters of all pipes, their lengths and roughness, as well as where reservoirs, pumps, pressure reduction valves and other fittings are located [26, 34].

Because the hydraulic network design distinguishes from a hydraulic network analysis by the choice of the variables that are regarded as unknown, in Table 2.1 it can be seen the necessary parameters for hydraulic network design.

Table 2.1. Hydraulic network design parameters

Water source	
Water source dynamic level	m
Water source maximum dynamic level variation	m
Water source maximum extractable flow	m^3/h
Hydraulic network	
Hydraulic network pressure requirements	m
Hydraulic network flow requirements	m^3/h
Water deposit	
Water deposit capacity	m^3
Water deposit height	m

2.1.5.2. Hydraulic networks typologies

Hydraulic networks are very complex system and it is very hard, if not impossible, to find two identical hydraulic networks. For this reason, in this section, a classification based on their typologies is presented:

- I. Single pump-pumping stations, that have only one pump pumping the water through the pipe network.
  1. Depending on the consumer type, the water can be delivered at variable pressure and flow into a water storage, deposit or pool, from:
     - a. A channel with a surface pump (Figure 2.3),
     - b. A well with a submersible pump (Figure 2.4);
  2. Or at a constant pressure and flow directly into a water distribution network, from:
     - a. A channel with a surface pump (Figure 2.5),
     - b. A well with a submersible pump (Figure 2.6).
- II. Multiple pump-pumping stations, that have more than one pump pumping the water through the pipe network.
  1. Delivering water at variable pressure and flow into a water storage, deposit or pool, from:
     - a. A channel with parallel surface pumps (Figure. 2.7),
     - b. Parallel wells with submersible pumps (Figure. 2.8);
  2. Delivering water at constant pressure and flow directly into a water distribution network, from:
     - a. A channel with parallel surface pumps (Figure. 2.9),
     - b. Parallel wells with submersible pumps (Figure. 2.10),
     - c. A single borehole with a submersible pump in series with a single surface pump working with a water deposit for balancing the flow (Figure 2.11),
     - d. A single well with a submersible pump in series with a single surface pump working with a pressurized flow (without a water deposit for balancing the flow) (Figure 2.12),
     - e. Parallel wells with submersible pumps in series with parallel surface pumps working with a pressurized flow (without a water deposit for balancing the flow) (Figure 2.13);
     - f. Parallel wells with submersible pumps in series with parallel surface pumps working with a water deposit for balancing the flow (Figure 2.14).

In Figure 2.3, a single surface pump is presented that pumps water from a river or water channel into a deposit, at variable pressure and flow into a water deposit. The river or channel water level cannot vary too much, not more than the net positive suction head (NPSH) of the pump. The water from the deposit can be further used in a hydraulic network with the help of gravity. This type of pumping station can be found mostly in small power pumping stations (smaller than 10 kW), because it is not the most energy efficient system, as the water has to be pumped to a height higher than it is required (wasting energy).

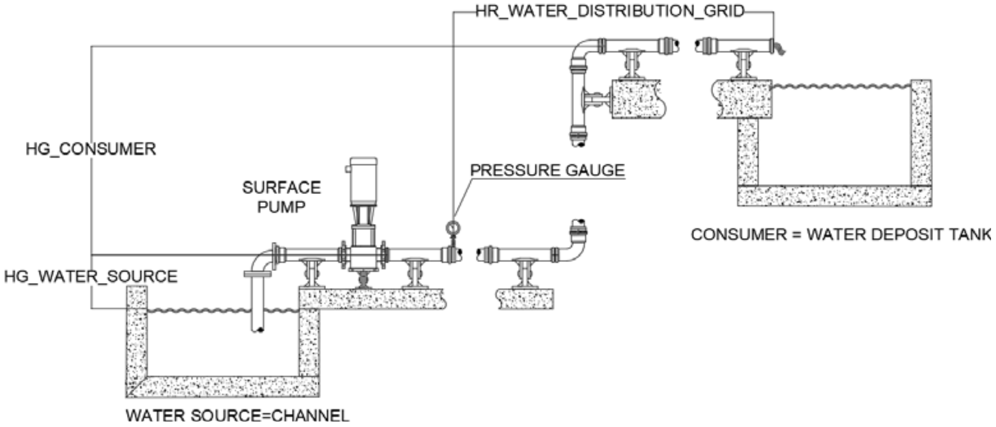

Figure 2.3. Single surface pump working at variable flow and pressure

In Figure 2.4, a similar single pump is presented pumping water at variable pressure and flow into a deposit as in Figure 2.3, the only difference is that the pump is a submersible one installed in a well/borehole below the lowest water level, in order to ensure that the water is always pumped. Similarly to the pumping station presented in Figure 2.3, this one can be found mostly in small power pumping stations (smaller than 10 kW) due to the same reason as not being the most energy efficient system, as it can waste some energy.

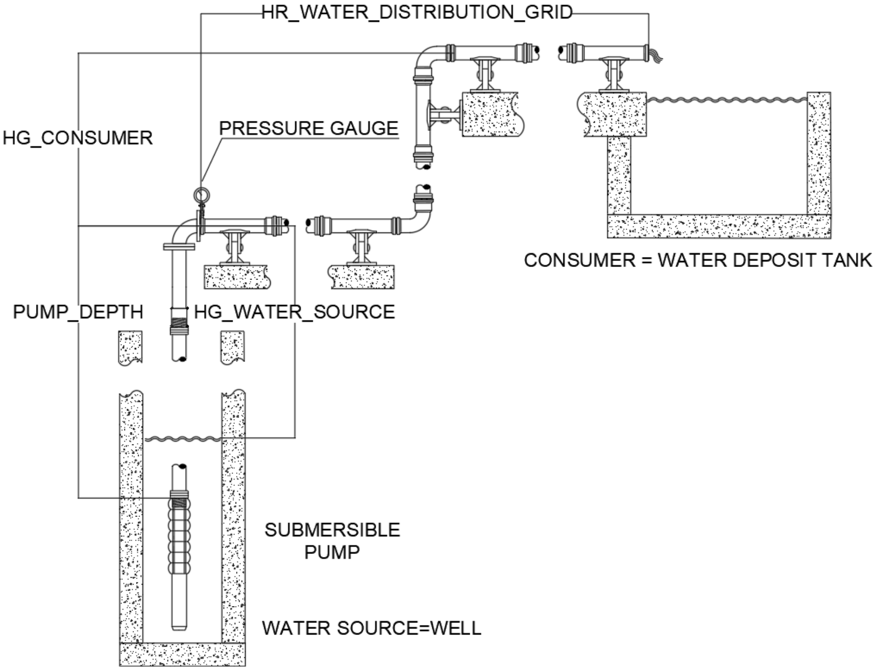

Figure 2.4. Single submersible pump working at variable flow and pressure

Figure 2.5 presents a single surface pump that pumps water from a river or a water channel into the hydraulic distribution network, at constant pressure and flow. The river or channel water level cannot vary too much, not more than the NPSH of the pump. This typology of pumping system can be found in irrigation systems close to rivers, lakes or open irrigation channels.

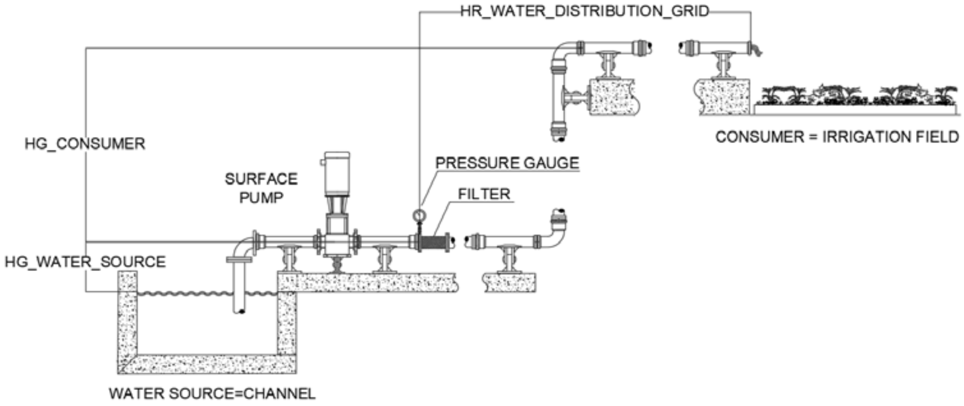

Figure 2.5. Single surface pump working at constant flow and pressure

Figure 2.6., presents a similar single pump pumping water into a hydraulic distribution network, at constant pressure and flow as the one presented in Figure 2.5, the only difference is that the pump is a submersible pump, installed below the lowest water level in the well/ borehole. This typology of the pumping system can be found in irrigation systems where the well/ borehole gives enough water flow.

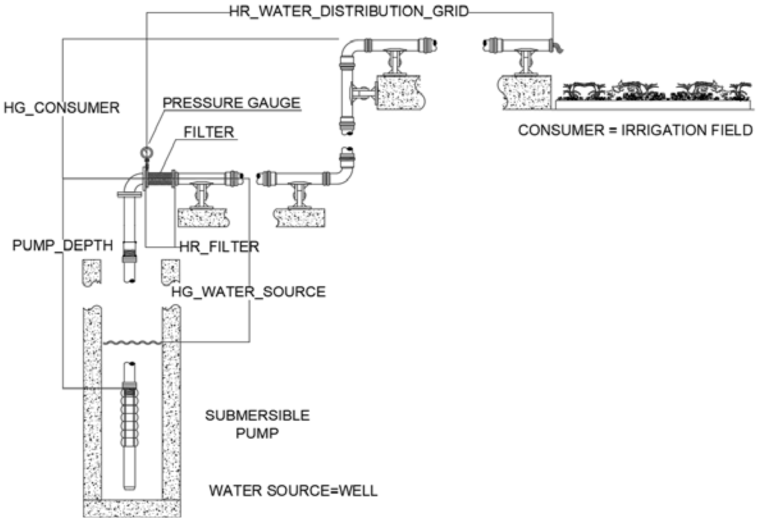

Figure 2.6. Single submersible pump working at constant flow and pressure

A multi-pump system, with parallel surface pumps, pumping water from a river, lake or channel at variable pressure and flow into a water storage such as an artificial (barrier) lake or dam, can be seen in Figure 2.7. The water level in the river, lake or channel cannot variate too much, not more than the NPSH of the pump. The water from the storage, the artificial (barrier) lake or dam, can be further used in a hydraulic network with the help of gravity. This typology of the pumping system can be found in systems where an enormous volume of water is delivered from a river or lake to a customer through a channel and all the volume of water must be quickly stored in a water storage.

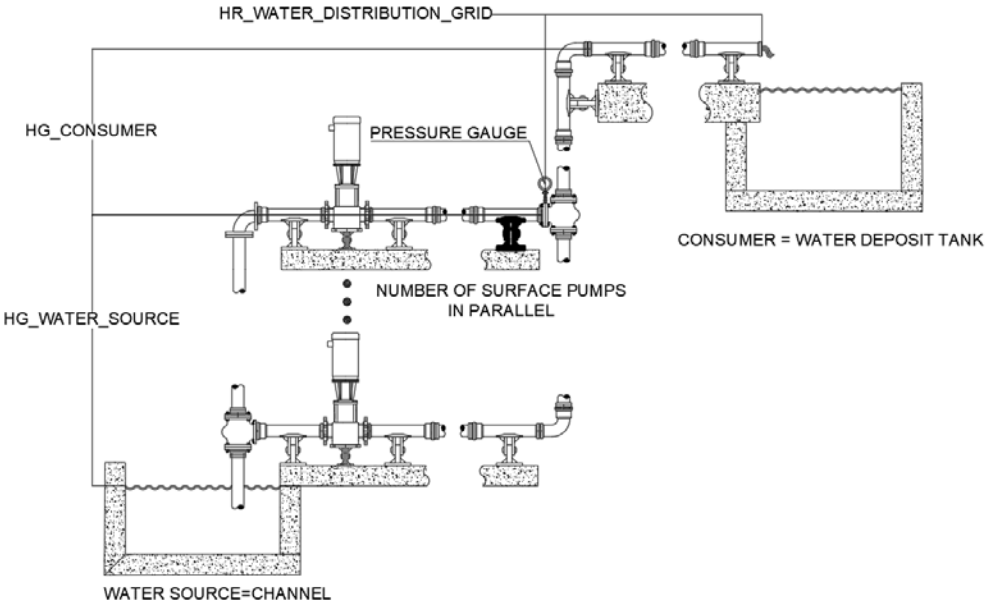

Figure 2.7. Parallel surface pumps working at variable flow and pressure

A similar pumping system as in Figure 2.7, is presented in Figure 2.8, where a multi-pump system, with parallel submersible pumps, pumping water from various wells/boreholes into a water storage such as an artificial (barrier) lake or dam. For correct operation, the pumps must be installed below the lowest water level in the wells/boreholes. The water from the storage (dam, artificial or barrier lake, can be further used in a hydraulic network with the help of gravity. This typology of the pumping system can be found in sites where the maximum extractable water flow from one well/ borehole is not enough; due to this reason, several wells/ boreholes are made for extracting the water from several aquifers into a water storage, such as an artificial (barrier) lake or dam.

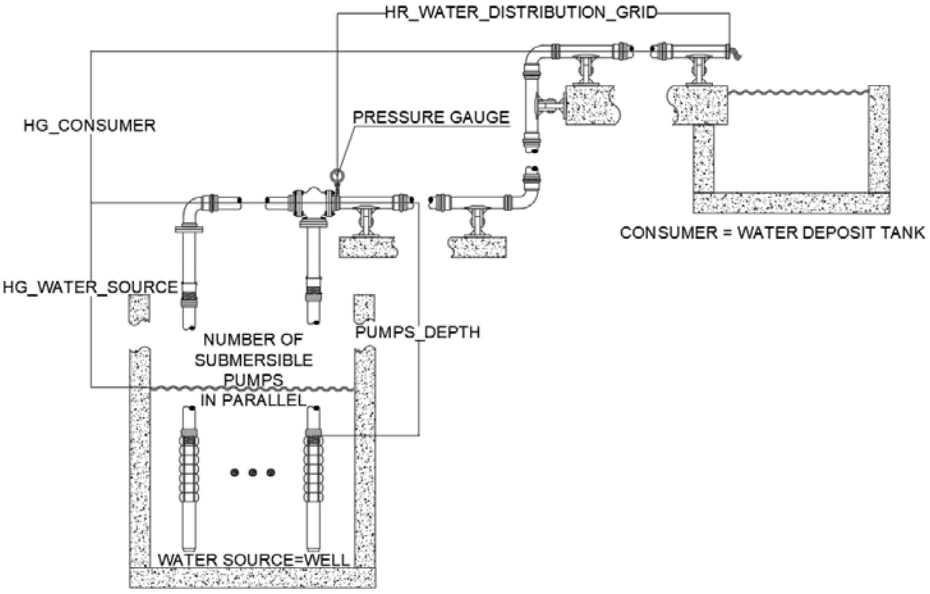

Figure 2.8. Parallel submersible pumps working at variable flow and pressure

A similar multi-pump system as in Figure 2.7, is presented in Figure 2.9, where parallel surface pumps pump water from a river, lake or channel at constant pressure and flow into a hydraulic distribution network. The water level in the river, lake or channel cannot variate too much, not more than the NPSH (Net Positive Suction Head) of the pump. This typology of the pumping system can be found in pumping systems that require a water flow with huge variations.

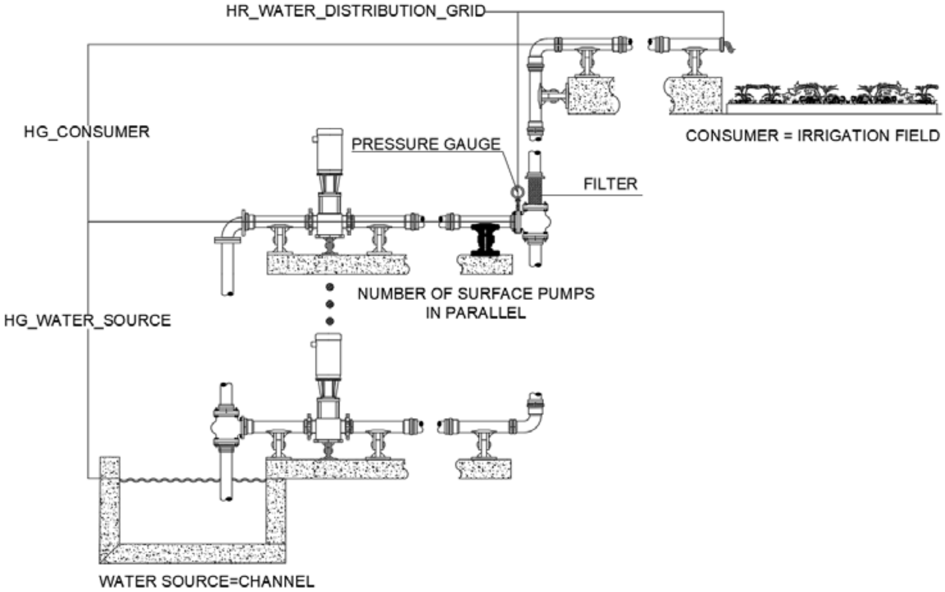

Figure 2.9. Parallel surface pumps working at constant flow and pressure

In Figure 2.10, a system similar to the one in Figure 2.8 is presented, where a multi-pump system, with parallel submersible pumps, pumps water from various wells/ boreholes into a hydraulic network. For correct operation, the pumps must be installed below the lowest water level in the wells/ boreholes. This typology of the pumping system can be found in sites where the maximum extractable water flow from one well/ borehole is not enough. Due to this reason, several wells/ boreholes are made to extract the water flow required by the consumer.

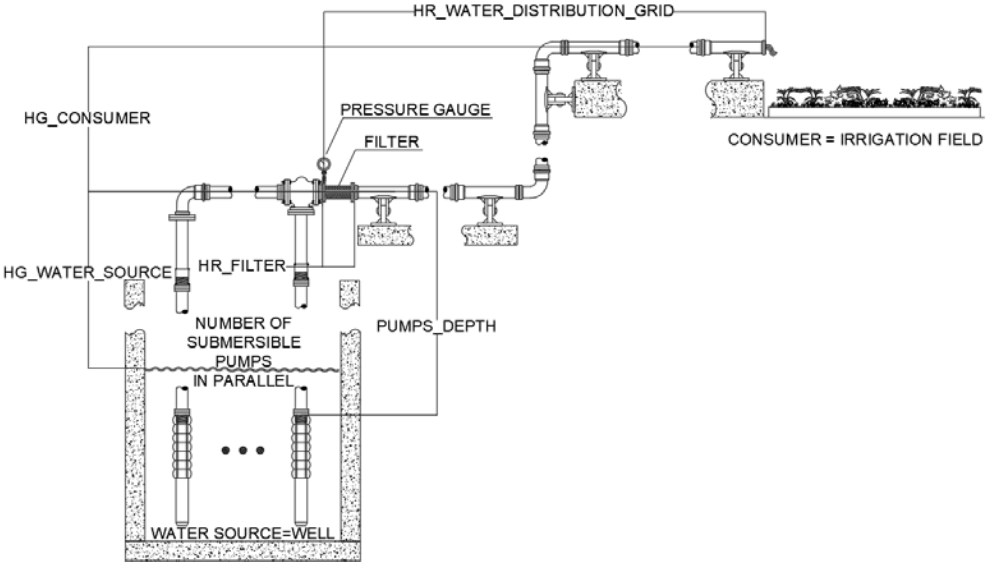

Figure 2.10. Parallel submersible pumps working at constant flow and pressure

In Figure 2.11, a pumping system with a single submersible pump is presented that pumps water at variable pressure and flow into a water storage (deposit tank or pool) from where the water is distributed at constant flow and pressure into a hydraulic network. For a correct operation, the submersible pump must be installed below the lowest water level in the well/ borehole. This typology of the pumping system can be found in irrigation systems, where the surface pump distributes a water flow higher (even four times higher) than the maximum flow that can be extracted from the well/ borehole by the submersible pump. Due to this reason, the water is stored in the deposit tank/ pool.

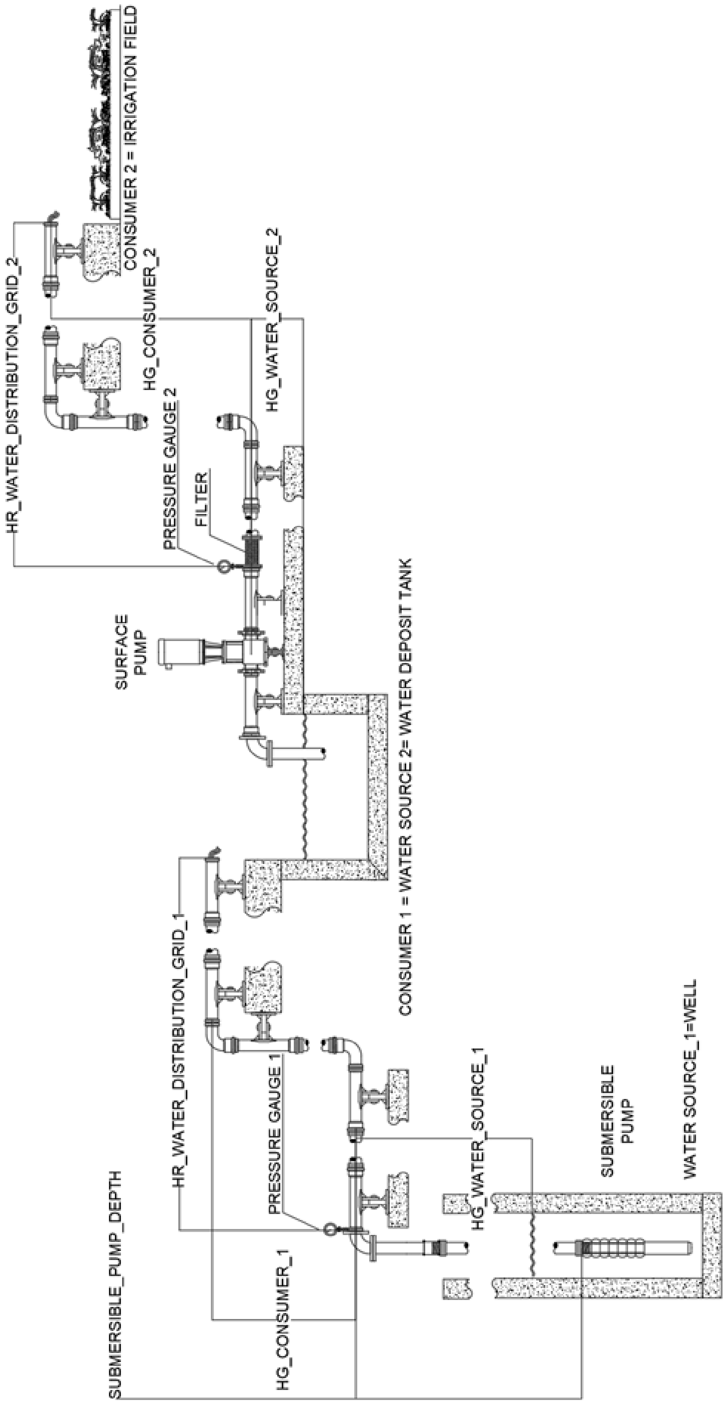

Figure 2.11. Single submersible pump in series with a single surface pump working at constant flow and pressure with a water deposit to balance the flow.

In Figure 2.12, it is presented pumping system with a single submersible pump in series with a single surface pump, where the water is pumped from a well/ borehole at constant flow and pressure into a hydraulic network. For a correct operation, the submersible pump must be installed below the lowest water level in the well/ borehole. This typology of the pumping system can be found in pumping systems, where a significant pumping head (pressure) is required.

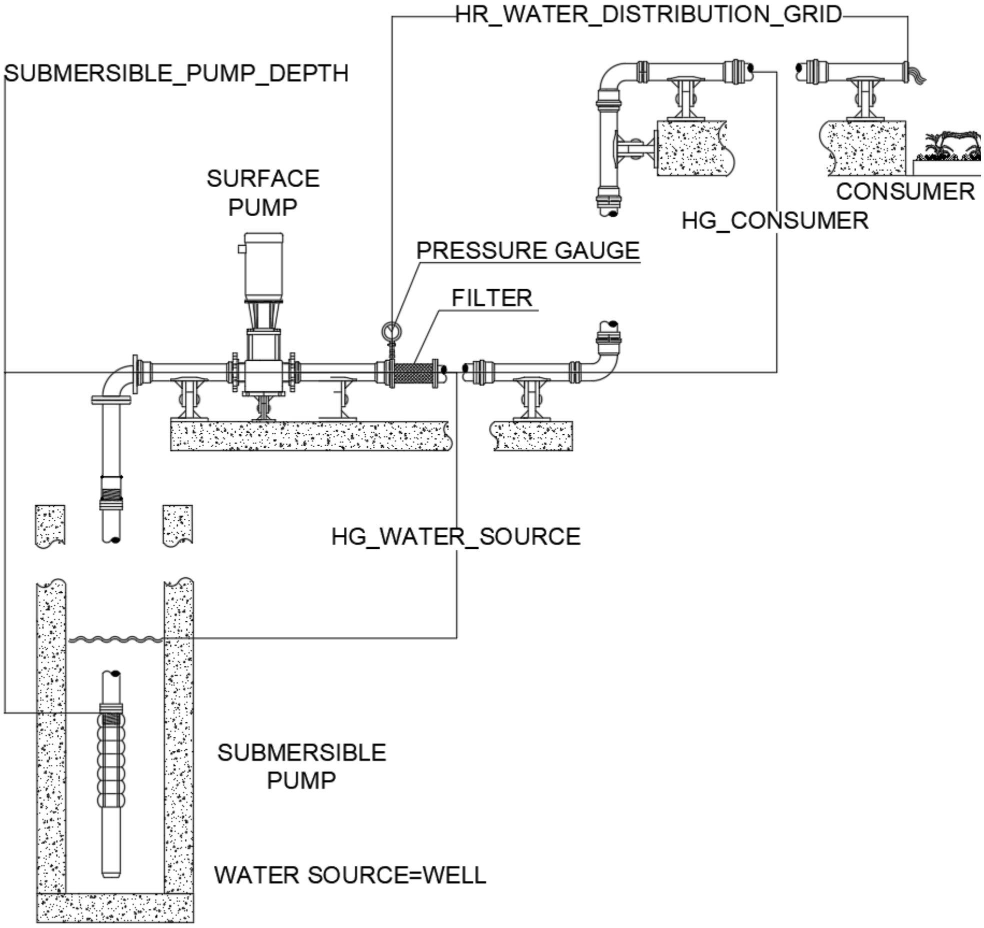

Figure 2.12. Single submersible pump in series with a single surface pump working at constant flow and pressure

In Figure 2.13, it is presented a pumping system with parallel submersible pumps in series with a parallel surface pump, where the water is pumped from several wells/ boreholes at constant flow and pressure into a hydraulic network. For a correct operation, the submersible pumps must be installed below the lowest water level in each well/ borehole. This typology of the pumping system can be found in pumping systems, where significant pumping head, pressure and a water flow with huge variations are required.

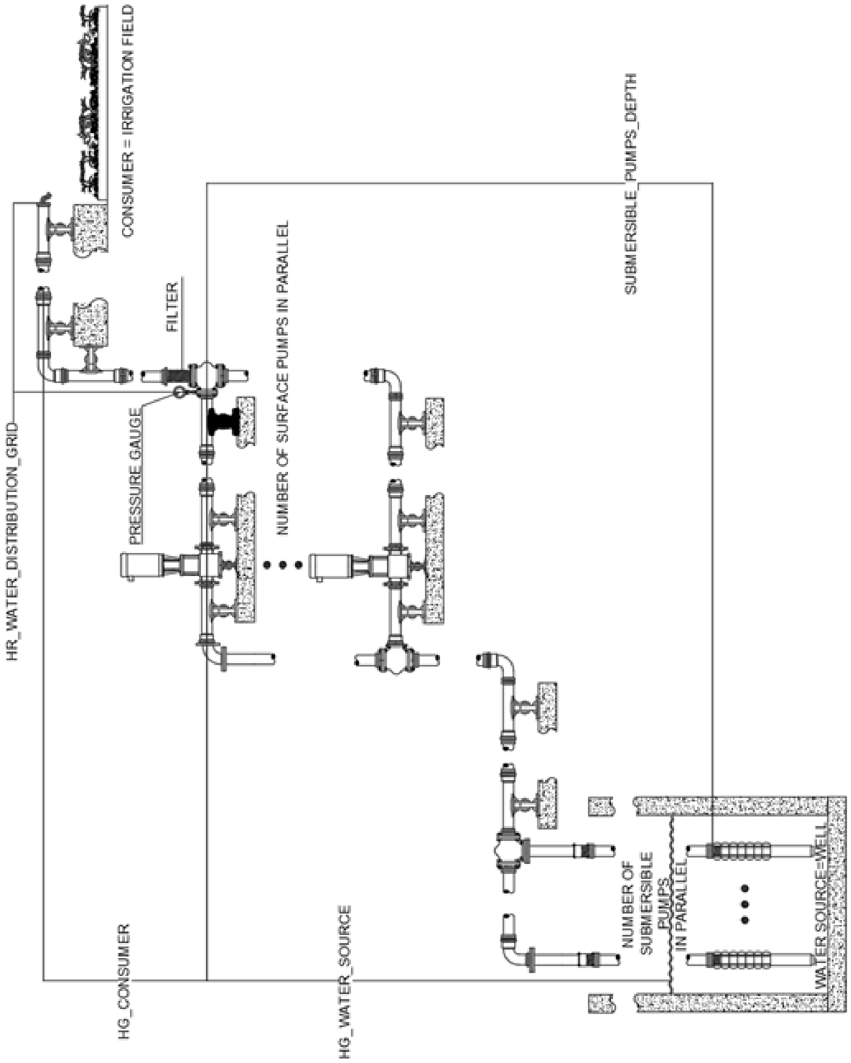

Figure 2.13. Parallel submersible pumps in series with parallel surface pumps working at constant flow and pressure

Figure 2.14 presents a pumping system with parallel submersible pumps that pumps water from several wells/ boreholes at variable pressure and flow into a water storage (pool, artificial lake, barrier lake or dam) from where the water is distributed at constant flow and pressure into a hydraulic network by parallel surface pumps. For a correct operation, the submersible pumps must be installed below the lowest water level in each well/ borehole. This type of pumping system can be found in shared irrigation systems, where the water is collected in an artificial (barrier) lake from several aquifers, to be used by several farmers to irrigate their fields, with a shared distribution hydraulic network and without restrictions.

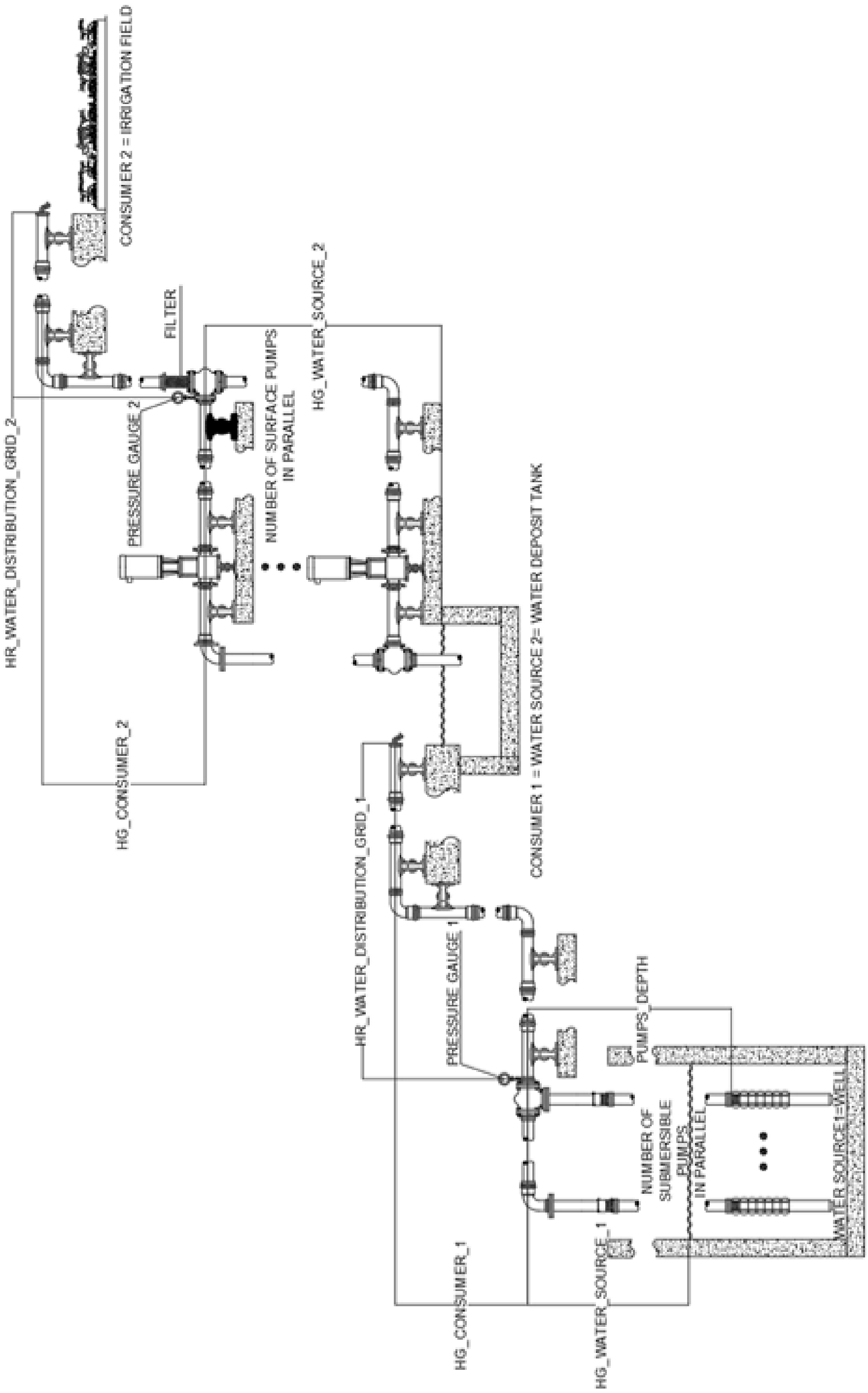

Figure 2.14. Parallel submersible pumps in series with parallel surface pumps working at constant flow and pressure with water deposit to balance the flow.

2.1.5.3. Hydraulic network analysis

From the hydraulic network design, the total head (pressure) and flow are obtained. In Table 2.2. are presented the parameters necessary to perform a hydraulic network analysis to obtain the discharges (and head losses) and pressures at each node in all pipes [26, 34].

Table 2.2. Necessary parameters for hydraulic network analysis

NECESSARY PARAMETERS FOR EACH WATER SOURCE	
Water source dynamic level	m
Water source maximum dynamic level variation	m
Water source maximum extractable flow	m^3/h
NECESSARY PARAMETERS FOR EACH SUBMERSIBLE PUMP	
Number of identical submersible pumps	-
Submersible pump installation depth	m
Submersible pump pipe diameter	m
Submersible pump operating limits	
Ambient temperature	°C
Minimum water speed to cool the jacket of the motor	m/s
Maximum number of starts in one hour	-
Minimum immersion depth	m
Submersible pump operating characteristics	
Submersible pump service flow rate curve (minimum 5 points)	m^3/h
Submersible pump service head curve (minimum same 5 points)	m
Submersible pump efficiency curve (minimum, at the same 5 duty points)	%
Submersible pump hydraulic power curve (minimum, at the same 5 duty points)	kW
Submersible pump maximum flow rate	m^3/h
Submersible pump head at theoretical 0 flow rate	m
Submersible pump minimum head (at maximum flow rate)	m
Submersible pump efficiency at maximum flow rate	%
Submersible pump hydraulic power at maximum flow rate	kW
Submersible pump electric motor characteristics	
Submersible pump motor nominal power	kw
Submersible pump motor power curve (minimum 4 points)	kw
Submersible pump motor efficiency curve (minimum the same 4 points)	%
Submersible pump motor rated frequency	Hz
Submersible pump motor rated voltage	V
Submersible pump motor rated current	A
Submersible pump motor number of poles	-
Submersible pump motor nominal speed	rpm
Submersible pump motor power factor ($\cos \varphi$)	%

NECESSARY PARAMETERS FOR EACH SURFACE PUMP	
Number of identical surface pumps	-
Surface pump installation height	m
Surface pump pipe diameter	m
Surface pump operating limits	
Ambient temperature	°C
Maximum operating time with closed port	-
Surface pump operating characteristics	
Surface pump service flow rate curve (minimum 5 points)	m^3/h
Surface pump service head curve (minimum same 5 points)	m
Surface pump efficiency curve (minimum, at the same 5 duty points)	%
Surface pump hydraulic power curve (minimum, at the same 5 duty points)	kW
Surface pump maximum flow rate	m^3/h
Surface pump head at theoretical 0 flow rate	m
Surface pump minimum head (at maximum flow rate)	m
Surface pump efficiency at maximum flow rate	%
Surface pump hydraulic power at maximum flow rate	kW
Surface pump electric motor characteristics	
Surface pump motor nominal power	kw
Surface pump motor power curve (minimum 4 points)	kw
Surface pump motor efficiency curve (minimum the same 4 points)	%
Surface pump motor rated frequency	Hz
Surface pump motor rated voltage	V
Surface pump motor rated current	A
Surface pump motor number of poles	-
Surface pump motor nominal speed	rpm
Surface pump motor power factor (cos φ)	%
HYDRAULIC NETWORK, NECESSARY PARAMETERS FOR EACH CONSUMER	
Hydraulic network pressure demand	m
Hydraulic network flow demand	m^3/h
Hydraulic network characteristics	h^2/m^5

2.2. Pumping system modelling

In the current section, a nonlinear mathematical model of the most demanding pumping systems typology containing a single pump is developed. This pumping system typology is presented in Figure 2.6 and contains a submersible centrifugal pump that delivers water from a well/ borehole directly into a hydraulic distribution network at different operating points. This pumping system model it was used by the author when publishing the paper from reference [35].

The mathematical model of the pumping system takes into consideration just the following aspects:

- The hydraulic network is characterized by a quadratic function equivalent to the entire pipeline;
- The standard properties of water (temperature=15, density=…).

All other aspects and parameters of the pumping system that are not mentioned above are neglected (for example, the influence of the ambient temperature, components temperature, etc.).

In Figures 2.15 and 2.16, are presented two typologies of pumping units delimited based on their driving unit, in Figure 2.15, it is presented a pumping system where the pump can only operate at a fixed speed (equivalent speed of the 50 Hz frequency), just the starting it is done with a soft-starter [36], and in Figure 2.16, it is presented a pumping system where the pump can operate at variable speed, with the help of a VFD [37].

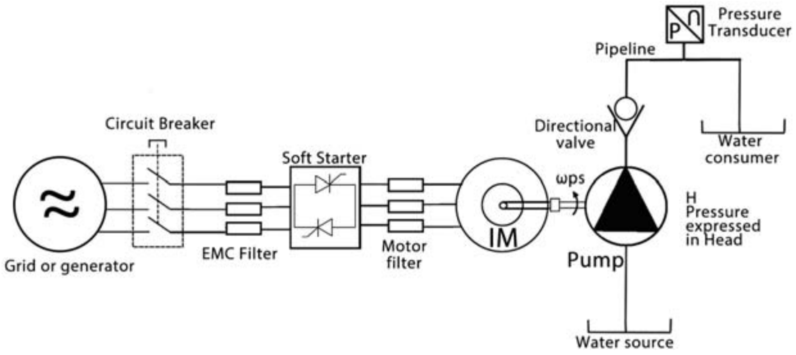

Figure 2.15. Pump motor powered by a soft starter

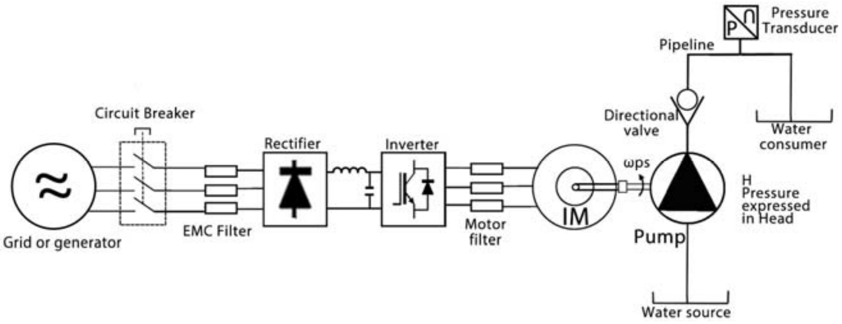

Figure 2.16. Pump motor powered by a VFD

The dynamic of the PS (Pumping System) is modelled according to the following equation of motion [38]:

$$I_p \cdot \dot{\omega}_p = T_{IM} - T_{pump} \tag{2.1}$$

that is based on the difference between the torques of the pump (T_{pump}) and induction motor (T_{IM}) torques, with I_{ps} being the PS moment of inertia and ω_{ps} - the angular velocity of the motor (pump) shaft.

2.2.1. Induction motor drives modelling

The efficiency of the motor drive is calculated based on the nominal power ($P_{drivenominal}$), output power ($P_{driveoutput}$) and the same three experimental parameters identified in reference [35]: "k0 representing no load losses, *k1* representing linear losses depending on the current (voltage drop across diodes) and *k2* representing losses depending on the square of the current (resistive losses) [39]".

$$\eta_{drive} = \frac{p}{p \cdot \left(k0 + k1 \cdot p_{driveoutput} + k2 \cdot \left(p_{driveoutput}\right)^2\right)} \tag{2.2}$$

where $p = P_{driveoutput/}P_{drivenominal}$, with the $P_{driveoutput}$ the induction motor drive output power.

The AC electrical power required (input) by the drive is:

$$P_{driveinput} = P_{driveoutput} / \eta_{drive} / \eta_{filter} / \eta_{cables} \tag{2.3}$$

where $P_{driveinput}$ is the induction motor drive input power, η_{drive} is the induction motor drive efficiency, η_{filter} is the DV/DT filter efficiency, and η_{cables} is the efficiency after the loss due to the voltage drop in the cables.

2.2.2. Induction motor modelling

The three-phase induction motor drives the pump, and it can be powered by power sources such as the national grid, diesel, gasoline, LPG (Liquefied petroleum gas), photovoltaic or wind generators, through soft starters [when running at a constant 50 Hz frequency (speed)], or through VFD [when running at a variable frequency (speed)].

2.2.2.1. Dynamic model

The dynamic model of the three-phase induction motor is modeled considering an ideal and linear machine where the space vector theory of the basic electric equations of the machines are applied [40]:

$$\vec{x}^{s} = x_\alpha + j \cdot x_\beta = \frac{2}{3}\left(x_a + e^{j\frac{2\pi}{3}} \cdot x_b + e^{2 \cdot j\frac{2\pi}{3}} \cdot x_b\right) \tag{2.4}$$

where:

x_a, x_b, x_c are three phases corresponding to the complex space vector;

x_α is the real component of the space vector;

x_β is the imaginary component of the space vector;

In order to develop induction motor space vector-based models, two different reference frames can be used: the stationary reference frame (α-β), and the synchronous reference frame (d-q), which rotates at synchronous speed. By using the direct or inverse rotational transformation, the space vector can be represented in any of these frames [40].

The electrical angular velocity ω_{IM} represents the angular velocity of the induction motor shaft angular velocity ω_{ps} multiplied by the pole pairs of the machine p_{motor}:

$$\omega_{IM} = \mathrm{p}_{\mathrm{motor}} \cdot \omega_{\mathrm{ps}} \tag{2.5}$$

The stator voltage is calculated based on the stator winding resistance R_s [40], in vector form, Equation 2.6 or in matrix form Equation 2.7:

$$\overrightarrow{v_s}^s = R_s \cdot \overrightarrow{i_s}^s + \frac{d\overrightarrow{\psi_s}^s}{dt} \tag{2.6}$$

$$\begin{bmatrix} v_{as} \\ v_{bs} \\ v_{cs} \end{bmatrix} = R_s \cdot \begin{bmatrix} i_{as} \\ i_{bs} \\ i_{cs} \end{bmatrix} + \begin{bmatrix} \dot{\Psi}_{as} \\ \Psi_{bs} \\ \Psi_{cs} \end{bmatrix} \tag{2.7}$$

where:
v_{as}, v_{bs}, v_{cs} [V] are the actual stator voltages for each phase winding;
i_{as}, i_{bs}, i_{cs} [A] are the actual stator currents for each phase winding;
Ψ_{as}, Ψ_{bs}, Ψ_{cs} [Vm] are the actual stator fluxes for each phase winding;
R_s [Ω] is the stator resistance;

Similarly to the stator voltage, the rotor voltage is calculated [40], in vector form, Equation 2.8 or in matrix form Equation 2.9:

$$\overrightarrow{v_r}^r = R_r \cdot \overrightarrow{i_r}^r + \frac{d\overrightarrow{\psi_r}^r}{dt} \tag{2.8}$$

$$\begin{bmatrix} v_{ar} \\ v_{br} \\ v_{cr} \end{bmatrix} = R_r \cdot \begin{bmatrix} i_{ar} \\ i_{br} \\ i_{cr} \end{bmatrix} + \begin{bmatrix} \dot{\Psi}_{ar} \\ \Psi_{br} \\ \Psi_{cr} \end{bmatrix} \tag{2.9}$$

where:
v_{ar}, v_{br}, v_{cr} [V] are the actual rotor voltages for each phase winding;
i_{ar}, i_{br}, i_{cr} [A] are the actual rotor currents for each phase winding;
Ψ_{ar}, Ψ_{br}, Ψ_{cr} [Vm] are the actual rotor fluxes for each phase winding;
R_r [Ω] is the rotor resistance;

The stator fluxes are obtained in the following equation [40]:

$$\begin{bmatrix} \Psi_{as} \\ \Psi_{bs} \\ \Psi_{cs} \end{bmatrix} = \begin{bmatrix} L_{\sigma s} + L_h & -\frac{1}{2}L_h & -\frac{1}{2}L_h \\ -\frac{1}{2}L_h & L_{\sigma s} + L_h & -\frac{1}{2}L_h \\ -\frac{1}{2}L_h & -\frac{1}{2}L_h & L_{\sigma s} + L_h \end{bmatrix} \cdot \begin{bmatrix} i_{as} \\ i_{bs} \\ i_{cs} \end{bmatrix} + \begin{bmatrix} \cos\omega_{\mathrm{P}} & \cos(\omega_{\mathrm{P}} + 2\pi/3) & \cos(\omega_{\mathrm{P}} - 2\pi/3) \\ \cos(\omega_{\mathrm{P}} - 2\pi/3) & \cos\omega_{\mathrm{P}} & \cos(\omega_{\mathrm{P}} + 2\pi/3) \\ \cos(\omega_{\mathrm{P}} + 2\pi/3) & \cos(\omega_{\mathrm{P}} - 2\pi/3) & \cos\omega_{\mathrm{P}} \end{bmatrix} \cdot \begin{bmatrix} i_{ar} \\ i_{br} \\ i_{cr} \end{bmatrix} \tag{2.10}$$

where:
L_h [H] is the self-inductance of the stator (twice the mutual inductance between the stator windings);
$L_{\sigma s}$ [H] is the leakage inductance of the stator windings;

Similarly, the rotor fluxes are obtained in the following equation [40]:

$$\begin{bmatrix}\Psi_{ar}\\ \Psi_{br}\\ \Psi_{cr}\end{bmatrix} = \begin{bmatrix} L_{\sigma r}+L_h & -\frac{1}{2}L_h & -\frac{1}{2}L_h \\ -\frac{1}{2}L_h & L_{\sigma r}+L_h & -\frac{1}{2}L_h \\ -\frac{1}{2}L_h & -\frac{1}{2}L_h & L_{\sigma r}+L_h \end{bmatrix} \cdot \begin{bmatrix} i_{ar}\\ i_{br}\\ i_{cr}\end{bmatrix} + \begin{bmatrix} cos\,\omega_P & cos(\omega_P - 2\pi/3) & cos(\omega_P + 2\pi/3) \\ cos(\omega_P + 2\pi/3) & cos\,\omega_P & cos(\omega_P - 2\pi/3) \\ cos(\omega_P - 2\pi/3) & cos(\omega_P + 2\pi/3) & cos\,\omega_P \end{bmatrix} \cdot \begin{bmatrix} i_{as}\\ i_{bs}\\ i_{cs}\end{bmatrix} \qquad (2.11)$$

where $L_{\sigma r}$ [H] is the leakage inductance of the rotor windings;

Stationary reference frame (α−β model)

For representing the voltage equations in the stationary reference frame, the rotor voltage equation must be multiplied by $e^{j\theta m}$ [41]:

$$\overrightarrow{v_s}^{s} = R_s \cdot \overrightarrow{i_s}^{s} + \frac{d\overrightarrow{\psi_s}^{s}}{dt} => \begin{cases} v_{\alpha s} = R_s \cdot i_{\alpha s} + \dfrac{d\psi_{\alpha s}}{dt} \\ v_{\beta s} = R_s \cdot i_{\beta s} + \dfrac{d\psi_{\beta s}}{dt} \end{cases} \qquad (2.12)$$

In Equation 2.13, it can be seen that the rotor voltage is 0, as there is no voltage supply to the rotor circuit in the induction machine of the squirrel cage [41]:

$$0 = R_r \cdot \overrightarrow{i_r}^{s} + \frac{d\overrightarrow{\psi_r}^{s}}{dt} - j \cdot \omega_{el} \cdot \overrightarrow{\psi_r}^{s} => \begin{cases} 0 = R_r \cdot i_{\alpha r} + \dfrac{d\psi_{\alpha r}}{dt} + \omega_{el} \cdot \psi_{\beta r} \\ 0 = R_s \cdot i_{\beta r} + \dfrac{d\psi_{\beta r}}{dt} - \omega_{el} \cdot \psi_{\alpha r} \end{cases} \qquad (2.13)$$

where:

$\overrightarrow{v_s}^{s}$ [V] is the stator voltage vector reference to the stator;
R_s [Ω] is the stator resistance;
$\overrightarrow{i_s}^{s}$ [A] is the stator current vector reference to the stator;
$\overrightarrow{\psi_s}^{s}$ [Vm] is the stator flux vector reference to the stator;
$v_{\alpha s}$, $v_{\beta s}$ [V] are the stator voltage vector α and β component;
$i_{\alpha s}$, $i_{\beta s}$ [A] is the stator current vector α and β component;
$\psi_{\alpha s}$, $\psi_{\beta s}$ [Vm] is the stator flux vector α and β component;
R_r [Ω] is the rotor resistance;
$\overrightarrow{i_r}^{s}$ [A] is the rotor current vector reference to the stator;
$\overrightarrow{\psi_r}^{s}$ [Vm] is the rotor flux vector reference to the stator
$i_{\alpha r}$, $i_{\beta r}$ [A] is the rotor current vector α and β component;
$\psi_{\alpha r}$, $\psi_{\beta r}$ [Vm] is the rotor flux vector α and β component;

Similarly to voltage equations, flux equations can be represented in stationary reference frame [41]:

$$\overrightarrow{\psi_s}^{s} = L_s \cdot \overrightarrow{i_s}^{s} + L_m \cdot \overrightarrow{i_r}^{s} => \begin{cases} \psi_{\alpha s} = L_s \cdot i_{\alpha s} + L_m \cdot i_{\alpha s} \\ \psi_{\beta s} = L_s \cdot i_{\beta s} + L_m \cdot i_{\beta s} \end{cases} \qquad (2.14)$$

$$\overrightarrow{\psi_r}^{s} = L_m \cdot \overrightarrow{i_s}^{s} + L_r \cdot \overrightarrow{i_r}^{s} => \begin{cases} \psi_{\alpha r} = L_m \cdot i_{\alpha r} + L_r \cdot i_{\alpha r} \\ \psi_{\beta r} = L_m \cdot i_{\beta s} + L_r \cdot i_{\beta r} \end{cases} \qquad (2.15)$$

In Figure 2.17 it is represented the equivalent circuit in the stationary (αβ) reference frame, where all the voltages, currents and fluxes magnitudes are sinusoidal with a frequency of synchronous speed ω_{ss} [41]:

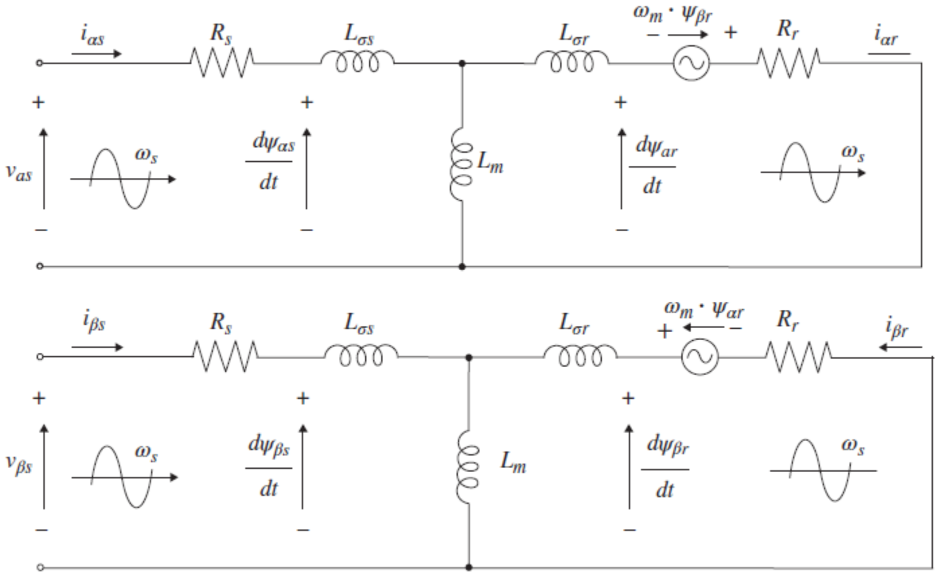

Figure 2.17. IM model (electric equivalent circuit) in α-β reference frame [40]

The synchronous speed of the IM is calculated according to [41]:

$$\omega_{ss} = \frac{60 \cdot f_s}{p_{motor}} \tag{2.16}$$

where:
ω_{ss}=104.72 [rad/s] is the generator stator synchronous speed;
f_s=50 [Hz] is the grid frequency of the balanced three phases;
p_{motor}=3 [pairs of poles] is the generator pairs of poles (6 poles).
The active power of the induction motor is calculated using the following formula [40, 42]:

$$P_{IM} = \frac{3}{2} \cdot \left(v_\alpha \cdot i_\alpha + v_\beta \cdot i_\beta\right) \tag{2.17}$$

where:
P_{IM} [w] is the induction motor active power;
v_α [V] is the voltage vector α component;
v_β [V] is the voltage vector β component;
i_α [A] is the current vector α component;
i_β [A] is the current vector β component;

The reactive power of the induction motor is calculated using the following formula [40]:

$$Q_{IM} = \frac{3}{2} \cdot \left(v_\beta \cdot i_\alpha - v_\alpha \cdot i_\beta\right) \tag{2.18}$$

where:
Q_{IM} [w] is the induction motor reactive power.

The electromagnetic torque of the induction motor can be calculated using any of the following formulas [41]:

$$\begin{gathered}
T_{IM} = \frac{3}{2} \cdot p_{motor} \cdot Im\{\psi_{\alpha\beta r} \cdot i^{*}_{\alpha\beta r}\} \\
T_{IM} = \frac{3}{2} \cdot p_{motor} \cdot \left(\psi_{\beta r} \cdot i_{\alpha r} - \psi_{\alpha r} \cdot i_{\beta r}\right) \\
T_{IM} = \frac{3}{2} \cdot p_{motor} \cdot Im\left\{\overrightarrow{\psi_s}^{s*} \cdot \overrightarrow{i_s}^{s}\right\} \\
T_{IM} = \frac{3}{2} \cdot p_{motor} \cdot \frac{L_m}{L_s} \cdot Im\left\{\overrightarrow{\psi_s}^{s*} \cdot \overrightarrow{i_r}^{s}\right\} \\
T_{IM} = \frac{3}{2} \cdot p_{motor} \cdot \frac{L_m}{L_r} \cdot Im\left\{\overrightarrow{\psi_r}^{s*} \cdot \overrightarrow{i_s}^{s}\right\} \\
T_{IM} = \frac{3}{2} \cdot p_{motor} \cdot \frac{L_m}{\sigma \cdot L_s \cdot L_r} \cdot Im\left\{\overrightarrow{\psi_r}^{s*} \cdot \overrightarrow{\psi_s}^{s}\right\} \\
T_{IM} = \frac{3}{2} \cdot p_{motor} \cdot L_m \cdot Im\{\overrightarrow{i_r}^{s*} \cdot \overrightarrow{i_s}^{s}\}
\end{gathered} \tag{2.19}$$

with the leakage coefficient being:

$$\sigma = 1 - \frac{(\mathrm{L_m})^2}{\mathrm{L_s} \cdot \mathrm{L_r}} \tag{2.20}$$

where:

$\overrightarrow{i_s}^{s}$ [A] is the stator current vector reference to the stator;

$\overrightarrow{i_r}^{s}$ [A] is the rotor current vector reference to the stator;

$\overrightarrow{\psi_s}^{s}$ [Vm] is the stator flux vector reference to the stator;

$\overrightarrow{\psi_r}^{s}$ [Vm] is the rotor flux vector reference to the stator.

$i_{\alpha r}$ [A] is the rotor current vector α component;

$i_{\beta r}$ [A] is the rotor current vector β component;

$\psi_{\alpha r}$ [Vm] is the rotor flux vector α component;

$\psi_{\beta r}$ [Vm] is the rotor flux vector β component;

L_m [H] is the mutual inductance;

L_s [H] is the stator inductance;

L_r [H] is the rotor inductance;

p_{motor} [pairs of poles] are the induction motor's pairs of poles.

Synchronous reference frame (d-q model)

The dynamic equations of the induction motor stator and rotor voltage Equations (2.21) and (2.22) can be represented in a synchronously rotating reference frame by multiplying them by $\mathrm{e}^{-j\omega ss}$ [40]:

$$\overrightarrow{v_s}^{a} = R_s \cdot \overrightarrow{i_s}^{a} + \frac{d\overrightarrow{\psi_s}^{a}}{dt} + j \cdot \omega_{ss} \cdot \overrightarrow{\psi_s}^{a} \Rightarrow \begin{cases} v_{ds} = R_s \cdot i_{ds} + \dfrac{d\psi_{ds}}{dt} - \omega_{ss} \cdot \psi_{qs} \\ v_{qs} = R_s \cdot i_{qs} + \dfrac{d\psi_{qs}}{dt} + \omega_{ss} \cdot \psi_{ds} \end{cases} \tag{2.21}$$

$$0 = R_r \cdot \overrightarrow{\imath_r}^a + \frac{d\overrightarrow{\psi_r}^a}{dt} - j \cdot (\omega_{ss} - \omega_{IM}) \cdot \overrightarrow{\psi_r}^a => \begin{cases} 0 = R_r \cdot i_{dr} + \dfrac{d\psi_{dr}}{dt} - (\omega_{ss} - \omega_{IM}) \cdot \psi_{qr} \\ 0 = R_s \cdot i_{qr} + \dfrac{d\psi_{qr}}{dt} + (\omega_{ss} - \omega_{IM}) \cdot \psi_{dr} \end{cases} \quad (2.22)$$

where:

a denotes that the space vectors refer to a synchronously rotating reference frame;

$\overrightarrow{v_s}^a$ [V] is the stator voltage vector reference to a synchronously rotating frame;

R_s, R_r [Ω] is the stator and rotor resistances;

$\overrightarrow{\imath_s}^a$ [A] is the stator current vector reference to a synchronously rotating frame;

$\overrightarrow{\psi_s}^a$ [Vm] is the stator flux vector reference to a synchronously rotating frame;

v_d, v_q [V] are the voltage vector d and q components;

ψ_{ds}, ψ_{qs} [Vm] are the d and q components of the stator flux;

i_{ds}, i_{qs} [A] are the d and q components of the stator current;

i_{dr}, i_{qr} [A] are the d and q components of the rotor current;

$\overrightarrow{\imath_r}^a$ [A] is the rotor current vector reference to a synchronously rotating frame;

$\overrightarrow{\psi_r}^a$ [Vm] is the rotor flux vector reference to a synchronously rotating frame;

ψ_{dr}, ψ_{qr} [Vm] are the d and q components of the rotor flux;

Similar to the voltage equations, the flux equations can be represented in an asynchronously rotating reference frame [40]:

$$\overrightarrow{\psi_s}^a = L_s \cdot \overrightarrow{\imath_s}^a + L_m \cdot \overrightarrow{\imath_r}^a => \begin{cases} \psi_{ds} = L_s \cdot i_{ds} + L_m \cdot i_{ds} \\ \psi_{qs} = L_s \cdot i_{qs} + L_m \cdot i_{qs} \end{cases} \quad (2.23)$$

$$\overrightarrow{\psi_r}^a = L_m \cdot \overrightarrow{\imath_s}^a + L_r \cdot \overrightarrow{\imath_r}^a => \begin{cases} \psi_{dr} = L_m \cdot i_{dr} + L_r \cdot i_{dr} \\ \psi_{qr} = L_m \cdot i_{qs} + L_r \cdot i_{qr} \end{cases} \quad (2.24)$$

In Figure 2.18 it is represented the equivalent circuit for d and q components, in which all the voltage, current and flux magnitudes are sinusoidal with a frequency of synchronous speed ω_{ss} [40].

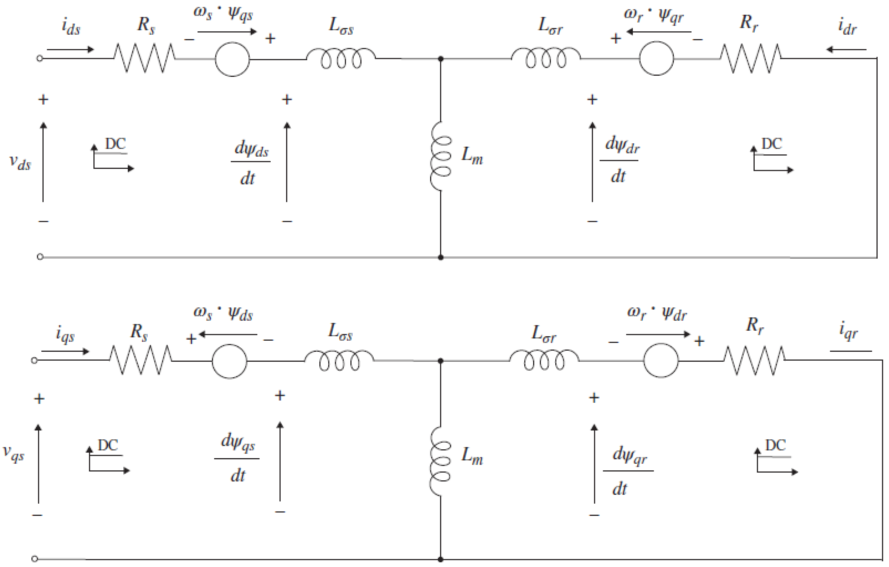

Figure 2.18. IM model (electric equivalent circuit) in d-q reference frame [41]

The active power for the synchronously rotating frame is calculated similar as for the stationary reference frame:

$$P_{IM} = \frac{3}{2} \cdot \left(v_d \cdot i_d + v_q \cdot i_q\right) \tag{2.25}$$

where:

P_{IM} [w] is the induction motor's active power;
v_d [V] is the voltage vector d component;
v_q [V] is the voltage vector q component;
i_d [A] is the current vector d component;
i_q [A] is the current vector q component.

The reactive power of the induction motor is calculated for the synchronous reference frame similar as, for the stationary rotating frame:

$$Q_{IM} = \frac{3}{2} \cdot \left(v_q \cdot i_d - v_d \cdot i_q\right) \tag{2.26}$$

where:

Q_{IM} [w] is the induction motor reactive power;
v_d [V] is the voltage vector d component;
v_q [V] is the voltage vector q component;
i_d [A] is the current vector d component;
i_q [A] is the current vector q component.

The electromagnetic torque of the induction motor considering a synchronously rotating frame can be calculated using one of the following equations [8]:

$$\begin{aligned} T_{IM} &= \frac{3}{2} \cdot p_{motor} \cdot \frac{L_m}{L_r} \cdot Im\left\{\overrightarrow{\psi_r}^{a*} \cdot \overrightarrow{i_s}^{a}\right\} \\ T_{IM} &= \frac{3}{2} \cdot p_{motor} \cdot \frac{L_m}{L_r} \cdot \left(\psi_{dr} \cdot i_{qs} - \psi_{qr} \cdot i_{ds}\right) \end{aligned} \tag{2.27}$$

where:

$\overrightarrow{\psi_r}^{a}$ [Vm] is the rotor flux vector reference to the synchronously rotating frame;
$\overrightarrow{i_s}^{a}$ [A] is the stator current vector reference to the synchronously rotating frame;
ψ_{dr} [Vm] is the rotor flux vector d component;
ψ_{qr} [Vm] is the rotor flux vector q component;
i_{qs} [A] is the stator current vector q component;
i_{ds} [A] is the stator current vector d component.
L_m [H] is the mutual inductance;
L_r [H] is the rotor inductance;
p_{motor} [pairs of poles] are the induction motor's pairs of poles.

In the diagram from Figure 2.19 it can be seen the flow chart of the induction motor model developed in Simulink [43]:

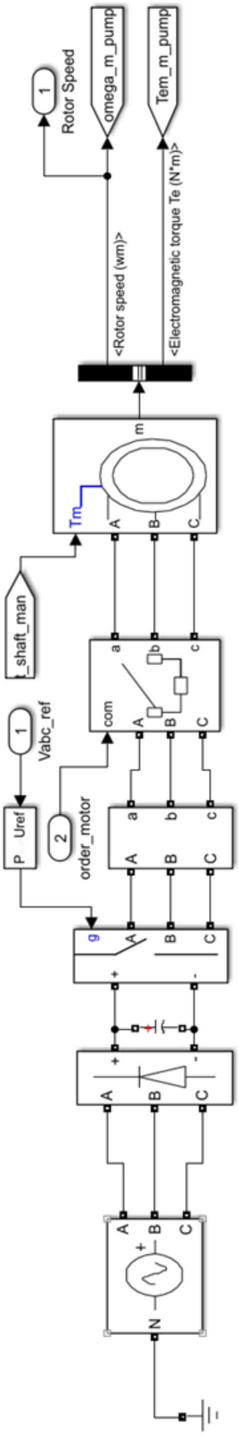

Figure 2.19. Induction Motor dynamic model Simulink diagram

2.2.2.2. State-space model

The state-space form of the dynamic Equations (2.6) and (2.8) defining the induction motor electromagnetic behavior is developed according to [40]:

$$\begin{bmatrix} \dot{\overrightarrow{i_s}}^{s} \\ \dot{\overrightarrow{\psi_r}}^{s} \end{bmatrix} = \begin{bmatrix} \frac{R_r \cdot (\sigma - 1)}{\sigma \cdot L_r \cdot L_s} - \frac{R_s}{\sigma \cdot L_s} & \frac{L_m \cdot (R_r - L_r \cdot j \cdot \omega_{IM})}{\sigma \cdot L_s \cdot {L_r}^2} \\ \frac{R_r \cdot L_m}{L_r} & -\frac{R_r}{L_r} + j \cdot \omega_{IM} \end{bmatrix} \cdot \begin{bmatrix} \overrightarrow{i_s}^{s} \\ \overrightarrow{\psi_r}^{s} \end{bmatrix} + \begin{bmatrix} \frac{1}{\sigma \cdot L_s} \\ 0 \end{bmatrix} \cdot \left[\overrightarrow{v_s}^{s} \right] \qquad (2.28)$$

where:

$\overrightarrow{\psi_r}^{s}$ [Vm] is the rotor flux vector reference to the stator;
$\overrightarrow{v_s}^{s}$ [V] is the stator voltage vector reference to the stator;
L_m [H] is the mutual inductance;
L_s [H] is the stator inductance;
L_r [H] is the rotor inductance;
R_s [Ω] is the stator resistance;
R_r [Ω] is the rotor resistance;
σ is the leakage coefficient;
ω_{IM} [rad/s] is the induction motor's electrical speed.

The state-space representation of the (d−q) induction motor model, is obtained [40]:

$$\begin{bmatrix} \dot{i}_{ds} \\ \dot{i}_{qs} \\ \dot{\psi}_{dr} \\ \dot{\psi}_{qr} \end{bmatrix} = \begin{bmatrix} \frac{R_r \cdot (\sigma - 1)}{\sigma \cdot L_r \cdot L_s} - \frac{R_s}{\sigma \cdot L_s} & 0 & \frac{L_m \cdot R_r}{\sigma \cdot L_s \cdot {L_r}^2} & \frac{j \cdot \omega_{IM}}{\sigma \cdot L_s \cdot L_r} \\ 0 & \frac{R_r \cdot (\sigma - 1)}{\sigma \cdot L_r \cdot L_s} - \frac{R_s}{\sigma \cdot L_s} & -\frac{j \cdot \omega_{IM}}{\sigma \cdot L_s \cdot L_r} & \frac{L_m \cdot R_r}{\sigma \cdot L_s \cdot {L_r}^2} \\ \frac{R_r \cdot L_m}{L_r} & 0 & -\frac{R_r}{L_r} & -j \cdot \omega_{IM} \\ 0 & \frac{R_r \cdot L_m}{L_r} & j \cdot \omega_{IM} & -\frac{R_r}{L_r} \end{bmatrix} \cdot \begin{bmatrix} i_{ds} \\ i_{qs} \\ \psi_{dr} \\ \psi_{qr} \end{bmatrix} + \begin{bmatrix} \frac{1}{\sigma \cdot L_s} & 0 \\ 0 & \frac{1}{\sigma \cdot L_s} \\ 0 & 0 \\ 0 & 0 \end{bmatrix} \cdot \begin{bmatrix} v_{ds} \\ v_{qs} \end{bmatrix} \qquad (2.29)$$

where:

i_{ds} [A] is the stator current vector d component;
i_{qs} [A] is the stator current vector q component;
ψ_{dr} [Vm] is the rotor flux vector d component;
ψ_{qr} [Vm] is the rotor flux vector q component;
v_{ds} [V] is the stator voltage vector d component;
v_{qs} [V] is the stator voltage vector q component;
L_m [H] is the mutual inductance;
L_s [H] is the stator inductance;
L_r [H] is the rotor inductance;
R_s [Ω] is the stator resistance;
R_r [Ω] is the rotor resistance;
σ is the leakage coefficient;
ω_{IM} [rad/s] is the induction motor's electrical speed.

2.2.3. *Variable speed centrifugal pump*

2.2.3.1. Dynamic model

The variable-speed centrifugal pump [44] is a submersible pump that collects water from a well and delivers it directly into an irrigation hydraulic distribution network at different operating points. Table 2.3 presents the technical and operating points of the centrifugal pump [44]. Even though the pump is installed at a depth of 40 m (PUMP_DEPTH≈ 40 m below the ground level in Figure 2.6), the water is extracted from a depth of 30.5 m (HG_WATER_SOURCE≈ 30.5 m dynamic level in Figure 2.6). The pump discharges a nominal flow of 91.85 m^3/h, with the maximum discharge being 95 m^3/h.

Table 2.3. Variable speed centrifugal pump technical specifications

Properties	Value	Symbol	Unit
Manufacturer	Caprari	-	-
Type	E8P95/7ZC	-	-
Pump operating limits			
Ambient temperature	35 °C		
Minimum water speed to cool the jacket of the motor	0.5 m/s		
Maximum number of starts in one hour	20		
Minimum immersion depth	507,5 m		
Submersible pump operating characteristics			
Pump service flow rate	91.85 m3/h	Q	m^3/h
Submersible pump service head	78.12 m	H	m
Pump rated efficiency	75.63 %	η	%
Pump rated hydraulic power	25.84 kW	P_{PSmax}	kW
Pump maximum flow rate	169.2 m3/h	Q_{max}	m^3/h
Pump head at theoretical 0 flow rate	97.35 m	H_{max}	m
Pump minimum head (at maximum flow rate)	83.29 m	H_{min}	m
Pump efficiency at maximum flow rate	81.5 %	η	%
Pump hydraulic power at maximum flow rate	30 kW	P_{pump}	m^3/h
Consumer pressure	1.5	Hg_{cons}	bar
Well Dynamic head	35.7	Hg_{well}	mca
Water level variation	18.6	ΔHg	mca
Pipe diameter	0.3	D_{pipe}	m
Head–flow 1st coefficient	185.2123	A	m
Head–flow 2nd coefficient	0.2608	B	h/m^2
Head–flow 3rd coefficient	-0.0076	C	h/m^5
Efficiency-flow 1st coefficient	1.8274	D	$1/m^2$
Efficiency-flow 2nd coefficient	-0.104	E	$1/m^5$

The variable centrifugal pump is modelled based on *A, B, C, D* and *E* coefficients from Table 2.3. The coefficients are identified through quadratic regression, using the Matlab curve fitting tool on 7 operating points on the pump head–flow (H_0-Q_0) and efficiency–flow (η_0-Q_0) curves at 50 Hz provided by the manufacturer (Figure 2.20).

Both curves (H_0-Q_0 and η_0-Q_0) are at nominal speed (ω_{ps0}) [45-47]. Using the same denotations as the ones published by the author in reference [35]: "starting from Equation (2.30), until Equation (2.74), the subscript "*0*" stands for the nominal value, and "*s*" for the current value".

$$H_0 = A + B \cdot Q_0 + C \cdot (Q_0)^2 \tag{2.30}$$

$$\eta_0 = D \cdot Q_0 + E \cdot (Q_0)^2 \tag{2.31}$$

where Q represents the pump discharge, H the pump head, and η the pump efficiency.

Table 2.4. Variable speed centrifugal pump 7 points on the 50 Hz curve

50Hz curve fitting point	Q [m³/h]	H [m]	P [kW]	η [%]	NPSH [m]
1.	0	185	0	0	0
2.	54	177	36.8	68.1	1.8
3.	69.84	166	41.19	76.7	2.37
4.	85.68	152	45.11	80	3.22
5.	101.52	133.5	48.09	78	4.28
6.	117.36	111	50.01	71	5.6
7.	133.2	85	50.03	58.35	7.2

The dynamic response of the pump to different speeds is modelled using the pump affinity laws (assuming a constant change in water density $\rho_{ws}=\rho_{w0}$ and pump geometry $G_s=G_0$) [27] (p. 776):

$$\frac{\mathrm{Q_s}}{Q_0} = \frac{\omega_{pss}}{\omega_{ps0}} \cdot \left(\frac{G_s}{G_0}\right)^3 \tag{2.32}$$

$$\frac{H_s}{H_0} = \left(\frac{\omega_{pss}}{\omega_{ps0}}\right)^2 \cdot \left(\frac{G_s}{G_0}\right)^2 \tag{2.33}$$

$$\frac{P_{\mathrm{pss}}}{P_{ps0}} = \left(\frac{\rho_{ws}}{\rho_{w0}}\right) \cdot \left(\frac{\omega_{pss}}{\omega_{ps0}}\right)^3 \cdot \left(\frac{G_s}{G_0}\right)^5 \tag{2.34}$$

where P_{ps} stands for the shaft pump power.

By combining the (H_0-Q_0) quadratic regression Equation (2.30) at nominal speed (ω_{ps0}) with the pump affinity laws (2.32)-(2.34), the pump characteristic (H_s-Q_s) as a function of pump speed is obtained (21):

$$H_s = \left(\frac{\omega_{pss}}{\omega_{ps0}}\right)^2 \cdot A + \left(\frac{\omega_{pss}}{\omega_{ps0}}\right) \cdot B \cdot Q_s + C \cdot (Q_s)^2 \tag{2.35}$$

Figure 2.20 shows the pump characteristics head-flow (H-Q) curves (representing on the x-axis the pumping head in meters, and on the y-axis the pump discharge in m³/h) at different electrical frequencies (variations from 5 to 50 Hz).

By combining the (η_0-Q_0) quadratic regression of Equation (2.31) at nominal speed (ω_{ps0}) with the pump affinity laws (2.32)-(2.34) using the equation from reference [48], the pump efficiency as a function of pump speed is obtained (2.36):

$$\begin{gathered} \eta_s(\omega_s) = 1 - (1 - \eta_0) \cdot \left(\frac{\omega_{ps0}}{\omega_{pss}}\right)^{0.1} \\ \eta_s(\omega_{ps}) = 1 - \left(\frac{\omega_{ps0}}{\omega_{pss}}\right)^{0.1} + D \cdot Q_s \cdot \left(\frac{\omega_{ps0}}{\omega_{pss}}\right)^{1.1} + E \cdot (Q_s)^2 \cdot \left(\frac{\omega_{ps0}}{\omega_{pss}}\right)^{2.1} \end{gathered} \tag{2.36}$$

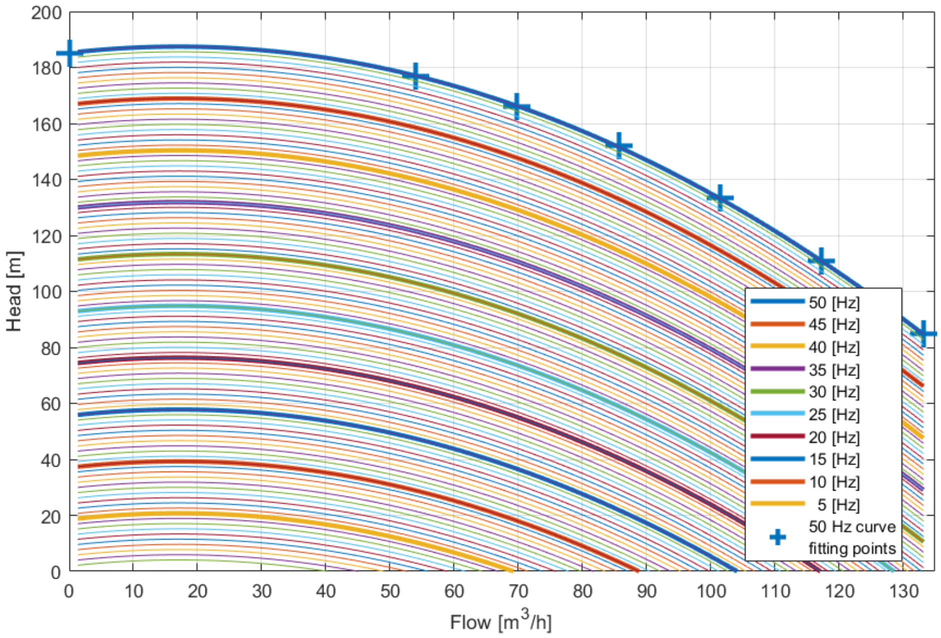

Figure 2.20. Pump head-flow H-Q curve at different speeds

Figure 2.21 shows the pump efficiencies (η-Q) curves (representing on the x-axis the pump efficiency, and on the y-axis the pump discharge in m^3/h) at different electrical frequencies (variations from 5 to 50 Hz).

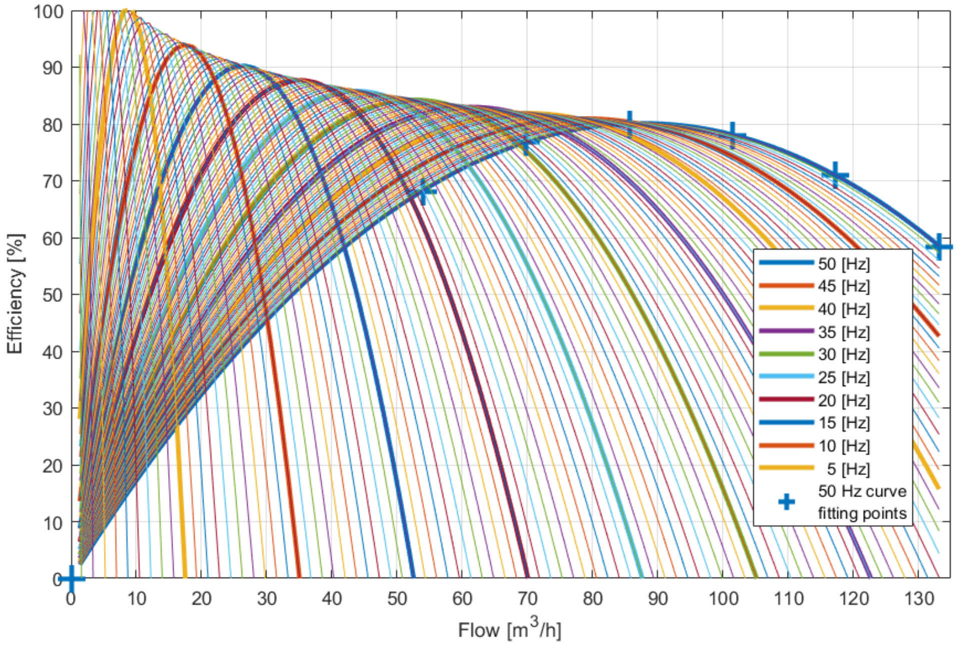

Figure 2.21. Pump efficiency-flow η-Q curve at different speeds

By combining the head-flow (*H-Q*) characteristic curves of the pump, Equation (2.35) with the pump efficiency-flow (η-Q) characteristic curves from Equation (2.36), the iso-efficiency curves are obtained in Figure 2.22, where x-axis represents the pumping head in meters, and y-axis represents the pump discharge in m^3/h. The pump efficiency is represented in percentages by the dotted lines while the pump frequency is represented in Hz by the dashed lines. The red line represents the hydraulic network characteristic curve from Equation (2.40). For an ideal operation, the controller strategy must operate the PS according to the hydraulic network characteristic curve.

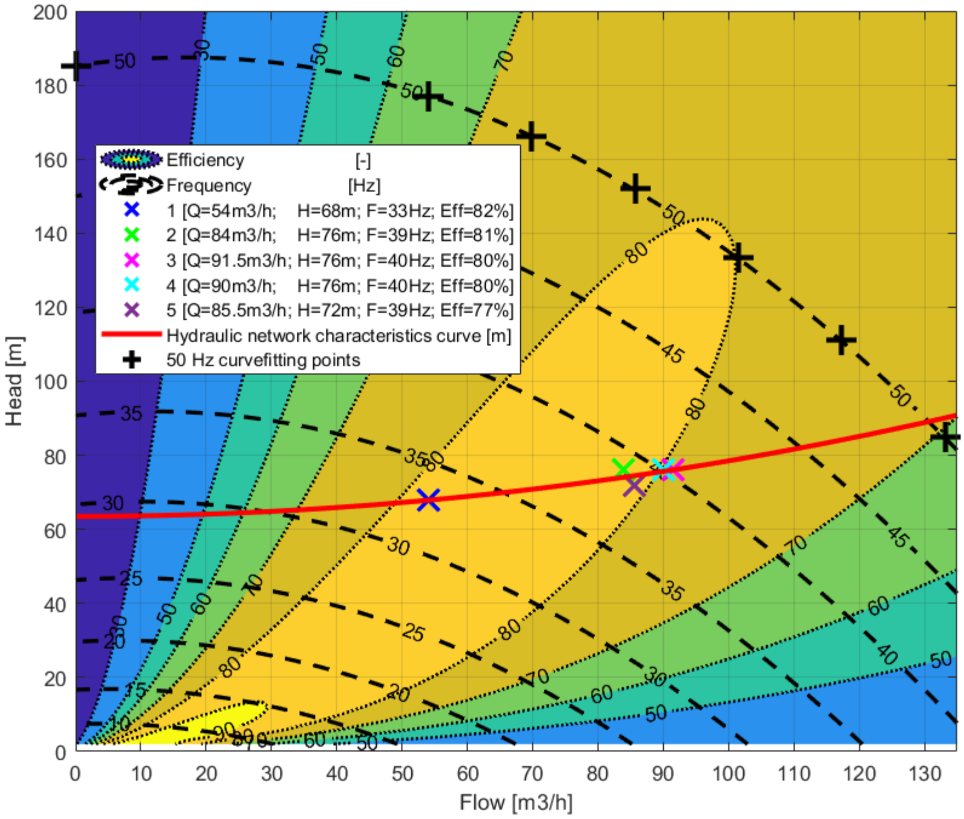

Figure 2.22. Pump Iso-efficiency curve

The pump iso-power curve is presented in Figure 2.23 where the pump power (P_{pump}) is calculated based on delivered hydraulic power ($P_{hydraulic}$) divided by the pump efficiency at the operating point (η_s), Equation (2.37) [49]:

$$P_{pump} = \frac{P_{hydraulic}}{\eta_s} = \frac{\rho_W \cdot g \cdot H_s \cdot Q_s}{\eta_s} \tag{2.37}$$

The pump iso-torque curve is presented in Figure 2.24 where the pump torque (T_{pump}) is calculated according to Equation (2.38) from reference [50]:

$$T_{pump} = \frac{60 \cdot P_{pump}}{2 \cdot \pi \cdot \omega_{pss}} \tag{2.38}$$

where ρ_w is the water density, g is the gravitational acceleration, $P_{hydraulic}$ being the current hydraulic power, ω_{pss} representing the current pump speed and η_s the current pump efficiency.

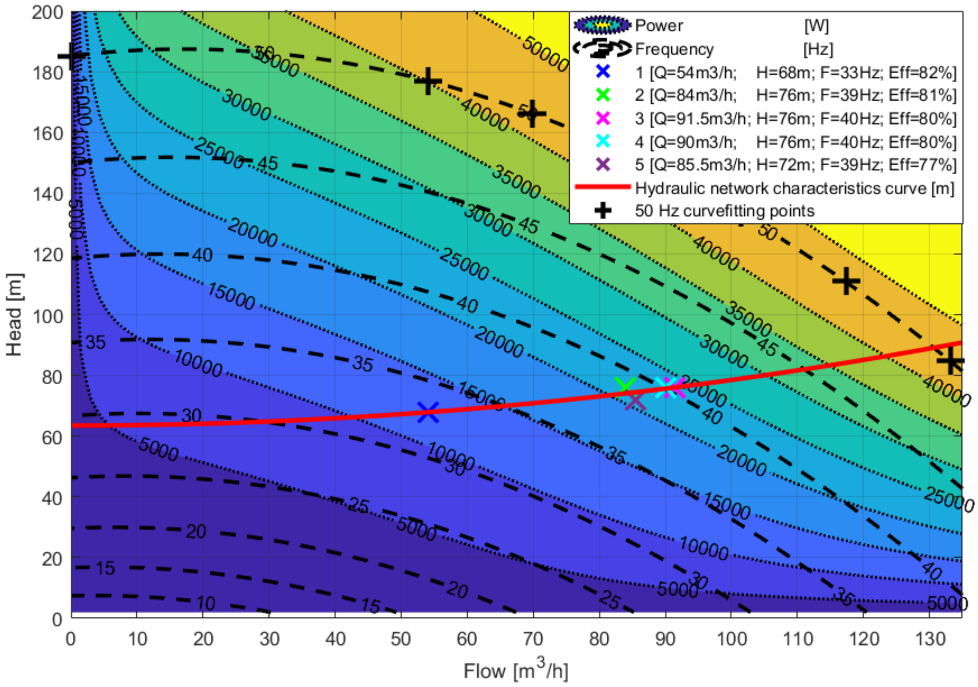

Figure 2.23. *Pump Iso-power curve*

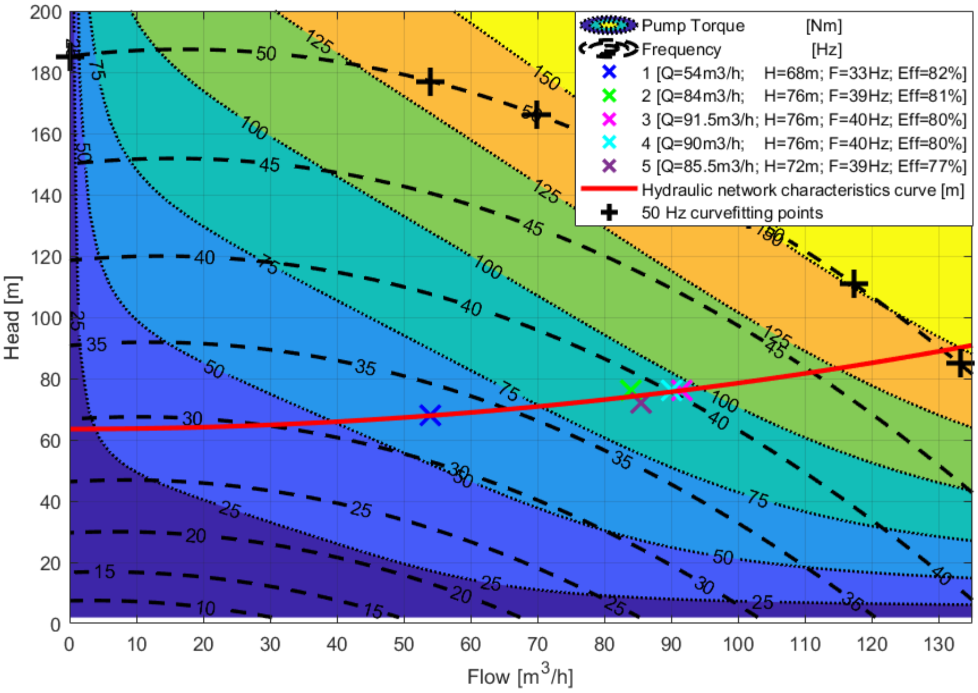

Figure 2.24. *Pump Iso-torque curve*

The pump iso-inertia curve is presented in Figure 2.25, where the pump inertia (I_{pump}) is calculated based on the equation from [51]:

$$I_{pump} = 0.03768 \cdot \left(\frac{P_{pump}}{1000 \cdot \omega_{pss}}\right)^{0.9556} \tag{2.39}$$

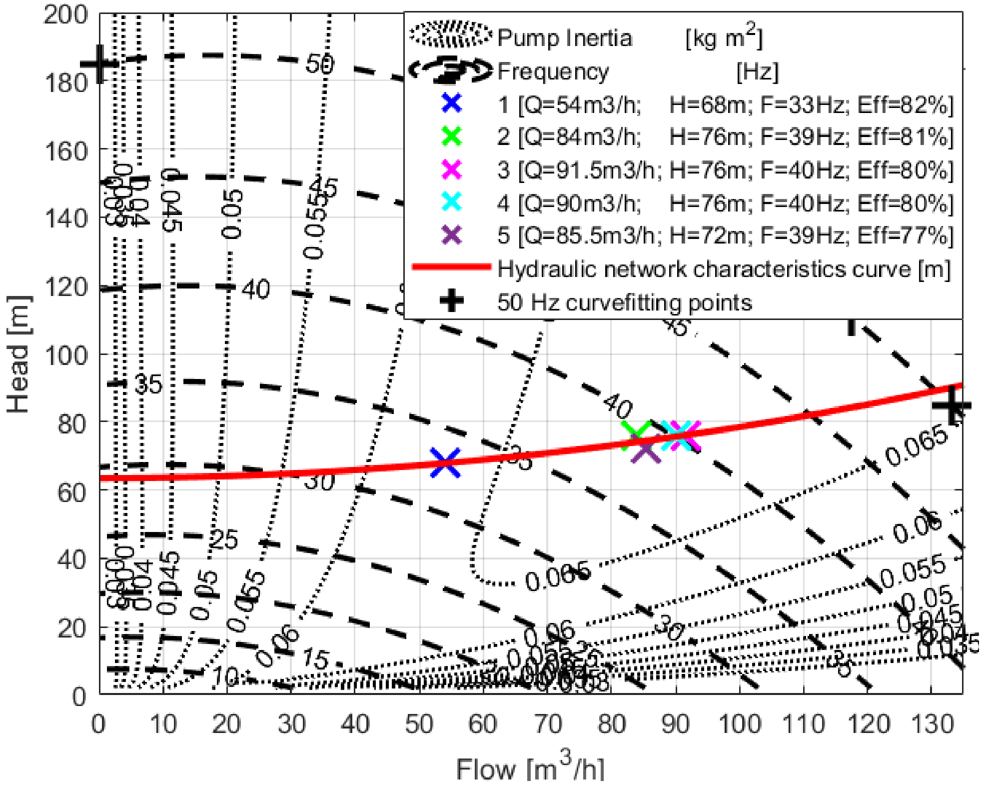

Figure 2.25. Pump Iso-Inertia curve

2.2.4. Hydraulic network

The considered pumping system irrigates 5 sectors. In Table 2.5 are presented the nominal values of the key parameters for each sector (operating points), obtained by analyzing the collected data with the monitoring system in section ***5.4.7. Monitoring system collected data***.

Table 2.5. Variable speed centrifugal pump identified operating parameters

Sector	Htotal (mca)	Q (m3/h)	Pressure (bar)	Pressure Reference (bar)	Power (kW)	Frequency (Hz)
1	68	54	3.4812354	3.5	12.029	33.0518
2	76	84	4.18822408	4.2	22.319	39.0077
3	76	91.5	4.42083782	4.4	25.301	40.3471
4	76	90	4.168346	4.2	24.676	40.0732
5	72	85.5	3.79069191	3.8	21.890	38.6260

The water distribution and irrigation system characteristic curve is expressed by equation [52]:

$$H_s = H_g + k \cdot (Q_s)^2 \tag{2.40}$$

where *Qs* is the current pump discharge, Hg is the static head, and *k* is the head loss coefficient. Figure 2.22 shows the iso-efficiency diagram of the pump together with the hydraulic network characteristic curve [35, 48].

The pump discharge (flow rate) as a function of pump speed (ω_{ps0}) is given by the cross-point of the pump head flow characteristic curve (2.35) with the hydraulic network characteristic curve (2.40):

$$H_g + k \cdot (Q_s)^2 = \left(\frac{\omega_{pss}}{\omega_{ps0}}\right)^2 \cdot \mathrm{A} + \left(\frac{\omega_{pss}}{\omega_{ps0}}\right) \cdot \mathrm{B} \cdot \mathrm{Q_s} + C \cdot (Q_s)^2 \tag{2.41}$$

From which results:

$$Q_s(\omega_{pss}) = \frac{-\left(\frac{\omega_{pss}}{\omega_{ps0}}\right) \cdot \mathrm{B} - \sqrt{\left(\frac{\omega_{pss}}{\omega_{ps0}}\right)^2 \cdot \mathrm{B}^2 - 4 \cdot \left[\left(\frac{\omega_{pss}}{\omega_{ps0}}\right)^2 \cdot \mathrm{A} - \mathrm{H_g}\right] \cdot (C - k)}}{2 \cdot (C - k)} \tag{2.42}$$

The pump power (P_{pump}) is calculated based on delivered hydraulic power ($P_{hydraulic}$) divided by the pump efficiency at the operating point (η_s), Equation (2.43) [47]:

$$P_{pump} = \frac{\rho_w \cdot g \cdot H_g \cdot Q_s + \rho \cdot g \cdot k_1 \cdot \left(Q_s(\omega_{pss})\right)^3}{\left(1 - \left(\frac{\omega_{ps0}}{\omega_{pss}}\right)^{0.1} + D \cdot Q_s(\omega_{pss}) \cdot \left(\frac{\omega_{ps0}}{\omega_{pss}}\right)^{1.1} + E \cdot \left(Q_s(\omega_{pss})\right)^2 \cdot \left(\frac{\omega_{ps0}}{\omega_{pss}}\right)^{2.1}\right)} \tag{2.43}$$

Finally, the pump torque as a function of pump speed can be obtained through the substitution of Equations (2.41), (2.42), and (2.43) into Equation (2.44):

$$T_{pump} = \frac{\rho_w \cdot g \cdot H_g \cdot Q_s + \rho \cdot g \cdot k_1 \cdot \left(Q_s(\omega_{pss})\right)^3}{\omega_{pss} \cdot \left(1 - \left(\frac{\omega_{ps0}}{\omega_{pss}}\right)^{0.1} + D \cdot Q_s(\omega_{pss}) \cdot \left(\frac{\omega_{ps0}}{\omega_{pss}}\right)^{1.1} + E \cdot \left(Q_s(\omega_{pss})\right)^2 \cdot \left(\frac{\omega_{ps0}}{\omega_{pss}}\right)^{2.1}\right)} \tag{2.44}$$

The pump inertia (I_{pump}) is calculated based on the equation from:

$$I_{pump} = 0.03768 \cdot \left(\frac{\dfrac{\rho_w \cdot g \cdot H_g \cdot Q_s + \rho \cdot g \cdot k_1 \cdot \left(Q_s(\omega_{pss})\right)^3}{\left(1 - \left(\frac{\omega_{ps0}}{\omega_{pss}}\right)^{0.1} + D \cdot Q_s(\omega_{pss}) \cdot \left(\frac{\omega_{ps0}}{\omega_{pss}}\right)^{1.1} + E \cdot \left(Q_s(\omega_{pss})\right)^2 \cdot \left(\frac{\omega_{ps0}}{\omega_{pss}}\right)^{2.1}\right)}}{1000 \cdot \omega_{pss}}\right)^{0.9556} \tag{2.45}$$

Figure 2.26 presents the structure of the fixed speed pump controller developed in Simulink [43].

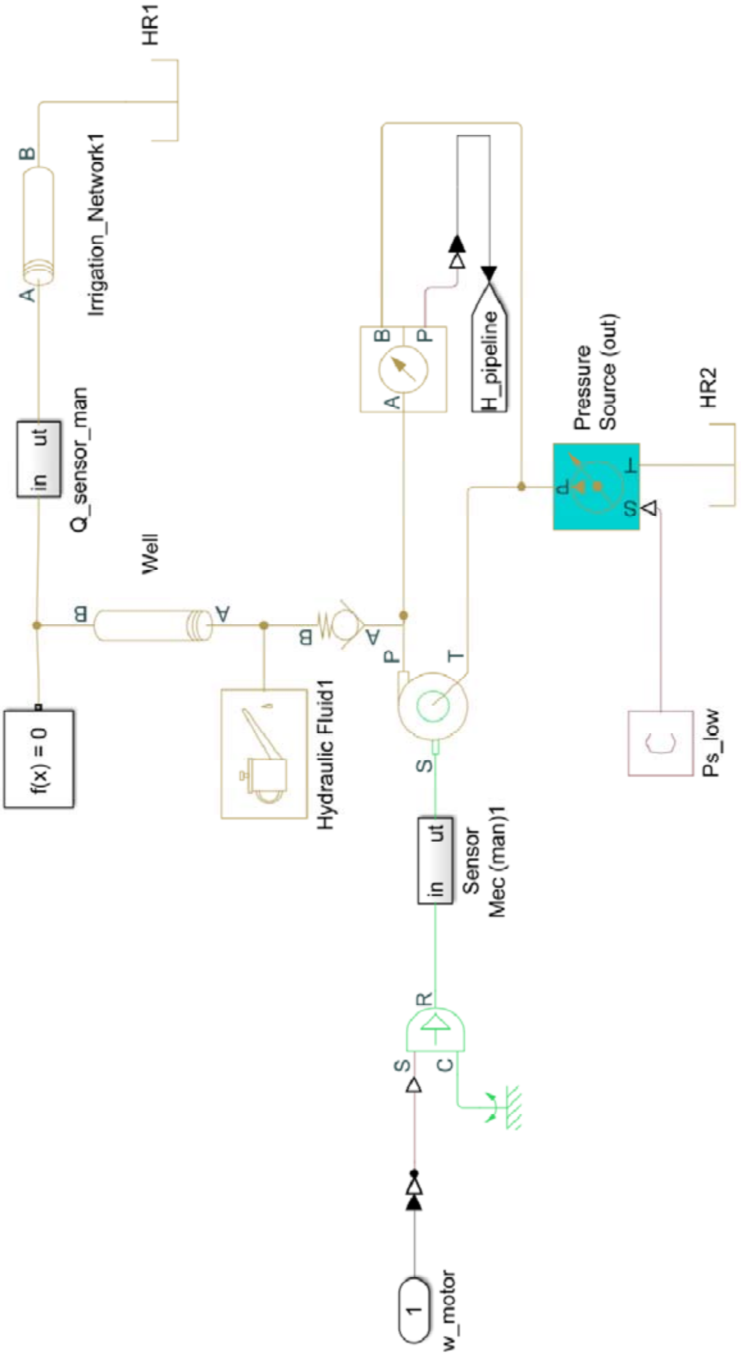

Figure 2.26. Simulink dynamic model diagram of the centrifugal pump together with the hydraulic network

2.3. Pumping system control strategy

In the current subchapter, several controllers and controlling strategies are developed in order to drive the induction motor of the pump at fixed (nominal) speed using a soft starter driver, or at variable speed (can differ from the nominal) using a VFD. This control strategy has been published by the author in reference [35]. Both motor drives contain, besides the controllers, also the execution elements. The soft driver contains, besides the controller, also the converter, and the VFD contains, besides the controller, also the rectifier and the inverter.

2.3.1. Fixed speed pump controller

The most common solution to drive high-power centrifugal pumps at a fixed (nominal) speed is to use a soft starter. A soft starter controls just the induction motor acceleration to nominal speed (equivalent electrical frequency of 50 Hz) and its deceleration (to 0 Hz). Figure 2.27 presents the structure of the fixed-speed pump controller.

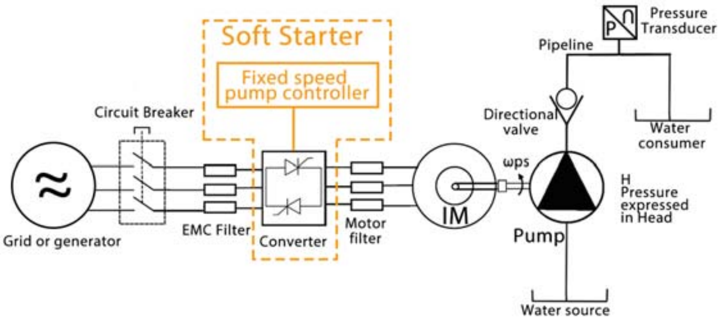

Figure 2.27. Pump motor powered by a soft starter at nominal frequency

Figure 2.28 published by the author in reference [35], presents the fixed and variable speed PS diagram, where the induction motor of the pump is controlled using a classical solution for current regulation in vector-controlled AC drives, called the current regulator. This solution considers a PI (Proportional Integral) current regulator, which is tuned using a second-order equivalent system of induction motor currents [40].

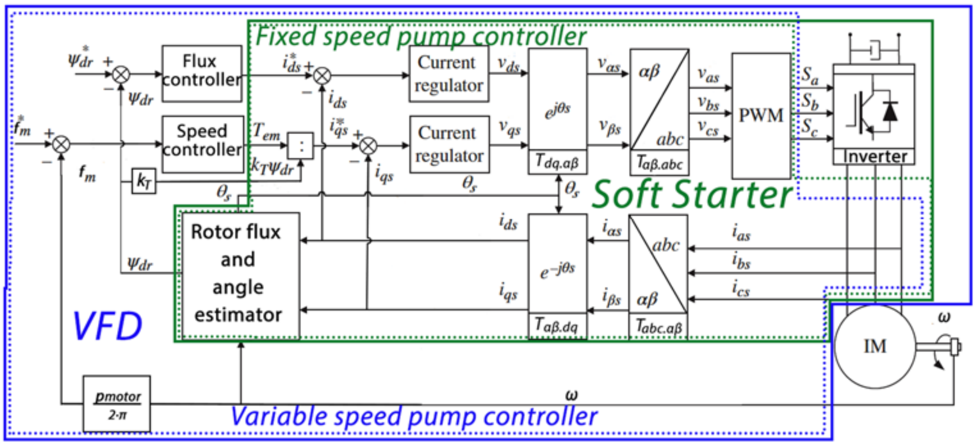

Figure 2.28. Induction motor control loops for one single pump [35]

Legend [35]:

- Sa, Sb, Sc are the switching commands (orders);
- PWM= pulse-width modulation;
- i_{as}, i_{bs}, i_{cs} are the stator three-phase AC currents;
- v_{as}, v_{bs}, v_{cs} are the stator three-phase AC voltage commands;
- i_d and i_q are the stator three-phase AC currents expressed in synchronous (dq) reference frame;
- v_{ds} and v_{qs} are the stator three-phase AC voltage commands transformed in synchronous (dq) reference frame;
- i_α and i_β are the stator three-phase AC currents expressed in stationary (αβ) reference frame;
- $v_{\alpha s}$ and $v_{\beta s}$ are the stator three-phase AC voltage commands transformed in stationary (αβ) reference frame;
- $T_{abc.\alpha\beta}$= transformation from three-phase (abc) complex space vector into stationary (αβ) reference frame [53];
- $T_{\alpha\beta.abc}$= transformation from stationary (αβ) reference frame into three-phase (abc) complex space vector [53];
- $T_{\alpha\beta.dq}$= transformation from stationary (αβ) reference frame into synchronous (dq) reference frame [53];
- $T_{dq.\alpha\beta}$= transformation from synchronous (dq) reference frame into stationary (αβ) reference frame [53];

where:

$$T_{\alpha\beta.dq} = \begin{bmatrix} \cos\theta_s & -\sin\theta_s \\ \sin\theta_s & \cos\theta_s \end{bmatrix} \qquad T_{dq.\alpha\beta} = \begin{bmatrix} \cos\theta_s & -\sin\theta_s \\ \sin\theta_s & \cos\theta_s \end{bmatrix}^{-1}$$
$$T_{abc.\alpha\beta} = \begin{bmatrix} 2/3 & -1/3 & -1/3 \\ 0 & \sqrt{3}/3 & -\sqrt{3}/3 \\ 1/3 & 1/3 & 1/3 \end{bmatrix} \qquad T_{\alpha\beta.abc} = \begin{bmatrix} 1 & 0 & 1 \\ -1/2 & \sqrt{3}/2 & 1 \\ -1/2 & -\sqrt{3}/2 & 1 \end{bmatrix} \tag{2.46}$$

The second-order transfer functions of the induction motor currents closed loop system of the considered the following forms [40].

$$\frac{i_{ds}(s)}{i_{ds}^{*}(s)} = \frac{s\cdot k_{p1} + k_{i1}}{s^2\cdot(\sigma\cdot L_S) + s\cdot\left(R_S + k_{p1}\right) + k_{i1}} \tag{2.47}$$
$$\frac{i_{qs}(s)}{i_{qs}^{*}(s)} = \frac{s\cdot k_{p1} + k_{i1}}{s^2\cdot(\sigma\cdot L_S) + s\cdot\left(R_S + k_{p1}\right) + k_{i1}} \tag{2.48}$$

With σ being leakage coefficient [40]:

$$\sigma = 1 - \frac{(L_m)^2}{L_s\cdot L_r} \tag{2.49}$$

where the i_{ds}* is the reference and i_{ds} is the output of the d-axis current loop and respectively i_{qs}* is the reference and i_{qs} is the output of the q-axis current loop. *Rs*=0.095 [Ω] representing the IM stator resistance, *Rr*=0.063 [Ω] representing the IM rotor resistance, *Lm*=0.032 [H] being the IM magnetizing inductance, *Ls*=0.034 [H] being the IM stator inductance and *Lr*=0.034 [H] the IM rotor inductance. k_{p1} and k_{i1} are the proportional gain and integral time constant of the both closed loop currents systems (“d” and “q”). The current regulators of both loops are equally tuned.

The tuning of the fixed speed pump controller is done, considering the closed loop denominator of equations (2.47) and (2.48) being matched to a standard second-order systems denominator [40]:

$$s^2 \cdot (\sigma \cdot L_S) + s \cdot \left(R_S + k_{p1}\right) + k_{i1} = s^2 + 2 \cdot \xi_1 \cdot \omega_{n1} \cdot s + (\omega_{n1})^2 \tag{2.50}$$

Developing equation (2.50), is obtained:

$$s^2 + s \cdot \left(\frac{R_S + k_{p1}}{\sigma \cdot L_S}\right) + \frac{k_{i1}}{\sigma \cdot L_S} = s^2 + 2 \cdot \xi_1 \cdot \omega_{n1} \cdot s + (\omega_{n1})^2 \tag{2.51}$$

where *ω_{n1}* and *ξ₁* are the first natural frequency and damping factor of the system.

From equation (2.51) results that the required proportional gain and integral time constant are:

$$k_{p1} = \sigma \cdot L_s \cdot 2 \cdot \xi_1 \cdot \omega_{n1} - R_s \tag{2.52}$$

and, respectively,

$$k_{i1} = \sigma \cdot L_s \cdot (\omega_{n1})^2 \tag{2.53}$$

For a critically damped response, the second order denominator equations (2.50), (2.51), must give a solution with double real poles, a solution obtainable only with a damping factor equal to 1, $\xi 1=1$:

$$\text{For } \xi_1 = 1 \text{ results} \rightarrow (s + {\omega_{n1}}^2) \tag{2.54}$$

According to the recommendation from reference [40], to choose the dynamics of the closed loop system faster than the one of the open-loop system, the poles of the closed-loop system (ω_{n1}) are chosen to be 10 times greater than the open loop poles ($\sigma \cdot Ls/Rs$). Recommendation that leads to good results.

$$\omega_{n1} = \frac{10}{\frac{\sigma \cdot L_s}{R_s}} \tag{2.55}$$

Figure 2.29 presents the structure of the fixed speed pump controller.

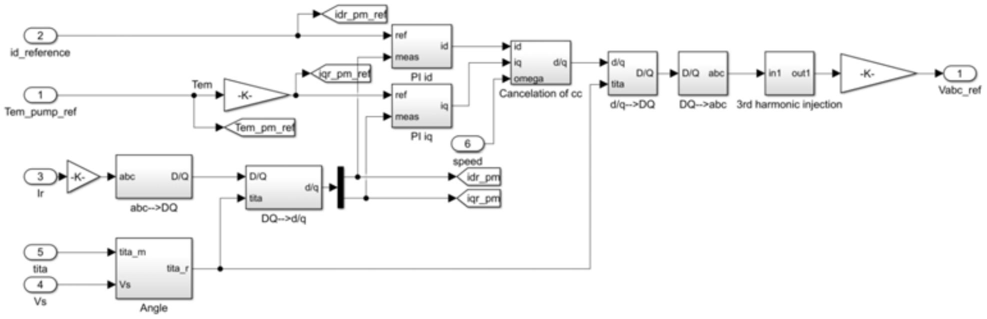

Figure 2.29. Fixed speed pump controller structure

2.3.2. Variable speed pump controller

The most common solution for driving high-power centrifugal pumps at a variable speed is using a VFD. A VFD besides controlling the acceleration and deceleration of the induction motor controls also the operating speed, which can differ from the nominal one. Due to this reason, the variable speed pump controller uses the same closed-loop systems as the fixed speed controller (**2.3.1 Fixed speed pump controller**), with the same transfer functions (2.47), (2.48), to which was added in the cascade the speed controller developed in this section (Figure 2.28). The speed controller, that becomes the main loop, provides the reference for the inner loop q-axis current (i_{qs}*) containing the current regulation (q-axis), from the electromechanical torque according to Equation (2.56) from [41]:

$$T_{em}^{*} \approx T_{em} = K \cdot \Psi_{dr} \cdot i_{qs} \tag{2.56}$$

which allows us to obtain the q-axis current reference, i_{ds}*.

The synthesis of the speed controller is done, starting from equation (2.57) [41], where the viscous friction has been neglected:

$$T_{em} - T_{pump} = I_{pump} \cdot (\dot{\omega_{pss}}) = \frac{2 \cdot \pi \cdot I_{pump}}{p_{motor}} \cdot (\dot{fm}) \tag{2.57}$$

where *fm* represents the motor electrical frequency ($fm = p_{motor} \cdot \omega_{pss}/2/\pi$) (2.58)

I_{pump} represents the total inertia of the pumping unit (induction motor plus pump), equations (2.44) and T_{pump} represents the mechanical torque (2.45).

Figure 2.30 presents the structure of the variable speed pump controller.

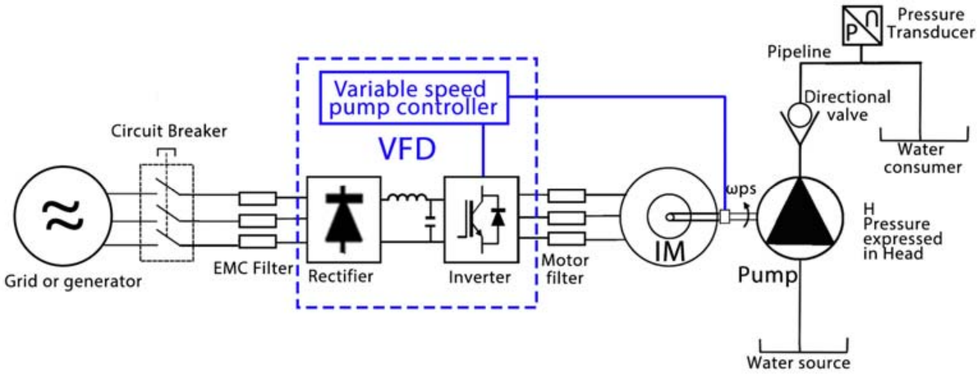

Figure 2.30. Pump motor powered by a VFD at variable frequency

Denoting $\Delta T = T_{em} - T_{pump}$, from equation (2.57), the following transfer function of the driving shaft system is obtained:

$$\frac{fm(s)}{\Delta T(s)} = \frac{p_{motor}}{2 \cdot \pi \cdot I_{pump} \cdot s} \tag{2.59}$$

Considering the transfer function of a Proportional and Integral controller (PI2) of the form (2.60):

$$PI_2 = k_{p2} + \frac{k_{i2}}{s} \tag{2.60}$$

in series with the transfer function from Equation (2.59), the transfer function of the closed loop with unitary feedback is obtained:

$$\frac{fm(s)}{fm^*(s)} = \frac{k_{p2} \cdot s + k_{i2}}{\frac{2 \cdot \pi}{p_{motor}} \cdot I_{pump} \cdot s^2 + k_{p2} \cdot s + k_{i2}} \tag{2.61}$$

with *fm** being the motor electrical frequency and representing the input and *fm* being the current motor electrical frequency and representing the output.

For the PI$_2$ pump speed controller the same tuning method as the one used for the current regulators of the induction motor, equations (2.47)-(2.55), has been used. Similarly, the closed loop denominator of equation (2.61) is matched to the denominator of a standard second-order system:

$$s^2 \cdot \left(2 \cdot \pi \cdot I_{pump}/p_{motor}\right) + s \cdot k_{p2} + k_{i2} = s^2 + 2 \cdot \xi_2 \cdot \omega_{n2} \cdot s + (\omega_{n2})^2 \tag{2.62}$$

The required proportional gain (k_{p2}) and integral time constant (k_{i2}) are:

$$k_{p2} = \frac{2 \cdot \xi_2 \cdot \omega_{n2} \cdot p_{motor}}{2 \cdot \pi \cdot I_p} \tag{2.63}$$

$$k_{i2} = \frac{(\omega_{n2})^2 \cdot p_{motor}}{2 \cdot \pi \cdot I_p} \tag{2.64}$$

In parallel, a flux controller loop is developed similarly to the speed controller loop. The flux controller provides directly the reference to the d-axis current regulator from its inner loop.

Same as the speed controller, the PI$_3$ flux controller is developed, with k_{p3} being the proportional gain and k_{i3} the integral time constant. The rotor flux estimator is modeled according to the transfer function from reference [40]:

$$\frac{\Psi_{dr}(s)}{i_{ds}(s)} = \frac{L_m}{\tau_r \cdot s + 1} \tag{2.65}$$

where the dynamics of the d-axis current control loop is neglected because the d-axis current loop dynamic is much faster than the rotor flux dynamic. τ_r represents the rotor time constant.

By including another PI regulator type, equation (2.60), (PI3) in series to the rotor flux estimator and closing the loop with unitary feedback, the transfer function of the rotor flux closed loop is obtained:

$$\frac{\Psi_{dr}(s)}{\Psi_{dr}{}^*(s)} = \frac{k_{p3} \cdot s + k_{i3}}{s^2 \cdot \frac{\tau_r}{L_m} + s \cdot \left(\frac{1}{L_m} + k_{p3}\right) + k_{i3}} \tag{2.66}$$

where the current rotor flux (Ψ_{dr}) being the output and the reference of the rotor flux (Ψ_{dr}*) being the input.

The proportional gain and the integral time constant of the flux controller are obtained from the identification of the closed-loop denominator of equation (2.66) with a standard second-order system denominator:

$$k_{p3} = \frac{\tau_r}{L_m} \cdot \omega_{n3}{}^2 \tag{2.67}$$

$$k_{i3} = \frac{\tau_r}{L_m} \cdot 2 \cdot \xi_3 \cdot \omega_{n3} - \frac{1}{L_m} \tag{2.68}$$

2.3.2.1. Variable flow pump controller

A particular application of the variable speed pump, is the pumping system that has to operate at the desired water discharge (volume flow). Due to this reason, a mathematical equation is introduced, in order to obtain the electrical frequency error *Δf=(fm*-fm)* expressed as a function of water discharge (flow) error *ΔQ=(Q*-Q)*, the first-order Taylor series approximation is used:

$$Q = Q^* + \frac{2 \cdot \pi}{p_{motor}} \cdot (fm - fm^*) \cdot \left(\dot{Q}\right)_{fm^*} \qquad (2.69)$$

where $\dot{Q}$ is obtained deriving equation (2.32) from the affinity laws, equations (2.32)-(2.34), the angular velocity (ω_{pss}) is converted into electrical frequency (*fm*) (equation (2.58)), and the nominal discharge (flow) (Q_0) and frequency (fm_0) are equals with the reference discharge ($Q^*=Q_0$) and frequency ($fm^*=fm_0$) [48]. From equation (2.69) results:

$$\Delta Q = \frac{2\cdot\pi}{p_{motor}} \cdot \Delta f \cdot \left(\dot{Q}\right)_{fm^*} = \frac{2\cdot\pi\cdot Q^*}{p_{motor}\cdot fm^*} \cdot \Delta f \quad \text{and} \quad \Delta f = \frac{p_{motor}\cdot fm^*}{2\cdot\pi\cdot H^*} \cdot \Delta Q \qquad (2.70)$$

Figure 2.31 presents the structure of the variable flow pump controller.

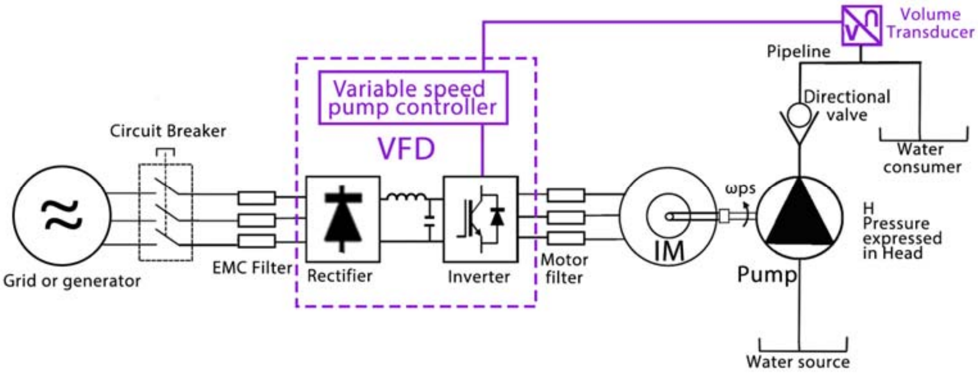

Figure 2.31. Pump motor powered by a VFD at variable flow

2.3.2.2. Variable pressure pump controller

Another particular application of the variable speed pump, is the pumping system that has to operate at the desired pressure. Due to this reason, a mathematical equation is introduced, in order to obtain the IM electrical frequency error *Δf=(fm*-fm)* as a function of pumping head error *ΔH=(H*-H)*, using the first-order Taylor series approximation:

$$H = H^* + \frac{2 \cdot \pi}{p_{motor}} \cdot (fm - fm^*) \cdot \left(\dot{H}\right)_{fm^*} \qquad (2.71)$$

where $\dot{H}$ is obtained deriving equation (2.33) from the affinity laws, equations (2.32)-(2.34), the angular velocity (ω_{pss}) is converted into electrical frequency (*fm*) (equation (2.58)), and the nominal head (H_0) and frequency (fm_0) are equals with the reference head ($H^*=H_0$) and frequency ($fm^*=fm_0$) [48]. From equation (2.71) results:

$$\Delta H = \frac{2\cdot\pi}{p_{motor}} \cdot \Delta f \cdot \left(\dot{H}\right)_{fm^*} = \frac{4\cdot\pi\cdot H^*}{p_{motor}\cdot fm^*} \cdot \Delta f \quad \text{and} \quad \Delta f = \frac{p_{motor}\cdot fm^*}{4\cdot\pi\cdot H^*} \cdot \Delta H \qquad (2.72)$$

Figure 2.32 presents the structure of the variable pressure pump controller.

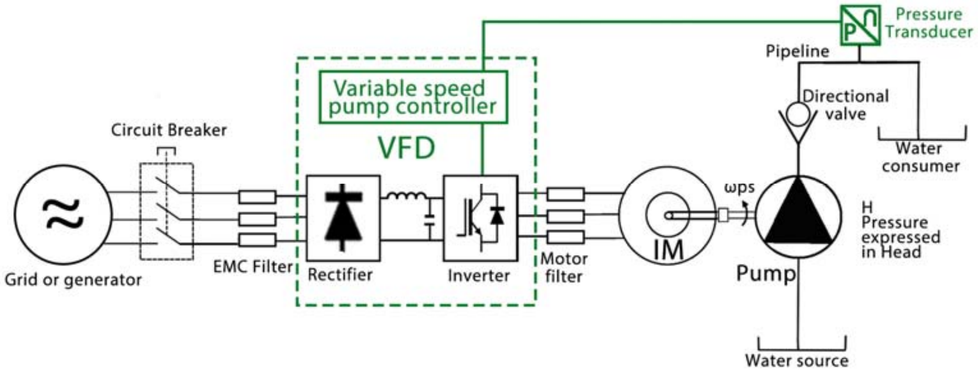

Figure 2.32. Pump motor powered by a VFD at variable pressure

2.3.2.3. Variable power pump controller

Another particular application of the variable speed pump is the pumping system where the absorption power is limited. For example, in the pumping systems powered by a photovoltaic (electrical wind) generator, where the pumping system absorption power has to track the photovoltaic (electrical wind) generator produced power. Due to this reason, a mathematical equation is introduced, in order to obtain the electrical frequency error $\Delta f=(fm^*-fm)$ expressed as a function of pump power error $\Delta P_{pump}=(P_{pump}^*-P_{pump})$, the first-order Taylor series approximation is used:

$$P_{pump} = \left(P_{pump}\right)^* + \frac{2\cdot\pi}{p_{motor}}\cdot(fm - fm^*)\cdot\left(\dot{P}_{pump}\right)_{fm^*} \tag{2.73}$$

where $\dot{P}_{pump}$ is obtained deriving equation (2.34) from the affinity laws, equations (2.32)-(2.34), the angular velocity (ω_{pss}) is converted into electrical frequency (fm) (equation (2.58)), and the nominal pump power (P_{pump0}) and frequency (fm_0) are equals with the reference pump power ($P_{pump}^*=P_{pump0}$) and frequency ($fm^*=fm_0$) [48]. From equation (2.73) results:

$$\Delta P_{pump} = \frac{2\cdot\pi}{p_{motor}}\cdot\Delta f\cdot\left(\dot{P}_{pump}\right)_{fm^*} = \frac{4\cdot\pi\cdot H^*}{p_{motor}\cdot fm^*}\cdot\Delta f \quad \text{and} \quad \Delta f = \frac{p_{motor}\cdot fm^*}{6\cdot\pi\cdot\left(P_{pump}\right)^*}\cdot\Delta P_{pump} \tag{2.74}$$

Figure 2.33 presents the structure of the variable flow pump controller.

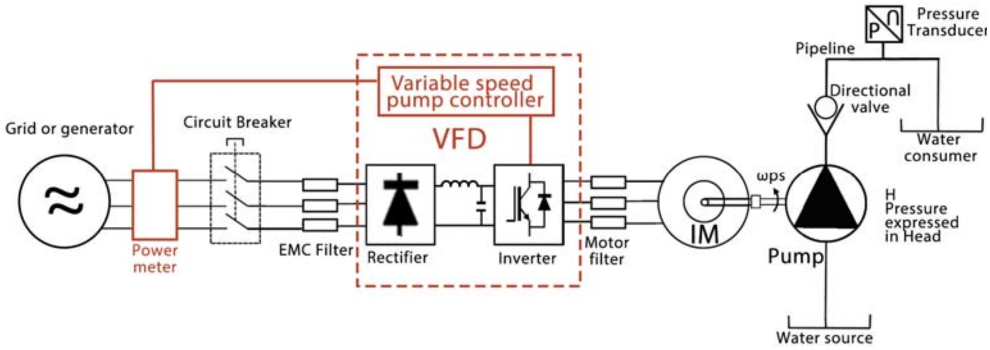

Figure 2.33. Pump motor powered by a VFD at variable power

2.4. Pumping system simulations

Combining the pumping system control strategy presented in the third subchapter (***2.3. Pumping system control strategy***), with the dynamic model of the pumping system presented in the second subchapter (***2.2. Pumping system modelling***), a simulator was developed in Simulink [43].

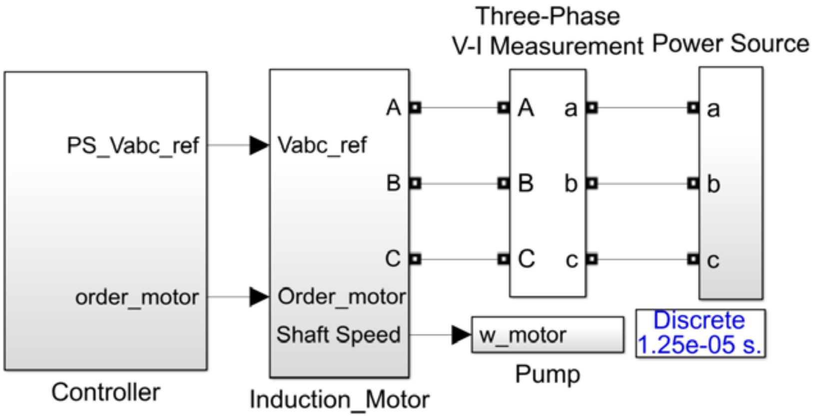

Figure 2.34. Pumping system simulator flow chart in Simulink

Using the developed pumping system simulator, five simulations were executed in order to analyze and evaluate the response of the: fixed speed pump controller, variable speed, flow, pressure and power pump controllers

2.4.1. Response of the pump driven by a soft starter (fixed speed pump controller)

In the first simulation (15 seconds), is presented the response of the pumping system when the induction motor is driven by a soft starter that accelerates to the rated speed in 10 s and then decelerates to 0. This simulation was executed in order to see the response of the pumping unit (induction motor plus centrifugal pump) driven by a soft starter.

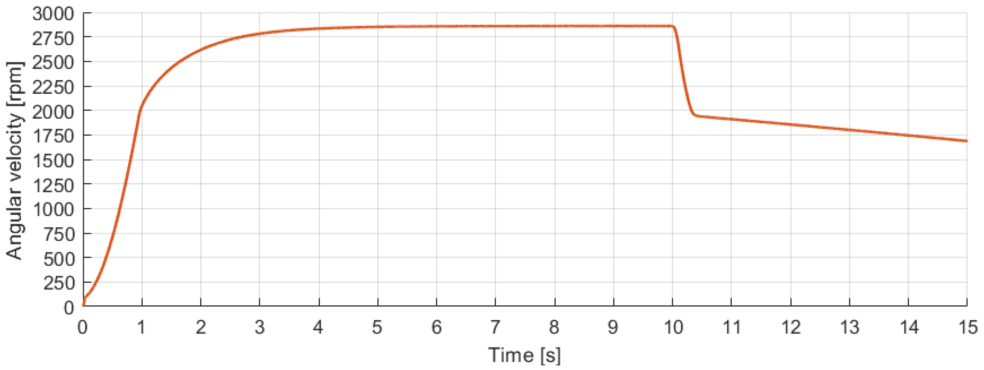

Figure 2.35. Agular velocity response of the fixed speed controller

In Figure 2.35, it can be seen that the developed strategy for controlling to a fixed speed through a soft starter, makes the presented pump accelerate to its nominal speed in less than 4 seconds without any overshoot or oscillations (<0.003 %).

Figure 2.36, presents the induction motor's speed reference expressed in electromechanical torque, the actual electromechanical torque and the load (pump) torque. It can be seen that the actual motor torque has a maximum residual deviation of 8%. It can also be observed a delay between the motor torque and the pump torque due to the reason that no torque it's applied to the pump until reaches the minimum head (pressure) for pumping water.

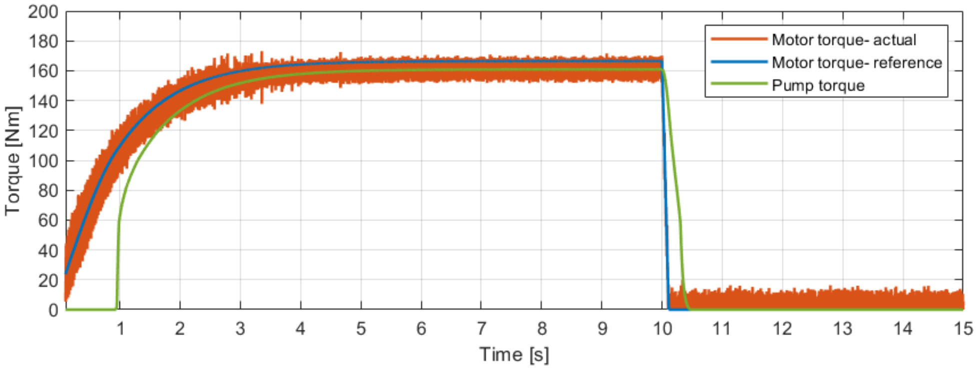

Figure 2.36. Torque response of the fixed speed controller

In Figure 2.37, it can be seen the 3 phases voltage supply from the power grid to the induction motor, are held constant during this simulation.

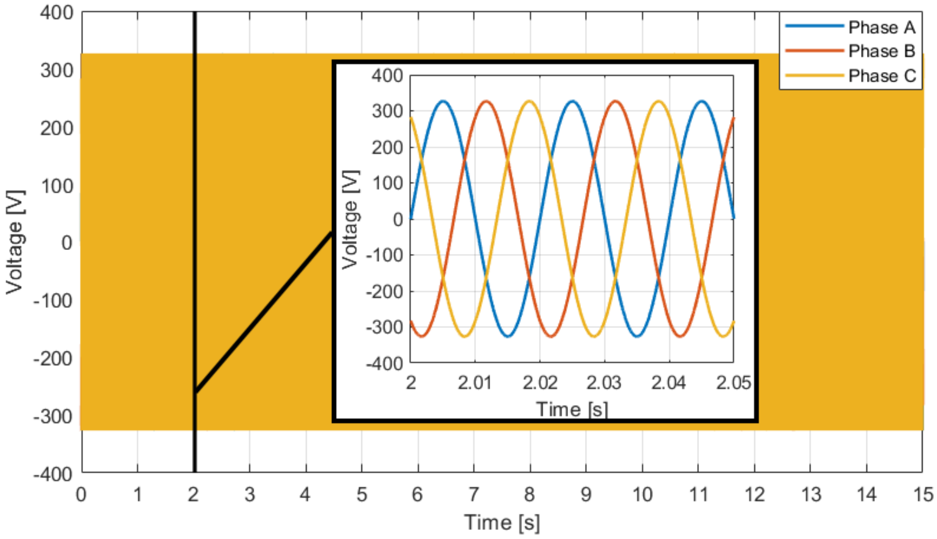

Figure 2.37. Induction motor voltage during the fixed speed controller simulation

In Figure 2.38., it can be seen the current variation of the 3 phases supplying the induction motor. This figure confirms that using a soft starter, the starting (first seconds) current flow from the power grid to the induction motor does not exceed the nominal current as in the case of a star-delta starter.

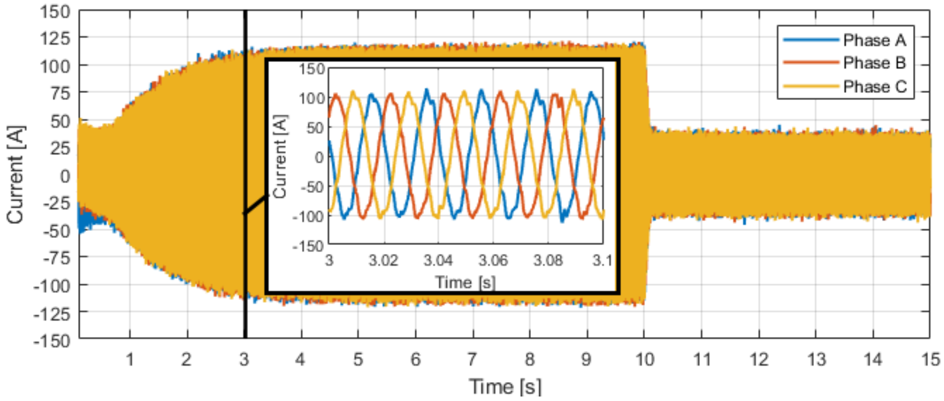

Figure 2.38. Induction motor current absorption of the fixed speed controller

Figure 2.39 depicts the electrical power flow from the power grid to the induction motor, how this power is converted into rotational (mechanical power), and transferred to the pump. Similar to Figure 2.38, this figure confirms that using a soft starter, the starting (first seconds) power flow from the power grid to the induction motor does not exceed the nominal power as in the case of a star-delta starter. It can be also seen that stopping the pump is done by deceleration and not by cutting off.

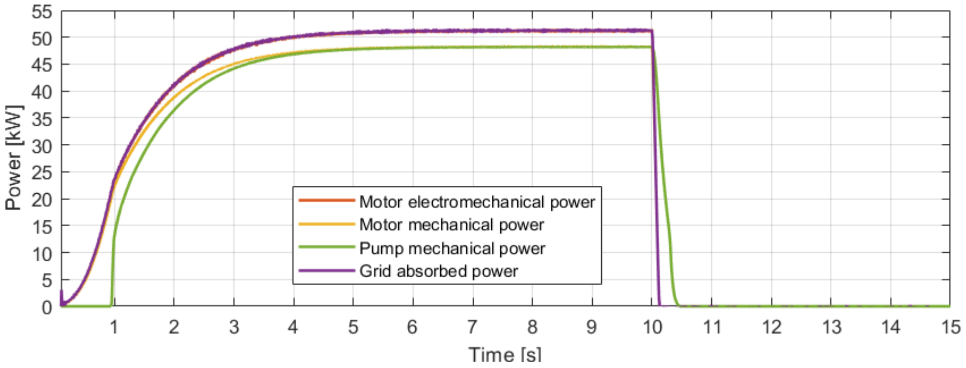

Figure 2.39. Power response of the fixed speed controller

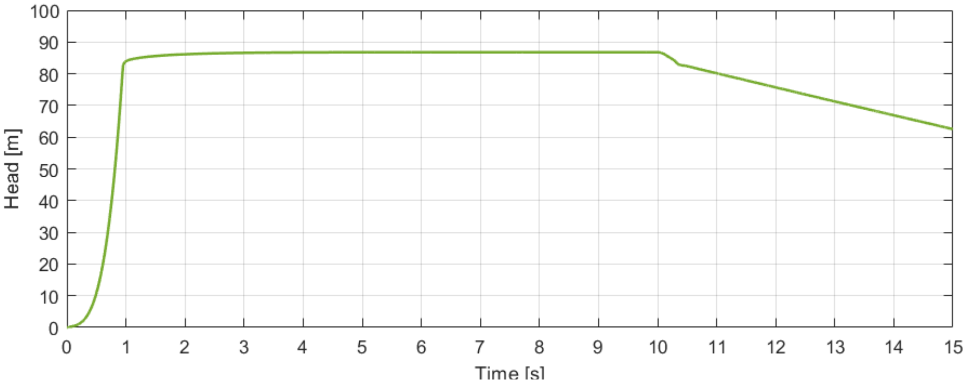

Figure 2.40. Pump head response of the fixed speed controller

In Figure 2.40 it can be seen that the presented control strategy reaches quickly (almost 1 second) the minimum pump head (pressure) for pumping water, and then slowly reaches the nominal pressure. In this diagram, it can be also seen that no water hammer or cavitation occurs during the operation of the pump.

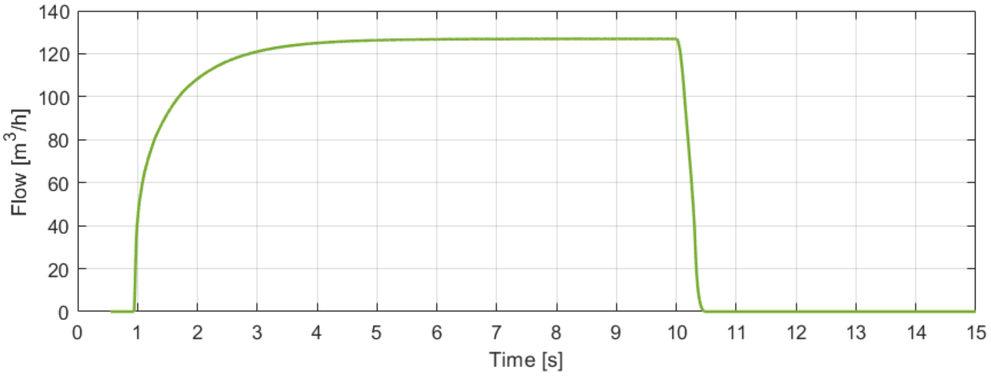

Figure 2.41. Pump flow response of the fixed speed controller

Figure 2.41 presents the pump water discharge (flow) into the irrigation network. This diagram shows, that in less than 1 second the pump starts pumping water in order to avoid the overheating of the induction motor due to only rotating the water inside the well/ hydraulic network, without pumping it. A phenomenon that can lead to short-circuiting the induction motor.

2.4.2. Response of the pump driven by a VFD (Variable frequency drive)

The following simulations are executed in order to see the response of the pumping unit (induction motor plus centrifugal pump) driven by a VFD in 4 different modes (considering 4 different references):

1. Variable speed;
2. Variable flow;
3. Variable head (pressure);
4. Variable power.

2.4.2.1. Response of the variable speed pump controller

In the second simulation (12 seconds), is presented the response of the pumping unit driven by a VFD (in the variable speed mode) by a reference speed step from 1800 rpm to 2400 rpm, occurring at the fourth second.

In Figure 2.42, it can be seen that the developed strategy for controlling the pump to various speeds, makes the pump seed reach its reference with a small overshoot (maximum overshoot<0.4%) or oscillations (<0.003 %).

Figure 2.43, presents the induction motor’s speed reference expressed in electromechanical torque, the actual electromechanical torque and the load (pump) torque. It can be seen that the proposed controller drives the induction motor with its maximum torque until reaches the torque equivalent to its reference speed. Compared to Figure 2.36 it can be observed that the delay between the motor torque and the pump torque has disappeared because the pump is already discharging water (flow).

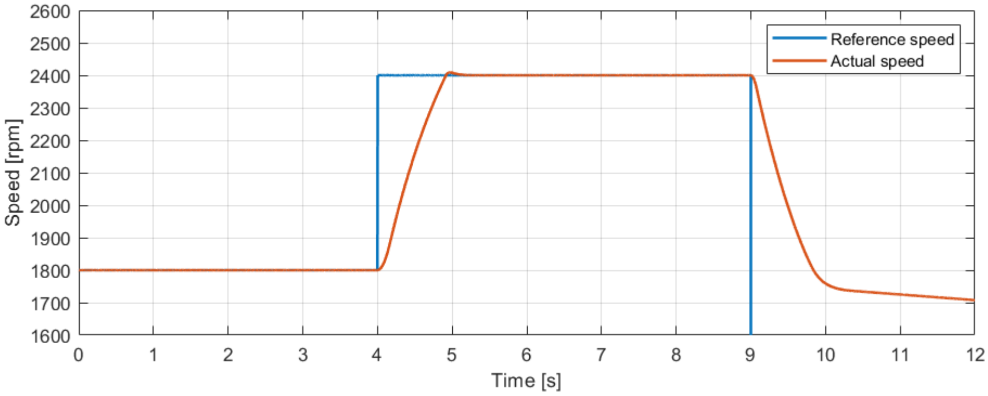

Figure 2.42. Agular velocity response of the variable speed controller

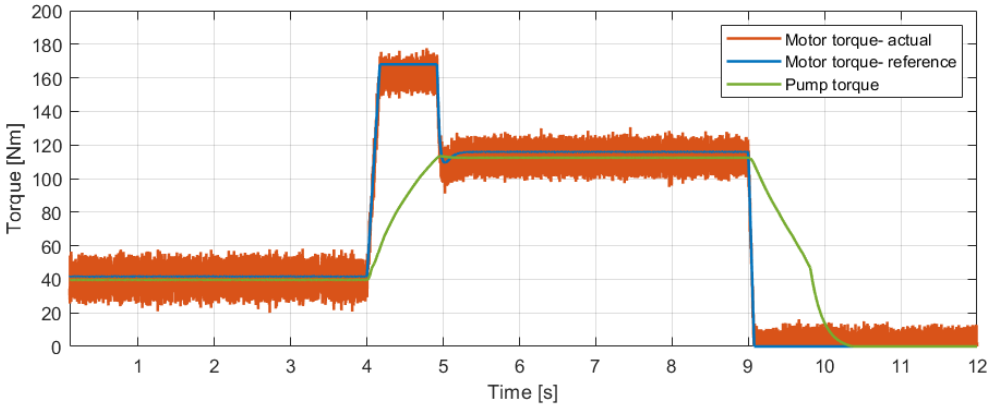

Figure 2.43. Torque response of the variable speed controller

As in the first simulation (Figure 2.37), in Figure 2.44 it can be seen that the 3 phases voltage supply from the power grid to the induction motor, is held constant.

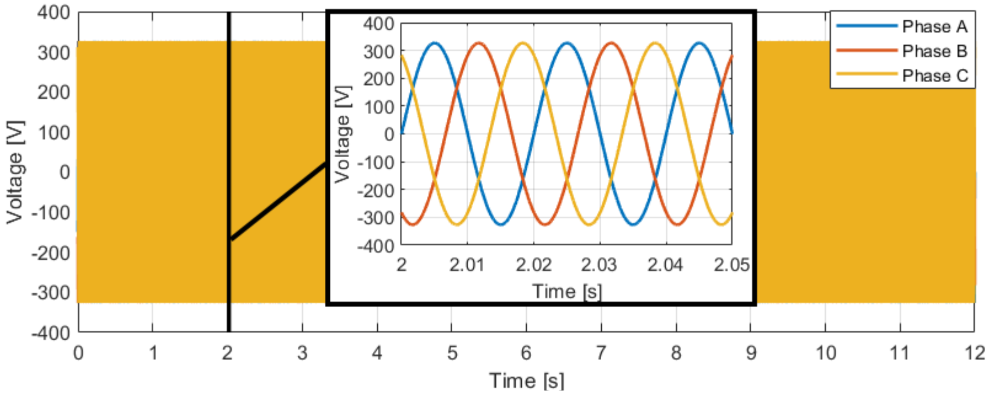

Figure 2.44. Induction motor voltage during the variable speed controller simulation

In Figure 2.45, it can be seen the current variation of the 3 phases supplying the induction motor.

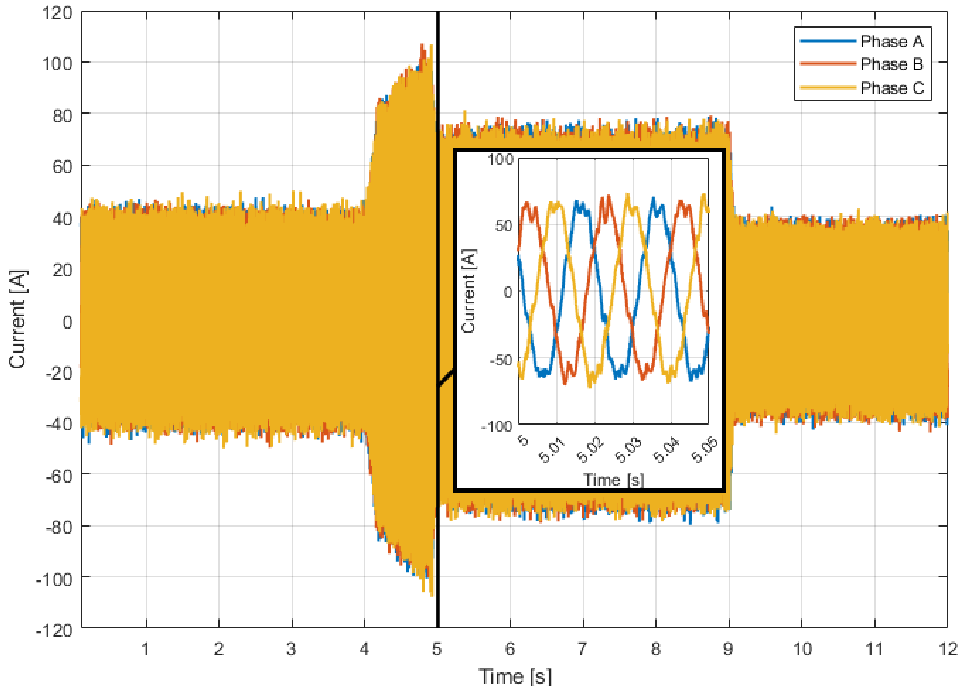

Figure 2.45. Induction motor current absorption during the variable speed controller simulation

Figure 2.46 depicts the electrical power absorbed from the power grid, the motor electromechanical power, the mechanical (rotational) power provided by the motor and the pump's shaft mechanical (rotational) power. During the power transition of the induction motor, the absorbed power from the grid does not exceed the nominal power of the motor. The fluctuations of the absorbed power do not exceed 1% (accepted by most of the power grids).

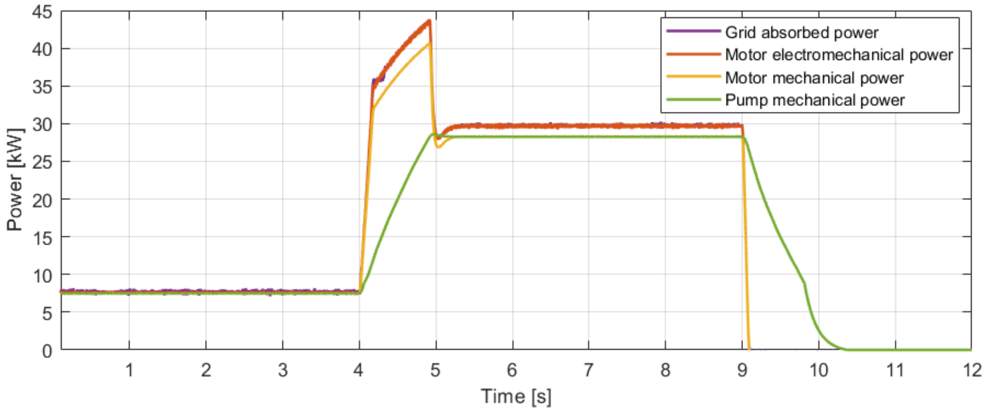

Figure 2.46. Power response of the variable speed controller

In Figure 2.47 it can be seen the pump head (pressure) variation during the variable speed step response.

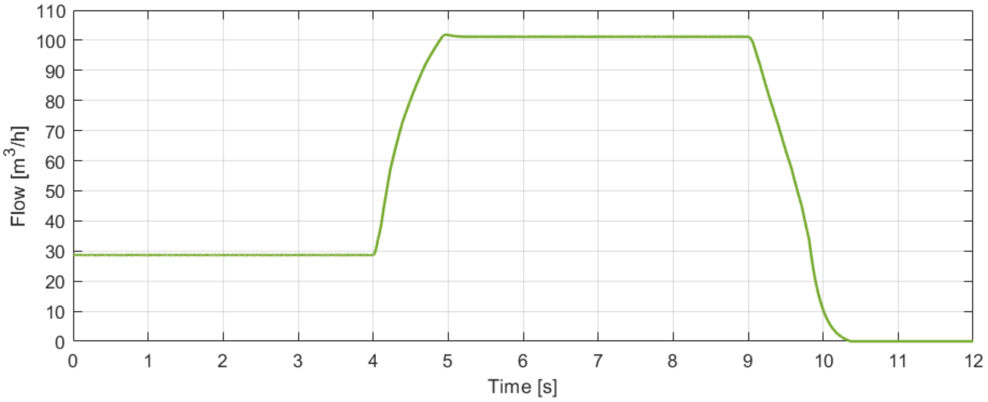

Figure 2.47. Pump flow response of the variable speed controller

Figure 2.48 presents the pump water discharge (flow) variation during the variable speed step response.

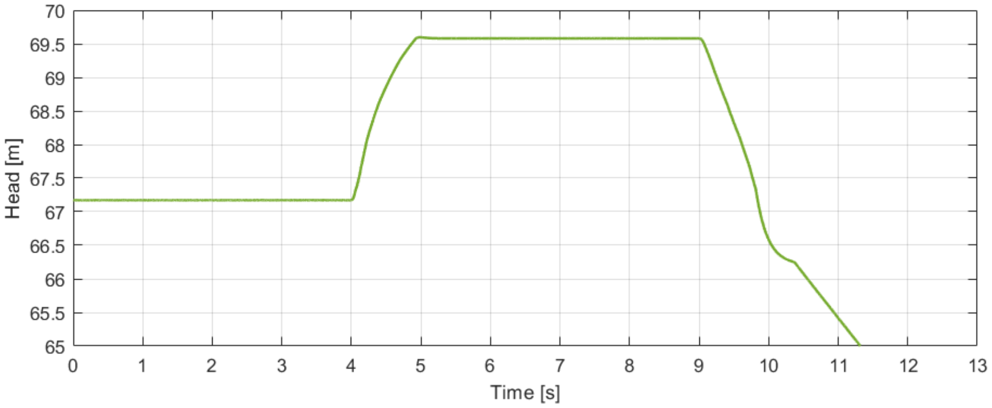

Figure 2.48. Pump head response of the variable speed controller

2.4.2.2. Variable flow pump controller

In the third simulation (12 seconds), is presented the response of the pumping unit driven by a VFD, in the variable flow mode, by a reference flow step from 84 m^3/h to 91.5 m^3/h, occurring in the fourth second. In the ninth second the proposed control strategy gives the stopping order.

In Figure 2.49, it can be seen that the developed strategy for controlling the pump to various flows (discharges), makes the pump flow reach its reference with a small overshoot (maximum overshoot<1.3%) or oscillations (<0.003 %).

Figure 2.50 presents the actual speed of the induction motor and the reference pump flow expressed in the motor's speed. In second four during the simulation, it can be seen how the equivalent speed reference changes as the actual volume flow start reaching its reference.

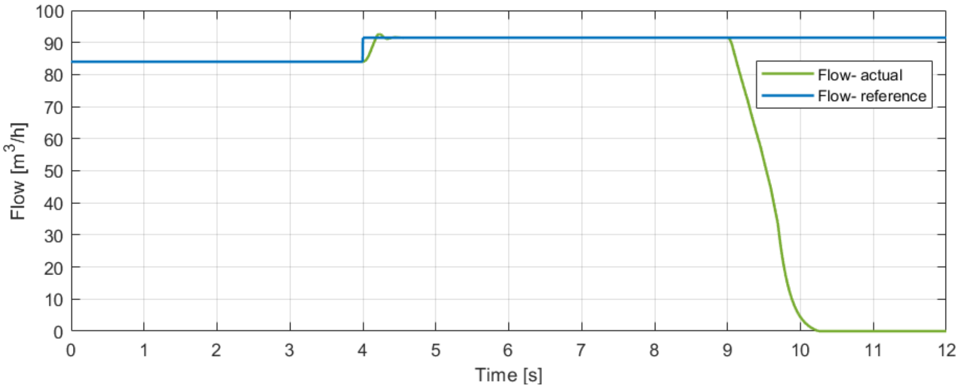

Figure 2.49. Pump flow response of the variable flow controller

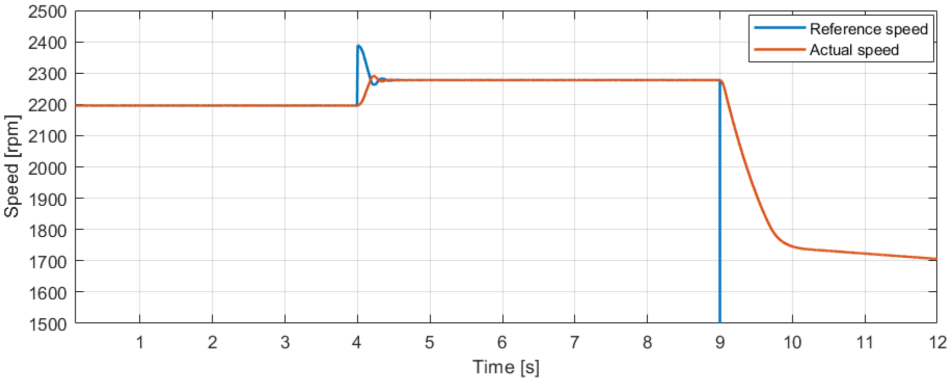

Figure 2.50. Agular velocity response of the variable flow controller

Figure 2.51 presents the pump water flow reference expressed in electromechanical torque, the actual electromechanical torque and the load (pump) torque.

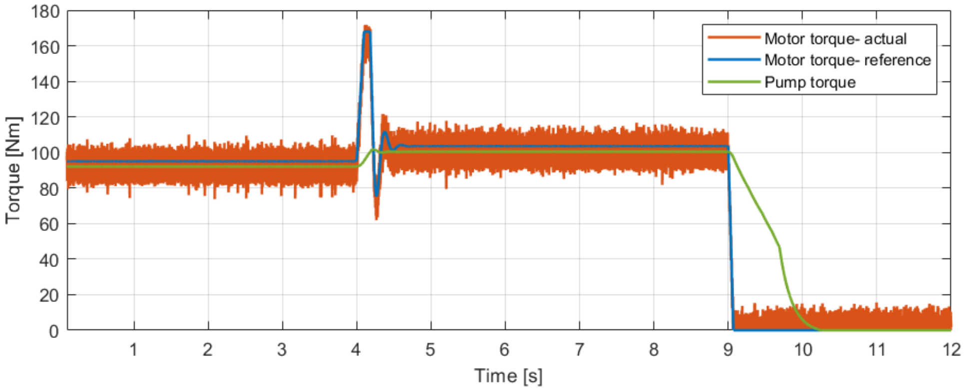

Figure 2.51. Torque response of the variable flow controller

Figure 2.52 shows the 3 phases voltage from the power grid being held constant.

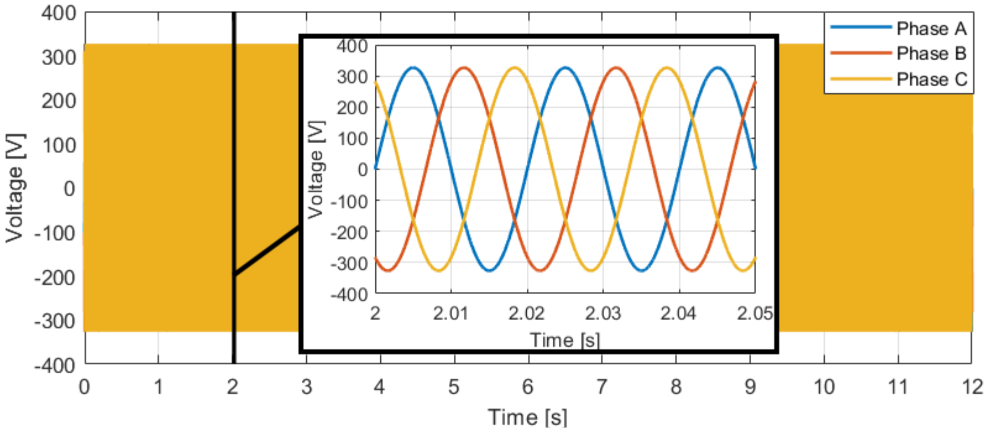

Figure 2.52. Induction motor voltage during the variable flow controller simulation

In Figure 2.53, it can be seen the current variation of the 3 phases supplying the induction motor.

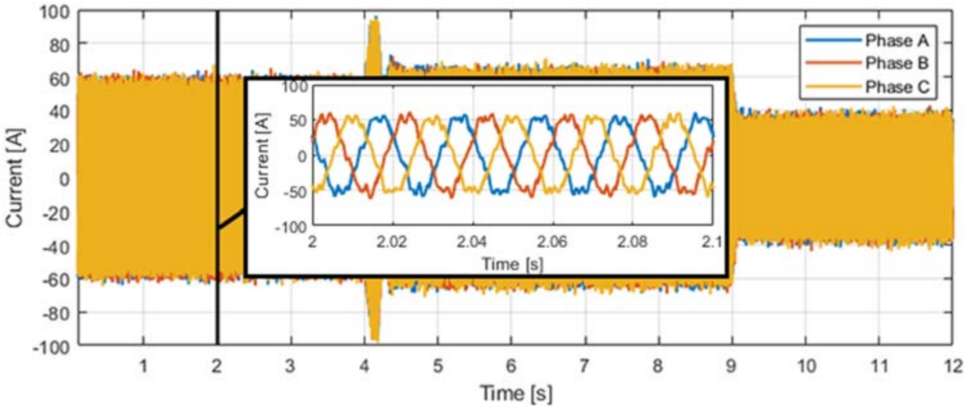

Figure 2.53. Induction motor current absorption of the variable flow controller

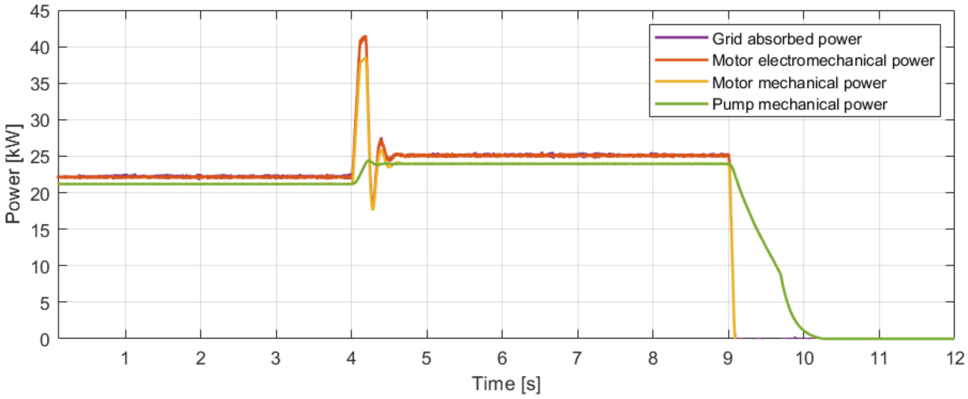

Figure 2.54. Power response of the variable flow controller

Figure 2.54 depicts the electrical power absorbed from the power grid, the motor electromechanical power, the mechanical (rotational) power provided by the motor and the pump's shaft mechanical (rotational) power. During the power transition of the induction motor, the absorbed power from the grid does not exceed the nominal power of the motor. The fluctuations of the absorbed power do not exceed 1% (accepted by most of the power grids).

In Figure 2.55 it can be seen the pump head (pressure) variation during the variable flow (discharge) step response.

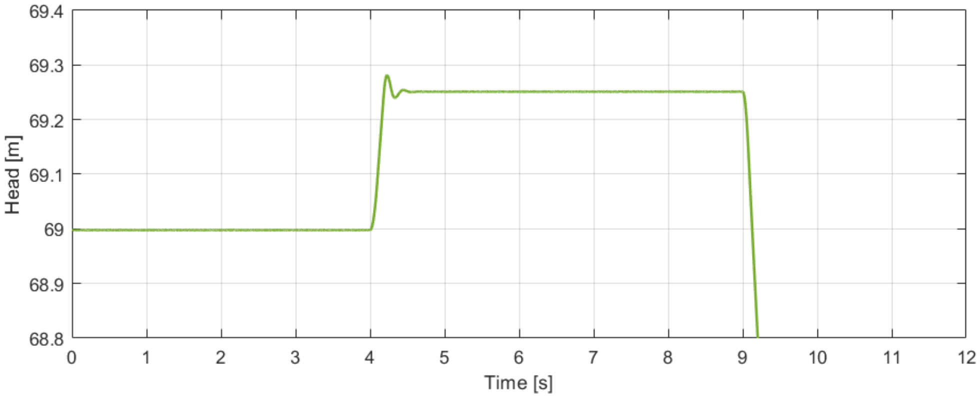

Figure 2.55. Pump head response of the variable flow controller

2.4.2.3. Variable pressure pump controller

In the fourth simulation (12 seconds), is presented the response of the pumping unit driven by a VFD, in the variable head (pressure) mode, by a reference head step from 68 m to 70 m, occurring at the fourth second. In the ninth second the proposed control strategy gives the order to stop the pump operation.

In Figure 2.56, it can be seen that the developed strategy for controlling the pump to various heads (pressures), makes the pump pressure reach its reference with a small overshoot (maximum overshoot<0.2%) or oscillations (<0.001%).

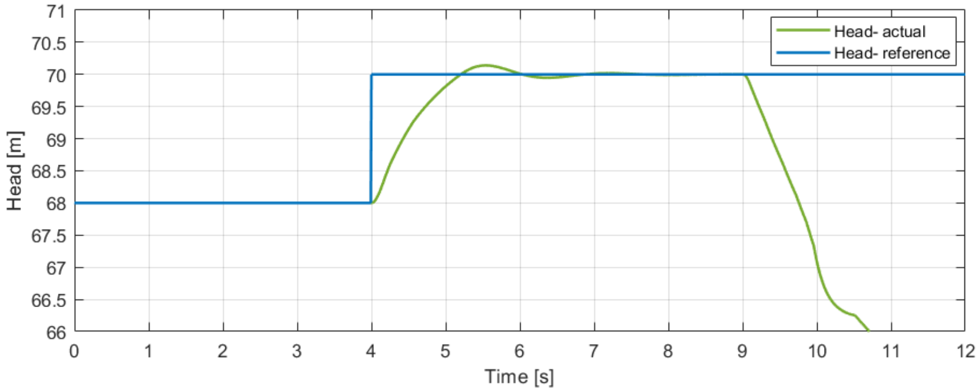

Figure 2.56. Pump head response of the variable head controller

Figure 2.57 presents how the actual speed of the induction motor tracks the reference pump head (pressure) expressed in motor’s speed.

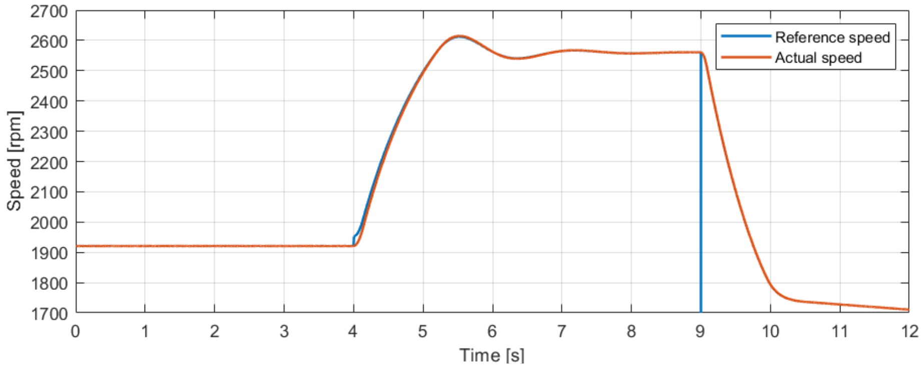

Figure 2.57. Agular velocity response of the variable head controller

Figure 2.58 presents the pump head reference expressed in electromechanical torque, the actual electromechanical torque and the load (pump) torque.

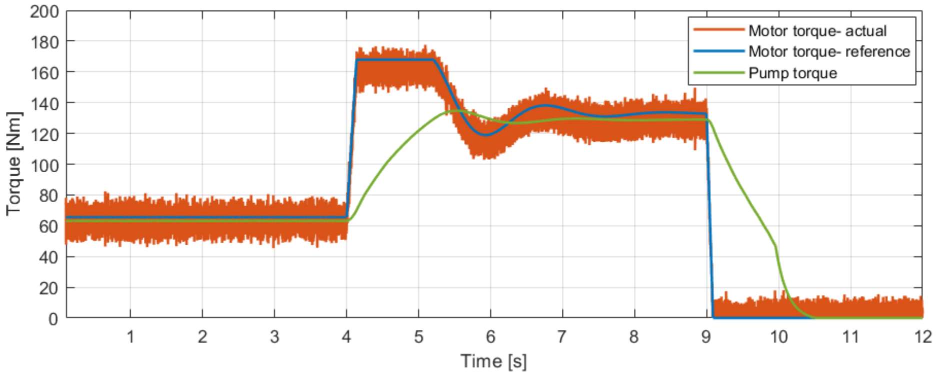

Figure 2.58. Torque response of the variable head controller

Figure 2.59 shows the 3 phases voltage from the power grid being held constant.

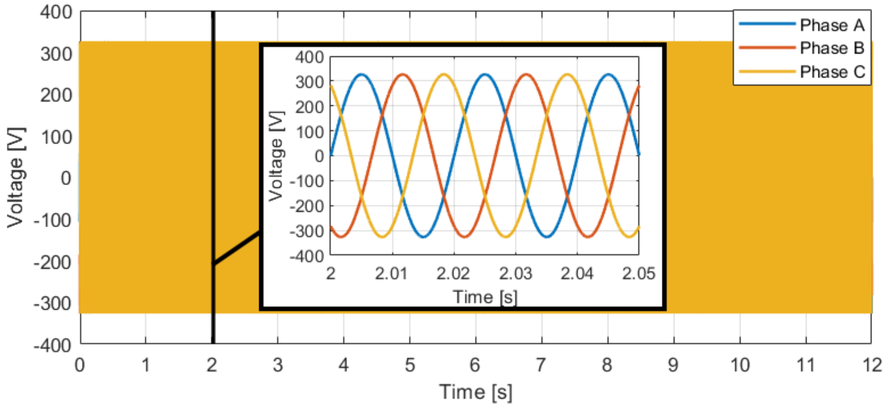

Figure 2.59. Induction motor voltage during the variable head controller simulation

In Figure 2.60, it can be seen the current variation of the 3 phases supplying the induction motor during the variable bead controller.

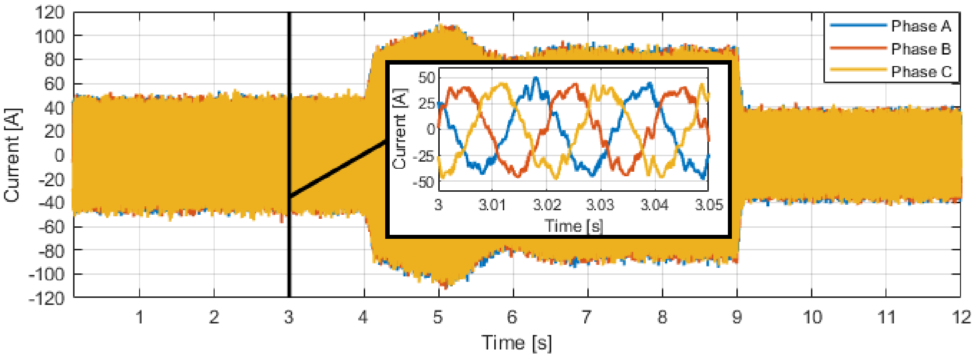

Figure 2.60. Induction motor current absorption of the variable head controller

Figure 2.61 depicts the electrical power absorbed from the power grid, the motor electromechanical power, the mechanical (rotational) power provided by the motor and the pump’s shaft mechanical (rotational) power. During the power transition of the induction motor, the absorbed power from the grid does not exceed the nominal power of the motor. The fluctuations of the absorbed power do not exceed 1% (accepted by most of the power grids).

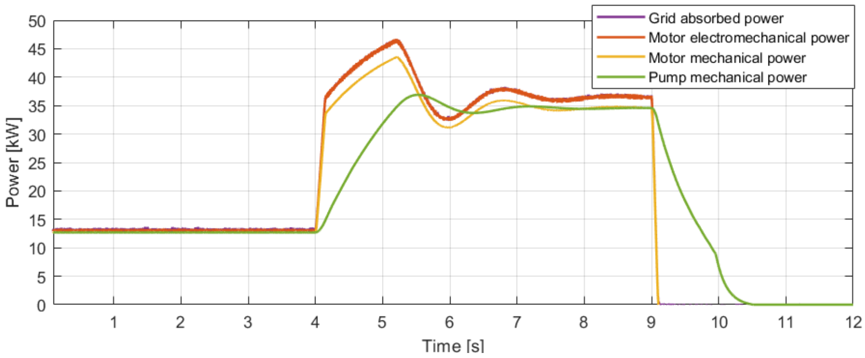

Figure 2.61. Power response of the variable head controller

In Figure 2.62, it can be seen the pump discharge (flow) variation during the variable head controller.

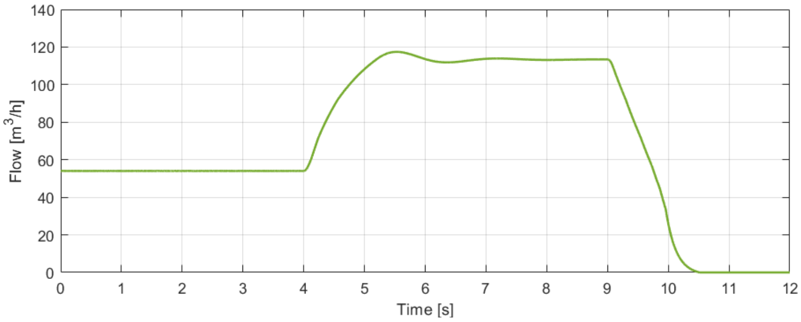

Figure 2.62. Pump flow response of the variable head controller

2.4.2.4. Variable power pump controller

In the last simulation (9 seconds), is presented the response of the pumping unit driven by a VFD, in the variable power mode, by a reference power step from 22 kW to 25 kW, occurring at one second. In the sixth second, the proposed control strategy gives the order to stop the pump operation.

In Figure 2.63 depicts the electrical power absorbed from the power grid, the motor electromechanical power, the mechanical (rotational) power provided by the motor and the pump's shaft mechanical (rotational) power and it can be seen that the developed strategy for controlling the pump to various powers makes the pump power to reach its reference with some oscillations around 5%.

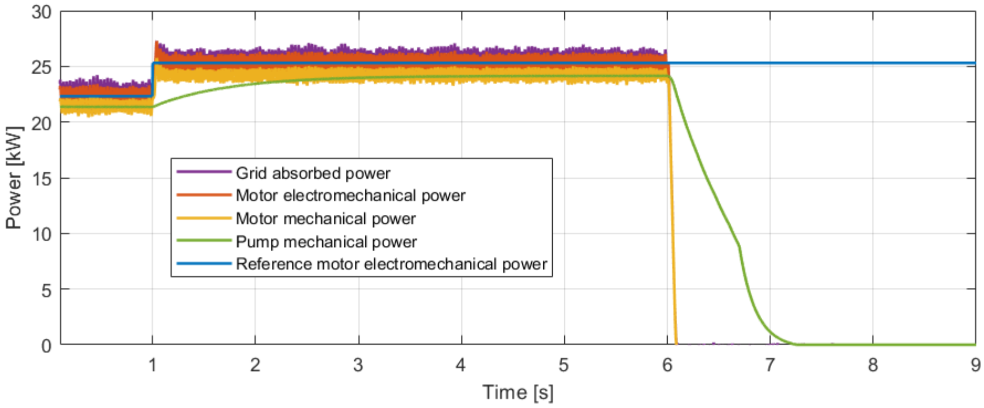

Figure 2.63. Power response of the variable power controller

Figure 2.64 presents the actual speed of the induction motor and the reference power expressed in the motor's speed. The fluctuations of the induction motors speed are maximum 1.5%.

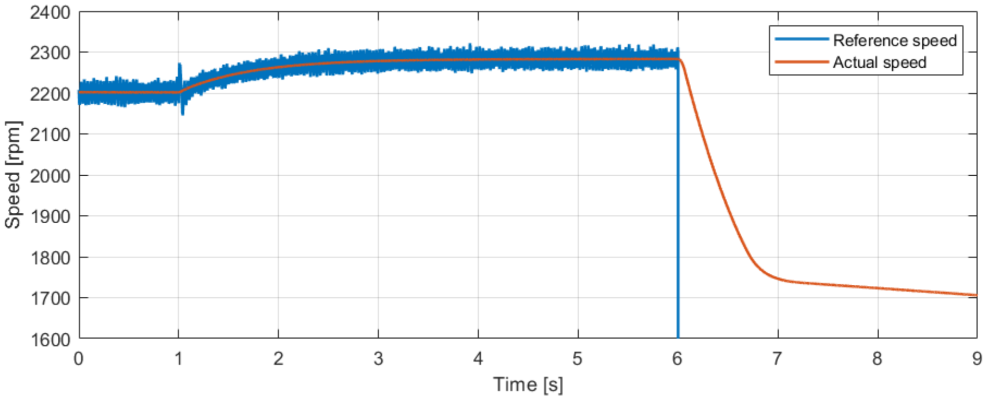

Figure 2.64. Agular velocity response of the variable power controller

Figure 2.65 presents the induction motor power reference expressed in electromechanical torque, the actual electromechanical torque and the pump torque.

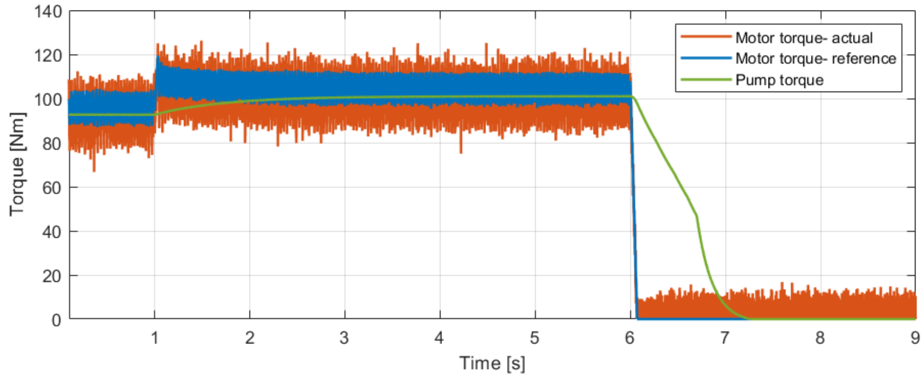

Figure 2.65. Torque response of the variable power controller

Figure 2.66 shows the 3 phases voltage from the power grid being held constant.

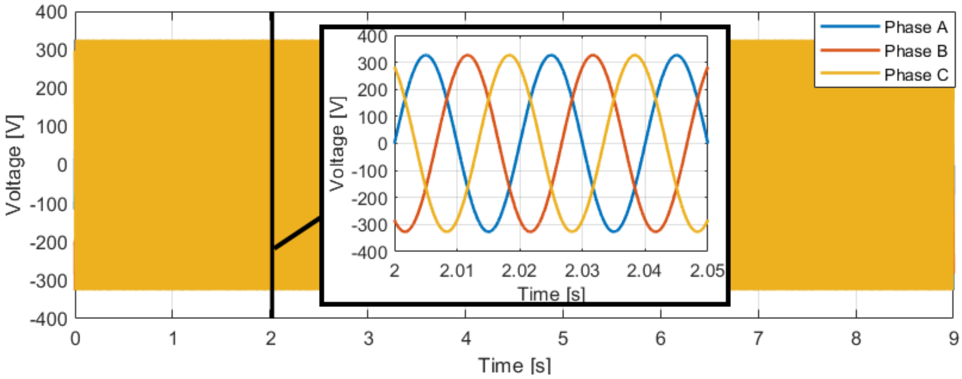

Figure 2.66. Induction motor voltage during the variable power controller simulation

In Figure 2.67, it can be seen the current variation of the 3 phases supplying the induction motor during the variable bead controller.

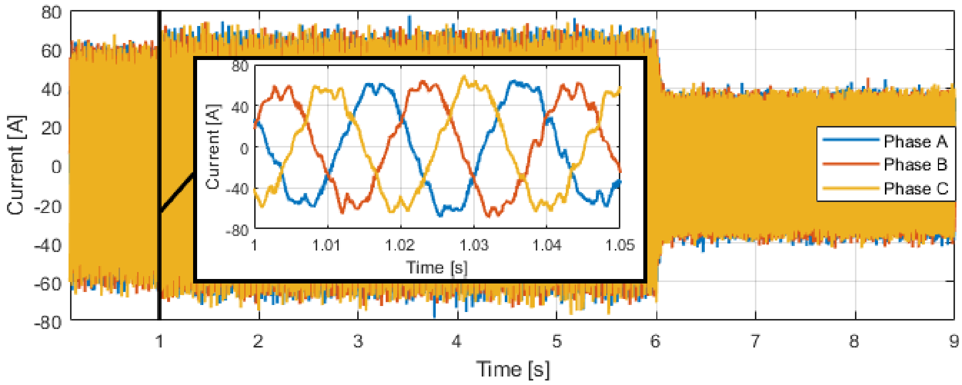

Figure 2.67. Induction motor current absorption during the variable power controller simulation

In Figure 2.68, it can be seen the pump discharge (flow) variation during the variable power controller.

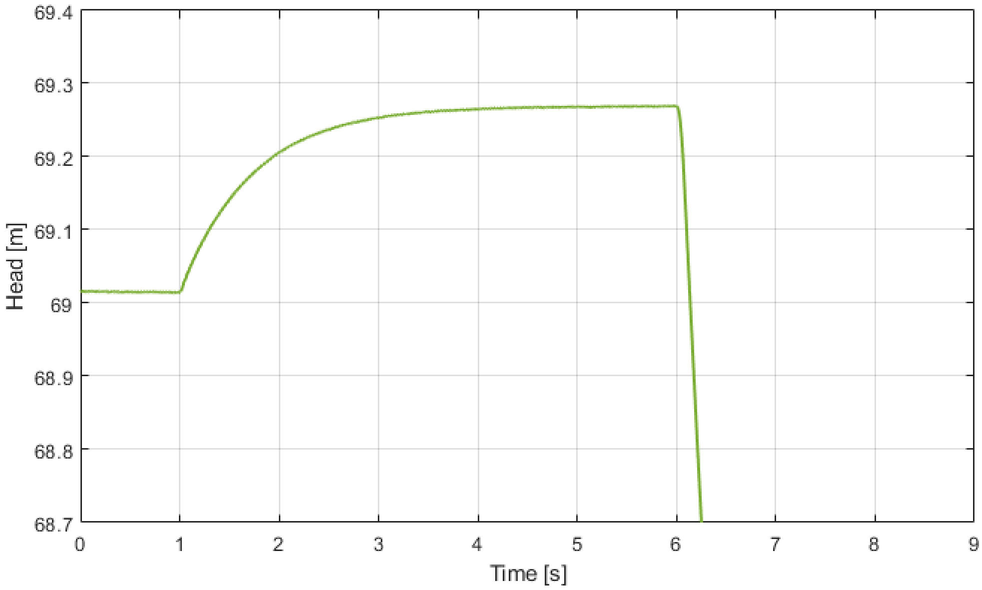

Figure 2.68. Pump head response of the variable power controller

In Figure 2.69, it can be seen the pump discharge (flow) variation during the variable power controller.

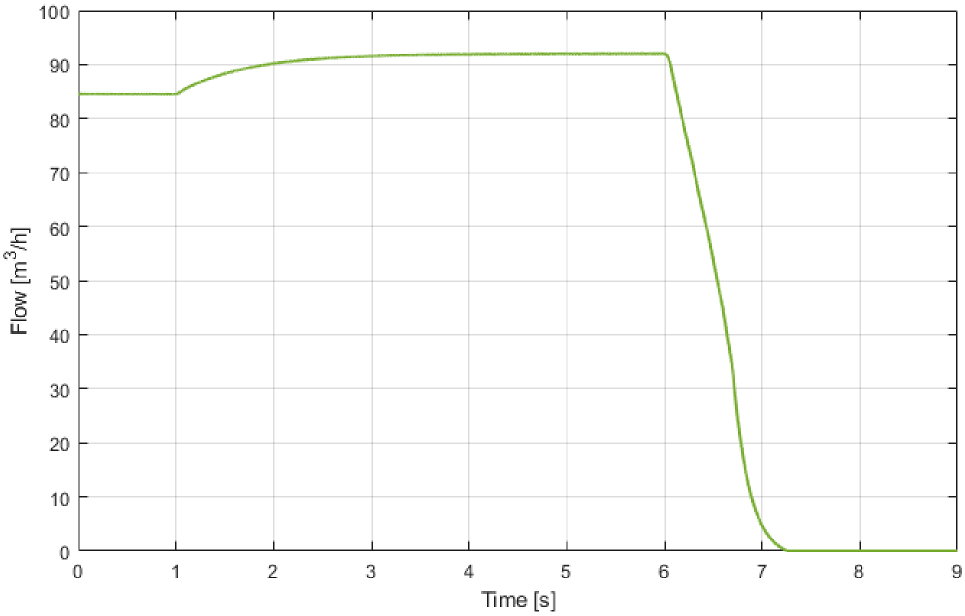

Figure 2.69. Pump flow response of the variable power controller

2.5. Pumping system chapter conclusion

According to chapter ***2. PUMPING SYSTEMS***, it can be concluded that the model of the pumping system developed in subchapter ***2.2 Pumping system modelling*** can be used for both dimensioning and simulating pumping systems. The personal contribution to pumping system modelling consists in developing a model capable of simulating also transitory regimes not only nominal regimes as the ones presented in the specialized literature [10, 11, 38, 45, 46, 49, 50, 52].

In subchapter ***2.3 Pumping system control strategy***, it is developed a strategy for controlling a pumping system based on the vectorial machine controller from reference [40, 41] whose current references are given by a PI speed controller in cascade. The personal contribution to the pumping system control strategy consists in adding several mathematical equations, in order to obtain the electrical frequency error expressed as a function of pump discharge (flow) error, head (pressure) error, or absorbed power error necessary for driving a pump through a VFD to desired flow, head or for tracking a fluctuating and intermittent power source.

Finally, in the fourth subchapter (section ***2.4. Pumping system simulations***), the pumping system model and the proposed control strategy are validated through five simulations where the pump is driven at a fixed speed, variable speed, variable flow, variable pressure and variable power pump controllers. The performance of the proposed control strategy is determined by analyzing several performance indicators: induction motor and pump speed, torque, the absorbed power by the induction motor from the power grid including the 3 phases voltages and currents and the pump’s water head and discharge.

3. PHOTOVOLTAIC ENERGY CONVERSION SYSTEMS (PECS)

The current chapter presents the modelling and simulation of a PECS (photovoltaic energy conversion system). The first subchapter (***3.1. PECS description***) presents a short description of a general PECS and its components. The second subchapter (***3.2. PECS modelling***) consists of a nonlinear mathematical model of the described PECS, and the third subchapter (***3.3. PECS controller***) presents the proposed control strategy. In the fourth subchapter (***3.4. PECS simulations***), the performance of the proposed control strategy is determined by analyzing several performance indicators during four simulations: a clear sky day, a day with a big cloud, a day with many small clouds and a fully cloudy day. Finally, in the last subchapter (***3.5. Conclusions***) are presented the chapter conclusions.

3.1. PECS description

The pumping systems used in the irrigation of agricultural fields are powered by electricity from the national grid in areas where this grid is found, and by diesel or gasoline generators, where it is missing. Since most of these systems are used during summer, with maximum demand on the hottest and sunniest days of the year, the solution for powering an irrigation PS may consist of PVG (photovoltaic generators) leading to an excellent integration of the PVG into such systems [54]. In the upcoming paragraphs, the main components of an existing PECS powering a PS in Aragon, Spain [54], a system used further in validating the proposed MM and control structures.

3.1.1. Photovoltaic panel

The PV (photovoltaic) cell is the core element of any PV generator [55] and consists of a p–n semiconductor junction that converts the PV energy received from the sun radiation into electrical energy [56]. A PV module (panel) is made of several series of PV cells connected in parallel [57]. In Table 3.1. it can be seen the technical specification of the PV panel [58] considered in the current work.

3.1.2. Array of photovoltaic panels

A PV array consists of strings of PV modules connected in parallel, several or a multitude, depending on PV array power. Each string is made up of several PV modules connected in series and their number depends on the voltage requirements of the PV array [59, 60].

Table 3.1. Photovoltaic panel technical specifications [58]

Photovoltaic panel characteristics	Value	Symbol	Unit
Manufacturer	Trina Solar		
Type	144 cell multi-crystalline		
Electrical data at standard conditions (Irradiance 1000 W/m², Cell Temperature 25 °C, Air Mass AM1.5)			
Peak Power Watts	335	P_{MAX}	Wp
Power Output Tolerance	0/+5	-	-
Maximum Power Voltage	37.4	V_{MPP}	V
Maximum Power Current	8.96	I_{MPP}	A
Open Circuit Voltage	45.9	V_{OC}	V
Short Circuit Current	9.45	I_{SC}	A
Module Efficiency	16.9	η_m	%
Temperature coefficients			
Nominal Operating Cell Temperature (NOCT)	44	T	°C
Temperature Coefficient of ISC (Short-Circuit Current)	0.05	K_I	%/K
Temperature Coefficient of VOC (Open Circuit Voltage)	- 0.32	K_V	%/K
Temperature Coefficient of PMAX (Maximum Power)	- 0.41	K_P	%/K
Initial PV module power loss	3	η_{PPV}	%
Yearly PV module power loss	0.7	$\eta_{PPVyear}$	%

3.1.3. Support structure

The 171 photovoltaic panels are distributed on 3 decentralized self-operated horizontal single-axis trackers (HSAT) [61] (57 on each tracker). The trackers have N-S (north-south) orientation and a 110º range of motion around their axis.

The tracker structure is made out of galvanized hot steel and complies with EN 1991 [62, 63] regarding the resistance to the loads created by the self-mass, snow and wind characteristics at the site location and with ISO 9223 [64] regarding the protection against corrosion.

A 5 meters distance between the trackers was determined to be the optimum distance to avoid most of the shadows between the rows and allows access for cleaning and periodic inspection and maintenance.

The tracker control system controls the motor of the tracker and includes the algorithm to track the sun irradiation, the backtracking algorithm to avoid the shadows from one tracker to another, and includes also protections and alarms regarding axis blockage (the tracker stops its movement when reaching ±55º, or if it detects more power consumption in rotating the tracker than usual) or wind speeds (the tracker goes into the safe position if it detects wind speeds greater than the limit).

The decentralized solar tracker incorporates a control and communication system with the following characteristics:

- Wireless: Wireless communications system with ZigBee technology
- Self-powered from a photovoltaic module with a backup battery.
- Autonomous flagging: autonomous flagging to protect the structure and the photovoltaic modules in situations of extreme wind.
- Alarms and states: Easy implementation in the plant's SCADA system to carry out O&M tasks.

- Personalized Backtracking: The backtracking algorithm modifies the position of each tracker based on the height of the adjacent trackers, avoiding shadows and optimizing the production of photovoltaic modules.

Table 3.2. Photovoltaic tracker technical specifications [61]

Photovoltaic tracker characteristics	Value	Symbol	Unit
Manufacturer	-	-	-
Type	-	-	-
Dimensions			
PV Modules per beam	57		-
Installed power (PV module of 335 W)	56.95		kWp
PV module height. Tracker in horizontal position 0	2		M
PV module height. Tracker in 55 deg position	2.37, 0.4		Min, max
Mechanical characteristics			
Rotating range	Up to +/- 55º		
Maximum wind speed in the horizontal position	140		Km/h
Structure	Hot galvanized steel		
Drive unit (DU)			
DU type	Electromechanical rotary actuator		
DU power supply	155W/ 24V	Self-powered	
DU electrical consumption	< 0.45		kWh/day
Motor power	155		W
Control system			
Tracking controller	Astronomical Algorithm		
Backtracking Management	Backtracking Algorithm		
Wind Management	User-configurable feathering table		
Tilt sensor	Inclinometer		
Considered dirt factor (%D)	0.22		-

3.1.4. Inverter

In order to take advantage at maximum from the PV generator, a variable frequency drive (VFD) [37] will drive the AC induction motor also at partial load, when there is not enough power in the PV generator to run the motor at nominal power.
The VFD complies with IEC 61000-6-2 [65], IEC 61000-6-4 (EMI) [66] and EN50178 [67] standards and can operate in ambient temperatures higher than 50ºC. Due to the fact that the maximum voltage of the system with the current configuration can exceed a voltage higher than 830Vdc at low temperatures, a switch will be installed at the DC bus input to disconnect the DC bus connection from the PV generator.

A 45-kW variable frequency drive [37] converts the PECS DC power into AC power at a working voltage of 400 V with a maximum continuous current of 94 A. The variable frequency drive has 2 analog inputs, 2 analog outputs, 3 digital inputs, 3 configurable digital outputs; 2 relay outputs, one safe torque off input, 2 Modbus RS485 communication ports and an on-board PLC (Programable Logic Controller). The onboard PLC includes besides the programming functions, two PID controllers [37].

Table 3.3. VFD specifications [37]

Variable frequency drive	Value	Symbol	Unit
Variable frequency drive rated power	45		kW
Variable frequency drive rated voltage	400		V AC
Variable frequency drive maximum continuous current	94		A
Analog inputs	2		
Analog outputs	2		
Digital inputs	2		
Digital outputs	2		
Relay outputs	2		
Safe torque inputs	1		
Communication protocols	2	x Modbus RS485	

3.2. PECS modelling

In this subchapter is presented a steady-state model for dimensioning the PECS, and a dynamic model for simulating the transitory regimes of the PECS.

3.2.1. Steady-state model

In Figure 3.1, can be seen the Horizontal single-axis trackers layout and in Table 3.4 it the parameters description and values from Figure 3.1.

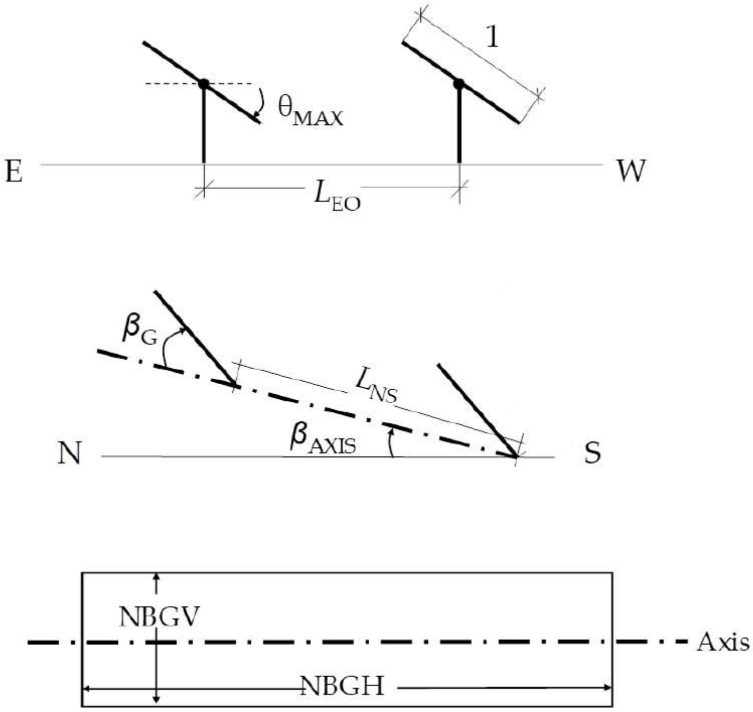

Figure 3.1. HSIT general layout [21]

Table 3.4. Photovoltaic tracker layout parameters technical specifications [21]

Variable frequency drive	Value	Symbol	Unit
Separation between trackers in E-W (East-West) direction	5	L_{EO}	m
Maximum Rotation	110	θ_{MAX}	°
Deviation of the rotating axis regarding the South (axis azimuth)	0	Dev	°
Axis inclination	0	β_{AXIS}	°
LNS: Separation between tracker rows in N-S direction	0	LNS	m
Module inclination	±55	β_G	°

The irradiation data from Table 3.5, considering a horizontal plane (parallel to the ground) at the site location, is obtained from PVGIS 5.2 [68] and it is depicted in Figure 3.2 and Figure 3.3:

Table 3.5. Irradiation data at site location from PVGIS 5.2 [68]

Parameter	Symbol	Unit
Global irradiation	G_{global}	W/m2
Diffuse irradiation	G_{diff}	W/m2
Clear sky irradiation	$G_{clearsky}$	W/m2
Environment temperature	T_{env}	°C
Direct irradiation	G_{direct}	W/m2
Solar time	H	hh:mm

Figure 3.2 presents the variation of the PV cell temperature during the representative day of each month at the site location. The representative day of each month refers to a day that represents an average of the considered characteristic (PV cell temperature in Figure 3.2 and Irradiation in Figure 3.3) of each month.

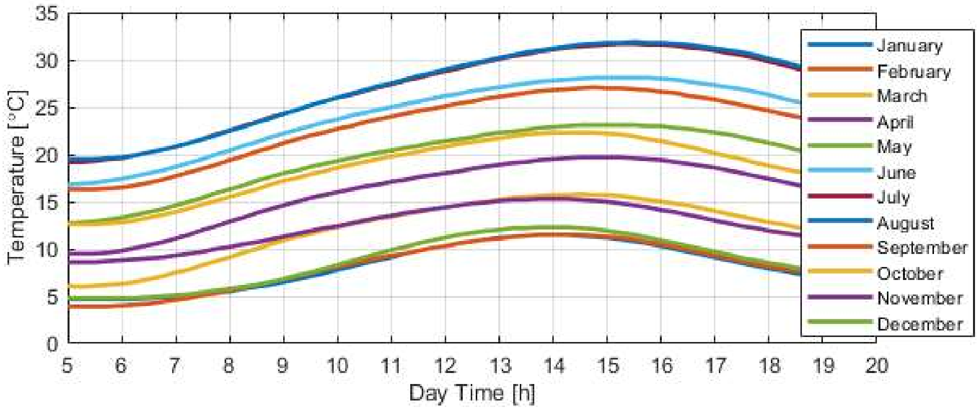

Figure 3.2. PV Cell temperature during the representative day of each month at the site location

Figure 3.3 presents the variation of the sun irradiance on the horizontal plane at the site location during the representative day of each month.

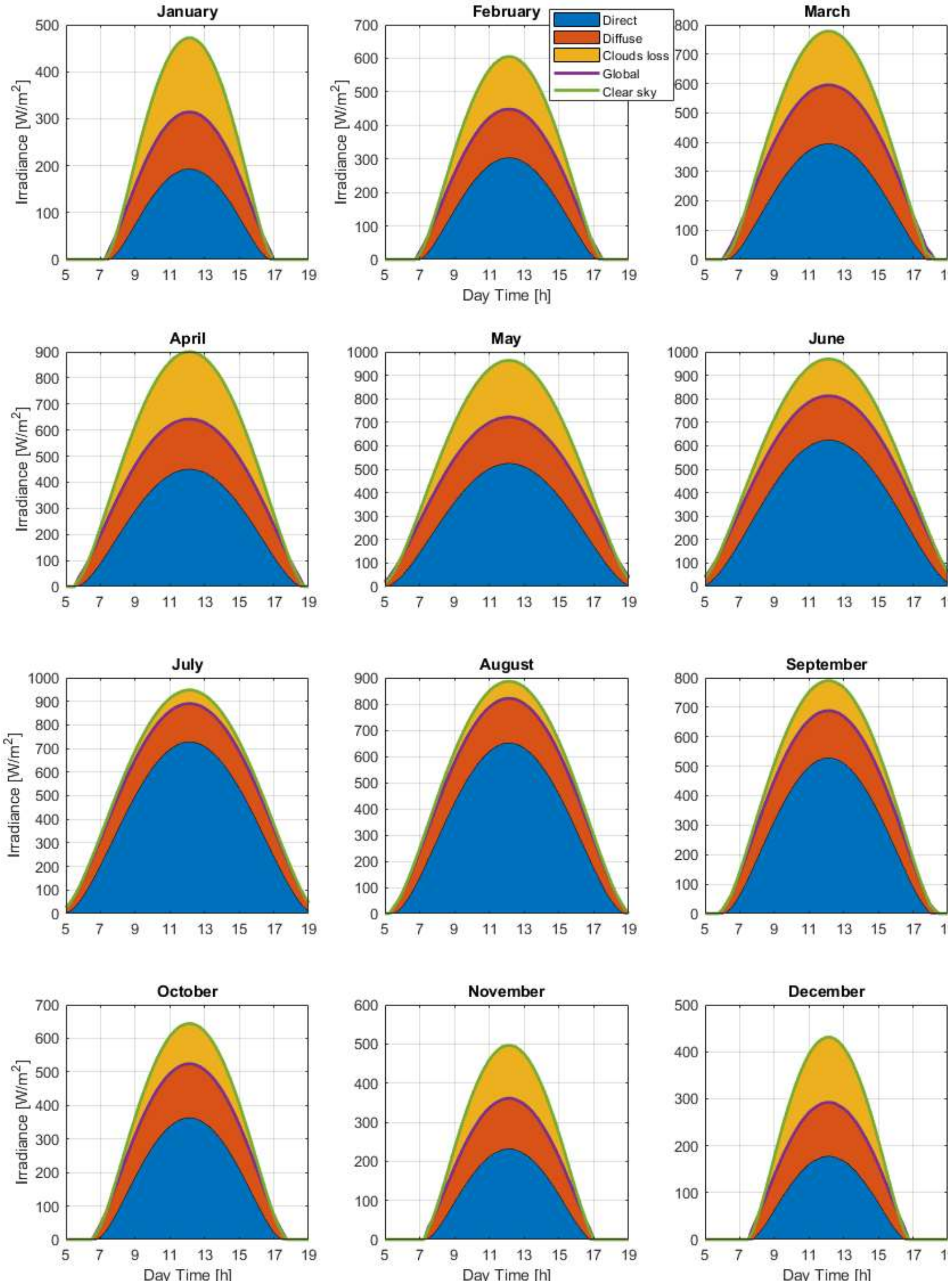

Figure 3.3. Irradiance during the representative day of each month at site location

The solar elevation is calculated according to the following formula [69]:

$$\gamma_S = \sin^{-1}\left((\sin PV\_declination \cdot \sin Lat + \cos PV\_declination \cdot \cos Lat) \cdot \cos H\right) \qquad (3.1)$$

The angle of incidence of the PV generator was calculated according to the following equation [22]:

$$\theta = \cos^{-1}(\sin\gamma_S \cdot \cos \beta\mathrm{G} + \sin\beta_G \cdot \cos\gamma_S \cdot \cos(Dev - \Psi_S)) \qquad (3.2)$$

A multiplier factor for direct irradiance according to generator position was calculated in Equation 3.3 [69]:

$$\%S = \frac{\cos\theta}{\sin\gamma_S} \qquad (3.3)$$

The sky losses are calculated as [23]:

$$\eta_{sky} = \frac{G_{dir}}{G_{clearsky}} \qquad (3.4)$$

The diffuse irradiation from the circumsolar region (equivalent to direct) in the plane of the generator is calculated according to [69]:

$$G_{diff0} = G_{diff} \cdot \%S \cdot \eta_{sky} \qquad (3.5)$$

A correction factor for losses in Direct Irradiance and Diffuse Circumsolar Irradiance, due to the angle of incidence and dirt implemented in equation (3.5) [69]:

$$C_{F1} = 0.98\left(1 - \frac{e^{\frac{-\theta}{\%D}} - e^{\frac{-1}{\%D}}}{e^{\frac{-1}{\%D}}}\right) \qquad (3.6)$$

A correction into the direct irradiation in the generator plane has been made [70]:

$$G_{dir0} = G_{dir} \cdot \%S \cdot \eta_{sky} \qquad (3.7)$$

The isotropic diffuse irradiation in the plane of the PV generator was calculated (G_{idiff} in W/m^2), [70]:

$$G_{idiff} = \left(1 - \eta_{sky}\right) \cdot \left(1 + \cos\beta_{\mathrm{G}}\right) \cdot G_{diff} \qquad (3.8)$$

A decomposition term C was implemented to calculate the correction factor for losses in Diffuse Isotropic, by the angle of incidence and dirt [70]:

$$C = \frac{4}{3\pi} \cdot \left(\sin\beta_{\mathrm{G}} + \frac{\pi - \beta_{\mathrm{G}} - \sin\beta_{\mathrm{G}}}{1 + \cos\beta_{\mathrm{G}}}\right) - 0.054 \cdot \left(\sin\beta_{\mathrm{G}} + \frac{\pi - \beta_{\mathrm{G}} - \sin\beta_{\mathrm{G}}}{1 + \cos\beta_{\mathrm{G}}}\right)^2 \qquad (3.9)$$

The correction factor for losses in Diffuse Isotropic, by the angle of incidence and dirt, was calculated according to equation 3.10 [69]:

$$CF_{idiff} = 0.98\left(1 - e^{-\frac{C}{D\%}}\right) \qquad (3.10)$$

The albedo irradiance in the plane of the generator (G_{albedo} in W/m^2) [69]:

$$G_{albedo} = 0.2 \cdot G_{global}\left(1 - \frac{\cos\beta_{\mathrm{G}}}{2}\right) \qquad (3.11)$$

The correction factor for the losses in Albedo, due to the angle of incidence and dirt is [69]:

$$CF_{albedo} = 0.98\left(1 - e^{-\frac{C}{D\%}}\right) \qquad (3.12)$$

Adjustment coefficient based on the solar elevation [69]:

$$C_{adj} = \begin{cases} 0.7; \gamma_S < 5 \\ 0.8; 5 \leq \gamma_S < 8 \\ 0.9; 8 \leq \gamma_S < 12 \\ 0.92; 12 \leq \gamma_S < 15 \\ 0.94; 15 \leq \gamma_S < 20 \\ 0.96; 20 \leq \gamma_S < 25 \\ 0.98; 25 \leq \gamma_S < 30 \\ 0.99; 30 \leq \gamma_S < 35 \\ 1; 35 \leq \gamma_S \end{cases} \tag{3.13}$$

Then, the global irradiance in the plane of the generator was obtained after considering losses due to dirt and angle of incidence [70]:

$$G_{D\theta} = \left(G_{dir0} \cdot C_{F1} + G_{diff0} \cdot C_{F1} + G_{idiff} \cdot CF_{idiff} + G_{albedo} \cdot CF_{albedo}\right) \cdot C_{adj} \tag{3.14}$$

The distance between the closest points of consecutive tracker panels was found in (H_{PV} being the PV module height in meters) [69]:

$$LNS_2 = LNS - \left(H_{PV} \cdot \cos \beta_G\right) \tag{3.15}$$

Calculation of the height to save with the inclined panel (horizontal panel height + extra height due to inclination), where H_{fence}=2 m is the height of the fence surrounding the PV generator [69]:

$$\Delta H = H_{fence} + \left(H_{PV}/2 \cdot \sin \beta_G\right) \tag{3.16}$$

The ideal tracking angle, ω_{ID}, is given by (XZ Axis Solar Vector Projection) [69]:

$$\omega_{ID} = \tan^{-1}\left(\frac{\cos \gamma_S \cdot \sin|\Psi_s|}{\sin \gamma_S}\right) \tag{3.17}$$

The consecutive tracker's shadow length projection on the ground (S_{EW1} m) [70]:

$$S_{EW1} = \Delta H \cdot \tan \omega_{ID} \tag{3.18}$$

And the equivalent length favorable for not shading, favorable by elevation to the ground of the consecutive tracker, in meters [70]:

$$S_{EW2} = \Delta H \cdot \tan \omega_{ID} \tag{3.19}$$

Length between trackers to avoid shadowing, (shadow length minus favorable equivalent length per elevation), (S_{EW3} m) [70]:

$$S_{EW3} = S_{EW1} - S_{EW2} \tag{3.20}$$

Valid distance to avoid shadow generation between the N-S axis (S_{EW}) [70]:

$$S_{EW} = \begin{cases} LNS_2 \, ; LNS - \left(H_{PV} \cdot \cos\left(\frac{\pi}{2} - \beta_G\right)\right) < 0 \\ \begin{cases} S_{EW3}; S_{EW3} \geq LNS_2 \\ LNS_2; S_{EW3} < LNS_2 \end{cases} ; LNS - \left(H_{PV} \cdot \cos\left(\frac{\pi}{2} - \beta_G\right)\right) \geq 0 \end{cases} \tag{3.21}$$

The shading factor: FS_{EW} between the 1-axis trackers (N-S) and the shadows (E-W) is calculated [69]:

$$FS_{EW} = 1 - \frac{S_{EW}3}{S_{EW}} \tag{3.22}$$

The length of the shadow generated by the fence (S_{fence} in meters) was approximated according to the following formula [69]:

$$S_{fence} = \frac{H_{fence} - H_{tracker}}{\tan \gamma_S} \tag{3.23}$$

The shadow Factor FS_{fence} generated by the fence was also obtained [69]:

$$FS_{fence} = 1 - \frac{LNS}{S_{fence}} \tag{3.24}$$

Finally, the global irradiance in the generator plane was obtained after considering losses due to dirt, the angle of incidence and the shadows between the trackers and the fence [69]:

$$G_{\beta G} = \left(1 - FS_{EW} - FS_{fence}\right) \cdot G_{D\theta} \tag{3.25}$$

The PVG considered in this work has a 56.95 kW installed power and is made out of 170 photovoltaic panels of 335 W [58], combined in 10 strings of 17 photovoltaic panels in series (5.695 kW). In Figure 3.4. and Figure 3.5 can be seen the global irradiance on the PVG plane, considering a fixed structure (30 º Slope) in Figure 3.4 and a one axis N-S tracking system in Figure 3.5:

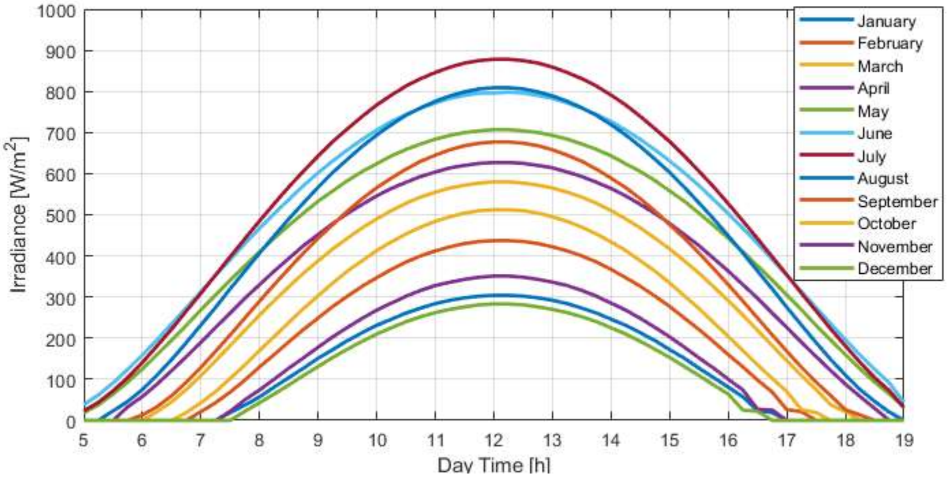

Figure 3.4. Global irradiation on the PVG plane considering a fixed structure, during the representative day of each month at the site location

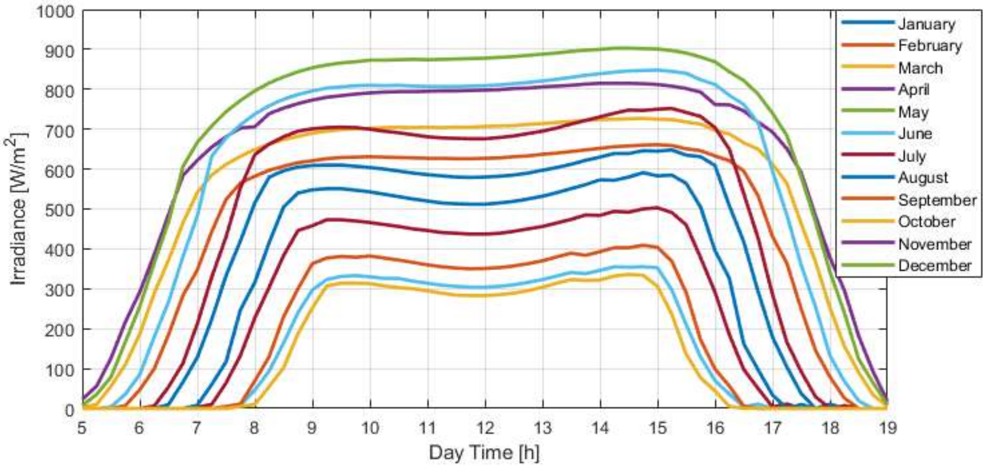

Figure 3.5. Global irradiation on the PVG plane considering a single axis N-S tracker, during the representative day of each month at the site location [54].

The average cell temperature of the PV array is calculated using equation [70]:

$$T_{cell} = T_{env} + (NOCT - 20^0C) \cdot \frac{G_{\beta G}}{800} \tag{3.26}$$

Figure 3.6. and Figure 3.7 depicts the average PV cell temperature variation of a PVG considering a fixed structure (30 ⁰ Slope) in Figure 3.6 and a one axis N-S tracking system in Figure 3.7, during the representative day of each month at site location:

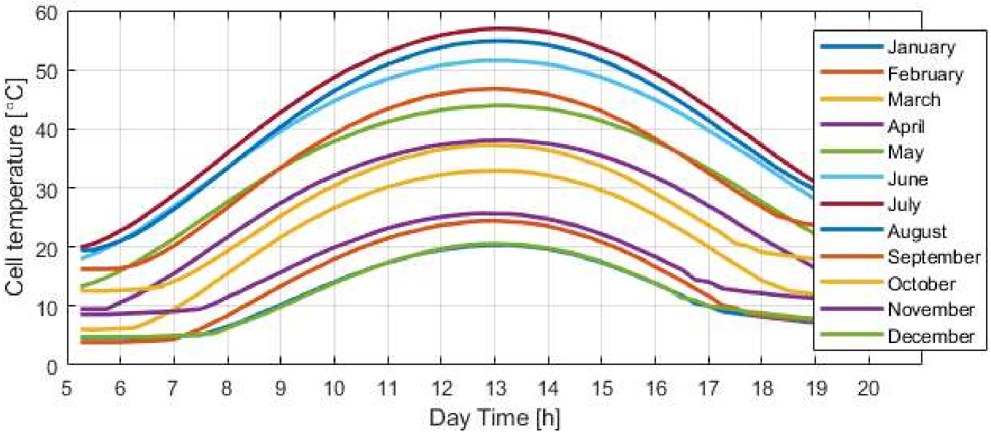

Figure 3.6. Average PV cell temperature of a PVG on a fixed structure, during the representative day of each month at the site location

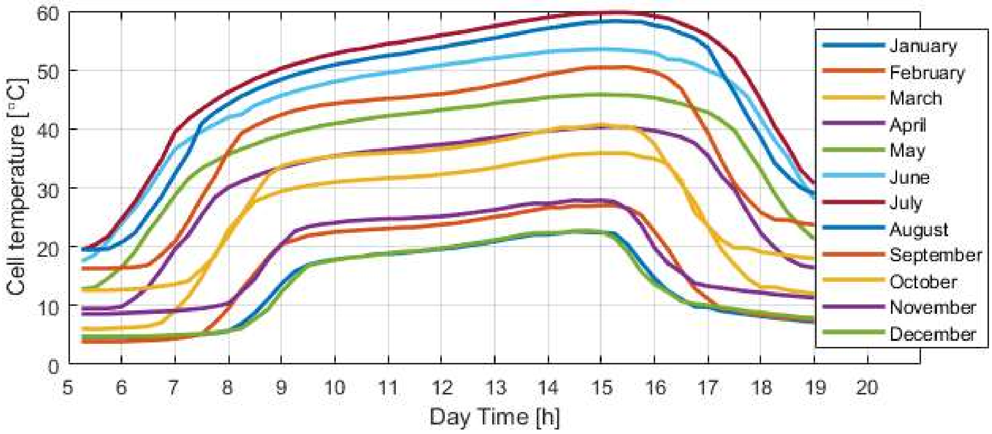

Figure 3.7. Average PV cell temperature of a PVG on a one axis N-S tracker, during the representative day of each month at the site location

The PV generator produced power is calculated using the equation:

$$P_{PVG} = (P_{MAX} \cdot \eta\mathrm{PPV}) \cdot G_{\beta G} \cdot [1 - K_V(T_{cell} - 25^0C)] \cdot K_P \cdot \eta_{\Delta dc} \tag{3.27}$$

where $\eta_{\Delta dc}$ is the efficiency including the losses due to the voltage drop in the DC cables (1-1.38%).

Finally, in Figure 3.8. and Figure 3.9 are depicted the produced powered by a PVG considering a fixed structure (30 º Slope) in Figure 3.8 and a single axis N-S tracking system in Figure 3.9, during the representative day of each month at site location:

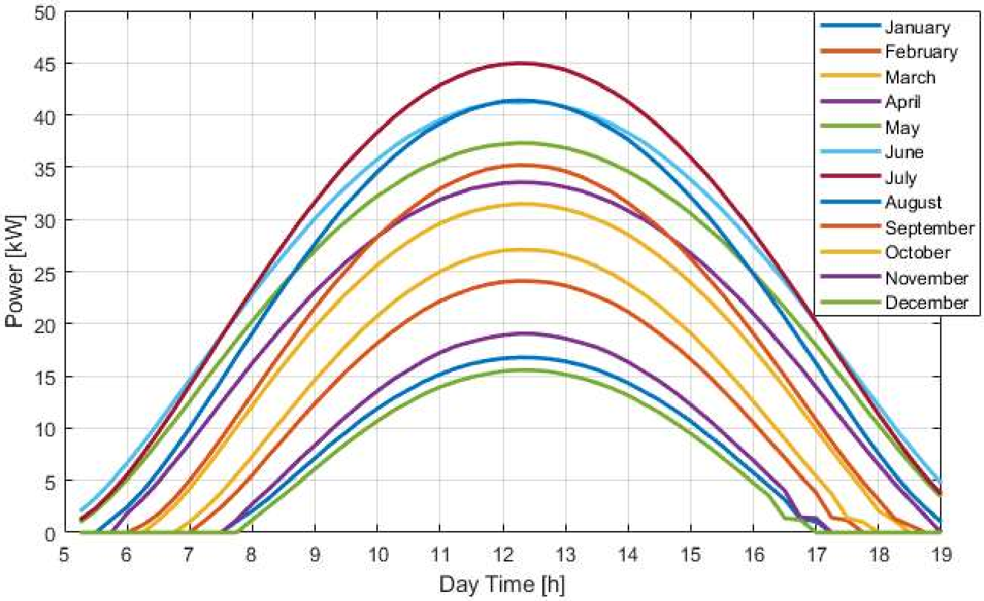

Figure 3.8. Power produced by a PVG on a fixed structure, during the representative day of each month at the site location.

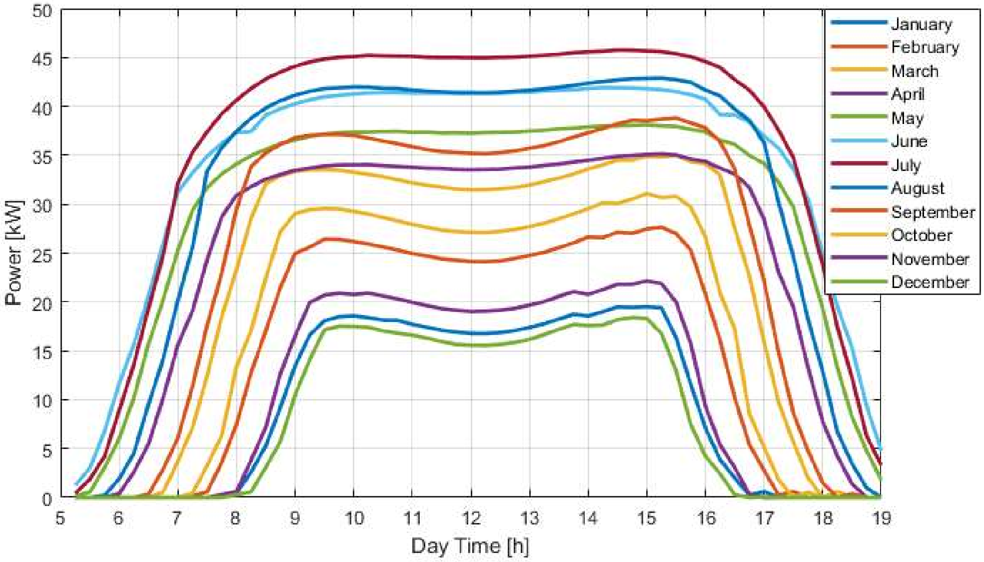

Figure 3.9. Power produced by a PVG on a single-axis N-S tracker, during the representative day of each month at the site location [54]

3.2.2. Dynamic model

In specialized literature [58], [71–76], are presented various mathematical models describing the characteristics of a PV generator, most of them are based on modelling an equivalent circuit of a single [57-58], [71-73] or double diode [58], [74-76]. Due to the reason, that most of the improvements of the double diode model [75, 76] are at lower irradiances [73], [74] and our system starts operating only at relatively high irradiances (the pumping system requires a minimum power for starting its operation, equivalent to relatively high irradiances in single pump systems powered by PV generators) in the current paper, is implemented a single diode model representing the equivalent circuit of a PV array with NP parallel connections of strings (one string contains NS PV modules connected in series).

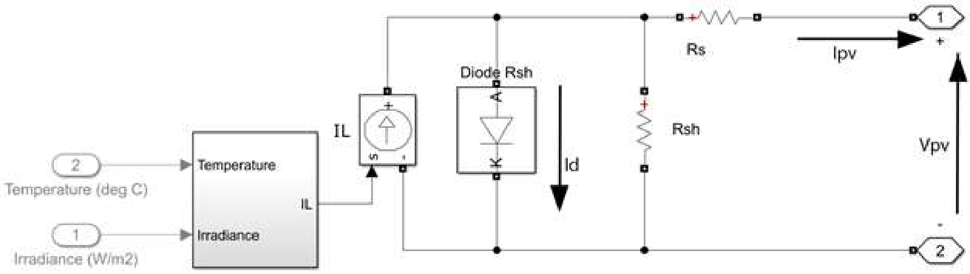

Figure 3.10. Equivalent circuit of a PV module (panel)

In Figure 3.10 it can be seen the equivalent circuit of a PV module. The characteristics of this PV module can be obtained using the following standard equation that describes the relationship between the current and the voltage of the cell [59], [71].

The PV cell has a non-linear characteristic [56], and equation (3.28) is the governing equation [55] of its dynamic model. The I_{PV} current and V_{PV} voltage of a single PV module are calculated according to the following equation:

$$I_{PV} = I_L - I_0\left[e^{\left(\frac{V_{PV}+R_S\cdot I_{PV}}{V_T}\right)} - 1\right] - \frac{V_{PV}+R_s\cdot I_{PV}}{R_{sh}} \tag{3.28}$$

where:
I_{PV} is the photovoltaic current that is generated by one PV module [A];
V_{PV} is the photovoltaic voltage that is generated by one PV module [V];
I_L is the light generated current at nominal condition (25ºC and 1000 W/ m2) by a PV module [A];
I_0 is the equivalent Diode saturation current of a PV module [A];
R_s is the equivalent resistance of the PV cells connected in series in a PV module [Ω];
R_{sh} is the shunt resistance representing the irradiance and temperature dependent I-V characteristics of a PV module (the equivalent resistance of the PV cells series connected in parallel in a PV module) [Ω];

In equation (3.29), V_T is the thermal voltage of PV module [71]:

$$V_T = \frac{k_B\cdot T_{cell}}{q}\cdot nI\cdot N_{cells}\cdot N_{series} \tag{3.29}$$

where:
N_{cells} = number of cells connected in series in a PV module [-]
T_{cell} = is the actual temperature of the p-n junction (cell temperature) [ºK]
k_B =1.3806e-23 is the Boltzmann constant [J/ºK]
q = 1.6022e-19 is the electron charge [C]
n_I is the ideality factor of the equivalent diode of the p-n junction [-].

The light generated current of the photovoltaic cell is obtained according to equation (3.30), where it can be seen its linearly dependency on the solar irradiation and its influence by the temperature:

$$I_L = I_{sc} = [I_{scN} + K_I \cdot \Delta T] \cdot \frac{G_{global}}{G_N} \tag{3.30}$$

with

$$\Delta T = T_{cell} - T_N \tag{3.31}$$

where:
T_N is the standard PV cell temperature [ºK];
T_{cell} is the operating PV cell temperature [ºK];
G_{global} is global irradiation received by the PV module [W/m2];
G_N is1000 standard irradiation [1000 W/m2];
I_{scN} is short circuit current of a single cell of the solar panel under the specified nominal conditions [A];
I_{SC} is the short circuit current of the solar panel [A]
K_I=0.05 is a coefficient that approximates linearly the change in ISC concerning the operating temperature [%/ºK].

The saturation current I_0 is strongly dependent on the temperature variation, is calculated according to the following equation (3.32) [55]:

$$I_0 = \frac{I_{sc} + K_I \cdot \Delta_T}{e^{\left(\frac{V_{OC}}{V_t}\right)} - 1} \tag{3.32}$$

with

$$V_{OC} = N_{series} \cdot (V_{OCN} + K_V \cdot \Delta T) \tag{3.33}$$

where:
V_{OC} is the open circuit voltage of the PV module [V];
V_{ocN} is the open circuit voltage of a single cell of the PV module under the standard conditions [V];
K_V=-0.32 is a coefficient that approximates linearly the change in VOC concerning the operating temperature [%/ºK];

The two internal resistors Rs and Rp are estimated according to reference [72]:

$$R_S = 0.09 \cdot \frac{V_{OC}}{I_{SC}} \tag{3.34}$$

$$Rsh = 11 \cdot \frac{V_{OC}}{I_{SC}} \cdot \frac{G_{global}}{G_N} \tag{3.35}$$

The technical specifications for the polycrystalline 144 cells PV module modeled in the current section and installed in monitored installation, are given in Table 3.1. In Figure 3.12, it can be seen the corresponding P–V (Power-Voltage) and I–V (Current-Voltage) curves of the PV module for different irradiations.

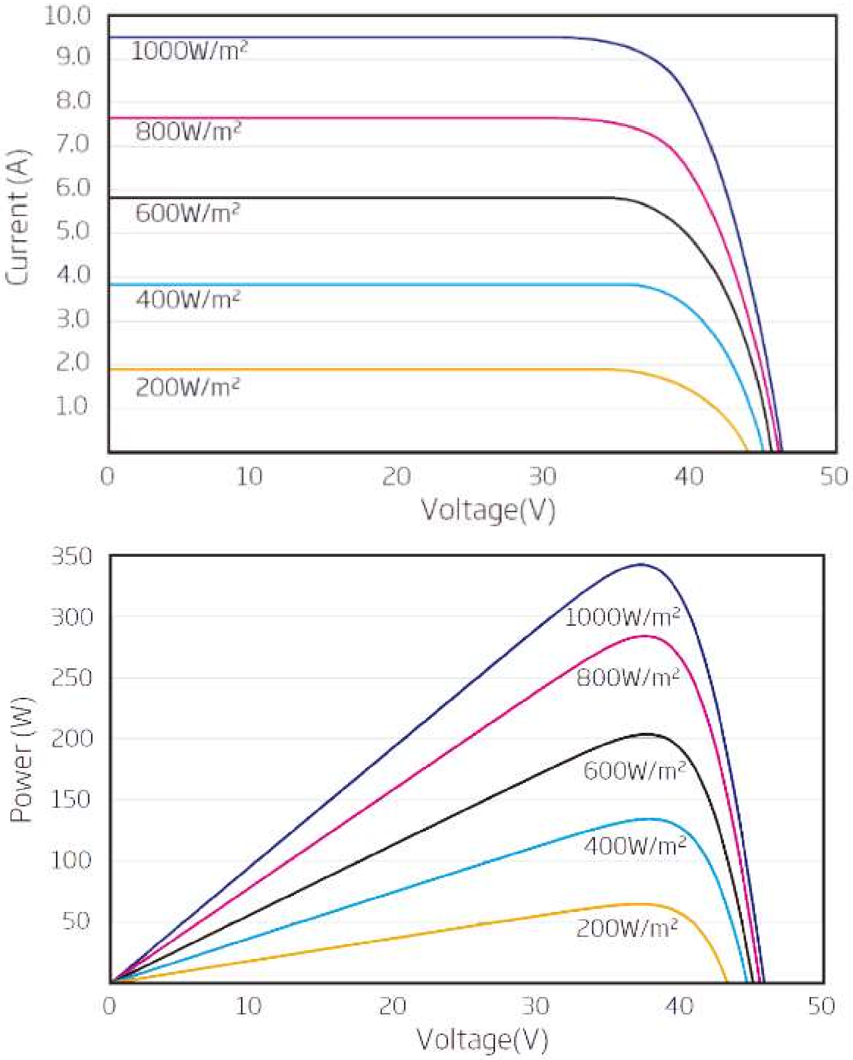

Figure 3.11. PV module I-V and P-V Curves [58]

The equivalent circuit model of the PV array is implemented in Simulink using the PV array module, available in the Simulink standard components in the SimPowerSystems toolbox [59].

$$I_{PV\_Array} = N_P \cdot I_L - N_P \cdot I_0 \left[e^{\left(\frac{V_{PV\_Array}+\left(\frac{N_S}{N_P}\right)\cdot R_S \cdot I_{pv}}{N_S \cdot V_T}\right)} - 1 \right] - \frac{V_{PV\_array} + \left(\frac{N_S}{N_P}\right) \cdot R_s \cdot I_{PV\_Array}}{\left(\frac{N_S}{N_P}\right) \cdot R_{sh}} \qquad (3.36)$$

3.3. PECS controller

The controller presented in the current subchapter is a MPPT (Maximum Power Point Tracking) control method based on the P&O (Perturb and Observed) algorithms developed and presented in [41, 55, 71, 77, 78, 79], with several modifications necessary for future integration in a high-power pumping system.

Maximum Power Point Tracking Control Methods

According to the P-V characteristics of the PV module presented in Figure 3.12, in order to maximize the power output of the PV generator, each string of PV modules should be operating around the MPP (Maximum Power Point). The MPP depends on the average solar irradiation and cell temperature. The PV string MPP can be reached by controlling the load curve of the PV string, in order to intersect the I-V curve at its maximum point [36]. The voltage giving the MPP is called v_{mp} representing also the reference of the controller. Many MPPT control methods can be found in the literature [55], but as this work doesn't focus on the PV MPPT control method itself, and just on its integration into a high power system, in the current work, the P&O (Perturb and Observed) algorithm it is considered, as it is the most used one in practice, and it will be adapted for its integration into a high-power pumping system.

Perturb and Observe (P&O) Algorithm

The P&O algorithm is a simple, effective and easy to implement MPPT control method based on hill-climbing algorithms that continuously searches the reference voltage through small perturbations of the reference voltage and by observing the response of the actual system in order to determine the direction of the next perturbation till reaching the MPP [36]. The reference voltage perturbations are executed in the direction where the power should increase. As can be seen in Figure 3.12, increasing the voltage reference (v^*) of the PV string when it operates on the left side of the MPP will increase the output power, while if the PV string operates on the right side of the MPP will decrease the output power and the voltage reference (v^*) has to be decreased during the next perturbation. Repeating constantly this procedure will reach the MPP point when the perturbations in the reference voltage (Δv) will make the power point oscillate around the MPP (the magnitude of the oscillations around the MPP depends on the magnitude of the perturbations $|\Delta v|$). [41]. When the changes occur in the irradiation or temperature, the P-V characteristic curve of the PV string will change, and the perturbations on the reference voltage will make the P&O algorithm to reach the new MPP.

The only drawbacks of this MPPT control method are its sensitiveness to measurement noise and its poor capabilities in reacting to a sudden change in solar irradiation when results in a power change significantly larger than the perturbations that can be created by the algorithm [36]. Due to this reason, it is important for a highly efficient algorithm, to select the proper perturbation increment (Δv). If the perturbation increment is too small it will take too long for reaching the MPP, while if the perturbation increment is too large, it will create large oscillations around MPP. Large oscillations around the MPP can lead to power ripples (check Figure 3.12) when the algorithm PPT falls on the right side of the MPP [41, 71].

In Figure 3.12 it can be seen the flowchart of the P&O algorithm.

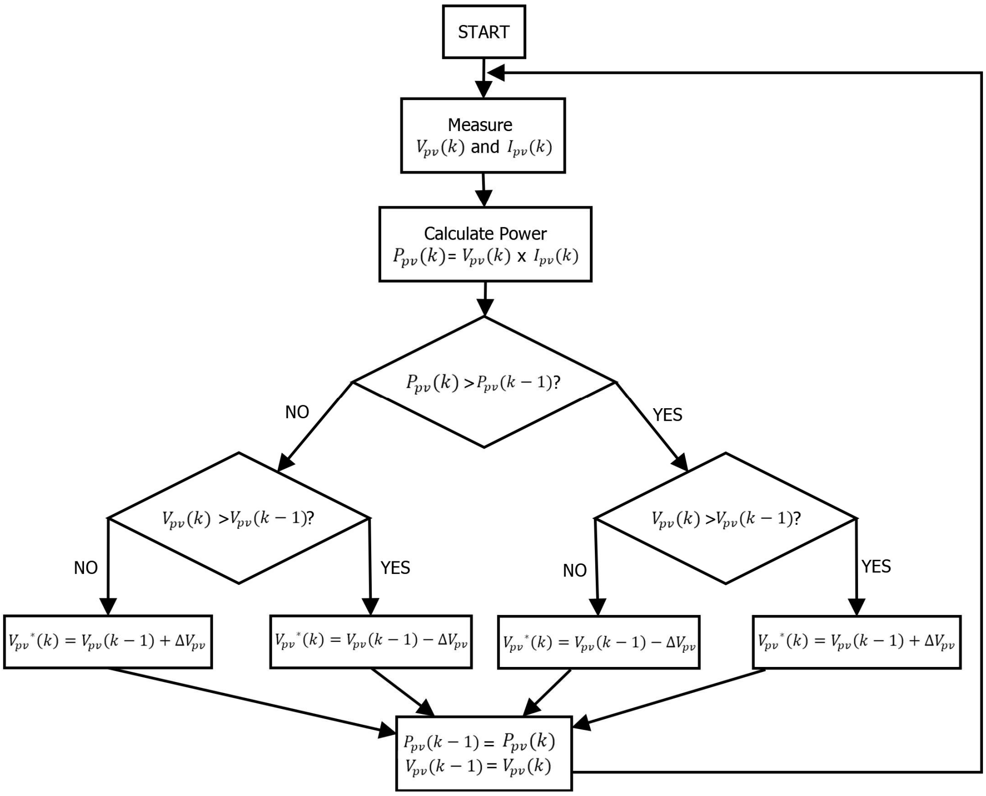

Figure 3.12. P&O algorithm flow chart

3.4. PECS simulations

The simulations in this chapter, consider a 56.95 kW PECS made out of 170 photovoltaic panels of 335 W [48], combined in 10 strings of 17 photovoltaic panels in series (5.695 kW), distributed on 3 decentralized self-operated horizontal single-axis trackers (HSAT) [49] (57 on each tracker). The trackers have N-S (north-south) orientation and a 110º range of motion around their axis.

Combining the PECS controller presented in the third subchapter (***3.3. PECS Controller***), with the dynamic model of the PECS presented in the second subchapter (***3.2.2. Dunamic model***, a simulator was developed in Simulink [43]. In Figure 3.13 it can be seen the PECS simulator developed Simulink.

Using the developed PECS simulator, four simulations were executed in order to analyze and evaluate the PECS response during a clear sky day, a day with a big cloud, a day with many small clouds and a fully cloudy day.

In Figure 3.14 and Figure 3.15 it can be seen the inputs to the simulator: the global irradiance and PV cell temperature variation during the clear sky day, the day with a big cloud, the day with many small clouds and the fully cloudy day.

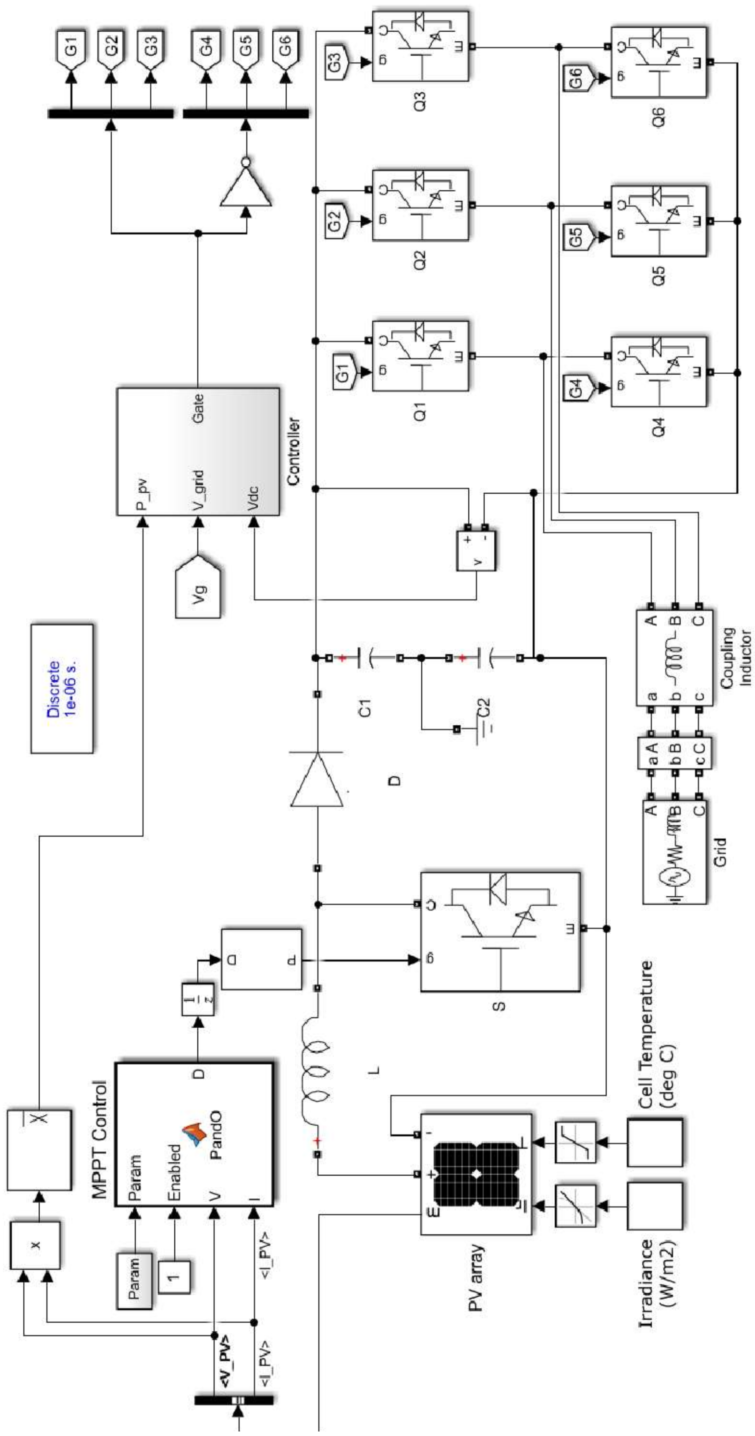

Figure 3.13. PECS simulator flow chart in Simulink

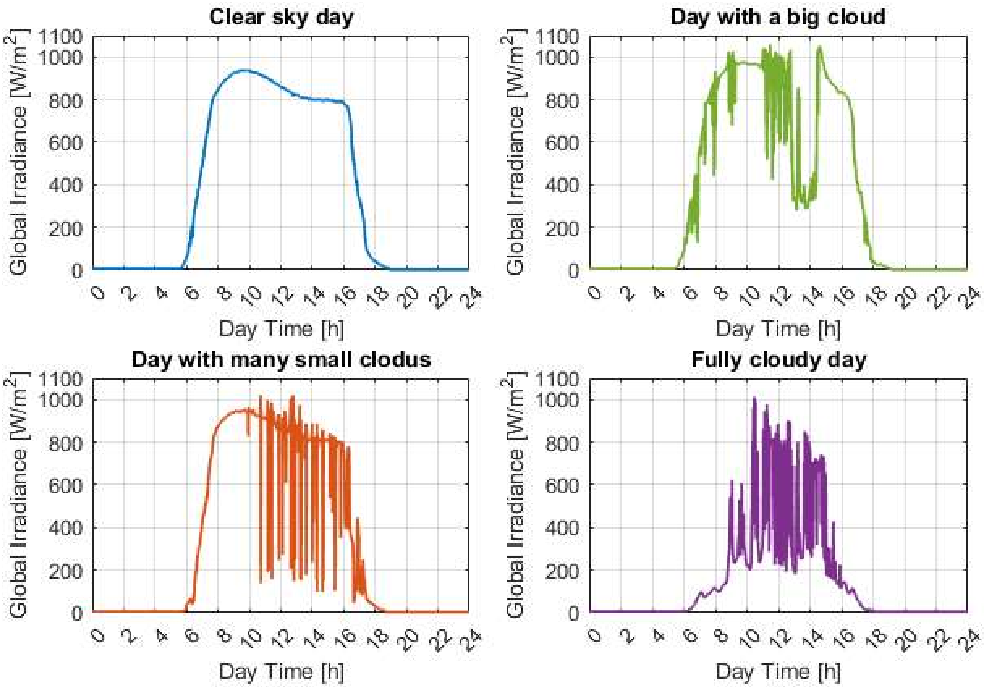

Figure 3.14. PECS average Global Irradiance

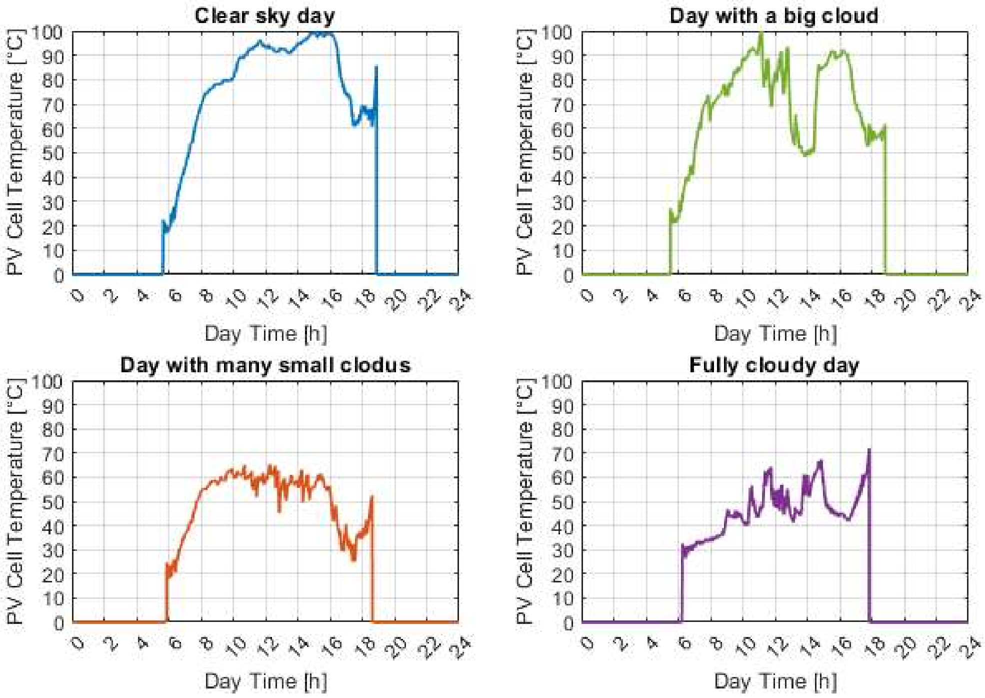

Figure 3.15. PECS average PV cell temperature

Finally, in Figure 3.16 it can be seen the PECS power production during the clear sky day, the day with a big cloud, the day with many small clouds and the fully cloudy day.

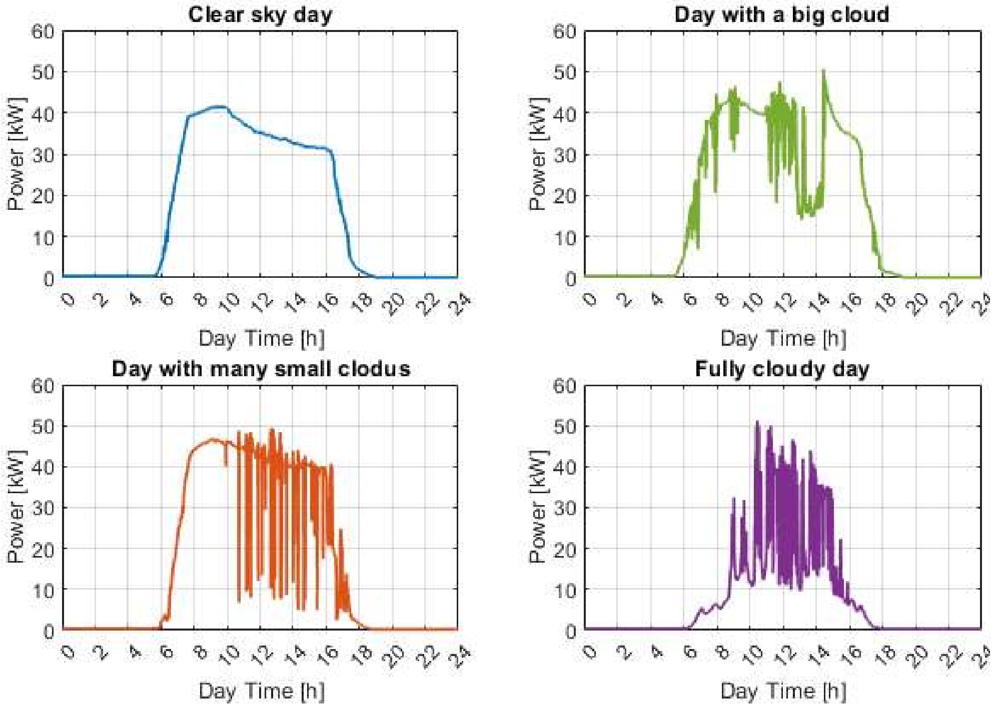

Figure 3.16. PECS power production

3.5. PECS chapter conclusion

According to chapter ***3. PECS***, it can be concluded, that the advanced steady-state and dynamic models of the PECS presented in subchapter ***3.2 PECS modelling*** can be used for both dimensioning and simulating nominal and transitory regimes.

In subchapter ***3.3 PECS controller***, it is presented a MPPT control method based on the P&O algorithm. The personal contribution to this PECS controller consists in preparing the PECS controller for integration into a pumping system controller.

Finally, in the fourth subchapter (***3.4. PECS simulations***), the PECS model and the proposed controller are validated through four simulations representing four different types of days: a clear sky day, a day with a big cloud, a day with many small clouds and a fully cloudy day.

4. WIND ENERGY CONVERSION SYSTEM (WECS)

The current chapter presents the modelling and simulation of a WECS (wind energy conversion system). The first paragraph (***4.1. WECS description***) presents a short description of a general WECS, consisting of a three blades upwind horizontal axis wind turbine with variable speed connected by a shaft to a generator. The second paragraph (***4.2. WECS modelling***) consists of a nonlinear mathematical model of the described WECS, and a linearization of the nonlinear model, which is used for the controller design development in the third paragraph (***4.3. WECS controlling***). In the fourth paragraph (***4.4. WECS simulations***) are presented the results and analysis of the WECS simulations. Finally, the chapter ends with the fifth paragraph (***4.5. WECS conclusions***), where the chapter conclusions are presented.

4.1. WECS description

A wind energy conversion system (WECS) converts part of the kinetic power from the wind into mechanical shaft power by rotating a rotor. The mechanical shaft power is converted further into electrical power by a generator.

Nowadays, most of the industrial wind turbines manufactured and operated are upwind three blades horizontal axis wind turbines [80]. A three blades horizontal axis wind turbine consists of a rotor-nacelle assembly on a tower, that is directed into the wind by a yaw system. The wind kinetics rotates aerodynamically the rotor with 3 blades. The angular speed of the rotor is variated by pitching the blades with the help of a pitch actuator. The rotor is connected to the nacelle low speed shaft by a hub. Inside the nacelle, the low-speed shaft is connected to a high-speed shaft through a gearbox. The high-speed shaft drives a generator that converts the mechanical power into electrical power. For preventing the WECS operation during extreme weather conditions [81], or maintenance a braking system prevents the rotor from rotating [80]. The main components of the WECS will be deeply described in upcoming paragraphs.

4.1.1. Rotor

The rotor consists of blades connected to a hub through blade supports. The blades have an airfoil cross-section [82] and extract power from wind power by a lift force caused by a pressure difference between the high and low pressure sides of the blade [80]. The blade supports contains bearings that allows the blades to be rotated around their axis by pitch actuators. Pitch actuators consists of hydraulic servo systems, controlled by a pitch controller. The angle difference in the blade before and after being pitched around its axis, it is called pitching angle.

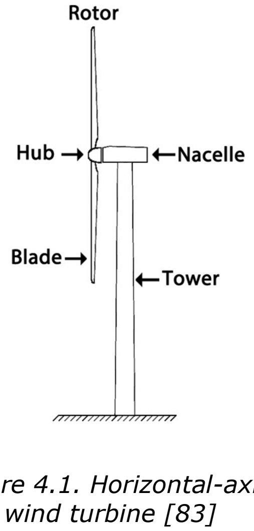

Figure 4.1. Horizontal-axis wind turbine [83]

4.1.2. *Nacelle*

The nacelle houses the key components of the WECS. The rotor torque and angular velocity are transferred through a main (low speed) shaft to the gearbox inside the nacelle frame. The gearbox transfers the torque and the angular velocity from the low-speed shaft to a high-speed shaft applying a ratio. Because the high-speed shaft heats more than the low-speed shaft, due to its operation at higher speeds, it is cooled down and lubricated by a hydraulic cooling device. The mechanical power given by the torque and angular velocity of the high-speed shaft is converted by a generator into electrical power. The AC electrical power given by the electric generator is converted into DC electrical power by a converter. The DC power given by the converter is converted and controlled by the power converter in the electric panel. The electric panel contains also the electrical control with the required protection. The main shaft brake is normally placed between the rotor and the gearbox in case of a gearbox failure and consists of a hydraulic system braking a disc connected to the low-speed shaft. The yawing system, positioned between the nacelle and tower, turns the rotor into the wind when the wind changes its direction [80], [82]-[84].

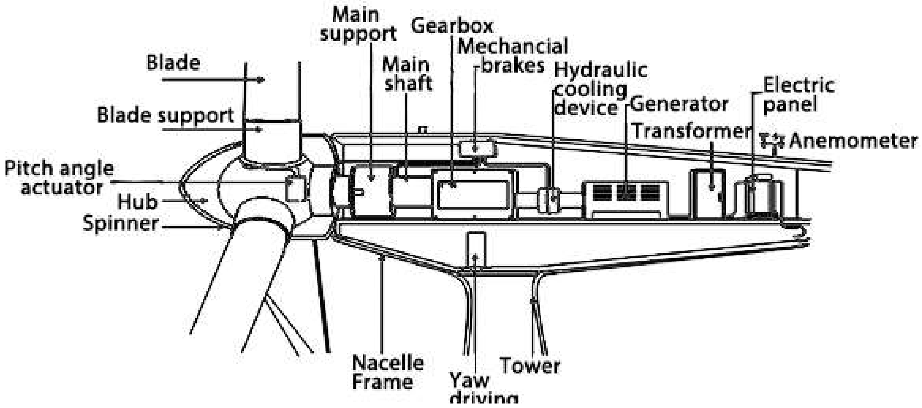

Figure 4.2. Rotor nacelle assembly components [85]

4.1.3. *Tower*

The tower supports the rotor nacelle assembly and rises the wind turbine at heights far above the terrain orography, in order to harvest faster, stronger and less turbulent winds. The tower consists of several tubular or lattice sections of steel or concrete [80], [84].

4.1.4. WECS technical data

The WECS considered and modeled in the current study is an upwind horizontal axis wind turbine with variable speed. It has three blades, a high-speed drive train, a multiple-stage gearbox with a variable speed and a collective pitch controller. The necessary parameters of the WECS, for modelling, defining the controller parameters and running the simulations are presented in Table 4.1. (the parameters of 5 MW NREL (National Renewable Energy Laboratory) WECS are used as an example) [86]:

Table 4.1. Necessary WECS parameters, for modelling, defining the controller and running the simulations [85]

Air density at hub height	Kg/m^3
Wind speed time series	[m/s, s]
Rated Power	5 MW
Rotor diameter[1]	126 m
Hub diameter	3 m
Hub height	90 m
Rotor mass	110000 kg
Nacelle mass	240000 kg
Tower mass	347460 kg
Cut-in wind speed	3 m/s
Cut-in rotor speed	6.9 rpm
Rated wind speed	11.4 m/s
Rated rotor speed	12.1 rpm
Rated generator speed	1173.7 rpm
Cut-out wind speed	25 m/s
Gearbox ratio	97:1
Electrical generator efficiency	94.4 %
Generator stator frequency	50 Hz
Generator rated stator voltage	690 V
Generator rated stator current	4404 A
Generator pole pairs	3
Generator stator/rotor turns	1/3
Generator rated rotor voltage	2070 V
Generator maximum slip	33.33%
Generator stator resistance	0.0016 Ω
Generator leakage inductance (stator and rotor)	0.000119 H
Generator magnetizing inductance	0.0022 H
Generator rotor resistance referred to stator	0.0014 Ω
Back to back converter DC bus voltage	1150 V
Generator damping	0.001 kg/s
Grid DC bus capacitance	0.08
Grid side filter’s resistance	0.00002 Ω
Grid side filter’s inductance	0.0004 H
Tower structural-damping ratio	0.08 %
Tower first eigen frequency	0.321 Hz

---

[1] *The rotor diameter ignores the effect of blade precone, which reduces the actual diameter and swept area.*

4.2. WECS modelling

In the current subchapter, a nonlinear mathematical model of a WECS together with its linearization is presented. A comparison between the WECS nonlinear and its linearization is done at the end of the subchapter.

Nonlinear model

The presented nonlinear mathematical model of a WECS takes into consideration just the following aspects [85]:

- The wind is evenly distributed through the entire rotor;
- The rotor is homogenous without any imperfections in the rotor symmetry;
- At all three blades, at the same time, the same deflections with the same accelerations and velocities occur;
- The blades are pitched at the same time with the same pitching angle;
- The power coefficient and thrust coefficient are obtained from a look up table given by the manufacturer;
- The blades are directly connected to the pitch actuator ignoring other components such as the bearings;
- The drive train is modeled as a third order equation, based on the rotor (low-speed shaft) and generator (high-speed shaft) angular velocities, and the shaft torsion;
- The considered generator is a doubly fed induction generator (DFIG);
- The tower is modeled as a mass-spring-damper system which approximates the tower deflection, velocity and acceleration;
- All three blades bending moments are equal and they are approximated based on the thrust force (evenly distributed to all three blades) acting on the rotor;
- The rotor diameter ignores the effect of the blade precone, which reduces the actual diameter and swept area [86].

All other aspects and parameters of the WECS which are not mentioned above are neglected (for example the ambient temperature, components temperature and secondary components friction).

Linearized model

The nonlinear model is linearized in order to use its linearization form for designing the controller (determining the gains of the gain scheduled PI blade-pitch controller). All the nonlinear parts of the nonlinear model are linearized using Taylor expansion approximation at rated operation.

4.2.1. *Wind Turbine*

4.2.1.1. Nonlinear model

The wind in front of the wind turbine, besides acting on the rotor, acts also on the tower and exerts a thrust force, that deflects the tower structure. Due to this reason, the actual wind speed acting on the rotor is equal to the wind speed in front of the wind turbine less the nacelle velocity resulting from the tower deflection Equation 4.79 [84, 85]:

$$v_{rot} = v - \dot{z} \tag{4.1}$$

where:
v [m/s] is the wind speed;
v_{rot} [m/s] is the average wind speed over the rotor;
$\dot{z}$ [m/s] is the tower velocity.

The tip speed ratio is calculated according to the following formula [84, 85]:

$$\lambda = \frac{R \cdot \Omega}{v_{rot}} \tag{4.2}$$

where:
λ [rad] is the tip speed ratio;
R [m] is the rotor radius;
Ω [rad/s] is the rotor angular velocity.

When the wind acts on the rotor, part of the kinetic energy of the wind is transferred to the rotor. The power extracted by the rotor from the wind is obtained with the following equation [84, 85]:

$$P_{rot} = \frac{1}{2} \cdot {v_{rot}}^3 \cdot \rho \cdot \pi \cdot R^2 \cdot CP(\lambda, \beta) \tag{4.3}$$

where:
P_{rot} [w] is the rotor power;
v_{rot} [m/s] is the average wind speed over the rotor;
R [m] is the rotor radius;
λ [rad] is the tip speed ratio;
CP [-] is the power coefficient;
β [°] is the pitch angle.
and ρ [kg/m3] is the air density;

The power coefficient (*CP*) is obtained from a look-up table derived from the geometry of the blades, based on the tip speed ratio and the blade's pitch angle. The maximum limit of the power coefficient is known as Betz limit and has a value of 0.59. Betz limit represents the maximum energy, approximately 59%, that can be extracted by a turbine from the total wind energy in ideal conditions [84, 85].

Figure 4.3 depicts the *CP* of the 5 MW NREL wind turbine, obtained from [85] and limited to operating range (pitch angle β from 0° to 90°, tips speed ratio from 0 to 25 and the power coefficient from 0 to Betz limit 0.59).

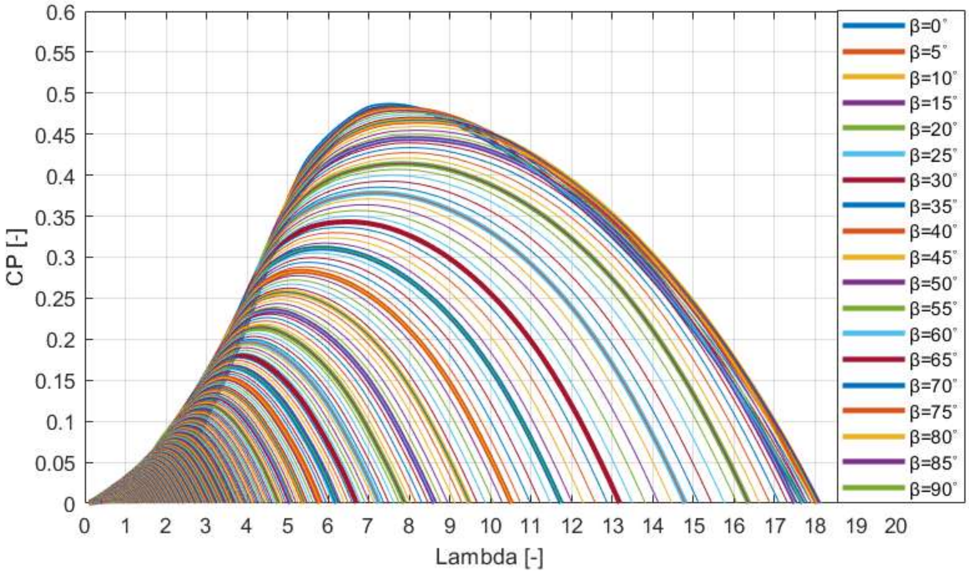

Figure 4.3. 5MW NREL wind turbine power coefficient

The rotor torque is calculated from the division of the rotor power (Equation 4.3) with the rotor angular speed velocity [84, 85]:

$$M_{rot} = \frac{P_{rot}}{\Omega} \tag{4.4}$$

Finally, substituting the rotor power in (Equation 4.4), results:

$$M_{rot} = \frac{1}{2} \cdot v_{rot}{}^{3} \cdot \rho \cdot \pi \cdot R^{2} \cdot CP \cdot \Omega^{-1} \tag{4.5}$$

where:
M_{rot} [Nm] is the rotor torque;
V_{rot} [m/s] is the average wind speed over the rotor;
Ω [rad/s] is the rotor angular velocity;
CP [-] is the power coefficient;
β [°] is the pitch angle;
and $C_P(\lambda,\beta)$ is the power coefficient look-up table.
The rotor thrust force is obtained according to the following formula [84, 85]:

$$F_{rot} = \frac{1}{2} \cdot v_{rot}{}^{2} \cdot \rho \cdot \pi \cdot R^{2} \cdot CT(\lambda, \beta) \tag{4.6}$$

where:
F_{rot} [N] is the rotor thrust force;
V_{rot} [m/s] is the average wind speed over the rotor;
CT [-] is the thrust coefficient;
β [°] is the pitch angle;
and *CT(λ,β)* is the thrust coefficient look-up table.

In Figure 4.4, is presented the thrust coefficient (*CT*) look up table of the 5 MW NREL wind turbine limited to the operating range (pitch angle β from 0° to 90°, tips speed ratio from 0 to 25 and only the positive thrust coefficients). Similar to the power coefficient, the thrust coefficient is a look-up table, obtained from [85], derived from the geometry of the blades based on the tips speed ratio and blades' pitch angle.

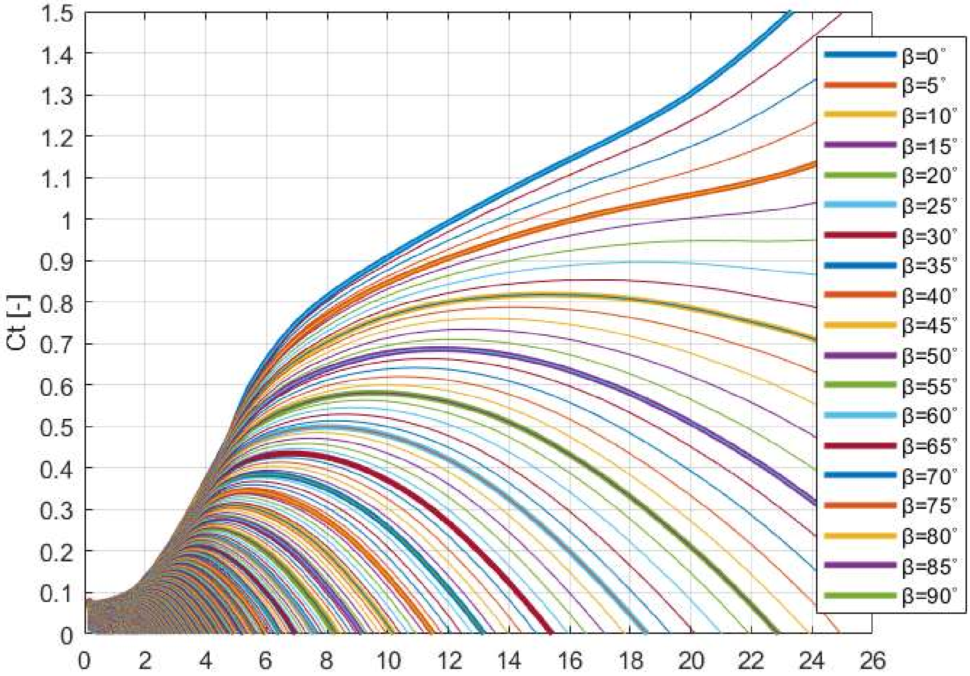

Figure 4.4. 5MW NREL wind turbine thrust coefficient

In the diagram from Figure 4.5, it can be seen the flow chart of the aerodynamics model developed in Simulink [43]:

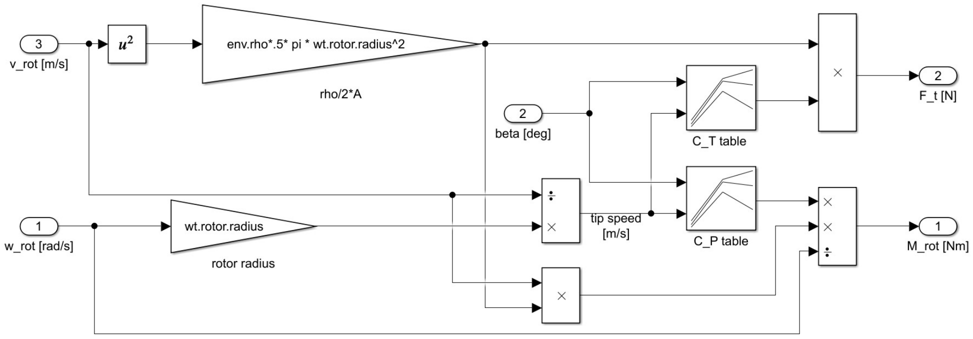

Figure 4.5. Wind turbine's nonlinear aerodynamics Simulink diagram

4.2.1.2. Linear model

Tip speed ratio linearization

The first equation that is linearized is the tip speed ratio Equation 4.2 by calculating the tip speed ratio at rated wind speed in front of the rotor of 11.4 [m/s], using the nonlinear Equation 4.2 [85]:

$$\lambda_0 = \lambda(\Omega_0, v_{rot0}) = \frac{R \cdot \Omega_0}{v_{rot0}} = 7 \tag{4.7}$$

where:
R=63 [m] is the rotor radius;
Ω_0=1.2671 [rad/s] is the rated rotor angular velocity;
v_{rot0}=11.4 [m/s] is the rated wind speed at rotor;
λ_0=7 [-] is the tip speed ratio at the linearization point.

The linearization will be done using first-order Taylor expansion approximation [85]:

$$\lambda_l(\Omega, v_{rot}) = \lambda(\Omega_0, v_{rot0}) + \left.\frac{\partial\lambda}{\partial\Omega}\right|_{(\Omega_0, v_{rot0})} \cdot (\Omega - \Omega_0) + \left.\frac{\partial\lambda}{\partial v_{rot}}\right|_{(\Omega_0, v_{rot0})} \cdot (v_{rot} - v_{rot0}) \tag{4.8}$$

where:
$\lambda_l(\Omega, v_{rot})$= λ_l [-] is the linearized tip speed ration;
$\lambda_0(\Omega_0, v_{rot0})$= λ_0=7 [-] is the tip speed ratio at the linearization point.;
Ω_0=1.2671 [rad/s] is the rotor angular velocity at the linearization point;
v_{rot0}=11.4 [m/s] is the rated wind speed at the linearization point;
Ω [rad/s] is the rotor angular velocity;
V_{rot} [m/s] is the wind speed at the rotor.

By replacing the changes in tip speed ratio, in wind speed at the rotor and in rotor angular velocity with Δ, Equation 4.8, becomes [85]:

$$\Delta\lambda = \left.\frac{\partial\lambda}{\partial\Omega}\right|_{(\Omega_0, v_{rot0})} \cdot \Delta\Omega + \left.\frac{\partial\lambda}{\partial v_{rot}}\right|_{(\Omega_0, v_{rot0})} \cdot \Delta v_{rot} \tag{4.9}$$

where:
$\Delta\lambda$ [-] is the change in tip speed ratio;
$\Delta\Omega$ [-] is the change in rotor angular velocity;
Δv_{rot} [-] is the change in wind speed;
Ω [rad/s] is the rotor angular velocity;
v [m/s] is the wind speed at the rotor.
Ω_0=1.2671 [rad/s] is the rated rotor angular velocity at the linearization point;
v_{rot0}=11.4 [m/s] is the wind speed at the linearization point.

Finally, the slopes in the angular velocity and wind speed at the rotor which contributes to the change in tip speed ratio are calculated:

$$\left.\frac{\partial\lambda}{\partial\Omega}\right|_{(\Omega_0, v_{rot0})} = \frac{R}{v_{rot0}} = 5.526 \tag{4.10}$$

$$\left.\frac{\partial \lambda}{\partial v_{rot}}\right|_{(\Omega_0, v_{rot0})} = -\frac{R \cdot \Omega_0}{(v_{rot0})^2} = -0.614 \qquad (4.11)$$

where:
R=63 [m] is the rotor radius;
Ω_0=1.2267 [rad/s] is the rotor angular velocity at the linearization point;
v_{rot0}=11.4 [m/s] is the wind speed at the linearization point.

Power coefficient linearization

The first step in linearizing the power coefficient look up table is to identify, using Matlab [43], a regression function with the following form[87]:

$$CP(\beta,\lambda) = k_{1cp}\left(k_{2cp} \cdot (\lambda + k_{8cp}) - k_{3cp} \cdot \beta - k_{4cp} \cdot \beta^{k_{5cp}} - k_{6cp}\right) \cdot e^{k_{7cp} \cdot (\lambda + k_{8cp})} \qquad (4.12)$$

With the help of Matlab [43], the following coefficients fit the best the regression Function 4.12 and the power coefficients values in the look up table:

k_{cp1}= 0.067
k_{cp2}= 4.664
k_{cp3}=-0.524
k_{cp4}= 3.360
k_{cp5}= 0.460
k_{cp6}= 3.222
k_{cp7}=-0.216
k_{cp8}=-1.998

In Figure 4.6, it can be seen the accuracy of the power coefficient regression curve when the pitch angle (β_0) is 0, during a wind speed variation from 0 to 25 m/s.

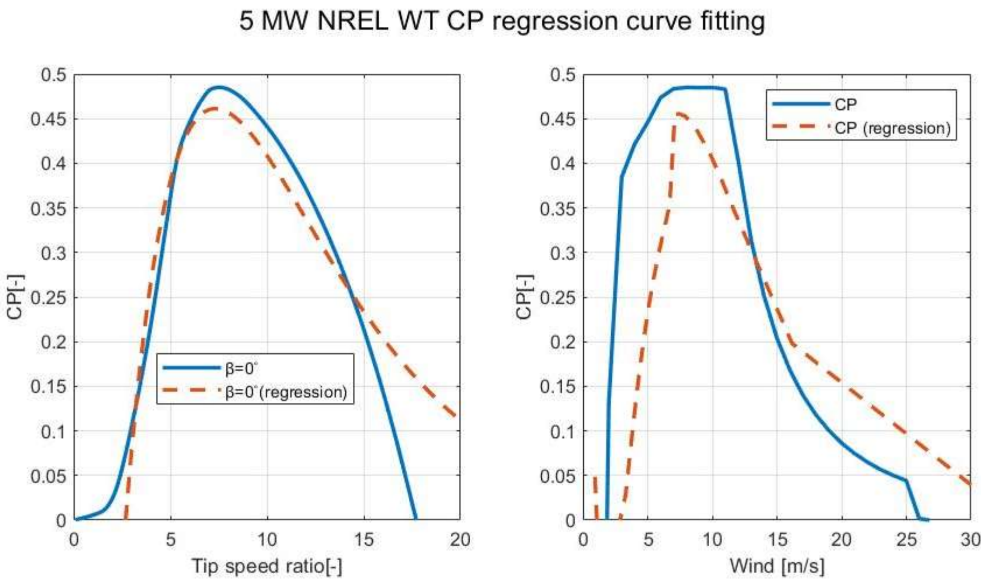

Figure 4.6. Graphical representation of the CP table

By using Equation 4.12, the rated tip speed ratio λ_0, the rated pitch angle β_0, at a wind speed in front of the rotor v_{rot0} of 11.4 [m/s], the rated power coefficient CP_0 at the linearization point is obtained:
λ_0=7 [-] is the tip speed ratio at the linearization point;
β_0= 0 [˚] is the pitch angle at the linearization point;
CP_0= 0.4772 [-] is the power coefficient at the linearization point.

The power coefficient linearization will be done using first-order Taylor expansion approximation on the polynomial regression of power coefficient look up table [85]:

$$CPl(\beta,\lambda) = CP(\beta_0,\lambda_0) + \left.\frac{\partial CP}{\partial \beta}\right|_{(\beta_0,\lambda_0)} \cdot (\beta-\beta_0) + \left.\frac{\partial CP}{\partial \lambda}\right|_{(\beta_0,\lambda_0)} \cdot (\lambda-\lambda_0) \qquad (4.13)$$

where:
$CP_l(\beta, \lambda)$=CP_l [-] is the linearized power coefficient;
$CP_0(\beta_0, \lambda_0)$=CP_0= 0.4772 [-] is the power coefficient at the linearization point.
λ_0=7 [-] is the tip speed ratio at the linearization point;
β_0=0 [°] is the pitch angle at the linearization point;
λ [-] is the tip speed ratio;
β [°] is the pitch angle;

By replacing the changes in power coefficient, pitch angle and tip speed ratio with Δ, Equation 4.13, becomes [85]:

$$\Delta CP = \left.\frac{\partial CP}{\partial \beta}\right|_{(\beta_0,\lambda_0)} \cdot \Delta\beta + \left.\frac{\partial CP}{\partial \lambda}\right|_{(\beta_0,\lambda_0)} \cdot \Delta\lambda \qquad (4.14)$$

where:
ΔCP [-]is the change in power coefficient;
$\Delta\lambda$ [-] is the change in tip speed ratio;
$\Delta\beta$ [-] is the change in pitch angle;
λ_0=7 [-] is the tip speed ratio at the linearization point;
β_0=0 [°] is the pitch angle at the linearization point;
λ [-] is the tip speed ratio and β [°] is the pitch angle.
By deriving Equation 4.12, Equation 4.14 becomes:

$$\begin{aligned}\Delta CP = {} & \left(-k_{1cp}\cdot k_{3cp} - k_{1cp}\cdot k_{4cp}\cdot k_{5cp}\cdot \beta_0^{(k_{5cp}-1)}\right)\cdot e^{k_{7cp}\cdot(\lambda_0+k_{8cp})}\cdot\Delta\beta \\ & + k_{1cp}\cdot k_{2cp}\cdot k_{7cp}\cdot e^{k_{7cp}\cdot(\lambda_0+k_{8cp})}\cdot\Delta\lambda\end{aligned} \qquad (4.15)$$

Finally, the slopes of the pitch angle and tip speed which contributes to the change in power coefficient are calculated:

$$\begin{aligned}\left.\frac{\partial CP}{\partial \beta}\right|_{(\beta_0,\lambda_0)} = {} & \left(-k_{1cp}\cdot k_{3cp} - k_{1cp}\cdot k_{4cp}\cdot k_{5cp}\cdot \beta_0^{(k_{5cp}-1)}\right) \\ & \cdot e^{k_{7cp}\cdot(\lambda_0+k_{8cp})} = -0.0395\end{aligned} \qquad (4.16)$$

$$\left.\frac{\partial CP}{\partial \lambda}\right|_{(\beta_0,\lambda_0)} = k_{1cp}\cdot k_{2cp}\cdot k_{7cp}\cdot e^{k_{7cp}\cdot(\lambda_0+k_{8cp})} = -0.0230 \qquad (4.17)$$

Thrust coefficient linearization

The first step in linearizing the thrust coefficient look up table is to identify, using Matlab [43], a regression function with the following form [87]:

$$CT(\beta,\lambda) = k_{1ct}(k_{2ct}\cdot(\lambda + k_{8ct}) - k_{3ct}\cdot\beta - k_{4ct}\cdot\beta^{k_{5ct}} - k_{6ct})\cdot e^{k_{7ct}\cdot(\lambda+k_{8ct})} \quad (4.18)$$

With the help of Matlab [43], the following coefficients fit the best the regression function and the thrust coefficients values in the look up table:

k_{ct1}= 0.056
k_{ct2}= 1.288
k_{ct3}=-0.827
k_{ct4}= 3.582

k_{ct5}= 0.677
k_{ct6}= 1.913
k_{ct7}=-0.013
k_{ct8}= 7.242

In the graph from Figure 4.7, it can be seen the accuracy of the thrust coefficient regression curve when the pitch angle (β_0) is 0, at a wind speed variation from 0 to 25 m/s.

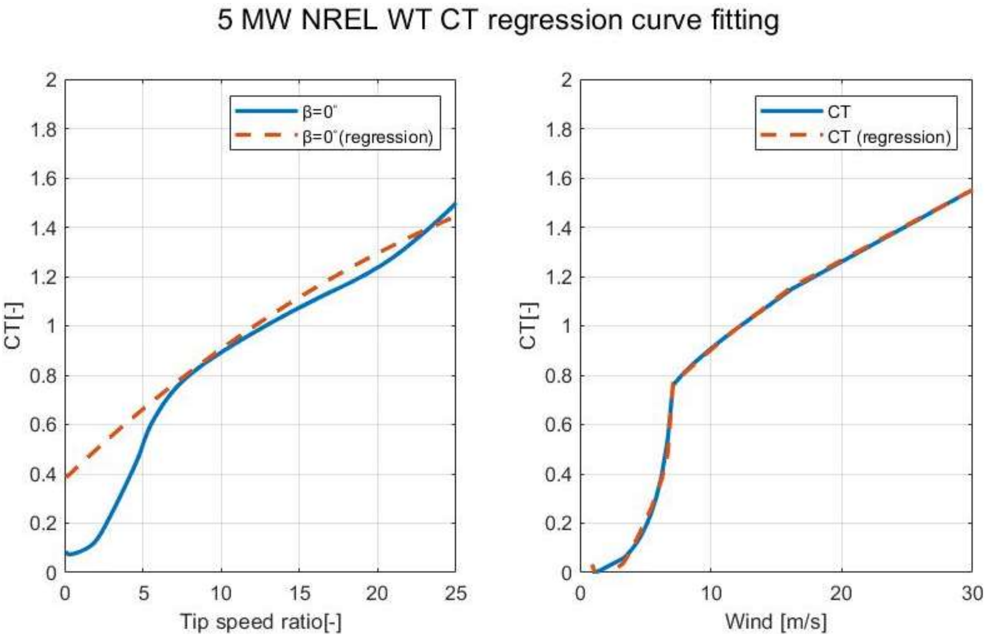

Figure 4.7. Graphical representation of the CT table

The thrust coefficient linearization will be done using first-order Taylor expansion approximation on the polynomial regression of power coefficient look up table [85]:

$$CTl(\beta,\lambda) = CT(\beta_0,\lambda_0) + \left.\frac{\partial CT}{\partial \beta}\right|_{(\beta_0,\lambda_0)} \cdot (\beta - \beta_0) + \left.\frac{\partial CT}{\partial \lambda}\right|_{(\beta_0,\lambda_0)} \cdot (\lambda - \lambda_0) \qquad \textit{(4.19)}$$

where:
$CT_l(\beta, \lambda)=CT_l$ [-] is the linearized thrust coefficient;
$CT_0(\beta_0, \lambda_0)=CT_0$= 0.7214 [-] is the thrust coefficient at the linearization point.
λ_0=7 [-] is the tip speed ratio at the linearization point;
β_0= 0 [°] is the pitch angle at the linearization point;
λ [-] is the tip speed ratio;
β [°] is the pitch angle.

By replacing the differences in thrust coefficient, pitch angle and tip speed ratio with Δ, Equation 4.19, becomes [85]:

$$\Delta\mathrm{CT} = \left.\frac{\partial \mathrm{CT}}{\partial \beta}\right|_{(\beta_0,\lambda_0)} \cdot \Delta\beta + \left.\frac{\partial \mathrm{CT}}{\partial \lambda}\right|_{(\beta_0,\lambda_0)} \cdot \Delta\lambda \qquad \textit{(4.20)}$$

where:
ΔCT [-] is the change in thrust coefficient;
$\Delta\lambda$ [-] is the change in tip speed ratio;
$\Delta\beta$ [-] is the change in pitch angle;
λ_0=7 [-] is the tip speed ratio at the linearization point;
β_0= 0 [°] is the pitch angle at the linearization point;
λ [rad] is the tip speed ratio;
β [°] is the pitch angle.

By deriving Equation 4.19, Equation 4.20 becomes:

$$\begin{aligned}\Delta CT = &\left(-k_{1ct} \cdot k_{3ct} - k_{1ct} \cdot k_{4ct} \cdot k_{5ct} \cdot \beta_0^{(k_{5ct}-1)}\right) \cdot e^{k_{7ct}\cdot(\lambda_0+k_{8ct})} \cdot \Delta\beta \\ &+ k_{1ct} \cdot k_{2ct} \cdot k_{7ct} \cdot e^{k_{7ct}\cdot(\lambda_0+k_{8ct})} \cdot \Delta\lambda\end{aligned} \qquad \textit{(4.21)}$$

Finally, the slopes of the pitch angle and tip speed which contributes to the change in thrust coefficient are calculated:

$$\begin{aligned}\left.\frac{\partial CT}{\partial \beta}\right|_{(\beta_0,\lambda_0)} &= \left(-k_{1ct} \cdot k_{3ct} - k_{1ct} \cdot k_{4ct} \cdot k_{5ct} \cdot \beta_0^{(k_{5ct}-1)}\right) \cdot e^{k_{7ct}\cdot(\lambda_0+k_{8ct})} \\ &= -0.1027\end{aligned} \qquad \textit{(4.22)}$$

$$\left.\frac{\partial CT}{\partial \lambda}\right|_{(\beta_0,\lambda_0)} = k_{1ct} \cdot k_{2ct} \cdot k_{7ct} \cdot e^{k_{7ct}\cdot(\lambda_0+k_{8ct})} = -0.0008 \qquad \textit{(4.23)}$$

Rotor torque linearization

The rotor torque equation from the nonlinear model (Equation 4.5) will be linearized using first-order Taylor expansion approximation, at a wind speed in front of the rotor of 11.4 [m/s] [85]:

$$\begin{aligned} M_{rotl}(v_{rot}, CP, \Omega) = M_{rot}(v_{rot0}, CP_0, \Omega_0) + \left.\frac{\partial M_{rot}}{\partial v_{rot}}\right|_{(v_{roto}, C_{P0}, \Omega_{0},)} \cdot (v_{rot} - v_{rot0}) \\ + \left.\frac{\partial M_{rot}}{\partial CP}\right|_{(v_{roto}, C_{P0}, \Omega_{0},)} \cdot (CP - CP_0) + \left.\frac{\partial M_{rot}}{\partial \Omega}\right|_{(v_{roto}, C_{P0}, \Omega_{0},)} \cdot (\Omega - \Omega_0) \end{aligned} \qquad (4.24)$$

where:
v_{rot0}=11.4 [m/s] is the wind speed at the linearization point;
Ω_0=1.2671 [rad/s] is the rotor angular velocity at the linearization point;
CP_0= 0.4772 is the power coefficient at the linearization point;
$M_{rot}(v_{rot0}, CP_0, \Omega_0)=M_{rot0}$= 4254651.011 [Nm] is the rotor torque at the linearization point;
v_{rot} [m/s] is the wind speed;
Ω [rad/s] is the rotor angular velocity;
CP is the power coefficient.
M_{rot} [Nm] is the rotor torque.

By replacing the changes in rotor torque, rotor angular velocity and power coefficient with Δ, Equation 4.24 becomes [85]:

$$\Delta M_{rot} = \left.\frac{\partial M_{rot}}{\partial v_{rot}}\right|_{(v_{roto}, C_{P0}, \Omega_{0},)} \cdot \Delta v_{rot} + \left.\frac{\partial M_{rot}}{\partial CP}\right|_{(v_{roto}, C_{P0}, \Omega_{0},)} \cdot \Delta CP + \left.\frac{\partial M_{rot}}{\partial \Omega}\right|_{(v_{roto}, C_{P0}, \Omega_{0},)} \cdot \Delta \Omega \qquad (4.25)$$

where:
v_{rot0}=11.4 [m/s] is the wind speed at the linearization point;
Ω_0=1.26717 [rad/s] is the rotor angular velocity at the linearization point;
CP_0= 0.4772 is the power coefficient at the linearization point;
M_{rot0}=4254651.011 [Nm] is the rotor torque at the linearization point;
$\Delta\Omega$ is the change in rotor angular velocity;
Δv_{rot} is the change in wind speed;
ΔCP is the change in power coefficient and ΔM_{rot} is the change in rotor torque.

By substituting the change in power coefficient (Equation 4.14) and the change in the tip speed ratio Δλ (Equation 4.9), (Equation 4.25) becomes [85]:

$$\Delta M_{rot} = \left.\frac{\partial M_{rot}}{\partial v_{rot}}\right|_{(v_{roto}, \Omega_0, \beta_0)} \cdot \Delta v_{rot} + \left.\frac{\partial M_{rot}}{\partial \Omega}\right|_{(v_{roto}, \Omega_0, \beta_0)} \cdot \Delta \Omega + \left.\frac{\partial M_{rot}}{\partial \beta}\right|_{(v_{roto}, \Omega_0, \beta_0)} \cdot \Delta \beta \qquad (4.26)$$

where:
v_{rot0}=11.4 [m/s] is the wind speed at the linearization point;
Ω_0=1.2671 [rad/s] is the rotor angular velocity at the linearization point;
CP_0= 0.4772 is the power coefficient at the linearization point;
β_0= 0 [°] is the pitch angle at the linearization point;
M_{rot0}=4254651.011 [Nm] is the rotor torque at the linearization point;
$\Delta\Omega$ is the change in rotor angular velocity;
Δv_{rot} is the change in wind speed;
ΔCP is the change in power coefficient;
$\Delta\beta$ is the change in pitch angle and ΔM_{rot} is the change in rotor torque.

The change in rotor torque in respect to wind speed at the rotor is derived from Equation 4.5 [85]:

$$\left.\frac{\partial M_{rot}}{\partial v_{rot}}\right|_{(v_{roto},\Omega_0,\beta_0)} = \frac{1}{2}\cdot\pi\cdot\rho\cdot R^2\cdot\frac{1}{\Omega_0}\cdot\left(3\cdot v_{rot}^2\ \cdot CP_0 - v_{roto}^2\cdot\lambda_0\cdot\frac{\partial CP(\lambda_0,\beta_0)}{\partial\lambda_0}\right) = 1245675.018 \qquad (4.27)$$

where:
ρ=1.2 [kg/m3] is the air density;
R=63 [m] is the rotor radius;
v_{rot0}=11.4 [m/s] is the wind speed at the linearization point;
Ω_0=1.2671 [rad/s] is the rotor angular velocity at the linearization point;
CP_0= 0.4772 [-] is the power coefficient at the linearization point;
β_0= 0 [°] is the pitch angle at the linearization point;
λ_0=7 [-] is the tip speed ratio at the linearization point.

The change in rotor torque in respect to rotor angular velocity is derived from Equation 4.5 [85]:

$$\left.\frac{\partial M_{rot}}{\partial \Omega}\right|_{(v_{roto},\Omega_0,\beta_0)} = \frac{1}{2}\cdot\pi\cdot\rho\cdot R^2\cdot v_{roto}^3\cdot\left(-\frac{1}{\Omega_0^2}\cdot CP_0 + \frac{1}{\Omega_0}\cdot\frac{R}{v_{roto}}\cdot\frac{\partial CP(\lambda_0,\beta_0)}{\partial\lambda_0}\right) = -4491636.493 \qquad (4.28)$$

where:
ρ=1.2 [kg/m3] is the air density;
R=63 [m] is the rotor radius;
v_{rot0}=11.4 [m/s] is the wind speed at the linearization point;
Ω_0=1.2671 [rad/s] is the rotor angular velocity at the linearization point;
CP_0= 0.4772 [-] is the power coefficient at the linearization point;
β_0= 0 [°] is the pitch angle at the linearization point;
λ_0=7 [-] is the tip speed ratio at the linearization point.

The change in rotor torque in respect to pitch angle is derived from Equation 4.5 [85]:

$$\left.\frac{\partial \mathrm{M_{rot}}}{\partial \beta}\right|_{(\mathrm{v_{roto}},\Omega_0,\beta_0)} = \frac{1}{2}\cdot\pi\cdot\rho\cdot\mathrm{R}^2\cdot\mathrm{v_{roto}^3}\cdot\frac{1}{\Omega_0}\cdot\left(\frac{\partial\mathrm{CP}(\lambda_0,\beta_0)}{\partial\beta_0}\right) = -351868.402 \qquad (4.29)$$

where:
ρ=1.2 [kg/m3] is the air density;
R=63 [m] is the rotor radius;
v_{rot0}=11.4 [m/s] is the wind speed at the linearization point;
Ω_0=1.2671 [rad/s] is the rotor angular velocity at the linearization point;
CP_0= 0.4772 [-] is the power coefficient at the linearization point;
β_0= 0 [°] is the pitch angle at the linearization point;
λ_0=7 [-] is the tip speed ratio at the linearization point;

By notating the sensitivity of the generator torque with a_{mrot}, b_{mrot}, c_{mrot}, in respect to wind speed at the rotor, rotor speed and pitch angle sensitivity, Equation 4.26 can be written in the following form [85]:

$$\Delta\mathrm{M_{rot}} = \mathrm{a_{mrot}}\cdot\Delta\mathrm{v_{rot}} + \mathrm{b_{mrot}}\cdot\Delta\Omega + \mathrm{c_{mrot}}\cdot\Delta\beta \qquad (4.30)$$

where:
a_{mrot}=1245675.018 is the rotor torque sensitivity in respect to change in wind speed at the rotor;
b_{mrot}=-4491636.493 is the rotor torque sensitivity in respect to change in rotor speed;
c_{mrot}=-351868.402 is the rotor torque sensitivity in respect to change in pitch angle.

Rotor thrust force linearization

The rotor thrust force equation from the nonlinear model (Equation 4.6) will be linearized using first-order Taylor expansion approximation, at rated wind speed in front of the rotor of 11.4 [m/s] [85]:

$$\begin{aligned} F_{rotl}(v_{rot}, CT, \Omega) = F_{rot}(v_{rot0}, CT_0, \Omega_0) + \left.\frac{\partial F_{rot}}{\partial v_{rot}}\right|_{(v_{rot0}, CT_0, \Omega_0,)} \cdot (v_{rot} - v_{rot0}) \\ + \left.\frac{\partial F_{rot}}{\partial CT}\right|_{(v_{rot0}, CT_0, \Omega_0,)} \cdot (CT - CT_0) + \left.\frac{\partial F_{rot}}{\partial \Omega}\right|_{(v_{rot0}, C_{T0}, \Omega_0,)} \cdot (\Omega - \Omega_0) \end{aligned} \qquad (4.31)$$

where:
v_{rot0}=11.4 [m/s] is the wind speed at the linearization point;
Ω_0=1.2671 [rad/s] is the rotor angular velocity at the linearization point;
CT_0= 0.7214 is the thrust coefficient at the linearization point;
$F_{rot}(v_{rot0}, CP_0, \Omega_0)=F_{rot0}$= 714925.552 [N] is the rotor thrust at the linearization point;
v_{rot} [m/s] is the wind speed;
Ω [rad/s] is the rotor angular velocity;
CT is the thrust coefficient.
F_{rot} [N] is the rotor thrust.

By replacing the changes in rotor thrust, rotor angular velocity and thrust coefficient with Δ, Equation 4.31 becomes [85]:

$$\Delta \mathrm{F_{rot}} = \left.\frac{\partial \mathrm{F_{rot}}}{\partial \mathrm{v_{rot}}}\right|_{(\mathrm{v_{rot0}}, \mathrm{CT_0}, \Omega_0,)} \cdot \Delta \mathrm{v_{rot}} + \left.\frac{\partial \mathrm{F_{rot}}}{\partial \mathrm{CT}}\right|_{(\mathrm{v_{rot0}}, \mathrm{CT_0}, \Omega_0,)} \cdot \Delta \mathrm{CP} + \left.\frac{\partial \mathrm{F_{rot}}}{\partial \Omega}\right|_{(\mathrm{v_{rot0}}, \mathrm{CT_0}, \Omega_0,)} \cdot \Delta \Omega \qquad (4.32)$$

where:
v_{rot0}=11.4 [m/s] is the wind speed at the linearization point;
Ω_0=1.2671 [rad/s] is the rotor angular velocity at the linearization point;
CT_0= 0.7214 is the thrust coefficient at the linearization point;
F_{rot0}=714925.552 [N] is the rotor torque at the linearization point;
$\Delta\Omega$ is the change in rotor angular velocity;
Δv_{rot} is the change in wind speed;
ΔCT is the change in thrust coefficient;
ΔF_{rot} is the change in rotor thrust.

By substituting the change in thrust coefficient (Equation 4.21) and the change in the tip speed ratio Δλ (Equation 4.23), equation (Equation 4.32) becomes [85]:

$$\Delta F_{rot} = \left.\frac{\partial F_{rot}}{\partial v_{rot}}\right|_{(v_{rot0}, \Omega_0, \beta_0)} \cdot \Delta v_{rot} + \left.\frac{\partial F_{rot}}{\partial \Omega}\right|_{(v_{rot0}, \Omega_0, \beta_0)} \cdot \Delta \Omega + \left.\frac{\partial F_{rot}}{\partial \beta}\right|_{(v_{rot0}, \Omega_0, \beta_0)} \cdot \Delta \beta \qquad (4.33)$$

where:
v_{rot0}=11.4 [m/s] is the wind speed at the linearization point;
Ω_0=1.2671 [rad/s] is the rotor angular velocity at the linearization point;
CT_0= 0.7214 is the thrust coefficient at the linearization point;
β_0= 0 [°] is the pitch angle at the linearization point;
F_{rot0}=714925.552 [N] is the rotor torque at linearization point;
$\Delta\Omega$ is the change in rotor angular velocity;

Δv_{rot} is the change in wind speed;
ΔCT is the change in thrust coefficient;
$\Delta\beta$ is the change in pitch angle;
ΔF_{rot} is the change in rotor thrust.

The change in rotor thrust in respect to wind speed at the rotor is derived from Equation 4.6 [85]:

$$\left.\frac{\partial F_{rot}}{\partial v_{rot}}\right|_{(v_{roto},\Omega_0,\beta_0)} = \pi\cdot\rho\cdot R\cdot v_{rot}\cdot CT_0 - \frac{1}{2}\cdot\pi\cdot\rho\cdot R^3\cdot\Omega\cdot\frac{\partial CT(\lambda_0,\beta_0)}{\partial\lambda_0} = 2482.653 \tag{4.34}$$

where:
ρ=1.2 [kg/m3] is the air density;
R=63 [m] is the rotor radius;
v_{rot0}=11.4 [m/s] is the wind speed at the linearization point;
Ω_0=1.2671 [rad/s] is the rotor angular velocity at the linearization point;
CT_0= 0.7214 is the thrust coefficient at the linearization point;
β_0= 0 [°] is the pitch angle at the linearization point;
λ_0=7 [-] is the tip speed ratio at the linearization point.

The change in rotor thrust in respect to rotor angular velocity is derived from Equation 4.6 [85]:

$$\left.\frac{\partial F_{rot}}{\partial\Omega}\right|_{(v_{roto},\Omega_0,\beta_0)} = \frac{1}{2}\cdot\pi\cdot\rho\cdot R^3\cdot v_{rot}\cdot\frac{\partial CT(\lambda_0,\beta_0)}{\partial\lambda_0} = -4424.4 \tag{4.35}$$

where:
ρ=1.2 [kg/m3] is the air density;
R=63 [m] is the rotor radius;
v_{rot0}=11.4 [m/s] is the wind speed at the linearization point;
Ω_0=1.2671 [rad/s] is the rotor angular velocity at the linearization point;
CT_0= 0.7214 is the thrust coefficient at the linearization point;
β_0= 0 [°] is the pitch angle at the linearization point;
λ_0=7 [-] is the tip speed ratio at the linearization point.

The change in rotor thrust in respect to pitch angle is derived from Equation 4.6 [85]:

$$\left.\frac{\partial F_{rot}}{\partial\beta}\right|_{(v_{roto},\Omega_0,\beta_0)} = \frac{1}{2}\cdot\pi\cdot\rho\cdot R^2\cdot(v_{roto})^2\cdot\left(\frac{\partial CT(\lambda_0,\beta_0)}{\partial\beta_0}\right) = -101749.811 \tag{4.36}$$

where:
ρ=1.2 [kg/m3] is the air density;
R=63 [m] is the rotor radius;
v_{rot0}=11.4 [m/s] is the wind speed at the linearization point;
Ω_0=1.2671 [rad/s] is the rotor angular velocity at the linearization point;
CT_0= 0.7214 is the thrust coefficient at the linearization point;
β_0= 0 [°] is the pitch angle at the linearization point;
λ_0=7 [-] is the tip speed ratio at the linearization point.

By notating the sensitivity of the generator thrust with a_{frot}, b_{frot}, c_{frot}, in respect to wind speed at the rotor, rotor speed and pitch angle sensitivity, Equation 4.33 can be written in the following form [85]:

$$\Delta F_{rot} = a_{frot} \cdot \Delta v_{rot} + b_{frot} \cdot \Delta \Omega + c_{frot} \cdot \Delta \beta \tag{4.37}$$

where:
a_{frot}=2482.653 is the rotor thrust sensitivity in respect to change in wind speed at the rotor;
b_{frot}=-4424.4 is the rotor thrust sensitivity in respect to change in rotor speed;
c_{frot}=-101749.811 is the rotor thrust sensitivity in respect to change in pitch angle.

4.2.1.3. State-space model

Based on the linearized model, the wind turbine is represented by the following state-space model [85]:

$$\begin{bmatrix} \Delta M_{rot} \\ \Delta F_{rot} \end{bmatrix} = \begin{bmatrix} a_{mrot} & b_{mrot} & b_{mrot} \\ a_{frot} & b_{frot} & c_{frot} \end{bmatrix} \cdot \begin{bmatrix} \Delta v_{rot} \\ \Delta \Omega \\ \Delta \beta \end{bmatrix} \tag{4.38}$$

where:

$$a_{mrot} = \left.\frac{\partial M_{rot}}{\partial v_{rot}}\right|_{(v_{roto},\Omega_0,\beta_0)} = \frac{1}{2} \cdot \pi \cdot \rho \cdot R^2 \cdot \frac{1}{\Omega_0} \cdot \left(3 \cdot v_{rot}^2 \cdot CP_0 - v_{rot0}^2 \cdot \lambda_0 \cdot \frac{\partial CP(\lambda_0,\beta_0)}{\partial \lambda_0}\right) \tag{4.39}$$

$$b_{mrot} = \left.\frac{\partial M_{rot}}{\partial \Omega}\right|_{(v_{roto},\Omega_0,\beta_0)} = \frac{1}{2} \cdot \pi \cdot \rho \cdot R^2 \cdot v_{rot0}^3 \cdot \left(-\frac{1}{\Omega_0^2} \cdot CP_0 + \frac{1}{\Omega_0} \cdot \frac{R}{v_{rot0}} \cdot \frac{\partial CP(\lambda_0,\beta_0)}{\partial \lambda_0}\right) \tag{4.40}$$

$$c_{mrot} = \left.\frac{\partial M_{rot}}{\partial \beta}\right|_{(v_{roto},\Omega_0,\beta_0)} = \frac{1}{2} \cdot \pi \cdot \rho \cdot R^2 \cdot v_{rot0}^3 \cdot \frac{1}{\Omega_0} \cdot \left(\frac{\partial CP(\lambda_0,\beta_0)}{\partial \beta_0}\right) \tag{4.41}$$

$$a_{frot} = \left.\frac{\partial F_{rot}}{\partial v_{rot}}\right|_{(v_{roto},\Omega_0,\beta_0)} = \pi \cdot \rho \cdot R \cdot v_{rot} \cdot CT_0 - \frac{1}{2} \cdot \pi \cdot \rho \cdot R^3 \cdot \Omega \cdot \frac{\partial CT(\lambda_0,\beta_0)}{\partial \lambda_0} \tag{4.42}$$

$$b_{frot} = \left.\frac{\partial F_{rot}}{\partial \Omega}\right|_{(v_{roto},\Omega_0,\beta_0)} = \frac{1}{2} \cdot \pi \cdot \rho \cdot R^3 \cdot v_{rot} \cdot \frac{\partial CT(\lambda_0,\beta_0)}{\partial \lambda_0} \tag{4.43}$$

$$c_{frot} = \left.\frac{\partial F_{rot}}{\partial \beta}\right|_{(v_{roto},\Omega_0,\beta_0)} = \frac{1}{2} \cdot \pi \cdot \rho \cdot R^2 \cdot (v_{rot0})^2 \cdot \left(\frac{\partial CT(\lambda_0,\beta_0)}{\partial \beta_0}\right) \tag{4.44}$$

where:
ρ=1.2 [kg/m3] is the air density;
R=63 [m] is the rotor radius;
v_{rot0}=11.4 [m/s] is the wind speed at the linearization point;
Ω_0=1.2671 [rad/s] is the rotor angular velocity at the linearization point;
CP_0= 0.4772 [-] is the power coefficient at the linearization point;
CT_0= 0.7214 is the thrust coefficient at the linearization point;
β_0= 0 [°] is the pitch angle at the linearization point;
λ_0=7 [-] is the tip speed ratio at the linearization point.

4.2.1.4. Linear vs. Nonlinear model

In Figure 4.8, is presented a comparison between the step responses of the generator angular velocity nonlinear and linear model:

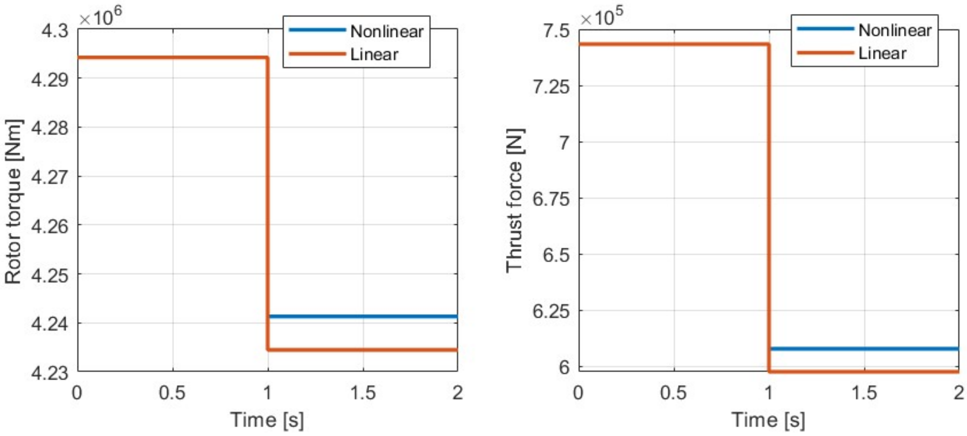

Figure 4.8. Rotor torque and thrust force linear vs nonlinear model

The error between the step responses of the nonlinear and linear model of the rotor torque is eM_{rot}=6853 [Nm], and of the thrust force is eF_{rot}=10237 [N]. The error occurs due to the error using the Taylor series approximation for linearizing the nonlinear equations.

4.2.2. Drive train

4.2.2.1. Nonlinear model

In the third order drive train model [89, 89], the rotor torque and angular velocity, are transferred by the low-speed shaft to the high-speed. The rotor inertia is taken by the low-speed shaft, while the generator inertia is taken by the high-speed shaft. The two rotating shafts are connected through a gearbox considering a torsion spring constant, viscous friction constant, and gear ratio. The drive train is modeled as a third order model, in order to include the rotor speed, generator speed and shaft torsion angle.

The change in rotor's speed is modeled as [88, 89]:

$$\dot{\Omega} = \frac{1}{I_{rot}} \cdot \left(M_{rot} - \Phi \cdot K_{shaft} - \dot{\Phi} \cdot B_{Shaft}\right) \tag{4.45}$$

where:
M_{rot} [Nm] is the rotor torque;
I_{rot}= 3.544e+7 [kg·m^2] is the rotor moment of inertia
Ω [rad/s]is the rotor angular velocity;
Φ is the shaft torsion angle;
K_{shaft}= 8.676e+8 [N·m/rad] is the shaft stiffness;
B_{shaft}= 6.215e+6 [N·m·s] is the rotor and generator damping;

$\dot{\Omega}$ [rad/s^2] is the change in rotor angular velocity;
$\dot{\Phi}$ [rad/s] is the change in shaft torsion angle.

The change in generator speed is modeled as [88, 89]:

$$\dot{\omega} = \frac{1}{I_{gen}} \cdot \left(-M_{gen} + \frac{1}{N} \cdot \left(\Phi \cdot K_{shaft} + \dot{\Phi} \cdot B_{Shaft} \right) \right) \tag{4.46}$$

where:
M_{gen} [N·m] is the generator torque;
I_{gen}= 534.116 [kg·m^2] is the generators’ moment of inertia
ω [rad/s] is the high-speed shaft angular velocity;
Φ [rad] is the shaft torsion angle;
K_{shaft}= 8.676e+8 [N·m/rad] is the shaft stiffness;
B_{shaft}= 6.215e+6 [N·m·s] is the rotor and generator damping;
N= 97 [-] is the gear ratio.
$\dot{\omega}$ [rad/s^2] is the change in high-speed shaft angular velocity;
$\dot{\Phi}$ [rad/s] is the change in shaft torsion angle.

The change in shaft torsion angle is modeled as [88, 89]:

$$\dot{\Phi} = \Omega - \frac{1}{N} \cdot \omega \tag{4.47}$$

where:
Ω [rad/s] is the rotor angular velocity;
ω [rad/s] is the high-speed shaft angular velocity;
N= 97 [-] is the gear ratio;
$\dot{\Phi}$ [rad/s] is the change in shaft torsion angle.

In the diagram from Figure 4.9., it can be seen the flow chart of the drive train model developed in Simulink [43]:

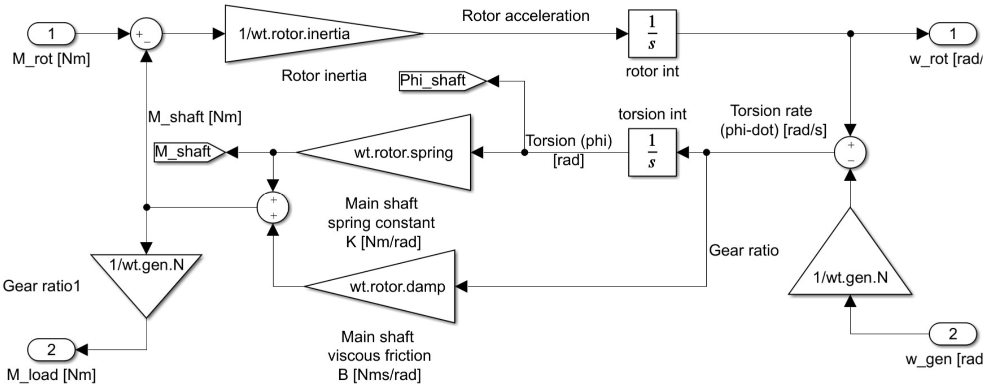

Figure 4.9. WECS nonlinear drivetrain Simulink diagram

4.2.2.2. State-space model

The state-space representation of the drive train model is the following:

$$\begin{bmatrix}\dot{\Omega}\\ \dot{\omega}\\ \dot{\Phi}\end{bmatrix} = \begin{bmatrix} -\frac{B_{Shaft}}{I_{rot}} & \frac{B_{Shaft}}{I_{rot}\cdot N} & -\frac{K_{shaft}}{I_{rot}} \\ \frac{B_{Shaft}}{I_{gen}\cdot N} & -\frac{B_{Shaft}}{I_{gen}\cdot N^2} & \frac{K_{shaft}}{I_{gen}\cdot N} \\ 1 & -\frac{1}{N} & 0 \end{bmatrix} \cdot \begin{bmatrix}\Omega\\ \omega\\ \Phi\end{bmatrix} + \begin{bmatrix} \frac{1}{I_{rot}} & 0 \\ 0 & -\frac{1}{I_{gen}} \\ 0 & 0 \end{bmatrix} \cdot \begin{bmatrix}M_{rot}\\ M_{gen}\\ 0\end{bmatrix} \tag{4.48}$$

where:
M_{rot} [Nm] is the rotor torque;
I_{rot}= 3.544e+7 [kg·m^2] is the rotor moment of inertia;
Ω [rad/s] is the rotor angular velocity;
ω [rad/s] is the high-speed shaft angular velocity;
Φ [rad] is the shaft torsion angle;
K_{shaft}= 8.676e+8 [N·m/rad] is the shaft stiffness;
B_{shaft}= 6.215e+6 [N·m·s] is the rotor and generator damping;
$\dot{\Omega}$ [rad/s^2] is the change in rotor angular velocity;
$\dot{\omega}$ [rad/s^2] is the change high speed shaft angular velocity;
$\dot{\Phi}$ [rad/s] is the change in shaft torsion angle;
M_{gen} [Nm] is the generator torque;
I_{gen}= 534.116 [kg·m^2] is the generator moment of inertia;
N= 97 [-] is the gear ratio.

4.2.3. Generator

As an electrical machine, for converting the rotor power into electrical power, a doubly fed induction machine (DFIM) or wound rotor induction machine (WRIM) is used. The DFIM is an alternative to common asynchronous and synchronous machines and has been used over many decades in various applications, mostly in the power range of megawatts. It can be advantageous in applications such as wind turbines and water pumping, which have a limited speed range, allowing a reduction in the size of the supplying power electronic converter [41].

A typical configuration of the DFIM is shown in Figure 4.10. The stator is connected to the grid at constant amplitude and frequency, creating the stator magnetic. The rotor is also connected to the grid with different amplitude and frequency in order to reach different operating conditions of the machine (speed, torque, etc.). All this is possible due to the back-to-back three-phase converter, as depicted in Figure 4.10 [41].

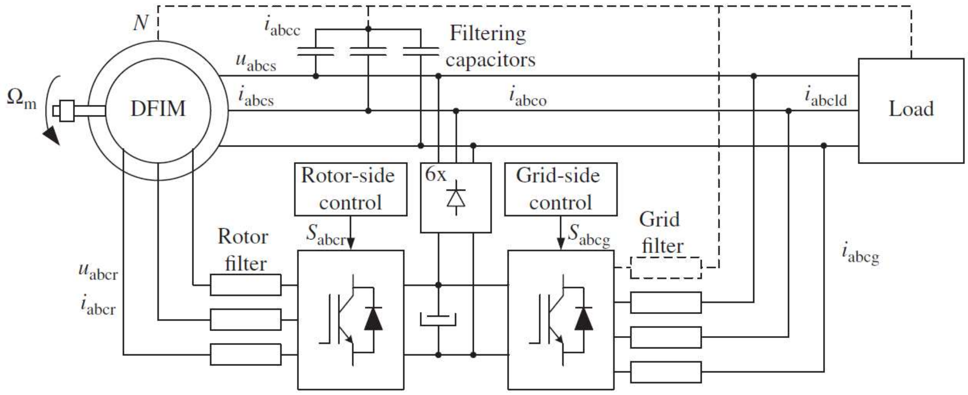

Figure 4.10. DFIM configuration [41]

4.2.3.1. Dynamic model

For developing the dynamic model of the DFIM, considering an ideal and linear machine, the space vector theory of the basic electric equations of the machines is applied. In order to develop the space vector-based models of the DFIM, three different rotating reference frames are used (Figure 4.11.). The stator reference frame (α-β), is stationary, the rotor reference frame (D-Q) rotates at rotor electrical speed, and the synchronous reference frame (d-q), rotates at synchronous speed. By using the direct or inverse rotational transformation, the space vector can be represented in any of these frames [41].

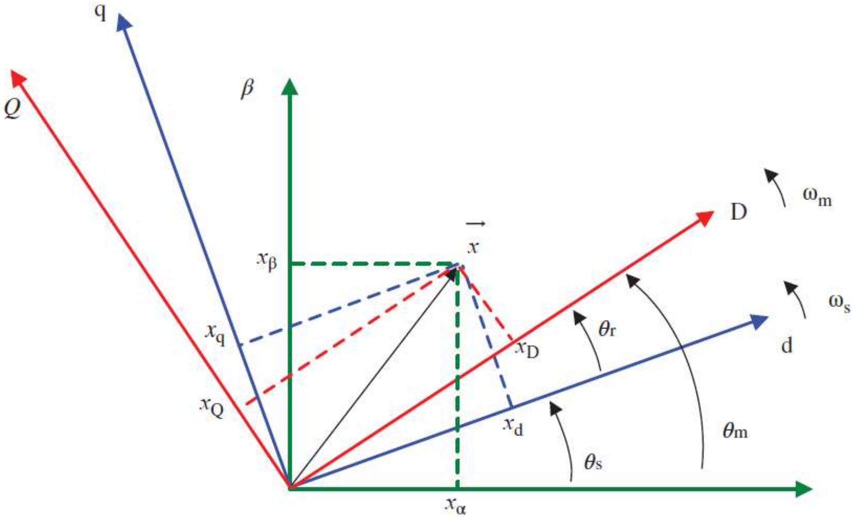

Figure 4.11. DFIM space vector reference frames [41]

Using space vector theory, the three coils can be represented by two stationary (α-β) coils for the stator and two rotating coils (D-Q) for the rotor obtaining the following voltage equations [41]:

$$\overrightarrow{v_s}^s = R_s \cdot \overrightarrow{i_s}^s + \frac{d\overrightarrow{\psi_s}^s}{dt} \qquad \overrightarrow{v_r}^r = R_r \cdot \overrightarrow{i_r}^r + \frac{d\overrightarrow{\psi_r}^r}{dt} \tag{4.49}$$

where:
$\overrightarrow{v_s}^s$ [V] is the stator voltage vector reference to the stator;
R_s [Ω] is the stator resistance;
$\overrightarrow{i_s}^s$ [A] is the stator current vector reference to the stator;
$\overrightarrow{v_r}^r$ [V] is the rotor voltage vector reference to the rotor;
R_r [Ω] is the rotor resistance;
$\overrightarrow{i_r}^r$ [A] is the rotor current vector reference to the rotor;
$\overrightarrow{\psi_s}^s$ [Vm] is the stator flux vector reference to the stator;
$\overrightarrow{\psi_r}^r$ [Vm] is the rotor flux vector reference to the rotor.
The generator electrical angular velocity represents the generator shaft angular velocity multiplied by the pole pairs of the machine:

$$\omega_{el} = \mathrm{p}_{\mathrm{wtgenerator}} \cdot \omega \tag{4.50}$$

where:
ω [rad/s] is the high-speed shaft angular velocity;
$\mathrm{p}_{\mathrm{wtgenerator}}=3$ [pairs of poles] is the generator pairs of poles (6 poles);
ω_{el} [rad/s] is the generator's electrical speed;

Stationary reference frame ($\alpha-\beta$ model)

For representing the voltage equations in the stationary reference frame, the rotor voltage equation must be multiplied by $e^{j\theta m}$ [41]:

$$\overrightarrow{v_s}^s = R_s \cdot \overrightarrow{i_s}^s + \frac{d\overrightarrow{\psi_s}^s}{dt} => \begin{cases} v_{\alpha s} = R_s \cdot i_{\alpha s} + \dfrac{d\psi_{\alpha s}}{dt} \\ v_{\beta s} = R_s \cdot i_{\beta s} + \dfrac{d\psi_{\beta s}}{dt} \end{cases} \tag{4.51}$$

$$\overrightarrow{v_r}^s = R_r \cdot \overrightarrow{i_r}^s + \frac{d\overrightarrow{\psi_r}^s}{dt} - j \cdot \omega_{el} \cdot \overrightarrow{\psi_r}^s => \begin{cases} v_{\alpha r} = R_r \cdot i_{\alpha r} + \dfrac{d\psi_{\alpha r}}{dt} + \omega_{el} \cdot \psi_{\beta r} \\ v_{\beta r} = R_s \cdot i_{\beta r} + \dfrac{d\psi_{\beta r}}{dt} - \omega_{el} \cdot \psi_{\alpha r} \end{cases} \tag{4.52}$$

where:
$\overrightarrow{v_s}^s$ [V] is the stator voltage vector reference to the stator;
R_s [Ω] is the stator resistance;
$\overrightarrow{i_s}^s$ [A] is the stator current vector reference to the stator;
$\overrightarrow{\psi_s}^s$ [Vm] is the stator flux vector reference to the stator;
$v_{\alpha s}$ [V] is the stator voltage vector α component;
$v_{\beta s}$ [V] is the stator voltage vector β component;
$i_{\alpha s}$ [A] is the stator current vector α component;
$i_{\beta s}$ [A] is the stator current vector β component;
$\psi_{\alpha s}$ [Vm] is the stator flux vector α component;
$\psi_{\beta s}$ [Vm] is the stator flux vector β component;
$\overrightarrow{v_r}^s$ [V] is the rotor voltage vector reference to the stator;

R_r [Ω] is the rotor resistance;
$\overrightarrow{i_r}^s$ [A] is the rotor current vector reference to the stator;
$\overrightarrow{\psi_r}^s$ [Vm] is the rotor flux vector reference to the stator
$v_{\alpha r}$ [V] is the rotor voltage vector α component;
$v_{\beta r}$ [V] is the rotor voltage vector β component;
$i_{\alpha r}$ [A] is the rotor current vector α component;
$i_{\beta r}$ [A] is the rotor current vector β component;
$\psi_{\alpha r}$ [Vm] is the rotor flux vector α component;
$\psi_{\beta r}$ [Vm] is the rotor flux vector β component;
ω_{el} [rad/s] is the generator's electrical speed.

Similar to the voltage equations, the flux equations can be represented in the stationary reference frame [41]:

$$\overrightarrow{\psi_s}^s = L_s \cdot \overrightarrow{i_s}^s + L_m \cdot \overrightarrow{i_r}^s => \begin{cases} \psi_{\alpha s} = L_s \cdot i_{\alpha s} + L_m \cdot i_{\alpha s} \\ \psi_{\beta s} = L_s \cdot i_{\beta s} + L_m \cdot i_{\beta s} \end{cases} \tag{4.53}$$

$$\overrightarrow{\psi_r}^s = L_m \cdot \overrightarrow{i_s}^s + L_r \cdot \overrightarrow{i_r}^s => \begin{cases} \psi_{\alpha r} = L_m \cdot i_{\alpha r} + L_r \cdot i_{\alpha r} \\ \psi_{\beta r} = L_m \cdot i_{\beta s} + L_r \cdot i_{\beta r} \end{cases} \tag{4.54}$$

where:
$\overrightarrow{\psi_s}^s$ [Vm] is the stator flux vector reference to the stator;
$\overrightarrow{\psi_r}^s$ [Vm] is the rotor flux vector reference to the stator;
$\overrightarrow{i_s}^s$ [A] is the stator current vector reference to the stator;
$\overrightarrow{i_r}^s$ [A] is the rotor current vector reference to the stator;
$L_{\sigma s}$ [H] is the stator leakage inductance;
$L_{\sigma r}$ [H] is the rotor leakage inductance;
L_m [H] is the mutual inductance;
$L_s = L_m + L_{\sigma s}$ [H] is the stator inductance;
$L_r = L_m + L_{\sigma s}$ [H] is the rotor inductance;
$\psi_{\alpha s}$ [Vm] is the stator flux vector α component;
$\psi_{\beta s}$ [Vm] is the stator flux vector β component;
$i_{\alpha s}$ [A] is the stator current vector α component;
$i_{\beta s}$ [A] is the stator current vector β component;
$\psi_{\alpha r}$ [Vm] is the rotor flux vector α component;
$\psi_{\beta r}$ [Vm] is the rotor flux vector β component;
$i_{\alpha r}$ [A] is the rotor current vector α component;
$i_{\beta r}$ [A] is the rotor current vector β component.

In Figure 4.12. it is represented as the equivalent circuit for α and β components, in which all the voltage, current and flux magnitudes are sinusoidal with a frequency of synchronous speed ω_{ss} [41]. The synchronous speed of the DFIM is calculated according to [87]:

$$\omega_{ss} = \frac{60 \cdot f_s}{p_{wtgenerator}} = 1000 \text{ rpm } (104.72 \text{ rad/s}) \tag{4.55}$$

where:
ω_{ss}=104.72 [rad/s] is the generator stator synchronous speed;

f_s=50 [Hz] is the grid frequency of the balanced three phases;
$p_{wtgenerator}$=3 [pairs of poles] is the generator pairs of poles (6 poles).

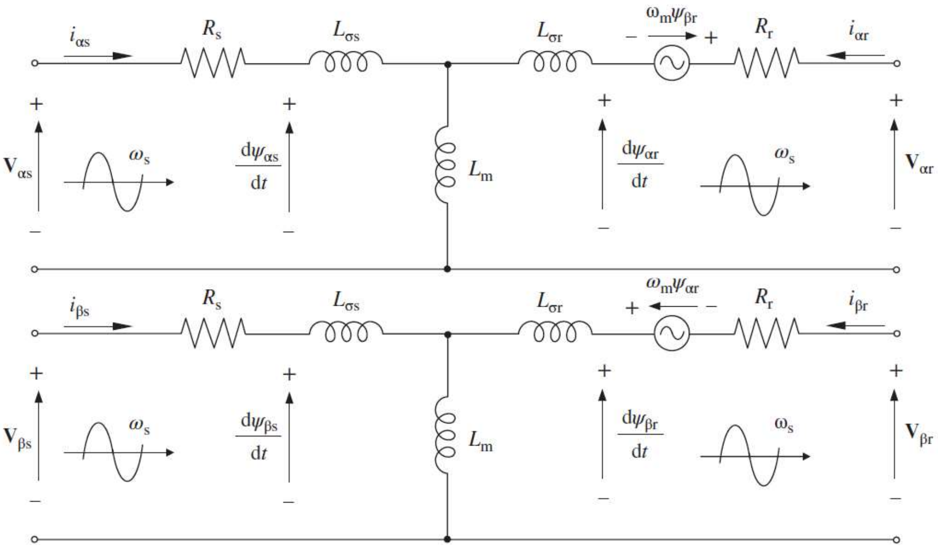

Figure 4.12. DFIM model in $\alpha-\beta$ reference frame [41]

The active power of the rotor and stator, are calculated using the following formula [41]:

$$P_s = \frac{3}{2} \cdot (v_{\alpha s} \cdot i_{\alpha s} + v_{\beta s} \cdot i_{\beta s}) \tag{4.56}$$

$$P_r = \frac{3}{2} \cdot (v_{\alpha r} \cdot i_{\alpha r} + v_{\beta r} \cdot i_{\beta r}) \tag{4.57}$$

where:
P_s [w] is the stator active power;
P_r [w] is the rotor's active power;
$v_{\alpha s}$ [V] is the stator voltage vector α component;
$v_{\beta s}$ [V] is the stator voltage vector β component;
$i_{\alpha s}$ [A] is the stator current vector α component;
$i_{\beta s}$ [A] is the stator current vector β component;
$v_{\alpha r}$ [V] is the rotor voltage vector α component;
$v_{\beta r}$ [V] is the rotor voltage vector β component;
$i_{\alpha r}$ [A] is the rotor current vector α component;
$i_{\beta r}$ [A] is the rotor current vector β component.

The reactive power of the rotor and stator, are calculated using the following formula [41]:

$$Q_s = \frac{3}{2} \cdot (v_{\beta s} \cdot i_{\alpha s} - v_{\alpha s} \cdot i_{\beta s}) \tag{4.58}$$

$$Q_r = \frac{3}{2} \cdot (v_{\beta r} \cdot i_{\alpha r} - v_{\alpha r} \cdot i_{\beta r}) \tag{4.59}$$

where:
Q_s [w] is the stator reactive power;

Q_r [w] is the rotor reactive power;

$v_{\alpha s}$ [V] is the stator voltage vector α component;

$v_{\beta s}$ [V] is the stator voltage vector β component;

$i_{\alpha s}$ [A] is the stator current vector α component;

$i_{\beta s}$ [A] is the stator current vector β component;

$v_{\alpha r}$ [V] is the rotor voltage vector α component;

$v_{\beta r}$ [V] is the rotor voltage vector β component;

$i_{\alpha r}$ [A] is the rotor current vector α component;

$i_{\beta r}$ [A] is the rotor current vector β component.

The electromagnetic torque of the DFIM is calculated using one of the following formulas [41]:

$$M_{gen} = \frac{3}{2} \cdot p_{wtgenerator} \cdot Im\{\overrightarrow{\psi_r} \cdot \overrightarrow{\iota_r}\}$$

$$M_{gen} = \frac{3}{2} \cdot p_{wtgenerator} \cdot \left(\psi_{\beta r} \cdot i_{\alpha r} - \psi_{\alpha r} \cdot i_{\beta r}\right)$$

$$M_{gen} = \frac{3}{2} \cdot p_{wtgenerator} \cdot Im\{\overrightarrow{\psi_s} \cdot \overrightarrow{\iota_s}\}$$

$$M_{gen} = \frac{3}{2} \cdot p_{wtgenerator} \cdot \frac{L_m}{L_s} \cdot Im\{\overrightarrow{\psi_s} \cdot \overrightarrow{\iota_r}\} \tag{4.60}$$

$$M_{gen} = \frac{3}{2} \cdot p_{wtgenerato} \cdot \frac{L_m}{L_r} \cdot Im\{\overrightarrow{\psi_r} \cdot \overrightarrow{\iota_s}\}$$

$$M_{gen} = \frac{3}{2} \cdot p_{wtgenerator} \cdot \frac{L_m}{\sigma \cdot L_s \cdot L_r} \cdot Im\{\overrightarrow{\psi_r} \cdot \overrightarrow{\psi_s}\}$$

$$M_{gen} = \frac{3}{2} \cdot p_{wtgenerator} \cdot L_m \cdot Im\{\overrightarrow{\iota_s} \cdot \overrightarrow{\iota_r}\}$$

With the leakage coefficient being:

$$\sigma = 1 - \frac{(L_m)^2}{L_s \cdot L_r} \tag{4.61}$$

where:

$\overrightarrow{\iota_s}^{s}$ [A] is the stator current vector reference to the stator;

$\overrightarrow{\iota_r}^{r}$ [A] is the rotor current vector reference to the rotor;

$\overrightarrow{\psi_s}^{s}$ [Vm] is the stator flux vector reference to the stator;

$\overrightarrow{\psi_r}^{r}$ [Vm] is the rotor flux vector reference to the rotor.

$i_{\alpha r}$ [A] is the rotor current vector α component;

$i_{\beta r}$ [A] is the rotor current vector β component;

$\psi_{\alpha r}$ [Vm] is the rotor flux vector α component;

$\psi_{\beta r}$ [Vm] is the rotor flux vector β component;

L_m [H] is the mutual inductance;

L_s [H] is the stator inductance;

L_r [H] is the rotor inductance;

$p_{wtgenerator}$=3 [pairs of poles] is the generator pairs of poles (6 poles).

Synchronous reference frame (d-q model)

For representing the voltage equations in the synchronously rotating reference frame, the stator voltage Equation 4.51 is multiplied with $e^{-j\theta s}$ and rotor voltage Equation 4.52 with $e^{-j\theta r}$ in order to obtain the voltages in d-q reference frame [41]:

$$\overrightarrow{v_s}^a = R_s \cdot \overrightarrow{i_s}^a + \frac{d\overrightarrow{\psi_s}^a}{dt} + j \cdot \omega_s \cdot \overrightarrow{\psi_s}^a => \begin{cases} v_{ds} = R_s \cdot i_{ds} + \dfrac{d\psi_{ds}}{dt} - \omega_{ss} \cdot \psi_{qs} \\ v_{qs} = R_s \cdot i_{qs} + \dfrac{d\psi_{qs}}{dt} + \omega_{ss} \cdot \psi_{ds} \end{cases} \tag{4.62}$$

$$\overrightarrow{v_r}^a = R_r \cdot \overrightarrow{i_r}^a + \frac{d\overrightarrow{\psi_r}^a}{dt} - j \cdot \omega_r \cdot \overrightarrow{\psi_r}^a => \begin{cases} v_{dr} = R_r \cdot i_{dr} + \dfrac{d\psi_{dr}}{dt} - \omega_{el} \cdot \psi_{qr} \\ v_{qr} = R_s \cdot i_{qr} + \dfrac{d\psi_{qr}}{dt} + \omega_{el} \cdot \psi_{dr} \end{cases} \tag{4.63}$$

where:

$\overrightarrow{v_s}^a$ [V] is the stator voltage vector reference to the synchronously rotating frame;
R_s [Ω] is the stator resistance;
$\overrightarrow{i_s}^a$ [A] is the stator current vector reference to the synchronously rotating frame;
$\overrightarrow{\psi_s}^a$ [Vm] is the stator flux vector reference to the synchronously rotating frame;
v_{ds} [V] is the stator voltage vector d component;
v_{qs} [V] is the stator voltage vector q component;
i_{ds} [A] is the stator current vector d component;
i_{qs} [A] is the stator current vector q component;
ψ_{ds} [Vm] is the stator flux vector d component;
ψ_{qs} [Vm] is the stator flux vector q component;
$\overrightarrow{v_r}^a$ [V] is the rotor voltage vector reference to the synchronously rotating frame;
R_r [Ω] is the rotor resistance;
$\overrightarrow{i_r}^a$ [A] is the rotor current vector reference to the synchronously rotating frame;
$\overrightarrow{\psi_r}^a$ [Vm] is the rotor flux vector reference to the synchronously rotating frame;
v_{dr} [V] is the rotor voltage vector d component;
v_{qr} [V] is the rotor voltage vector q component;
i_{dr} [A] is the rotor current vector d component;
i_{qr} [A] is the rotor current vector q component;
ψ_{dr} [Vm] is the rotor flux vector d component;
ψ_{qr} [Vm] is the rotor flux vector q component.
ω_{ss}=104.72 [rad/s] is the generator stator synchronous speed;
ω_{el} [rad/s] is the generator's electrical speed.

Similar to the voltage equations, the flux equations can be represented in the synchronously rotating reference frame [41]:

$$\overrightarrow{\psi_s}^a = L_s \cdot \overrightarrow{i_s}^a + L_m \cdot \overrightarrow{i_r}^a => \begin{cases} \psi_{ds} = L_s \cdot i_{ds} + L_m \cdot i_{ds} \\ \psi_{qs} = L_s \cdot i_{qs} + L_m \cdot i_{qs} \end{cases} \tag{4.64}$$

$$\overrightarrow{\psi_r}^a = L_m \cdot \overrightarrow{i_s}^a + L_r \cdot \overrightarrow{i_r}^a => \begin{cases} \psi_{dr} = L_m \cdot i_{dr} + L_r \cdot i_{dr} \\ \psi_{qr} = L_m \cdot i_{qs} + L_r \cdot i_{qr} \end{cases} \tag{4.65}$$

where:

$\overrightarrow{\psi_s}^a$ [Vm] is the stator flux vector reference to the synchronously rotating frame;
$\overrightarrow{\psi_r}^a$ [Vm] is the rotor flux vector reference to the synchronously rotating frame;

$\overrightarrow{i_s}^a$ [A] is the stator current vector reference to the synchronously rotating frame;
$\overrightarrow{i_r}^a$ [A] is the rotor current vector reference to the synchronously rotating frame;
$L_{\sigma s}$ [H] is the stator leakage inductance; $L_{\sigma r}$ [H] is the rotor leakage inductance;
L_m [H] is the mutual inductance; $L_s = L_m + L_{\sigma s}$ [H] is the stator inductance;
$L_r = L_m + L_{\sigma s}$ [H] is the rotor inductance;
ψ_{ds} [Vm] is the stator flux vector d component;
ψ_{qs} [Vm] is the stator flux vector q component;
i_{ds} [A] is the stator current vector d component;
i_{qs} [A] is the stator current vector q component;
ψ_{dr} [Vm] is the rotor flux vector d component;
ψ_{qr} [Vm] is the rotor flux vector q component;
i_{dr} [A] is the rotor current vector d component;
i_{qr} [A] is the rotor current vector q component.

In Figure 4.13. it is represented the equivalent circuit for d and q components, in which all the voltage, current and flux magnitudes are sinusoidal with a frequency of synchronous speed ω_{ss} [41].

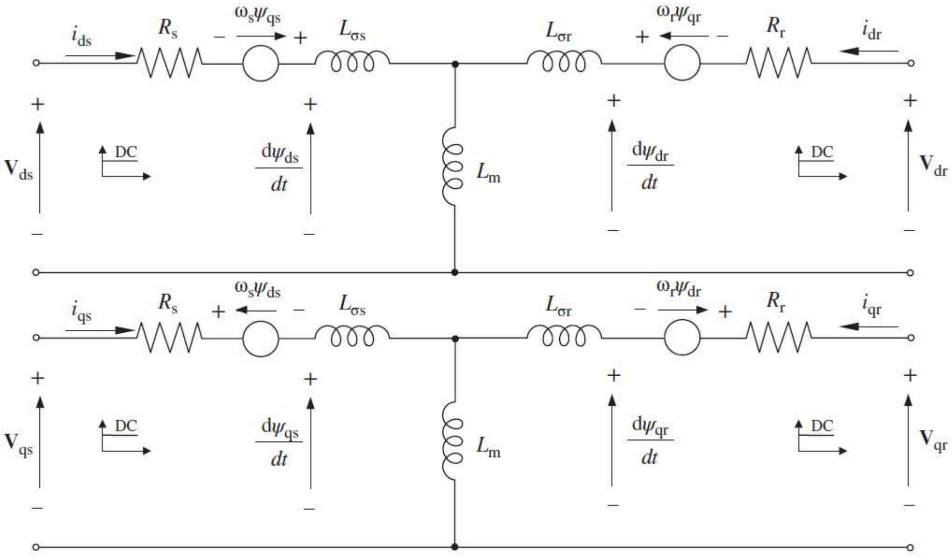

Figure 4.13. DFIM model in d-q reference frame [41]

The active power of the rotor (Equation 4.56) and stator (Equation 4.57) are calculated similarly as for the stationary reference frame, for the synchronously rotating frame:

$$P_s = \frac{3}{2} \cdot \left(v_{ds} \cdot i_{ds} + v_{qs} \cdot i_{qs}\right) \tag{4.66}$$

$$P_r = \frac{3}{2} \cdot \left(v_{dr} \cdot i_{dr} + v_{qr} \cdot i_{qr}\right) \tag{4.67}$$

where:
P_s [w] is the stator active power;
P_r [w] is the rotor's active power;

v_{ds} [V] is the stator voltage vector d component;
v_{qs} [V] is the stator voltage vector q component;
i_{ds} [A] is the stator current vector d component;
i_{qs} [A] is the stator current vector q component;
v_{dr} [V] is the rotor voltage vector d component;
v_{qr} [V] is the rotor voltage vector q component;
i_{dr} [A] is the rotor current vector d component;
i_{qr} [A] is the rotor current vector q component.

The reactive power of the rotor (Equation 4.58) and stator (Equation 4.59) are calculated similarly as for the stationary reference frame, for the synchronously rotating frame:

$$Q_s = \frac{3}{2} \cdot \left(v_{qs} \cdot i_{ds} - v_{ds} \cdot i_{qs}\right) \tag{4.68}$$

$$Q_r = \frac{3}{2} \cdot \left(v_{qr} \cdot i_{dr} - v_{dr} \cdot i_{qr}\right) \tag{4.69}$$

where:
Q_s [w] is the stator reactive power;
Q_r [w] is the rotor reactive power;
v_{ds} [V] is the stator voltage vector d component;
v_{qs} [V] is the stator voltage vector q component;
i_{ds} [A] is the stator current vector d component;
i_{qs} [A] is the stator current vector q component;
v_{dr} [V] is the rotor voltage vector d component;
v_{qr} [V] is the rotor voltage vector q component;
i_{dr} [A] is the rotor current vector d component;
i_{qr} [A] is the rotor current vector q component.

The electromagnetic torque of the DFIM is calculated using one of the following formulas [41]:

$$\begin{gathered}
M_{gen} = \frac{3}{2} \cdot p_{wtgenerator} \cdot Im\left\{\overrightarrow{\psi_r} \cdot \overrightarrow{i_r}\right\} \\
M_{gen} = \frac{3}{2} \cdot p_{wtgenerator} \cdot \left(\psi_{qr} \cdot i_{dr} - \psi_{dr} \cdot i_{qr}\right) \\
M_{gen} = \frac{3}{2} \cdot p_{wtgenerator} \cdot \frac{L_m}{L_s} \cdot \left(\psi_{qs} \cdot i_{ds} - \psi_{ds} \cdot i_{qs}\right)
\end{gathered} \tag{4.70}$$

where:
$\overrightarrow{\psi_r}^{a}$ [Vm] is the rotor flux vector reference to the synchronously rotating frame;
$\overrightarrow{i_r}^{a}$ [A] is the rotor current vector reference to the synchronously rotating frame;
ψ_{dr} [Vm] is the rotor flux vector d component;
ψ_{qr} [Vm] is the rotor flux vector q component;
i_{dr} [A] is the rotor current vector d component;
i_{qr} [A] is the rotor current vector q component.
$p_{wtgenerator}=3$ [pairs of poles] is the generator pairs of poles (6 poles).

In the diagram below it can be seen the DFIM model developed in Simulink [43]:

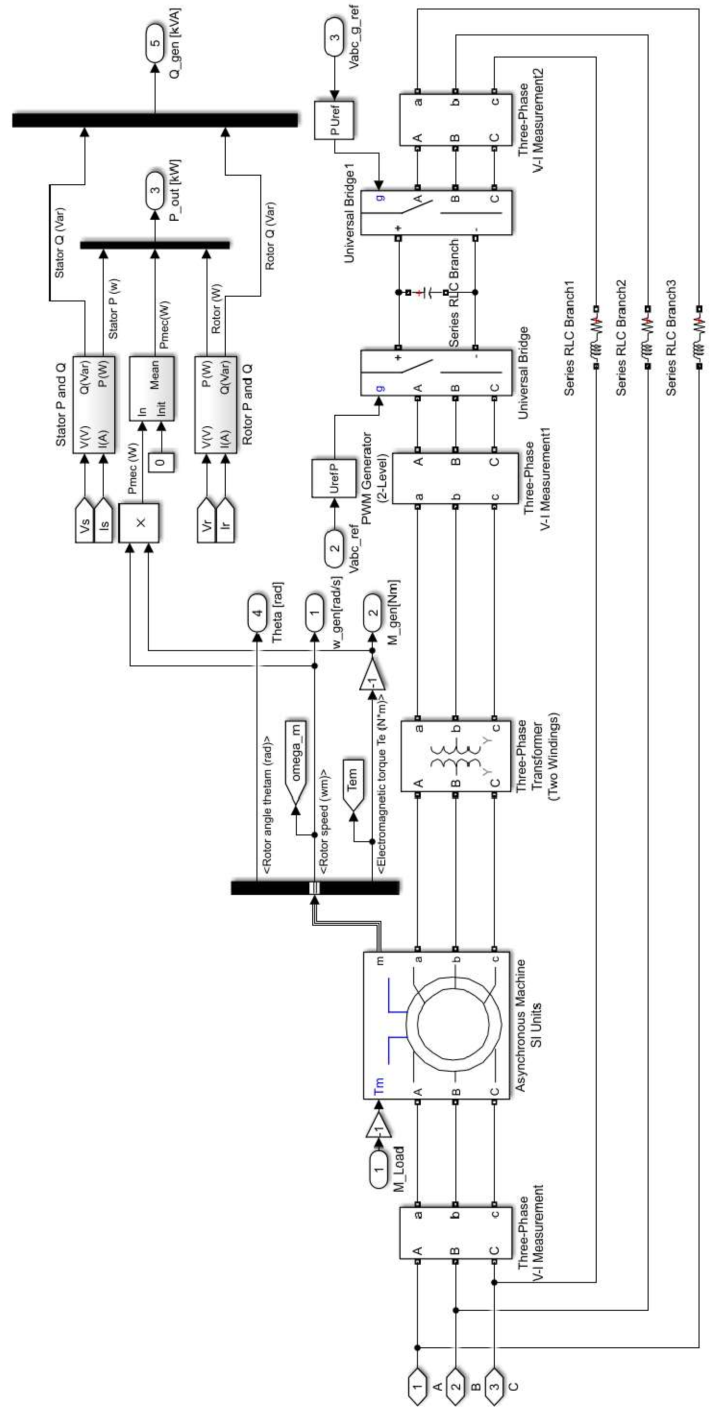

Figure 4.14. WECS DFIM dynamic model Simulink diagram

4.2.3.2. State-space model

Vectorial state-space representation of the $(\alpha-\beta)$ DFIM model considering the fluxes as states, is according to [41]:

$$\begin{bmatrix} \dot{\overrightarrow{\psi_s}}^s \\ \dot{\overrightarrow{\psi_r}}^s \end{bmatrix} = \begin{bmatrix} -\dfrac{R_s}{\sigma \cdot L_s} & \dfrac{R_s \cdot L_m}{\sigma \cdot L_s \cdot L_r} \\ \dfrac{R_r \cdot L_m}{\sigma \cdot L_s \cdot L_r} & -\dfrac{R_s}{\sigma \cdot L_s} + j \cdot \omega_{el} \end{bmatrix} \cdot \begin{bmatrix} \overrightarrow{\psi_s}^s \\ \overrightarrow{\psi_r}^s \end{bmatrix} + \begin{bmatrix} \overrightarrow{v_s}^s \\ \overrightarrow{v_r}^s \end{bmatrix} \qquad (4.71)$$

where:

$\overrightarrow{\psi_s}^s$ [Vm] is the stator flux vector reference to the stator;
$\overrightarrow{\psi_r}^s$ [Vm] is the rotor flux vector reference to the stator;
$\overrightarrow{v_s}^s$ [V] is the stator voltage vector reference to the stator;
$\overrightarrow{v_r}^s$ [V] is the rotor voltage vector reference to the stator;
L_m [H] is the mutual inductance;
L_s [H] is the stator inductance;
L_r [H] is the rotor inductance;
R_s [Ω] is the stator resistance;
R_r [Ω] is the rotor resistance;
ω_{el} [rad/s] is the generator's electrical speed.

The state-space representation of the $(\alpha-\beta)$ DFIM model, considering the fluxes as states, is:

$$\begin{bmatrix} \dot{\psi}_{\alpha s} \\ \dot{\psi}_{\beta s} \\ \dot{\psi}_{\alpha r} \\ \dot{\psi}_{\beta r} \end{bmatrix} = \begin{bmatrix} -\dfrac{R_s}{\sigma \cdot L_s} & 0 & \dfrac{R_s \cdot L_m}{\sigma \cdot L_s \cdot L_r} & 0 \\ 0 & -\dfrac{R_s}{\sigma \cdot L_s} & 0 & \dfrac{R_s \cdot L_m}{\sigma \cdot L_s \cdot L_r} \\ \dfrac{R_r \cdot L_m}{\sigma \cdot L_s \cdot L_r} & 0 & -\dfrac{R_s}{\sigma \cdot L_s} & -\omega_{el} \\ 0 & \dfrac{R_r \cdot L_m}{\sigma \cdot L_s \cdot L_r} & \omega_{el} & -\dfrac{R_s}{\sigma \cdot L_s} \end{bmatrix} \cdot \begin{bmatrix} \psi_{\alpha s} \\ \psi_{\beta s} \\ \psi_{\alpha r} \\ \psi_{\beta r} \end{bmatrix} + \begin{bmatrix} v_{\alpha s} \\ v_{\beta s} \\ v_{\alpha r} \\ v_{\beta r} \end{bmatrix} \qquad (4.72)$$

where:

$\psi_{\alpha s}$ [Vm] is the stator flux vector α component;
$\psi_{\beta s}$ [Vm] is the stator flux vector β component;
$\psi_{\alpha r}$ [Vm] is the rotor flux vector α component;
$\psi_{\beta r}$ [Vm] is the rotor flux vector β component;
$v_{\alpha s}$ [V] is the stator voltage vector α component;
$v_{\beta s}$ [V] is the stator voltage vector β component;
$v_{\alpha r}$ [V] is the rotor voltage vector α component;
$v_{\beta r}$ [V] is the rotor voltage vector β component;
L_m [H] is the mutual inductance;
L_s [H] is the stator inductance;
L_r [H] is the rotor inductance;
R_s [Ω] is the stator resistance;
R_r [Ω] is the rotor resistance;
ω_{el} [rad/s] is the generator's electrical speed.

Similar, the vectorial state-space representation of the $(\alpha-\beta)$ DFIM model considering the currents as states, is according to [41, 48, 89]:

$$\begin{bmatrix} \dot{\overrightarrow{i_s}}^{s} \\ \dot{\overrightarrow{i_r}}^{s} \end{bmatrix} = \left(\frac{1}{\sigma \cdot L_s \cdot L_r}\right) \begin{bmatrix} -R_s \cdot L_r - j \cdot \omega_{el} \cdot (L_m)^2 & R_r \cdot Lm - j \cdot \omega_{el} \cdot L_m \cdot L_r \\ R_s \cdot L_m - j \cdot \omega_{el} \cdot L_m \cdot L_s & -R_r \cdot L_s + j \cdot \omega_{el} \cdot L_r \cdot L_s \end{bmatrix} \cdot \begin{bmatrix} \overrightarrow{i_s}^{s} \\ \overrightarrow{i_r}^{s} \end{bmatrix} + \left(\frac{1}{\sigma \cdot L_s \cdot L_r}\right) \begin{bmatrix} L_r & -L_m \\ -L_m & L_s \end{bmatrix} \cdot \begin{bmatrix} \overrightarrow{v_s}^{s} \\ \overrightarrow{v_r}^{s} \end{bmatrix} \tag{4.73}$$

where:

$\overrightarrow{i_s}^{s}$ [A] is the current vector reference to the stator;
$\overrightarrow{i_r}^{s}$ [A] is the current vector reference to the stator;
$\overrightarrow{v_s}^{s}$ [V] is the stator voltage vector reference to the stator;
$\overrightarrow{v_r}^{s}$ [V] is the rotor voltage vector reference to the stator;
L_m [H] is the mutual inductance;
L_s [H] is the stator inductance;
L_r [H] is the rotor inductance;
R_s [Ω] is the stator resistance;
R_r [Ω] is the rotor resistance;
ω_{el} [rad/s] is the generator's electrical speed.

The state-space representation of the $(\alpha-\beta)$ DFIM model, considering the currents as states, is calculated similarly to the one where the states are the fluxes:

$$\begin{bmatrix} \dot{i}_{\alpha s} \\ \dot{i}_{\beta s} \\ \dot{i}_{\alpha r} \\ \dot{i}_{\beta r} \end{bmatrix} = \left(\frac{1}{\sigma \cdot L_s \cdot L_r}\right) \begin{bmatrix} -R_s \cdot L_r & \omega_{el} \cdot (L_m)^2 & R_r \cdot Lm & \omega_{el} \cdot L_m \cdot L_r \\ -\omega_{el} \cdot (L_m)^2 & -R_s \cdot L_r & -\omega_{el} \cdot L_m \cdot L_r & R_r \cdot Lm \\ R_s \cdot L_m & -\omega_{el} \cdot L_s \cdot L_m & -R_r \cdot L_s & -\omega_{el} \cdot L_r \cdot L_s \\ \omega_{el} \cdot L_s \cdot L_m & R_s \cdot L_m & \omega_{el} \cdot L_r \cdot L_s & -R_r \cdot L_s \end{bmatrix} \cdot \begin{bmatrix} i_{\alpha s} \\ i_{\beta s} \\ i_{\alpha r} \\ i_{\beta r} \end{bmatrix} + \left(\frac{1}{\sigma \cdot L_s \cdot L_r}\right) \begin{bmatrix} L_r & 0 & -Lm & 0 \\ 0 & L_r & 0 & -Lm \\ -L_m & 0 & L_s & 0 \\ 0 & -L_m & 0 & L_s \end{bmatrix} \begin{bmatrix} v_{\alpha s} \\ v_{\beta s} \\ v_{\alpha r} \\ v_{\beta r} \end{bmatrix} \tag{4.74}$$

where:

$i_{\alpha s}$ [A] is the stator current vector α component;
$i_{\beta s}$ [A] is the stator current vector β component;
$i_{\alpha r}$ [A] is the rotor current vector α component;
$i_{\beta r}$ [A] is the rotor current vector β component;
$v_{\alpha s}$ [V] is the stator voltage vector α component;
$v_{\beta s}$ [V] is the stator voltage vector β component;
$v_{\alpha r}$ [V] is the rotor voltage vector α component;
$v_{\beta r}$ [V] is the rotor voltage vector β component;
L_m [H] is the mutual inductance;
L_s [H] is the stator inductance;
L_r [H] is the rotor inductance;
R_s [Ω] is the stator resistance;
R_r [Ω] is the rotor resistance;
ω_{el} [rad/s] is the generator's electrical speed.

The vectorial state-space representation of the (d−q) DFIM model considering the fluxes as states, is calculated similarly to the (α−β) DFIM model (Equation 4.71):

$$\begin{bmatrix} \dot{\overrightarrow{\psi_s}}^{a} \\ \dot{\overrightarrow{\psi_r}}^{a} \end{bmatrix} = \begin{bmatrix} -\dfrac{R_s}{\sigma \cdot L_s} - j \cdot \omega_{ss} & \dfrac{R_s \cdot L_m}{\sigma \cdot L_s \cdot L_r} \\ \dfrac{R_r \cdot L_m}{\sigma \cdot L_s \cdot L_r} & -\dfrac{R_s}{\sigma \cdot L_s} + j \cdot \omega_{ss} \end{bmatrix} \cdot \begin{bmatrix} \overrightarrow{\psi_s}^{a} \\ \overrightarrow{\psi_r}^{a} \end{bmatrix} + \begin{bmatrix} \overrightarrow{v_s}^{a} \\ \overrightarrow{v_r}^{a} \end{bmatrix} \tag{4.75}$$

where:
$\overrightarrow{\psi_s}^{a}$ [Vm] is the stator flux vector reference to the synchronously rotating frame;
$\overrightarrow{\psi_r}^{a}$ [Vm] is the rotor flux vector reference to the synchronously rotating frame;
$\overrightarrow{v_s}^{a}$ [V] is the stator voltage vector reference to the synchronously rotating frame;
$\overrightarrow{v_r}^{a}$ [V] is the rotor voltage vector reference to the synchronously rotating frame;
L_m [H] is the mutual inductance;
L_s [H] is the stator inductance;
L_r [H] is the rotor inductance;
R_s [Ω] is the stator resistance;
R_r [Ω] is the rotor resistance;
ω_{ss} [rad/s] is DFIM synchronous speed.

The state-space representation of the (d−q) DFIM model, considering the fluxes as states is obtained similarly to the (α−β) DFIM model:

$$\begin{bmatrix} \dot{\psi}_{ds} \\ \dot{\psi}_{qs} \\ \dot{\psi}_{dr} \\ \dot{\psi}_{qr} \end{bmatrix} = \begin{bmatrix} -\dfrac{R_s}{\sigma \cdot L_s} & \omega_{ss} & \dfrac{R_s \cdot L_m}{\sigma \cdot L_s \cdot L_r} & 0 \\ -\omega_{ss} & -\dfrac{R_s}{\sigma \cdot L_s} & 0 & \dfrac{R_s \cdot L_m}{\sigma \cdot L_s \cdot L_r} \\ \dfrac{R_r \cdot L_m}{\sigma \cdot L_s \cdot L_r} & 0 & -\dfrac{R_s}{\sigma \cdot L_s} & -\omega_{ss} \\ 0 & \dfrac{R_r \cdot L_m}{\sigma \cdot L_s \cdot L_r} & \omega_{ss} & -\dfrac{R_s}{\sigma \cdot L_s} \end{bmatrix} \cdot \begin{bmatrix} \psi_{ds} \\ \psi_{qs} \\ \psi_{dr} \\ \psi_{qr} \end{bmatrix} + \begin{bmatrix} v_{ds} \\ v_{qs} \\ v_{dr} \\ v_{qr} \end{bmatrix} \tag{4.76}$$

where:
ψ_{ds} [Vm] is the stator flux vector d component;
ψ_{qs} [Vm] is the stator flux vector q component;
ψ_{dr} [Vm] is the rotor flux vector d component;
ψ_{qr} [Vm] is the rotor flux vector q component;
v_{ds} [V] is the stator voltage vector d component;
v_{qs} [V] is the stator voltage vector q component;
v_{dr} [V] is the rotor voltage vector d component;
v_{qr} [V] is the rotor voltage vector q component;
L_m [H] is the mutual inductance;
L_s [H] is the stator inductance;
L_r [H] is the rotor inductance;
R_s [Ω] is the stator resistance;
R_r [Ω] is the rotor resistance;
ω_{ss} [rad/s] is DFIM synchronous speed.

The vectorial state-space representation of the (d−q) DFIM model, considering the currents as states is calculated similarly to the model where the fluxes are taken as states [48, 89]:

$$\begin{bmatrix} \dot{\overrightarrow{i_s}}^{a} \\ \dot{\overrightarrow{i_r}}^{a} \end{bmatrix} = \left(\frac{1}{\sigma \cdot L_s \cdot L_r}\right) \cdot$$
$$\cdot \begin{bmatrix} -R_s \cdot L_r - j \cdot \omega_{el} \cdot (L_m)^2 - j \cdot \omega_{ss} \cdot \sigma \cdot L_r \cdot L_s & R_r \cdot Lm - j \cdot \omega_{el} \cdot L_m \cdot L_r \\ R_s \cdot L_m - j \cdot \omega_{el} \cdot L_m \cdot L_s & -R_r \cdot L_s + j \cdot \omega_{el} \cdot L_r \cdot L_s - j \cdot \omega_{ss} \cdot \sigma \cdot L_r \cdot L_s \end{bmatrix} \cdot \tag{4.77}$$
$$\cdot \begin{bmatrix} \overrightarrow{i_s}^{a} \\ \overrightarrow{i_r}^{a} \end{bmatrix} + \left(\frac{1}{\sigma \cdot L_s \cdot L_r}\right) \begin{bmatrix} L_r & -L_m \\ -L_m & L_s \end{bmatrix} \cdot \begin{bmatrix} \overrightarrow{v_s}^{a} \\ \overrightarrow{v_r}^{a} \end{bmatrix}$$

where:

$\overrightarrow{i_s}^{a}$ [A] is the current vector reference to the stator;
$\overrightarrow{i_r}^{a}$ [A] is the current vector reference to the stator;
$\overrightarrow{v_s}^{a}$ [V] is the stator voltage vector reference to the synchronously rotating frame;
$\overrightarrow{v_r}^{a}$ [V] is the rotor voltage vector reference to the synchronously rotating frame;
L_m [H] is the mutual inductance;
L_s [H] is the stator inductance;
L_r [H] is the rotor inductance;
R_s [Ω] is the stator resistance;
R_r [Ω] is the rotor resistance;
ω_{ss} [rad/s] is DFIM synchronous speed.

The state-space representation of the (d−q) DFIM model is:

$$\begin{bmatrix} \dot{i}_{ds} \\ \dot{i}_{qs} \\ \dot{i}_{dr} \\ \dot{i}_{qr} \end{bmatrix} = \left(\frac{1}{\sigma \cdot L_s \cdot L_r}\right) \begin{bmatrix} -R_s \cdot L_r & \omega_{el} \cdot (L_m)^2 + \omega_{ss} \cdot \sigma \cdot L_r \cdot L_s & R_r \cdot Lm & \omega_{el} \cdot L_m \cdot L_r \\ -\omega_{el} \cdot (L_m)^2 - \omega_{ss} \cdot \sigma \cdot L_r \cdot L_s & -R_s \cdot L_r & -\omega_{el} \cdot L_m \cdot L_r & R_r \cdot Lm \\ R_s \cdot L_m & -\omega_{el} \cdot L_s \cdot L_m & -R_r \cdot L_s & -\omega_{el} \cdot L_r \cdot L_s + \omega_{ss} \cdot \sigma \cdot L_r \cdot L_s \\ \omega_{el} \cdot L_s \cdot L_m & R_s \cdot L_m & \omega_{el} \cdot L_r \cdot L_s - \omega_{ss} \cdot \sigma \cdot L_r \cdot L_s & -R_r \cdot L_s \end{bmatrix} \cdot \begin{bmatrix} i_{ds} \\ i_{qs} \\ i_{dr} \\ i_{qr} \end{bmatrix}$$
$$+ \left(\frac{1}{\sigma \cdot L_s \cdot L_r}\right) \begin{bmatrix} L_r & 0 & -Lm & 0 \\ 0 & L_r & 0 & -Lm \\ -L_m & 0 & L_s & 0 \\ 0 & -L_m & 0 & L_s \end{bmatrix} \begin{bmatrix} v_{ds} \\ v_{qs} \\ v_{dr} \\ v_{qr} \end{bmatrix} \tag{4.78}$$

where:

i_{ds} [A] is the stator current vector d component;
i_{qs} [A] is the stator current vector q component;
i_{dr} [A] is the rotor current vector d component;
i_{qr} [A] is the rotor current vector q component;
v_{ds} [V] is the stator voltage vector d component;
v_{qs} [V] is the stator voltage vector q component;
v_{dr} [V] is the rotor voltage vector d component;
v_{qr} [V] is the rotor voltage vector q component;
L_m [H] is the mutual inductance;
L_s [H] is the stator inductance;
L_r [H] is the rotor inductance;
R_s [Ω] is the stator resistance;
R_r [Ω] is the rotor resistance;
ω_{ss} [rad/s] is DFIM synchronous speed.

4.2.3.3. State-space model vs. Dynamic model

In Figure 4.15., is presented a comparison between the step responses of the DFIG state-space model and the dynamic model:

a) Time 4.9 s to 5.1 s

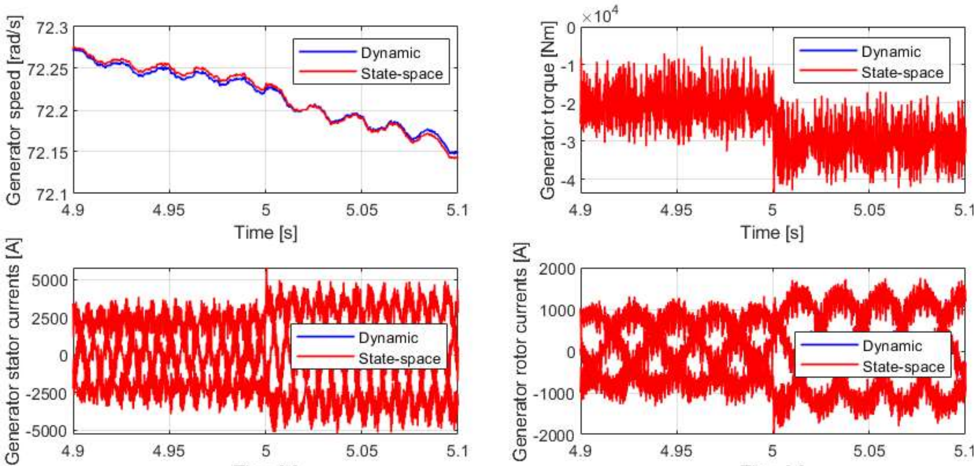

b) Time 4.999 s to 5.001 s

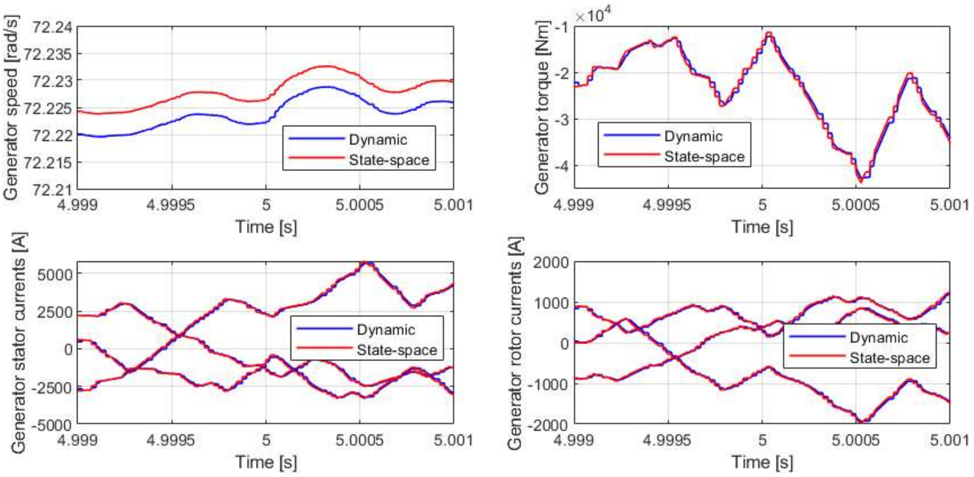

Figure 4.15. State-space vs dynamic DFIG models

The error between the generator speed responses of the dynamic model and the state-space model is $ew_{gen}\approx0.0051$ [rad/s]. The error of the generator torque is $eM_{gen}\approx-1090.892$ [N]. For the generator stator currents, the error is $eI_s\approx100$ [A] and for the rotor currents, the error is $eI_r\approx30$ [A].

4.2.4. Tower

4.2.4.1. Nonlinear model

The tower is modeled as a mass-spring-damper system, in order to approximate the tower deflection due to the thrust force created by the wind acting on the rotor [84, 85, 89]:

$$m_{wt} \cdot \ddot{z} = F_{rot} - k_{tow} \cdot z - b_{tow} \cdot \dot{z} \tag{4.79}$$

$$\ddot{z} = \frac{F_{rot}}{m_{wt}} - \frac{k_{tow}}{m_{wt}} \cdot z - \frac{b_{tow}}{m_{wt}} \cdot \dot{z} \tag{4.80}$$

with:

$$\frac{k_{tow}}{m_{tow}} = (\omega_{ntow})^2 = (2 \cdot \pi \cdot f_{ntow})^2 = 4 \cdot \pi \cdot (f_{ntow})^2 \tag{4.81}$$

$$\frac{b_{tow}}{m_{tow}} = 2 \cdot \zeta_{tow} \cdot \omega_{ntow} = 4 \cdot \pi \cdot f_{ntow} \cdot \zeta_{tow} \tag{4.82}$$

By substituting (Equations 4.81, 4.82 and 4.80) becomes

$$\ddot{z} = \frac{F_{rot}}{m_{wt}} - 4 \cdot \pi \cdot (f_{ntow})^2 \cdot z - 4 \cdot \pi \cdot f_{ntow} \cdot \zeta_{tow} \cdot \dot{z} \tag{4.83}$$

where:
F_{rot} [N] is the rotor thrust force;
m_{wt}=588562 [kg] is the WECS mass (including the tower, rotor and nacelle mass);
k_{tow} [N/m] is the spring constant of the tower;
b_{tow} [N·s/m] is the damping constant of the tower;
ω_{ntow}=2.0196 [rad/s] is the tower's first eigenfrequency;
f_{ntow}=0.321 [Hz] is the tower's first eigenfrequency;
ζ_{tow}=0.08 [%] is the tower damping ratio;
H_{tow}=87.6 [m] is the tower height;
z [m] is the position of the nacelle;
$\dot{z}$ [m/s] is the velocity of the nacelle;
$\ddot{z}$ [m/s2] is the acceleration of the nacelle.

In Figure 4.16., it can be seen the drive train model developed in Simulink [43]:

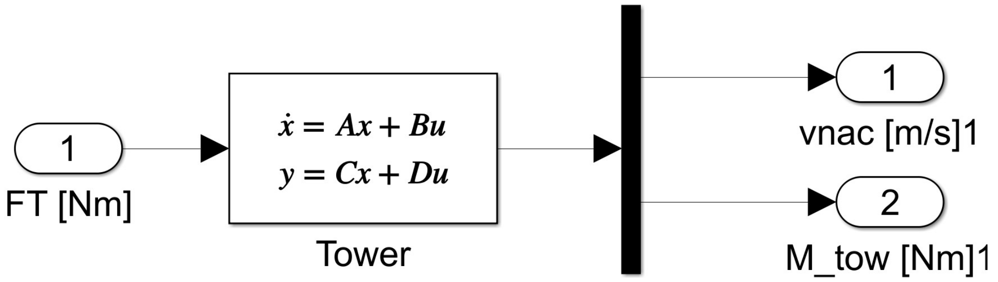

Figure 4.16. WECS nonlinear tower Simulink diagram

4.2.4.2. State-space model

The tower model has the following state space representation:

$$\begin{bmatrix} \ddot{z} \\ \dot{z} \\ \dot{z} \\ M_{tow} \end{bmatrix} = \begin{bmatrix} -4 \cdot \pi \cdot f_{ntow} \cdot \zeta_{tow} & -4 \cdot \pi \cdot (f_{ntow})^2 & \frac{1}{m_{wt}} \\ 1 & 0 & 0 \\ 1 & 0 & 0 \\ 0 & -4 \cdot \pi \cdot (f_{ntow})^2 \cdot m_{wt} \cdot H_{tow} & 0 \end{bmatrix} \cdot \begin{bmatrix} \dot{z} \\ z \\ F_{rot} \end{bmatrix} \qquad (4.84)$$

where:
F_{rot} [N] is the rotor thrust force;
m_{wt}=588562 [kg] is the WECS mass (including the tower, rotor and nacelle mass);
f_{ntow}=0.321 [Hz] is the tower's first eigenfrequency;
ζ_{tow}=0.08 [%] is the tower damping ratio;
H_{tow}=87.6 [m] is the tower height;
z [m] is the position of the nacelle;
$\dot{z}$ [m/s] is the velocity of the nacelle;
$\ddot{z}$ [m/s2] is the acceleration of the nacelle.

4.2.5. *Blade*

4.2.5.1. Linear model

The blade bending moment created by the thrust force of the wind acting on the is modeled according to the following equation [84, 85, 89]:

$$M_{blade} = \frac{1}{3} \cdot 2 \cdot R \cdot F_{rot} \qquad (4.85)$$

where:
F_{rot} [N] is the rotor thrust force;
R=63 [m] is the rotor radius;
M_{blade} [Nm] is the blade bending moment.

In Figure 4.17. it can be seen in the blade bending moment model developed in Simulink [43].

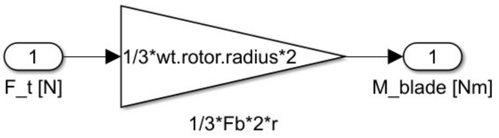

Figure 4.17. Wind turbine blade bending moment Simulink diagram

4.2.5.2. State-space model

The state space representation of the blade momentum is:

$$[M_{blade}] = \left[\frac{1}{3} \cdot 2 \cdot \mathrm{R}\right] \cdot [F_{rot}] \qquad (4.86)$$

where:
F_{rot} [N] is the rotor thrust force;
R=63 [m] is the rotor radius;
M_{blade} [Nm] is the blade bending moment.

4.2.6. *Pitch actuator*

4.2.6.1. Linear model

The pitch actuator is modeled as a second order system with a hydraulic time delay and time constant [85, 88, 89]:

$$\ddot{\beta} = \frac{1}{\tau_\beta} \cdot \left(u_\beta^{\lambda\beta} - \dot{\beta}\right) \tag{4.87}$$

where:
$\dot{\beta}$ [°/s] is the change in the pitch angle;
$\ddot{\beta}$ [°/s^2] is the sensitivity of the pitch angle
τ_β=0.05 [s] is the pitch time constant;
$u\beta$ is the input pitch angle to the pitch actuator
$\lambda\beta$=0.05 [s] is the input delay from the input pitch angle to the rated pitch angle.

The pitch actuator is controlled by a proportional regulator with constant K_β [85, 88, 89]:

$$u_\beta = K_\beta \cdot \left(\beta_{ref} - \beta_{meas}\right) \tag{4.88}$$

where:
u_β [°] is the input pitch angle to the pitch actuator;
K_β=10 [-] is the proportional regulator constant;
β_{ref} [°] is the reference pitch angle;
β_{meas} [°] is the measured pitch angle.

In the diagram from Figure 4.18, it can be seen the flow chart of the pitch actuator model developed in Simulink [43]:

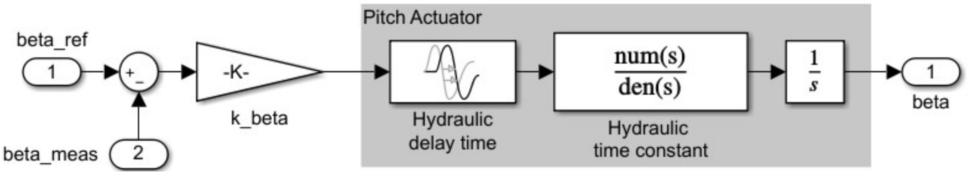

Figure 4.18. WECS pitch actuator Simulink diagram

4.2.6.2. State-space model

The state space representation of the pitch actuator is:

$$\begin{bmatrix} \dot{\beta} \\ \ddot{\beta} \end{bmatrix} = \begin{bmatrix} 0 & 1 \\ 0 & -\dfrac{1}{\tau_\beta} \end{bmatrix} \cdot \begin{bmatrix} \beta \\ \dot{\beta} \end{bmatrix} + \begin{bmatrix} 0 \\ \dfrac{K_\beta}{\tau_\beta} \end{bmatrix} \cdot \left[\beta_{ref} - \beta_{meas}\right] \tag{4.89}$$

where:
$\dot{\beta}$ is the change in the pitch angle;
$\ddot{\beta}$ is the sensitivity of the pitch angle
K_β=10 [-] is the proportional regulator constant;
β_{ref} [°] is the reference pitch angle;
β_{meas} [°] is the measured pitch angle.
τ_β =0.05 [s] is the pitch time constant;
λ=0.05 [s] is the input delay from the input pitch angle to the rated pitch angle.

4.2.7. WECS modelling summary

4.2.7.1. Nonlinear model

Finally, all the parts of the nonlinear model (aerodynamics, generator, tower, blades and pitch actuator) of the WECS are combined in order to be obtained the nonlinear model. In Figure 4.19, it can be seen the nonlinear model developed in Simulink [43]:

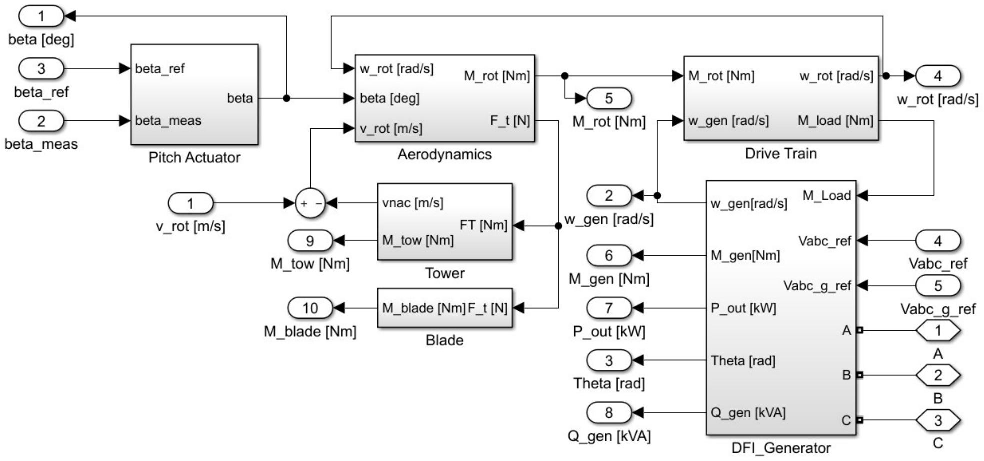

Figure 4.19. WECS nonlinear model Simulink diagram

4.2.7.2. Linear model

All the linearized nonlinear equations are combined with the already linear equations from the nonlinear model into a system of equations that represents the linear model [85, 89].

$$\dot{\Omega} = \frac{1}{I_{rot}} \cdot \left(a_{mrot} \cdot v_{rot} + b_{mrot} \cdot \Omega + c_{mrot} \cdot \beta - \Phi \cdot K_{shaft} - \dot{\Phi} \cdot B_{Shaft}\right) \qquad (4.90)$$

$$\dot{\omega} = \frac{1}{I_{gen}} \cdot \left(-M_{gen} + \frac{1}{N} \cdot \left(\Phi \cdot K_{shaft} + \dot{\Phi} \cdot B_{Shaft}\right)\right) \qquad (4.91)$$

$$\dot{\Phi} = \Omega - \frac{1}{N} \cdot \omega \qquad (4.92)$$

$$\dot{M}_{gen} = \frac{1}{\tau_{gen}} \cdot \left(-\frac{1}{(\omega_0)^2} \cdot \omega - M_{gen}\right) \qquad (4.93)$$

$$P_{out} = \eta_{gen} \cdot \left(\omega_0 \cdot M_{gen} + M_{gen0} \cdot \omega\right) \qquad (4.94)$$

with:

$$a_{mrot} = \frac{1}{2} \cdot \pi \cdot \rho \cdot R^2 \cdot \frac{1}{\Omega_0} \cdot \left(3 \cdot v_{rot}^2 \cdot CP_0 - v_{rot0}^2 \cdot \lambda_0 \cdot \frac{\partial CP(\lambda_0, \beta_0)}{\partial \lambda_0} \right) \tag{4.95}$$

$$b_{mrot} = \frac{1}{2} \cdot \pi \cdot \rho \cdot R^2 \cdot v_{rot0}^3 \cdot \left(-\frac{1}{\Omega_0^2} \cdot CP_0 + \frac{1}{\Omega_0} \cdot \frac{R}{v_{rot0}} \cdot \frac{\partial CP(\lambda_0, \beta_0)}{\partial \lambda_0} \right) \tag{4.96}$$

$$c_{mrot} = \frac{1}{2} \cdot \pi \cdot \rho \cdot R^2 \cdot v_{rot0}^3 \cdot \frac{1}{\Omega_0} \cdot \left(\frac{\partial CP(\lambda_0, \beta_0)}{\partial \beta_0} \right) \tag{4.97}$$

where:
I_{rot}= 3.5444067 [kg·m^2] is the rotor moment of inertia;
v_{rot} [m/s] is the average wind speed over the rotor;
Φ [rad] is the shaft torsion angle;
$\dot{\Phi}$ [rad/s] is the change in shaft torsion angle;
K_{shaft}= 867639000 [N·m/rad] is the torsion spring constant;
B_{shaft}= 6215000 [N·m·s] is the viscous friction constant;
Ω [rad/s] is the rotor angular velocity;
$\dot{\Omega}$ [rad/s^2] is the change in rotor angular velocity;
β [°] is the pitch angle;
β_0=0 [°] is the pitch angle at the linearization point;
ω [rad/s] is the generator's angular velocity;
$\dot{\omega}$ [rad/s^2] is the change in generator angular velocity;
N= 97 [-] is the gear ratio;
I_{gen}= 534.116 [kg·m^2] is the generators' moment of inertia
M_{gen} [Nm]is the generator torque;
$\dot{M}_{gen}$ [Nm/s] is the change in generator torque;
T_{gen}=0.1 [s] is the generator time constant.
P_{out} [w] is the generator output power;
η_{gen}=0.944 [-] is the generator efficiency;
ρ=1.2 [kg/m3] is the air density;
R=63 [m] is the rotor radius;
v_{rot0}=11.4 [m/s] is the rated wind speed;
Ω_0=1.2671 [rad/s] is the rated rotor angular velocity;
CP_0= 0.4816 [-] is the power coefficient at the linearization point;
λ_0=7 [-] is the tip speed ratio at the linearization point;
T_{gen}=0.1 [s] is the generator time constant;
a_{mrot}=1948808.73 is the rotor torque sensitivity in respect to change in wind speed at the rotor;
b_{mrot}=-11006550666.638 is the rotor torque sensitivity in respect to change in rotor speed;
c_{mrot}=-367632.5798 is the rotor torque sensitivity in respect to change in pitch angle;
M_{gen0}=43093.551 [Nm] is the rated generator torque;
ω_0=122.91 [rad/s] is the rated generator angular velocity.

4.2.7.3. State-space model

The first order linearized model can be represented by the following state-space model [85]:

$$\begin{bmatrix} \dot{\Omega} \\ \dot{\omega} \\ \dot{\Phi} \\ \dot{M}_{gen} \\ \omega \\ P_{out} \end{bmatrix} = \begin{bmatrix} \frac{b_{mrot} - B_{shaft}}{I_{rot}} & \frac{B_{shaft}}{I_{rot} \cdot N} & -\frac{K_{shaft}}{I_{rot}} & 0 \\ \frac{B_{shaft}}{I_{gen} \cdot N} & -\frac{B_{shaft}}{I_{gen} \cdot N^2} & \frac{K_{shaft}}{I_{gen} \cdot N} & -\frac{1}{I_{gen}} \\ 1 & -\frac{1}{N} & 0 & 0 \\ 0 & -\frac{1}{\tau_{gen} \cdot (\omega_0)^2} & 0 & -\frac{1}{\tau_{gen}} \\ 0 & 1 & 0 & 0 \\ 0 & \eta_{gen} \cdot M_{gen0} & 0 & \eta_{gen} \cdot \omega_0 \end{bmatrix} \cdot \begin{bmatrix} \Omega \\ \omega \\ \Phi \\ M_{gen} \end{bmatrix} + \begin{bmatrix} \frac{a_{mrot}}{I_{rot}} & \frac{-c_{mrot}}{I_{rot}} \\ 0 & 0 \\ 0 & 0 \\ 0 & 0 \\ 0 & 0 \\ 0 & 0 \end{bmatrix} \cdot \begin{bmatrix} v_{rot} \\ \beta \end{bmatrix} \tag{4.98}$$

with:

$$a_{mrot} = \frac{1}{2} \cdot \pi \cdot \rho \cdot R^2 \cdot \frac{1}{\Omega_0} \cdot \left(3 \cdot v_{rot}^2 \cdot CP_0 - v_{rot0}^2 \cdot \lambda_0 \cdot \frac{\partial CP(\lambda_0, \beta_0)}{\partial \lambda_0} \right) \tag{4.99}$$

$$b_{mrot} = \frac{1}{2} \cdot \pi \cdot \rho \cdot R^2 \cdot v_{rot0}^3 \cdot \left(-\frac{1}{\Omega_0^2} \cdot CP_0 + \frac{1}{\Omega_0} \cdot \frac{R}{v_{rot0}} \cdot \frac{\partial CP(\lambda_0, \beta_0)}{\partial \lambda_0} \right) \tag{4.100}$$

$$c_{mrot} = \frac{1}{2} \cdot \pi \cdot \rho \cdot R^2 \cdot v_{rot0}^3 \cdot \frac{1}{\Omega_0} \cdot \left(\frac{\partial CP(\lambda_0, \beta_0)}{\partial \beta_0} \right) \tag{4.101}$$

where:

I_{rot}= 3.5444067 [kg·m^2] is the rotor moment of inertia;
v_{rot} is the average wind speed over the rotor;
Φ [rad] is the shaft torsion angle;
$\dot{\Phi}$ [rad/s] is the change in shaft torsion angle;
K_{shaft}= 867639000 [N·m/rad] is the torsion spring constant;
B_{shaft}= 6215000 [N·m·s] is the viscous friction constant;
Ω [rad/s] is the rotor angular velocity;
$\dot{\Omega}$ [rad/s^2] is the change in rotor angular velocity;
β [°] is the pitch angle and β_0=0 [°] is the pitch angle at linearization point;
ω [rad/s] is the generator's angular velocity;
$\dot{\omega}$ [rad/s^2] is the change in generator angular velocity;
ω_0=122.91 [rad/s] is the rated generator angular velocity;
I_{gen}= 534.116 [kg·m^2] is the generators' moment of inertia
M_{gen} [Nm]is the generator torque;
$\dot{M}_{gen}$ [Nm/s] is the change in generator torque;
M_{gen0}=43093.551 [Nm] is the rated generator torque;
T_{gen}=0.1 [s] is the generator time constant.
P_{out} [w] is the generator output power;
η_{gen}=0.944 [-] is the generator efficiency;
ρ=1.2 [kg/m3] is the air density;
R=63 [m] is the rotor radius and N= 97 [-] is the gear ratio;
v_{rot0}=11.4 [m/s] is the rated wind speed;
Ω_0=1.2671 [rad/s] is the rated rotor angular velocity;
CP_0= 0.4816 [-] is the power coefficient at the linearization point;
λ_0=7 [-] is the tip speed ratio at the linearization point;
T_{gen}=0.1 [s] is the generator time constant;
a_{mrot}=1948808.73, b_{mrot}=-11006550666.638, c_{mrot}=-367632.5798 are the rotor torque sensitivities in respect to change in wind speed at the rotor, rotor speed and pitch angle.

4.2.7.4. Linear vs. nonlinear model

In Figure 4.18, is presented a comparison between the dynamic and state-space step responses of the generator power and angular velocity:

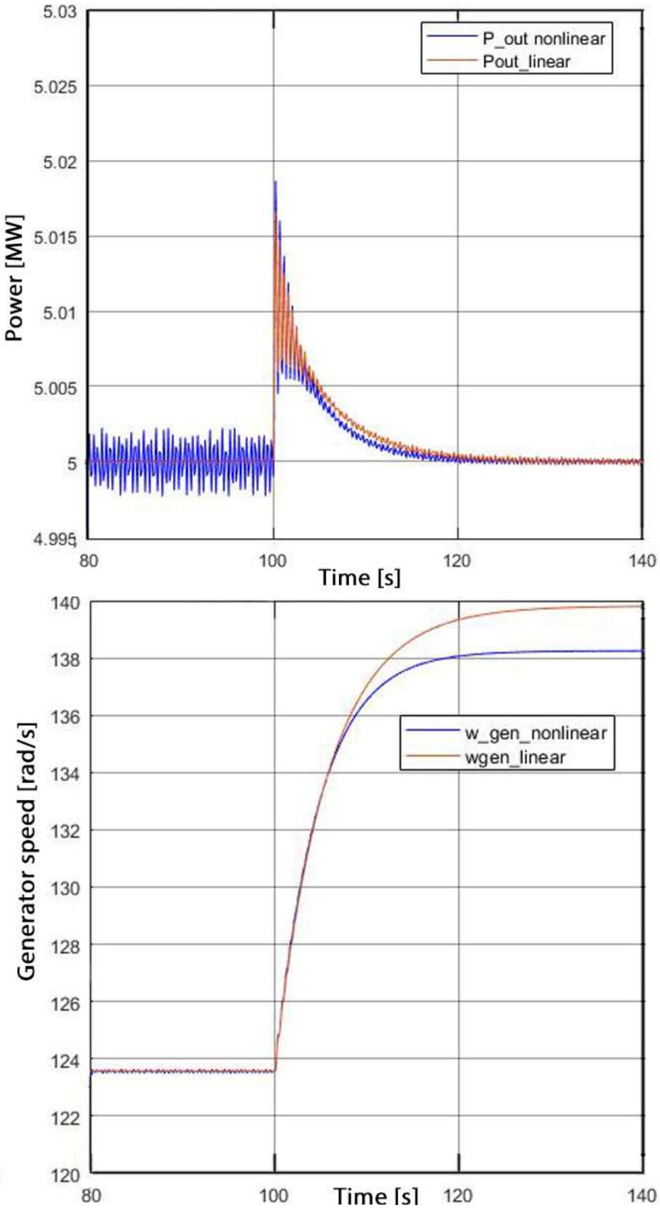

Figure 4.20. Generator angular velocity response of the nonlinear vs. linear model

The error between the dynamic and state-space models step responses of the WECS generator power is eP_{out}=-110 [w], and for the generator's angular velocity is $e\omega_{gen}$=-1.575 [rad/s].

4.3. WECS control strategy

The control strategy developed in the current subchapter it has been published in reference [89], is based on the controller developed in [86], with the following modifications in order to be further integrated in an application that requires the WECS to adapt its power production to a required power demand:

1. The presented controller adapts the wind turbine power production to power demand.
2. The controller design is based on the linearized model from the second subchapter (***4.2. WECS modelling***), while the controller developed in reference [86] is based on a first order WECS model.
3. The maximum power point tracking was determined based on the maximum value of the CP table, while in the controller developed in reference [86] was determined by using an external software where the wind turbine had already implanted a controller.
4. The gain schedule for the PI controller is determined based on the linearization of the rotor torque sensitivity to the blade-pitching angle, while in the reference [86], was determined by performing a linearization analysis of the aerodynamic power sensitivity in a third-party software where the wind turbine had already implemented a gain schedule PI controller.
5. The WECS controller presented in this subchapter can be developed for any WECS based on the required parameters from Table 4.1.

Considering the NREL 5-MW WECS a conventional variable-speed, variable blade-pitch-to-feather configuration, the conventional approach for controlling power-production operation is based on two controllers:

1. A generator-torque (partial load) controller, based on a lookup-table with generator speed as input and generator power reference as output. The goal of the generator-torque controller is to maximize power capture below the rated operation point, while the blade pitch is kept constant at 0.
2. The second controller is a full-span rotor-collective blade-pitch (full load) controller where the reference is the generator demanded power and the rotor speed is controlled using the blade pitch angle actuator operated by a gain scheduled PI controller. The goal of the blade-pitch controller is to regulate generator speed at the rated operation point.

Delimitations:

In the controller that is implemented in the current work, there are no control actions to regulate the nacelle-yaw angle because its response is slow enough that it does not generally contribute to large extreme loads or fatigue damages.

4.3.1. Control-measurement filter

Both, the generator-torque and blade-pitch controllers requires the generator speed measurement as feedback input. In order to mitigate high-frequency excitation of the control systems, the generator speed measurement has to be filtered. In the present work, the generator speed measurement is filtered using a recursive, single-pole low-pass filter with exponential smoothing [90], due to its effectiveness in the time domain. According to [86], even though other linear low pass filters (such as Butterworth, Chebyshev, Elliptic, and Bessel filters) have implicit advantages relative to the chosen filter, none of these filters have given a superior performance in the overall system response.

The discrete-time recursion (difference) equation considered for this filter is:

$$y[n] = (1-\alpha)\cdot u[n] + \alpha \cdot y[n-1] \tag{4.102}$$

with

$$\alpha = e^{-2\cdot\pi\cdot T_S\cdot f_C} \tag{4.103}$$

where:

$y[n]$ [rad/s] is the filtered generator speed;
$y[n\text{-}1]$ [rad/s] is the previous filtered generator speed;
$u[n]$ [rad/s] is the measured generator speed;
n [-] is the discrete-time-step counter;
T_s= 0.0125 [s] is the discrete time step;
F_c=0.25 [Hz] is the corner frequency[2];
α= 0.980556556146257 is the low-pass filter coefficient.

In the control strategy implemented in Simulink, the single-pole low-pass filter was implemented as a discrete state-space model:

$$x[n] = y[n-1] \tag{4.104}$$

or

$$x[n+1] = y[n] \tag{4.105}$$

The discrete-time state-space representation of this filter is derived as:

$$x[n+1] = A_d\cdot x[n] + B_d\cdot u[n] \quad \text{with} \quad A_d = \alpha \quad \text{and} \quad B_d = 1-\alpha \tag{4.106}$$

$$y[n] = C_d\cdot x[n] + D_d\cdot u[n] \quad \text{with} \quad C_d = \alpha \quad \text{and} \quad D_d = 1-\alpha \tag{4.107}$$

where:

A_d=0.980556556146257 is the discrete-time state matrix;
B_d=0.019443443853743 is the discrete-time input matrix;
C_d=0.980556556146257 is the discrete-time output state matrix;
D_d=0.019443443853743 is the discrete-time input transmission matrix;

In the diagram from Figure 4.21, it can be seen single-pole low-pass filter, is a discrete state-space model developed in Simulink [43]:

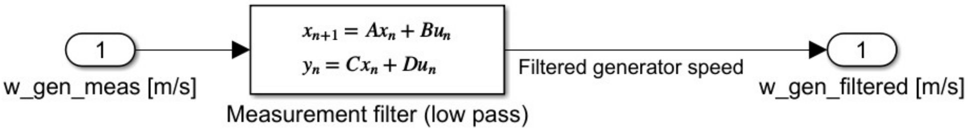

Figure 4.21. WECS generator's speed measurement filter Simulink diagram

---

[2] *The corner frequency (the -0.1 dB point in Figure 11) of the low-pass filter to be 0.25 Hz, as this value represents roughly one-quarter of the blade's first edgewise natural.*

In order to analyze the frequency response of the filter, from the state-space model, the transfer function was obtained using the following formula [91].

$$H_{filter}(z) = \frac{Y(z)}{U(z)} = C_d \cdot (z \cdot I - A_d)^{-1} \cdot B_d + D_d \qquad (4.108)$$

where:
A_d=0.980556556146257 is the discrete-time state matrix;
B_d=0.019443443853743 is the discrete-time input matrix;
C_d=0.980556556146257 is the discrete-time output state matrix;
D_d=0.019443443853743 is the discrete-time input transmission matrix;
$H_{filter}(z)$ is the discrete transfer function of the filter.

By substituting the state, input, output and input transmission discrete-time matrices with:

$$A_d = \alpha; \quad B_d = 1 - \alpha; \quad C_d = \alpha; \quad \text{and} \quad D_d = 1 - \alpha \qquad (4.109)$$

The transfer function of the filter becomes:

$$H_{filter}(z) = \alpha \cdot (z \cdot I - \alpha)^{-1} \cdot (1 - \alpha) + (1 - \alpha) \qquad (4.110)$$

Simplifying the above Equation 4.108, the discrete transfer function of the filter becomes:

$$H_{filter}(z) = \frac{(1 - \alpha) \cdot z}{z - \alpha} = \frac{0.01944 \cdot z}{z - 0.9806} \qquad (4.111)$$

where:
α= 0.980556556146257 is the low-pass filter coefficient;
$H_{filter}(z)$ is the discrete transfer function of the filter.

In the bode diagram from Figure 4.22., it can be seen the frequency response of the recursive, single-pole low-pass filter with exponential smoothing:

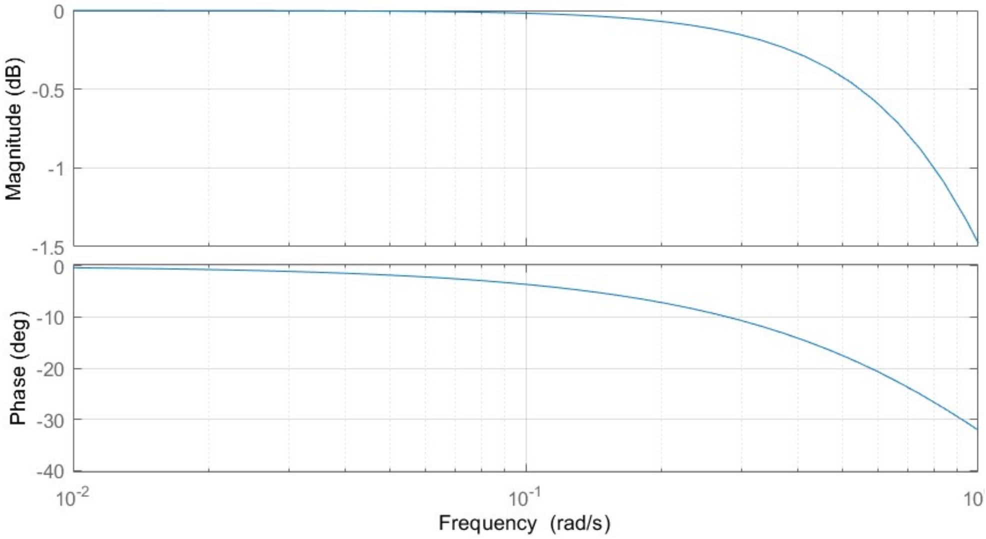

Figure 4.22. Frequency response of the WECS generator's speed measurement filter

4.3.2. Generator-torque controller

The goal of the generator-torque controller is to maximize power capture below the rated operation point, keeping the blade pitch constant at 0. The generator-torque controller is developed according to the following 3 main regions and 2 transitional regions:

2.1.1.1. Region 1

In region 1, the generator desired torque is held constant at zero and no power is extracted from the wind for wind turbine power generation, the wind is used only to accelerate the rotor for the start-up. Region 1 starts from 0 rpm (rad/s) until the cut-in wind speed. According to the wind turbine reference [92], the cut-in wind speed is 3 m/s and the cut in rotor speed is 6.9 rpm (0.723 rad/s). Assuming no change in shaft torsion angle (Φ=0), according to Equation 4.47, at a rotor speed of 6.9 rpm (0.723 rad/s), with a 97:1 gearbox ratio, in ideal conditions (no losses) the generator speed is expected to be:

$$\omega_{cut.in} = N \cdot \Omega_{cut.in} = 97 \cdot 0.723 = 70.089 \cdot rad/s\ (669.3\ rpm) \qquad (4.112)$$

where:
$\Omega_{cut.in}$=0.723 [rad/s] is the rotor angular velocity at cut-in wind speed;
$\omega_{cut.in}$=70.089 [rad/s] is the generator angular velocity at cut-in wind speed;
N= 97 [-] is the gear ratio.

Region 1 can be defined by the following equation, where the generator desired torque is 0 and the speed ranges between 0 rpm (0 rad/s) and generator speed at cut-in wind speed (669.3 rpm = 70.089 rad/s).

$$M_{gen.region1} = 0, \qquad 0 \le \omega_{region1} \le \omega_{cut.in} \ \ or \ \ v_{rot} > v_{cutout} \qquad (4.113)$$

where:
v_{rot} [m/s] is the average wind speed over the rotor;
v_{cutout}=25 [m/s] is the cutout wind speed over the rotor;
$M_{gen.region1}$=0 [Nm] is the generator torque in region 1;
$\Omega_{cut.in}$=0.723 [rad/s] is the rotor angular velocity at cut-in wind speed;
$\omega_{cut.in}$=70.089 [rad/s] is the generator angular velocity at cut-in wind speed;
$\omega_{region1}$ is the generator angular velocity at in region 1.

2.1.1.2. Region 2

In region 2, the generator torque is proportional to the square of the filtered generator speed in order to maintain a constant (optimal) tip-speed ratio. Region 2 starts at a filtered generator speed of 30% above region 1, at 870.09 rpm (91.116 rad/s)[3].

$$\omega_{optimal} = 130\% \cdot \omega_{cut.in} \qquad (4.114)$$

where:
$\omega_{cut.in}$=70.089 [rad/s] is the generator angular velocity at cut-in wind speed;
$\omega_{optimal}$=91.116 [rad/s] is the generator angular velocity at peak tip speed ratio;

---

[3] *130% x 669.3 rpm = 870.09 rpm (130% x 70.089 rad/s=91.116 rad/s).*

From the power coefficient look-up table (Figure 4.23.), as it can be seen in the Figure 4.23., when the rotor-collective blade-pitch angle is 0°, the peak value is 0.4851, occurring at an optimal tip-speed ratio of 7.5.

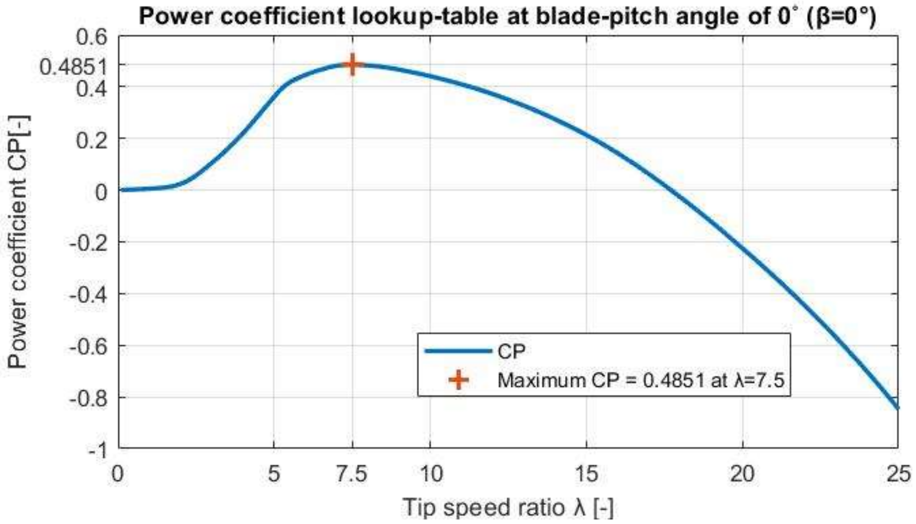

Figure 4.23. Power coefficient look-up table at blade-pitch angle of 0°

Assuming no change in shaft torsion angle ($\dot{\Phi}$=0), according to Equation 4.47, at a generator speed of 870.09 rpm (91.116 rad/s), in ideal conditions (no losses) the rotor speed is expected to be:

$$\Omega_{optimal} = \frac{1}{N} \cdot \omega_{optimal} = 0.939 \cdot rad/s\ (8.97\ rpm) \tag{4.115}$$

where:
N= 97 [-] is the gear ratio.
$\Omega_{optimal}$=0.939 [rad/s] is the rotor angular velocity at peak tip speed ratio;
$\omega_{optimal}$=91.116 [rad/s] is the generator angular velocity at peak tip speed ratio;

From the tip speed ratio Equation 4.2 and the wind speed at the rotor it is:

$$v_{rot.optimal} = \frac{R \cdot \Omega}{\lambda_{peak}} = \frac{R \cdot \omega}{\lambda_{peak} \cdot N} \tag{4.116}$$

where:
$v_{rot.optimal}$ is the average wind speed over the rotor at peak tip speed ratio;
R=63 [m] is the rotor radius;
N= 97 [-] is the gear ratio;
Ω [rad/s] is the rotor angular velocity;
ω [rad/s] is the generator's angular velocity;
λ_{preak}=7.5 [-] is the tip speed ratio at power coefficient peak value when pitch angle=0°.

The optimal generator torque is equaled to rotor torque, Equation 4.5:

$$M_{gen.optimal} = \frac{1}{2} \cdot {v_{rot}}^{3} \cdot \rho \cdot \pi \cdot R^{2} \cdot Cp_{peak} \cdot \omega^{-1}$$

$$M_{gen.optimal} = \frac{1}{2} \cdot \left(\frac{R \cdot \omega}{\lambda_{peak} \cdot N}\right)^{3} \cdot \rho \cdot \pi \cdot R^{2} \cdot Cp_{peak} \cdot \omega^{-1}$$

$$M_{gen.optimal} = \frac{1}{2} \cdot \frac{R^{3} \cdot (\omega)^{3}}{\left(\lambda_{peak}\right)^{3} \cdot N^{3}} \cdot \rho \cdot \pi \cdot R^{2} \cdot Cp_{peak} \cdot \omega^{-1}$$

$$M_{gen.optimal} = \frac{1}{2} \cdot \frac{R^{5} \cdot \omega^{2}}{\left(\lambda_{peak}\right)^{3} \cdot N^{3}} \cdot \rho \cdot \pi \cdot Cp_{peak}$$

$$M_{gen.optimal} = \left(\frac{1}{2} \cdot \frac{R^{5}}{\left(\lambda_{peak}\right)^{3} \cdot N^{3}} \cdot \rho \cdot \pi \cdot Cp_{peak}\right) \cdot \omega^{2}$$

The optimal generator torque is proportional to the square of the filtered generator speed in order to maintain a constant (optimal) tip-speed ratio.

$$M_{gen.optimal} = k \cdot \omega^{2} \qquad \text{with} \qquad k = \frac{1}{2} \cdot \frac{R^{5}}{\left(\lambda_{peak}\right)^{3} \cdot N^{3}} \cdot \rho \cdot \pi \cdot Cp_{peak} \qquad (4.117)$$

where:
$M_{gen.optimal}$ [Nm] *is the optimal generator torque;*
k= 2.402242643637481 [s^2/rad^2] is the optimal constant;
v_{rot} is the average wind speed over the rotor;
ω [rad/s] is the generator angular velocity at peak tip speed ratio;
ρ=1.2 [kg/m3] is the air density;
Cp_{peak}=0.4851 is the power coefficient peak value when pitch angle=0°;
λ_{preak}=7.5 [-] is the tip speed ratio at power coefficient peak value when pitch angle=0°;
R=63 [m] is the rotor radius and N= 97 [-] is the gear ratio.

Desired generator torque in region 2 is defined by the optimal generator torque equation:

$$M_{gen.region2} = k \cdot \left(\omega_{region2}\right)^{2}, \qquad \omega_{optimal} \leq \omega_{region2} \qquad (4.118)$$

where:
k= 2.402242643637481 s^2/rad^2 is the optimal constant;
$M_{gen.region2}$ [Nm] is the generator torque in region 2;
$\omega_{region2}$ is the generator angular velocity at in region 2;
$\omega_{optimal}$=91.116 [rad/s] is the generator angular velocity at peak tip speed ratio.

2.1.1.3. Region 3

Region 3, begins when the rotor reached the rated speed of 12.1 rpm (1.267 rad/s) or the demanded power is less than rated power ($P_{dem} \leq P_{gen.rated}$). Considering no change in shaft torsion angle (Φ=0), according to Equation 4.47, in ideal conditions the generator rated speed is:

$$\omega_{rated} = N \cdot \Omega_{rated} = 122.91 \cdot rad/s\ (1173.7\ rpm) \qquad (4.119)$$

where:
Ω_{rated}=1.267 [rad/s] is the rated rotor angular velocity;
ω_{rated}=122.91 [rad/s] is the rated generator angular velocity and
N= 97 [-] is the gear ratio.
The rated generator torque is calculated using Equation 4.60:

$$M_{gen.rated} = \frac{P_{gen.rated}}{\omega_{rated} \cdot \eta_{gen}} = \frac{P_{gen.rated}}{N \cdot \Omega_{rated} \cdot \eta_{gen}} = 43093.552\ N \cdot m \qquad (4.120)$$

where:
Ω_{rated}=1.267 [rad/s] is the rated rotor angular velocity;
ω_{rated}=122.91 [rad/s] is the rated generator angular velocity;
N= 97 [-] is the gear ratio;
$P_{gen.rated}$= 5 [MW] is the rated generator power;
η_{gen}=94.4 [%] is the rated generator efficiency;
$M_{gen.rated}$= 43095.552 [Nm] is the rated generator torque.

In region 3, the generator power has to be held constant at its rated value, so the generator torque is calculated using Equation 4.60:

$$M_{gen.region3} = \frac{P_{gen.rated}}{\omega_{region3} \cdot \eta_{gen}}, \qquad \omega_{region3} \geq \omega_{rated} \qquad (4.121)$$

where:
$M_{gen.reagion3}$ [Nm] is the generator torque in region 3;
$P_{gen.rated}$= 5 [MW] is the rated generator power;
η_{gen}=94.4 [%] is the rated generator efficiency;
$\omega_{reagion3}$ is the generator angular velocity at in region 3;
ω_{rated}=122.91 [rad/s] is the rated generator angular velocity.

2.1.1.4. Region 1½

Region 1½, is the start-up region and is used to place a lower limit on the generator speed to limit the wind turbine's operational speed range. In the start-up region, the filtered generator speed ranges within 30% above region 1, between 669.3 rpm (70.089 rad/s) and 870.09 rpm (91.116 rad/s)[4]. This region offers a linear transition between region 1 (last generator speed where the torque is 0) and region 2 (30% above region 1, where the generator starts maintaining a constant optimal tip-speed ratio). The desired generator torque, in region 1½, has the following form:

$$M_{gen.region1.1/2} = a_{1.1/2} \cdot \omega_{1.1/2} + b_{region1.1/2} \qquad (4.122)$$

when

---

[4] *130% x 669.3 rpm = 870.09 rpm (130% x 70.089 rad/s=91.116 rad/s).*

$$\omega_{cut.in} \leq \omega_{region1.1/2} \leq \omega_{optimal}$$

where:
$M_{gen.reagion1.1/2}$ [Nm] is the generator torque in region 1½;
$\omega_{reagion1.1/2}$ is the generator angular velocity in region 1½;
$a_{1.1/2}$ is the slope for region 1½ linear equation;
$b_{1.1/2}$ is the y-intercept for region 1½ linear equation;
$\omega_{cut.in}$=70.089 [rad/s] is the generator angular velocity at cut-in wind speed;
$\omega_{optimal}$=91.116 [rad/s] is the generator angular velocity at optimal tip speed ratio.
As region 1½ is an interpolation linear function between regions 1 and 2, the desired generator torque at cut-in filtered generator speed ($\omega_{\text{reagion1.1/2}}$= $\omega_{\text{cut.in}}$) is 0, Equation 4.112:

$$\begin{gathered} M_{gen.region1.1/2} = M_{gen.region1} \text{ when } \omega_{region1.1/2} = \omega_{cut.in} \\ a_{1.1/2} \cdot \omega_{cut.in} + b_{1.1/2} = 0 \end{gathered} \qquad (4.123)$$

where:
$M_{gen.reagion1}$=0 [Nm] is the generator torque in region 1;
$M_{gen.reagion1.1/2}$ [Nm] is the generator torque in region 1½;
$\omega_{cut.in}$=70.089 [rad/s] is the generator angular velocity at cut-in wind speed;
$\omega_{reagion1.1/2}$ is the generator angular velocity in region 1½;
$a_{1.1/2}$ is the slope for region 1½ linear equation;
$b_{1.1/2}$ is the y-intercept for region 1½ linear equation.

Rearranging Equation 4.123, the y-intercept for region 1½ linear equation can be expressed as:

$$b_{1.1/2} = -\, a_{1.1/2} \cdot \omega_{cut.in} \qquad (4.124)$$

where:
$\omega_{cut.in}$=70.089 [rad/s] is the generator angular velocity at cut-in wind speed;
$a_{1.1/2}$ is the slope for region 1½ linear equation;
$b_{1.1/2}$ is the y-intercept for region 1½ linear equation.

As region 1½ is an interpolation linear function between regions 1 and 2, the desired generator torque at optimal filtered generator speed ($\omega_{reagion1.1/2}$= $\omega_{optimal}$) has the same form as the optimal generator torque, Equation 4.118:

$$\begin{gathered} M_{gen.region1.1/2} = M_{gen.region2} \text{ when } \omega_{region1.1/2} = \omega_{optimal} \\ a_{1.1/2} \cdot \omega_{optimal} + b_{1.1/2} = k \cdot \left(\omega_{optimal}\right)^2 \end{gathered} \qquad (4.125)$$

where:
$M_{gen.reagion1.1/2}$ [Nm] is the generator torque in region 1½;
$M_{gen.reagion2}$ [Nm] is the generator torque in region 2;
$\omega_{reagion1.1/2}$ is the generator angular velocity at in region 1½;
$a_{1.1/2}$ is the slope for region 1½ linear equation;
$b_{1.1/2}$ is the y-intercept for region 1½ linear equation;
k= 2.402242643637481 [s^2/rad^2] is the optimal constant;
$\omega_{optimal}$=91.116 [rad/s] is the generator angular velocity at peak tip speed ratio.

Substituting the y-intercept for region 1½ linear equation from Equation 4.124 and optimal generator speed from Equation 4.118, Equation 4.105 becomes:

$$a_{1.1/2} \cdot 1.3 \cdot \omega_{cut.in} - a_{1.1/2} \cdot \omega_{cut.in} = k \cdot (1.3 \cdot \omega_{cut.in})^2 \tag{4.126}$$

where:

$a_{1.1/2}$ is the slope for region 1½ linear equation;

k= 2.402242643637481 s^2/rad^2 is the optimal constant;

$\omega_{cut.in}$=70.089 [rad/s] is the generator angular velocity at cut-in wind speed.

From Equation 4.126, the slope for region 1½ linear equation is calculated as:

$$a_{1.1/2} = \frac{k \cdot (1.3 \cdot \omega_{cut.in})^2}{0.3 \cdot \omega_{cut.in}} = 13.533 \cdot \omega_{cut.in} = 948.488 \tag{4.127}$$

where:

$a_{1.1/2}$=948.488 is the slope for region 1½ linear equation;

k= 2.402242643637481 s^2/rad^2 is the optimal constant;

$\omega_{cut.in}$=70.089 [rad/s] is the generator angular velocity at cut-in wind speed.

Substituting the slop for region 1½ linear equation from Equation 4.127 in Equation 4.123, the y-intercept for region 1½ linear equation is calculated as:

$$b_{1.1/2} = -\, a_{1.1/2} \cdot \omega_{cut.in} = -66478.5 \tag{4.128}$$

where:

$\omega_{cut.in}$=70.089 [rad/s] is the generator angular velocity at cut-in wind speed;

$a_{1.1/2}$=948.488 is the slope for region 1½ linear equation;

$b_{1.1/2}$=-66478.5 is the y-intercept for region 1½ linear equation.

2.1.1.5. Region 2½

Region 2½, is defined by linear interpolation between region 2 and region 3, and has a slope corresponding to the slope of an induction machine. The synchronous speed of the wind turbine generator is calculated according to [80]:

$$\omega_{ss} = \frac{60 \cdot f_s}{p_{wtgenerator}} = 1000\, rpm\ (104.72\, rad/s) \tag{4.129}$$

where:

ω_{ss}=104.72 [rad/s] is the generator stator synchronous speed;

f_s=50 [Hz] is the grid frequency of the balanced three phases;

$p_{wtgenerator}$=3 [pairs of poles] is the generator pairs of poles (6 poles).

The generator-slip percentage in region 2½ is considered 10% according to reference [86]. The generator mechanical rotational speed at the generator stator synchronous speed is calculated using the equation [87]:

$$s_{wtgenerator} = \frac{\omega_{ss} - \omega_{ms}}{\omega_{ss}} \tag{4.130}$$

where:

ω_{ss}=104.72 [rad/s] is the generator stator synchronous speed;

ω_{ms} [rad/s] is the generator rotor mechanical speed at synchronous stator speed;

$s_{wtgenerator}$=-10 [%] is the generator slip in region 2½.

Rearranging Equation 4.129, the generator rotor mechanical speed is calculated:

$$\omega_{ms} = \left(1 - s_{wtgenerator}\right) \cdot \omega_{ss} = 1100\, rpm\ (115.192\, rad/s) \tag{4.131}$$

where:
ω_{ss}=104.72 [rad/s] is the generator stator synchronous speed;
$s_{wtgenerator}$=-10[%] is the generator slip in region 2½;
ω_{ms}=115.192 [rad/s] is the generator rotor mechanical speed at synchronous stator speed.

The desired generator torque, in region 2½, has the following form:

$$M_{gen.region2.1/2} = a_{2.1/2} \cdot \omega_{region2.1/2} + b_{2.1/2}$$
$$\text{when} \qquad (4.132)$$
$$\omega_{ms} \leq \omega_{region2.1/2} \leq \omega_{rated}$$

where:
$M_{gen.region2.1/2}$ [Nm] is the generator torque in region 2½;
$\omega_{region2.1/2}$ is the generator angular velocity in region 2½;
$a_{2.1/2}$ is the slope for region 2½ linear equation;
$b_{2.1/2}$ is the y-intercept for region 2½ linear equation;
ω_{rated}=122.91 [rad/s] is the rated generator angular velocity;
ω_{ms}=115.192 [rad/s] is the generator rotor mechanical speed at synchronous stator speed;

As region 2½ is an interpolation linear function between regions 2 and 3, the desired generator torque at synchronous stator speed ($\omega_{reagion2.1/2}= \omega_{ms}$) has the same form as the optimal generator torque, Equation 4.118:

$$M_{gen.region2.1/2} = M_{gen.region2} \quad \text{when} \quad \omega_{region2.1/2} = \omega_{ms}$$
$$a_{2.1/2} \cdot \omega_{ms} + b_{2.1/2} = k \cdot (\omega_{ms})^2 \qquad (4.133)$$

where:
$M_{gen.region2.1/2}$ [Nm] is the generator torque in region 2½;
$M_{gen.region2}$ [Nm] is the generator torque in region 2;
$\omega_{region2.1/2}$ is the generator angular velocity in region 2½;
$a_{2.1/2}$ is the slope for region 2½ linear equation;
$b_{2.1/2}$ is the y-intercept for region 2½ linear equation;
k= 2.402242643637481 s^2/rad^2 is the optimal constant;
ω_{ms}=115.192 [rad/s] is the generator rotor mechanical speed at synchronous stator speed;

Rearranging Equation 4.133, the y-intercept for region 2½ linear equation can be expressed as:

$$b_{2.1/2} = k \cdot (\omega_{ms})^2 - a_{2.1/2} \cdot \omega_{ms} \qquad (4.134)$$

where:
$a_{2.1/2}$ is the slope for region 2½ linear equation;
$b_{2.1/2}$ is the y-intercept for region 2½ linear equation;
k= 2.402242643637481 s^2/rad^2 is the optimal constant;
ω_{ms}=115.192 [rad/s] is the generator rotor mechanical speed at synchronous stator speed;

As region 2½ is an interpolation linear function between regions 2 and 3, at 99% rated filtered generator speed ($\omega_{reagion2.1/2}$= 99% ω_{rated}), the desired generator torque is the rated one, Equation (4.121):

$$M_{gen.region2.1/2} = M_{gen.rated} \quad \text{when} \quad \omega_{region2.1/2} = 99\% \cdot \omega_{rated}$$
$$a_{2.1/2} \cdot 99\% \cdot \omega_{rated} + b_{2.1/2} = M_{gen.rated} \qquad (4.135)$$

where:

$M_{gen.region2.1/2}$ [Nm] is the generator torque in region 2½;
$M_{gen.rated}$= 43095.552 [Nm] is the rated generator torque;
ω_{rated}=122.91 [rad/s] is the rated generator angular velocity;
$a_{2.1/2}$ is the slope for region 2½ linear equation;
$b_{2.1/2}$ is the y-intercept for region 2½ linear equation;

Substituting the y-intercept for region 2½ linear equation from Equation (4.133), Equation (4.135) becomes:

$$a_{2.1/2} \cdot 99\% \cdot \omega_{rated} + k \cdot (\omega_{ms})^2 - a_{2.1/2} \cdot \omega_{ms} = M_{gen.rated} \tag{4.136}$$

where:

$M_{gen.rated}$= 43095.552 [Nm] is the rated generator torque;
ω_{rated}=122.91 [rad/s] is the rated generator angular velocity;
$a_{2.1/2}$ is the slope for region 2½ linear equation;
k= 2.402242643637481 s^2/rad^2 is the optimal constant;
ω_{ms}=115.192 [rad/s] is the generator rotor mechanical speed at synchronous stator speed.

From Equation (4.136), the slope for region 2½ linear equation is calculated as:

$$a_{2.1/2} = \frac{M_{gen.rated} - k \cdot (\omega_{ms})^2}{99\% \cdot \omega_{rated} - \omega_{ms}} = 1728.818 \tag{4.137}$$

where:

$M_{gen.rated}$= 43095.552 [Nm] is the rated generator torque;
ω_{rated}=122.91 [rad/s] is the rated generator angular velocity;
$a_{2.1/2}$=1728.818 [-] is the slope for region 2½ linear equation;
k= 2.402242643637481 s^2/rad^2 is the optimal constant;
ω_{ms}=115.192 [rad/s] is the generator rotor mechanical speed at synchronous stator speed.

Substituting the slop for region 2½ linear equation from Equation 4.133 in Equation (4.135), the y-intercept for region 2½ linear equation is calculated as:

$$b_{2.1/2} = -167269.89 \tag{4.138}$$

Besides smoothing the transitions between the second and the third regions, region 2½ also limits the tip speed (and hence noise emissions) at rated power.

2.1.1.6. Summary of the generator torque controller

Finally, using Equations (4.113, 4.118, 4.121, 4.122, 4.127, 4.128, 4.132, 4.137, 4.138) the generator-torque controller is summarized as [48, 89]:

$$M_{gen.ctr}(\omega_f) = \begin{cases} 0, & \omega_f \le \omega_{cut.in} \;\; or \; v_{rot} > v_{cutout}, & P_{dem} \ge P_{gen.rated} \\ a_{1.1/2} \cdot \omega_f + b_{1.1/2}\,, & \omega_{cut.in} < \omega_f < \omega_{optimal}, & P_{dem} \ge P_{gen.rated} \\ k \cdot (\omega_f)^2, & \omega_{optimal} \le \omega_f \le \omega_{ms}, & P_{dem} \ge P_{gen.rated} \\ a_{2.1/2} \cdot \omega_f + b_{2.1/2}, & \omega_{ms} < \omega_f < \omega_{rated}, & P_{dem} \ge P_{gen.rated} \\ \dfrac{P_{gen.rated}}{\omega_f \cdot \eta_{gen}}, & \omega_f \ge \omega_{rated}, & P_{dem} \le P_{gen.rated} \end{cases} \tag{4.139}$$

where:
v_{rot} [m/s] is the average wind speed over the rotor;
v_{cutout}=25 [m/s] is the cutout wind speed over the rotor;
$M_{gen.ctr}$ [Nm] is the controller desired generator torque;
ω_f [rad/s] is the filtered generator speed;
$a_{1.1/2}$=948.488 is the slope for region 1½ linear equation;
$b_{1.1/2}$=-66478.5 is the y-intercept for region 1½ linear equation.
k= 2.402242643637481 s^2/rad^2 is the optimal constant;
$a_{2.1/2}$=1728.818 [-] is the slope for region 2½ linear equation;
$b_{2.1/2}$=-167269.89 [-] is the y-intercept for region 2½ linear equation;
$P_{gen.rated}$= 5 [MW] is the rated generator power;
P_{dem} [MW] is the demanded power;
η_{gen}=94.4 [%] is the rated generator efficiency;
$\omega_{cut.in}$=70.089 [rad/s] is the generator angular velocity at cut-in wind speed;
$\omega_{optimal}$=91.116 [rad/s] is the generator angular velocity at optimal tip speed ratio.
ω_{rated}=122.91 [rad/s] is the rated generator angular velocity.
ω_{ms}=115.192 [rad/s] is the generator rotor mechanical speed at synchronous stator speed.

In graph from Figure 4.24., it can be seen the controller desired generator torque:

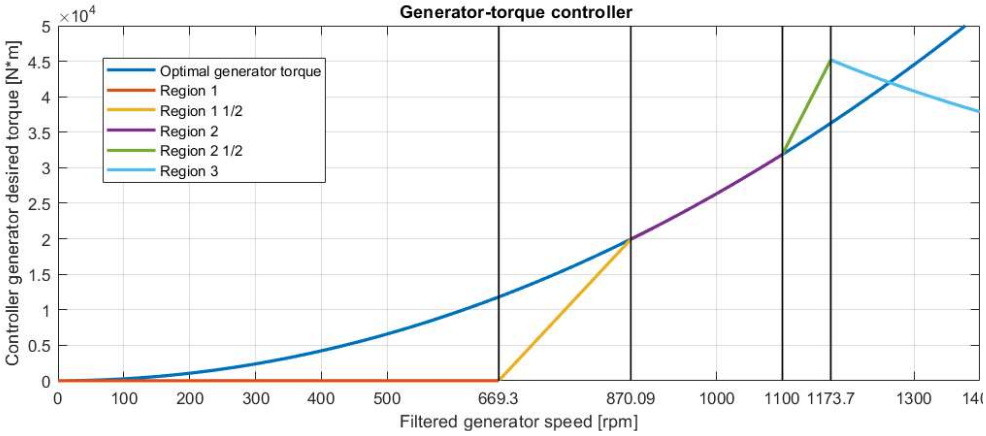

Figure 4.24. Controller desired generator torque [48, 87]

In the present work, because of the high intrinsic structural damping of the drive train, the generator-torque controller doesn't have incorporated a control loop for damping the drivetrain torsional vibration. However, a conditional statement is placed on the generator-torque controller, so that the torque can be computed as if it was in Region 3 whenever the previous blade-pitch-angle command was 1º or greater regardless of the generator speed. This improves the output power quality (fewer power dips below rated) at the expense of short-term overloading of the generator and the gearbox. The maximum torque was saturated to 10% above rated torque (47402.91 Nm) in order to avoid excessive overloading. The generator torque controller has a torque rate limit of 15,000 Nm/s.

In the diagram from Figure 4.25, it can be seen the generator torque controller (Equation 4.139) developed in Simulink [43]:

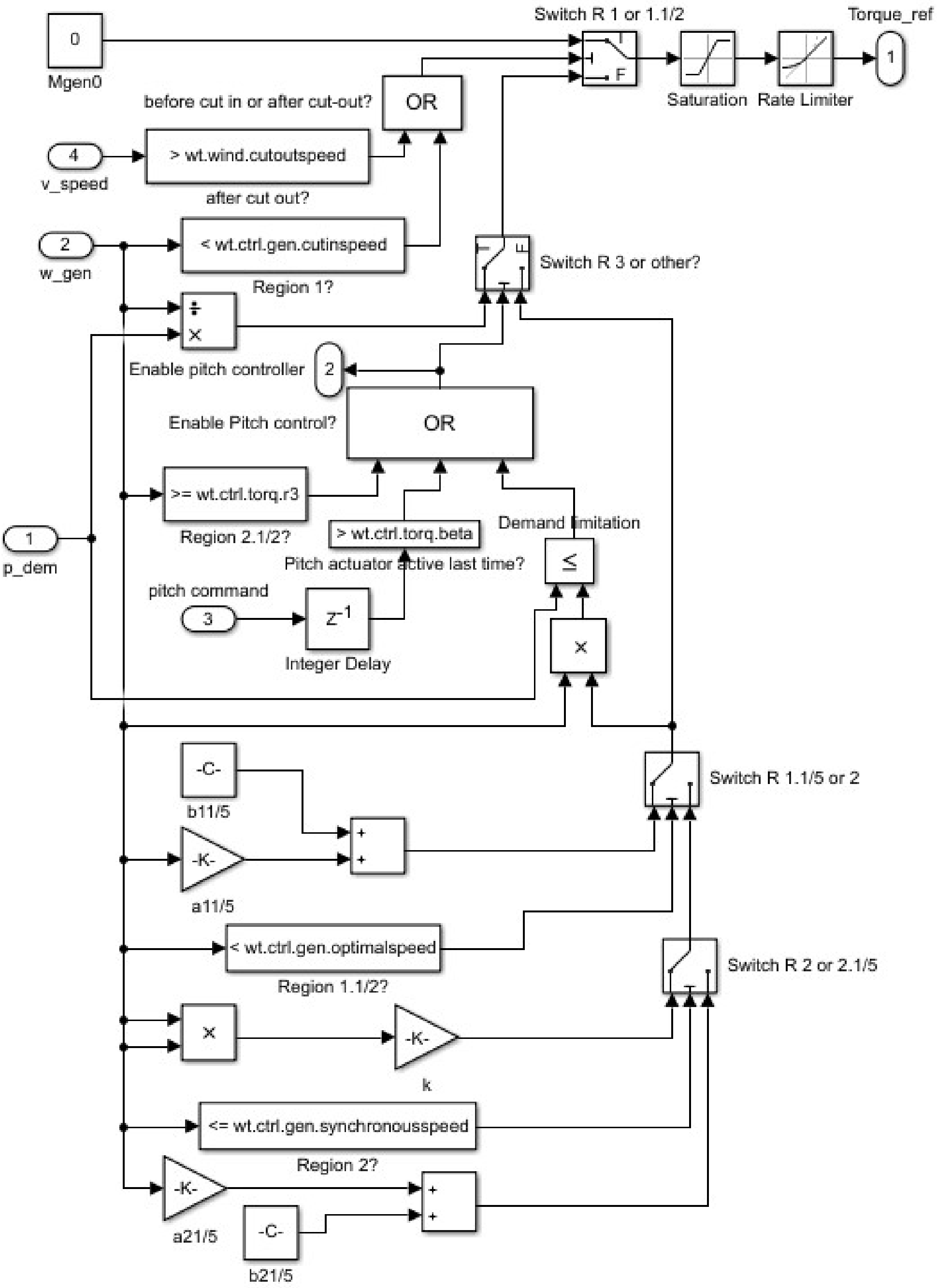

Figure 4.25. Generator-torque controller Simulink Flowchart

4.3.3. Blade-pitch controller

The second controller is a full-span rotor-collective blade-pitch controller and operates only in region 3 of the torque controller (at full load), where the generator power reference is kept constant while the generator speed is controlled indirectly, by directly controlling the rotor speed using the blade pitch angle with a gain scheduled proportional-integral (PI) controller. The blade-pitch controller acts on the speed error between the filtered and the rated generator speed, in order to regulate the generator speed at the rated operation point.

Because the purpose of the blade-pitch controller is to regulate the angular velocity of the generator, the controller is designed considering a SISO (single input, single output) state-space model part of the MIMO (multiple inputs, multiple outputs) state-space model established in Equation 4.98 with β, pitch angle, as input and ω, generator angular velocity, as output:

$$\begin{bmatrix} \dot{\Omega} \\ \dot{\omega} \\ \dot{\Phi} \\ \dot{M}_{gen} \\ \omega \end{bmatrix} = \begin{bmatrix} \frac{b_{mrot} - B_{shaft}}{I_{rot}} & \frac{B_{shaft}}{I_{rot} \cdot N} & -\frac{K_{shaft}}{I_{rot}} & 0 \\ \frac{B_{shaft}}{I_{gen} \cdot N} & -\frac{B_{shaft}}{I_{gen} \cdot N^2} & \frac{K_{shaft}}{I_{gen} \cdot N} & -\frac{1}{I_{gen}} \\ 1 & -\frac{1}{N} & 0 & 0 \\ 0 & -\frac{1}{\tau_{gen} \cdot (\omega_0)^2} & 0 & -\frac{1}{\tau_{gen}} \\ 0 & 1 & 0 & 0 \end{bmatrix} \cdot \begin{bmatrix} \Omega \\ \omega \\ \Phi \\ M_{gen} \end{bmatrix} + \begin{bmatrix} \frac{-c_{mrot}}{I_{rot}} \\ 0 \\ 0 \\ 0 \\ 0 \end{bmatrix} \cdot [\beta] \qquad (4.140)$$

$$\begin{bmatrix} \dot{\Omega} \\ \dot{\omega} \\ \dot{\Phi} \\ \dot{M}_{gen} \\ \omega \end{bmatrix} = \begin{bmatrix} -0.49 & 0.0018008 & -24.48 & 0 \\ 120 & -1.237 & 16747 & -0.001872 \\ 1 & -0.01031 & 0 & 0 \\ 0 & -0.000662 & 0 & -10 \\ 0 & 1 & 0 & 0 \end{bmatrix} \cdot \begin{bmatrix} \Omega \\ \omega \\ \Phi \\ M_{gen} \end{bmatrix} + \begin{bmatrix} 0.01024 \\ 0 \\ 0 \\ 0 \\ 0 \end{bmatrix} \cdot [\beta] \qquad (4.141)$$

with:

$$b_{mrot} = \frac{1}{2} \cdot \pi \cdot \rho \cdot R^2 \cdot v_{rot0}^3 \cdot \left(-\frac{1}{\Omega_0^2} \cdot CP_0 + \frac{1}{\Omega_0} \cdot \frac{R}{v_{rot0}} \cdot \frac{\partial CP(\lambda_0, \beta_0)}{\partial \lambda_0} \right) \qquad (4.142)$$

$$c_{mrot} = \frac{1}{2} \cdot \pi \cdot \rho \cdot R^2 \cdot v_{rot0}^3 \cdot \frac{1}{\Omega_0} \cdot \left(\frac{\partial CP(\lambda_0, \beta_0)}{\partial \beta_0} \right) \qquad (4.143)$$

where:
I_{rot}= 3.5444067 [kg·m^2] is the rotor moment of inertia;
v_{rot} [m/s] is the average wind speed over the rotor;
Φ [rad] is the shaft torsion angle;
$\dot{\Phi}$ [rad/s] is the change in shaft torsion angle;
K_{shaft}= 8.676e+8 [N·m/rad] is the torsion spring constant;
B_{shaft}= 6.215e+6 [N·m·s] is the viscous friction constant;
Ω [rad/s] is the rotor angular velocity;
$\dot{\Omega}$ [rad/s^2] is the change in rotor angular velocity;
β [°]is the pitch angle;
ω [rad/s] is the generator's angular velocity;
$\dot{\omega}$ [rad/s^2] is the change in generator’s angular velocity;
N= 97 [-] is the gear ratio;
I_{gen}= 534.116 [kg·m^2] is the generators’ moment of inertia

M_{gen} [Nm] is the generator torque;
$\dot{M}_{gen}$ [Nm/s] is the change in generator torque;
T_{gen}=0.1 [s] is the generator time constant.
ρ=1.2 [kg/m3] is the air density;
R=63 [m] is the rotor radius;
v_{rot0}=11.4 [m/s] is the rated wind speed;
Ω_0=1.2671 [rad/s] is the rotor angular velocity at the linearization point;
CP_0= 0.387 [-] is the power coefficient at the linearization point;
β_0= 0 [°] is the pitch angle at the linearization point;
λ_0=7 [-] is the tip speed ratio at the linearization point;
M_{gen0}=43093.551 [Nm] is the rated generator torque;
ω_0=122.91 [rad/s] is the rated generator angular velocity;
b_{mrot}=-11006550666.638 is the generator torque sensitivity of rotor speed change;
c_{mrot}=-367632.5798 is the generator torque sensitivity of pitch angle change.
T_{gen}=0.1 [s] is the generator time constant.

The SISO state space model with pitch angle as input and generator speed as output, Equation 4.141 is transformed to the following transfer function, using Laplace transform:

$$H_{wt}(z) = \frac{y_{wt}(z)}{u_{wt}(z)} = \frac{1.229 \cdot z^2 + 183.8 \cdot z + 1715}{z^4 + 11.73 \cdot z^3 + 214.8 \cdot z^2 + 2029 \cdot z + 543.2} \tag{4.144}$$

where:
H_{wt}(z) [-] is the transfer function;
u_{wt}(z) [°] is the input of the transfer function (β pitch angle);
y_{wt}(z) [rad/s] is the output of the transfer function (ω generator angular velocity);
z=0.0125 [s] is the sampling time.

The bode diagram from Figure 4.26, representing the transfer function from β pitch angle to ω generator angular velocity, shows that the minimum stability gain margin is 3.37 dB at 0 [rad/s] and the minimum stability phase margin is -110° at 175 [rad/s]:

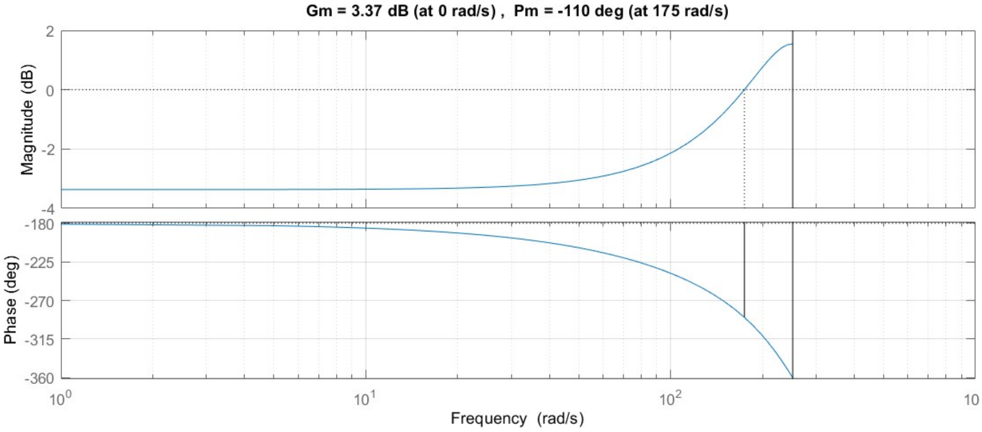

Figure 4.26. Bode diagram of the WECS transfer function from pitch angle to generator angular velocity

In the pole-zero map from Figure 4.27., are represented the poles and zeros of the transfer function (Equation 4.144). From the poles position, all the poles are in Left Half Plane (LHP), it can be seen that the represented model of the system is stable.

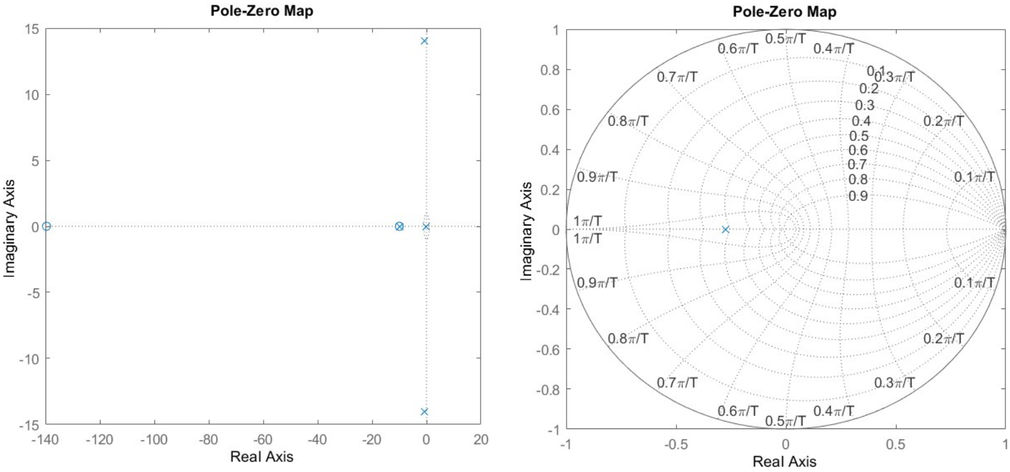

Figure 4.27. Pole-zero map of the wind turbine transfer function from pitch angle to generator angular velocity (a,b)

Zeros:	Poles:
-139.6040	-0.7255 +14.0210 i
-10	-0.7255 -14.0210 i
	-10.0000
	-0.2756

Combining the blade pitch controller with K_P and K_I, the proportional gain and integral time constant in a standard negative feedback loop with the linearized state-space model at rated operation point, from Equation 4.141, results in the following closed-loop equation:

$$\beta_{ref} = Kp_{rated} \cdot \omega_{err} + Ki_{rated} \cdot \int \omega_{err} \tag{4.145}$$

where:
β_{ref} [°] is the reference pitch angle;
Kp_{rated} [-]is the pitch controller proportional gain at rated operation point;
Ki_{rated} [-]is the pitch controller integral time constant at rated operation point;
$\omega_{err} = \omega_{rated} - \omega$ [rad/s] is the difference between rated and actual generator angular velocity.

Solving the closed-loop equation at rated operation, Equation 4.145 with the help of Matlab [43] a negative proportional gain K_P= -1.474 that adds a negative damping, and an integral time constant K_I = -0.026 that adds restoring are identified.

Due to the reason that the aerodynamic power has to be held constant in region 3, by pitching the blade, the sensitivity of aerodynamic torque to rotor-collective blade pitch varies considerably in this region. Due to this reason, constant PI gains are not adequate for effective speed control, the reason why a gain correction has to be implemented in the blade pitching PI controller.

For the synthesis of the PI regulator used to control the blade-pitch angle, an improved version is proposed in which the proportional gain (K_p) and the integral time (K_i) are scheduled using the GK(β) function:

$$Kp(\beta) = Kp_{rated} \cdot GK(\beta) \tag{4.146}$$

$$Ki(\beta) = Ki_{rated} \cdot GK(\beta) \tag{4.147}$$

where:
β [˚] is the pitch angle;
$GK(\beta)$ [-] is the linear gain correction factor, based on the blade-pitch angle;
$Kp(\beta)$ [-]is the controller proportional gain at β pitch angle;
$Ki(\beta)$ [-]is the controller integral time constant at β pitch angle;
Kp_{rated} [-]is the base pitch controller proportional gain at rated operation point;
Ki_{rated} [-]is the pitch controller integral time constant at rated operation point.

According to reference [93], the gain correction factor is obtained based on the current value of the WT blade-pitch angle (β) and the value of the blade-pitch angle where the WT rotor torque has doubled (βk):

$$GK(\beta) = \frac{1}{1 + \dfrac{\beta}{\beta_k}} \tag{4.148}$$

where:
$GK(\beta)$ [-] is the linear gain correction factor, based on the blade-pitch angle;
β [rad] is the current value of the WT blade-pitch angle;
β_k [rad] is the value of the blade-pitch angle where the WT rotor torque has doubled.

To determine the pitch angle that doubles the WT rotor, Equation 4.26 is considered, in which the wind speed variation is ignored and the angular velocity is considered to be held constant at the rated point:

$$2 \cdot M_{rot0} = M_{rot0} + \left.\frac{\partial M_{rot}}{\partial \beta}\right|_{(v_{rot0},\Omega_0,\beta_0)} \cdot (\beta_0 - \beta_k) \tag{4.149}$$

where:
M_{rot0}=4268603.528 [Nm] is the rotor torque at the linearization point;
β_0= 0 [rad/s] is the rated pitch angle;
β_k [rad/s] is the value of the blade-pitch angle where the WT rotor torque has doubled;
$\left.\frac{\partial M_{rot}}{\partial \beta}\right|_{(v_{rot0},\Omega_0,\beta_0)}$=-367632.5798 [Nm/°] is the blade-pitch sensitivity Equation 4.29.

Resulting, that the blade pitch angle that doubles the WT rotor torque is:

$$\beta_k = \beta_0 - \frac{M_{rot0}}{\left.\frac{\partial M_{rot}}{\partial \beta}\right|_{(v_{rot0},\Omega_0,\beta_0)}} = 0.2065\ [rad/s\ ] \tag{4.150}$$

where:
M_{rot0}=4268603.528 [Nm] is the rotor torque at the linearization point;
β_0= 0 [rad/s] is the rated pitch angle;
β_k=0.2056 [rad/s] is the pitch angle where the pitch sensitivity has doubled;
$\left.\frac{\partial M_{rot}}{\partial \beta}\right|_{(v_{rot0},\Omega_0,\beta_0)}$=-367632.5798 [Nm/°] is the blade-pitch sensitivity.

In the graphs from Figure 4.28., 4.29. and 4.30., the gain correction, proportional gain and integral time constant are plotted according to the blade-pitch angle variation:

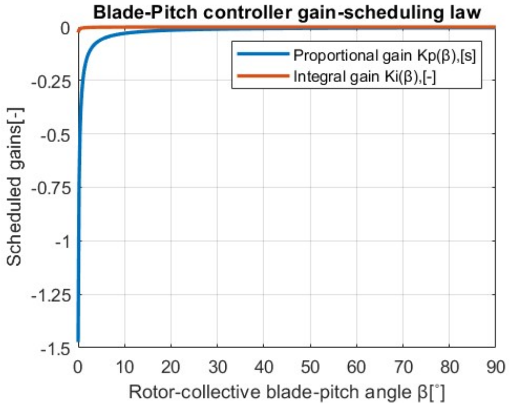

Figure 4.28. Wind turbine blade-pitch controller gain-scheduling law [48]

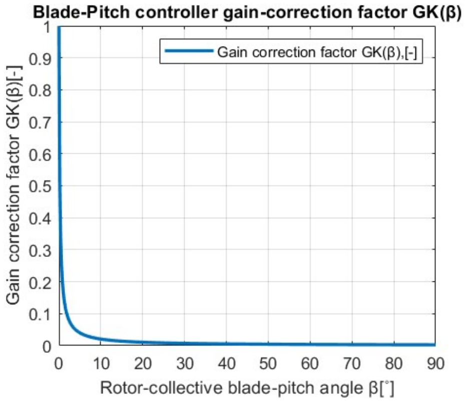

Figure 4.29. Wind turbine blade-pitch controller gain-correction factor [48]

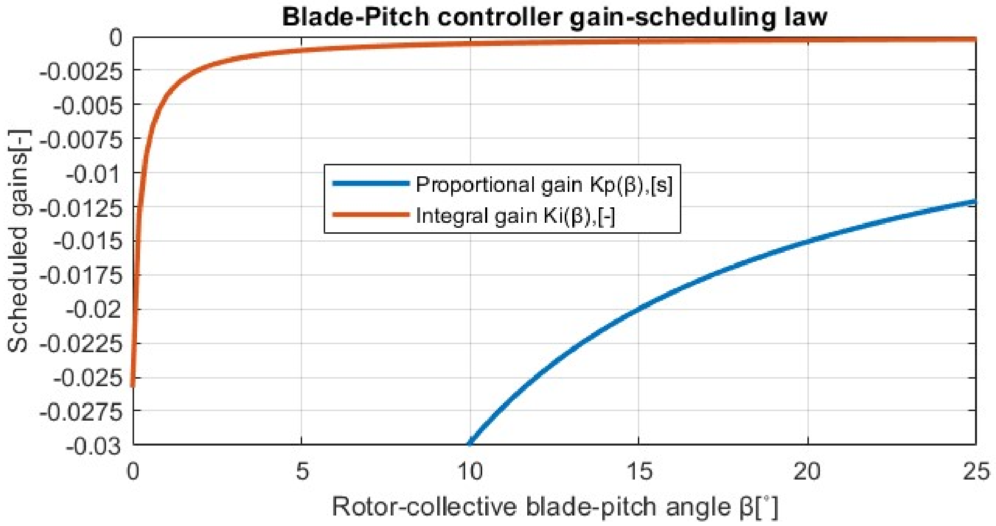

Figure 4.30. Wind turbine blade-pitch controller gain-scheduling low [48]

By combining the closed-loop Equation 4.145 with the linear gain correction Equation 4.150, the final closed-loop equation is obtained [87]:

$$\beta_{ref} = \frac{\beta_k}{\beta_k + \beta_{ref}} \cdot Kp_{rated} \cdot \omega_{err} + \frac{\beta_k}{\beta_k + \beta_{ref}} \cdot Ki_{rated} \cdot \int \omega_{err} \qquad (4.151)$$

where:
β_{ref} [°] is the reference pitch angle;
β_k=0.2056 [rad/s] is the pitch angle where the pitch sensitivity has doubled;
Kp_{rated} [-]is the pitch controller proportional gain at rated operation point;
Ki_{rated} [-]is the pitch controller integral time constant at rated operation point;
ω_{err}= ω_{rated}- ω [rad/s] is the difference between rated and actual generator angular velocity.

In the blade-pitch controller, there is a conditional statement that sets the upper limit of the blade-pitch angle as reference when the wind speed in front of the rotor reaches the cutout wind speed. The blade-pitch rate limit is set according to the rate limit of the conventional 5-MW General Electric (GE) machine to 8°/s in absolute value. Maximum blade-pitch angle is set to be 90°, representing the fully feathered blade pitch for neutral torque. limit of conventional 5-MW General Electric (GE) machine to 8°/s in absolute value. Minimum blade-pitch angle is set to be -90° in order to be able to derate the power of the wind turbine when the reference power is below rated power. The integral term of the PI controller it is also limited between these values in order to ensure a fast response in the transitions between Regions 2 and 3.

In the diagram from Figure 4.31, it can be seen the blade pitch controller (Equation 4.151) implementation in Simulink [43]:

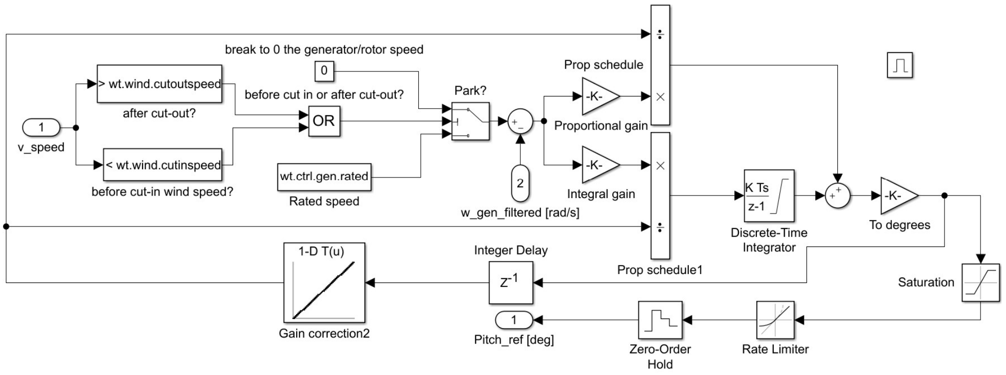

Figure 4.31. Generator-torque controller Simulink Flowchart

4.3.4. DFIG rotor side controller

The vector control of the DFIM is performed in a synchronously rotating d-q frame, in which the d-axis is aligned with the stator flux space vector, as shown in Figure 4.32 [41]. Because the direct rotor current is proportional to the stator reactive power, and the quadrature rotor current is proportional to the torque or active stator power, the rotor voltage can be calculated as a function of rotor currents and stator flux by substituting equations (Equation 4.64 and Equation 4.65) into voltage Equation 4.63 (note that ψ_{qs}=0) [41]:

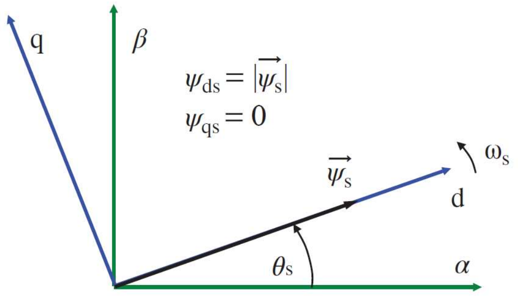

Figure 4.32. Synchronous rotating dq reference frame aligned with the stator flux space vector [41]

$$\begin{aligned} v_{dr} &= R_r \cdot i_{dr} + \sigma \cdot L_r \cdot \frac{di_{dr}}{dt} - \omega_r \cdot \sigma \cdot L_r \cdot i_{qr} + \frac{L_m}{L_s} \cdot \frac{d\left[\overrightarrow{\psi_s}\right]}{dt} \\ v_{qr} &= R_r \cdot i_{qr} + \sigma \cdot L_r \cdot \frac{di_{qr}}{dt} + \omega_r \cdot \sigma \cdot L_r \cdot i_{dr} + \omega_r \cdot \frac{L_m}{L_s} \cdot \frac{d\left[\overrightarrow{\psi_s}\right]}{dt} \end{aligned} \tag{4.152}$$

where:

$\overrightarrow{\psi_s}$ [Vm] is the stator flux vector;
L_m [H] is the mutual inductance;
L_s [H] is the stator inductance;
L_r [H] is the rotor inductance;
ψ_{ds} [Vm] is the stator flux vector d component;
ψ_{qs} [Vm] is the stator flux vector q component;
R_r [Ω] is the rotor resistance;
v_{dr} [V] is the rotor voltage vector d component;
v_{qr} [V] is the rotor voltage vector q component;
i_{dr} [A] is the rotor current vector d component;
i_{qr} [A] is the rotor current vector q component;
ψ_{dr} [Vm] is the rotor flux vector d component;
ψ_{qr} [Vm] is the rotor flux vector q component.

From equation (4.51), by assuming the voltage drop in the stator resistance is very small because the stator is connected directly to the grid at constant AC voltage, the stator flux becomes constant, canceling the derivative term (d|ψ s|/dt=0). By canceling the derivative term in Equation (4.152), the dq rotor currents control is performed by using a regulator for each current component, as shown in Figure 4.34. The rotor voltage and currents are transformed into dq coordinates as the control must be performed in those coordinates. For the stator voltage grid synchronization is used a phase-locked loop (PLL) [41].

The gains for the proportional-integral (PI) regulators for the current loops are calculated in Equation 4.153 according to the second-order system with two poles and a zero developed in reference [41]. As seen in Figure 4.33, the PI regulators employ a compensation of the cross terms and neglect the effect of the voltage source converter and the possible delays in computation or measurements [48, 89].

$$k_p = \frac{2 \cdot 100 \cdot \sigma^2 \cdot (L_r)^2}{R_r} - R_r \qquad k_i = \frac{10000 \cdot \sigma^3 \cdot (L_r)^3}{(R_r)^2} \tag{4.153}$$

where:
L_r [H] is the rotor inductance;
R_r [Ω] is the rotor resistance;

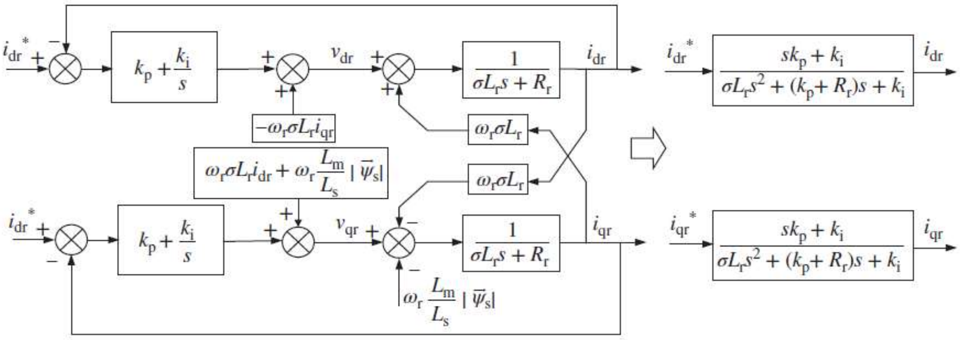

Figure 4.33. Equivalent second-order system of closed-loop current control with PI regulators [41]

By combining the pi regulators with the current control loops and the flux angle calculation, the complete control system is obtained. The electromechanical torque expression in the dq frame can be simplified using reference [41], as the d-axis of the reference frame is aligned with the stator flux space vector:

$$M_{gen} = \frac{3}{2} \cdot p_{wtgenerator} \cdot \frac{L_m}{L_s} \cdot (\psi_{qs} \cdot i_{dr} - \psi_{ds} \cdot i_{dr}) \;=> \\ M_{gen} = -\frac{3}{2} \cdot p_{wtgenerator} \cdot \frac{L_m}{L_s} \cdot |\overrightarrow{\psi_s}| \cdot i_{qr} => M_{gen} = K_T \cdot i_{qr} \tag{4.154}$$

with:

$$K_T = -\frac{3}{2} \cdot p_{wtgenerator} \cdot \frac{L_m}{L_s} \cdot |\overrightarrow{\psi_s}| \tag{4.155}$$

where:
$\overrightarrow{\psi_s}$ [Vm] is the stator flux vector reference to the stator;
i_{dr} [A] is the rotor current vector d component;
i_{qr} [A] is the rotor current vector q component;
ψ_{ds} [Vm] is the stator flux vector d component;
ψ_{qs} [Vm] is the stator flux vector q component;
L_m [H] is the mutual inductance;
L_s [H] is the stator inductance;
L_r [H] is the rotor inductance;

$p_{wtgenerator}$=3 [pairs of poles] is the generator pairs of poles (6 poles).

Figure 4.34, illustrates the complete vector control of the DFIM, where the DFIM simply imposes an electromagnetic torque M_{gen}*, while the speed of the shaft is controlled by other elements.

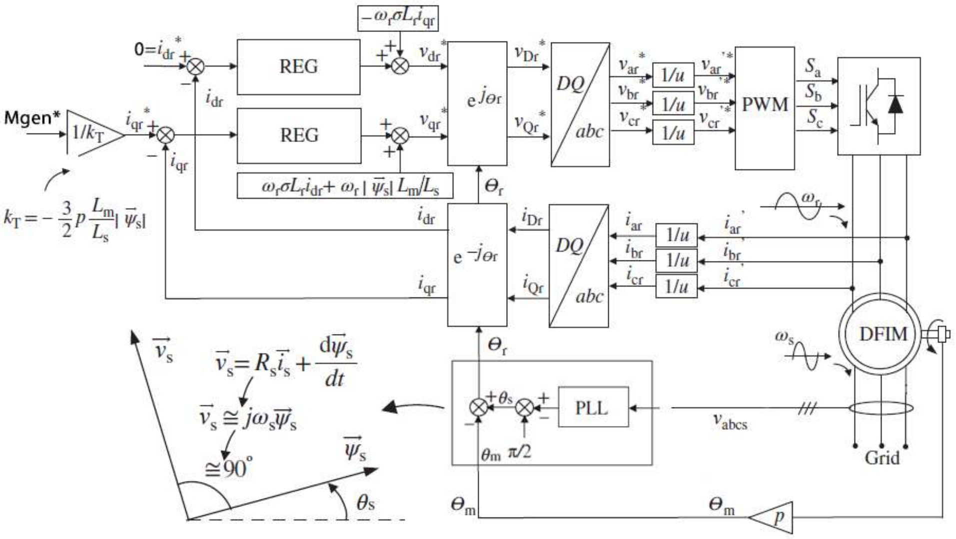

Figure 4.34. DFIM rotor vector control

As can be seen in Figure 4.34, the q rotor current component is proportional to the torque, and because of the iqr, it is possible to control the torque. The i_{dr} current is responsible for reactive power control, *Qs*, as it can be seen in reference [41] in the current work the reference reactive power is set to 0.

In Figure 4.35, it can be seen the DFIM rotor vector control implementation in Simulink [43]:

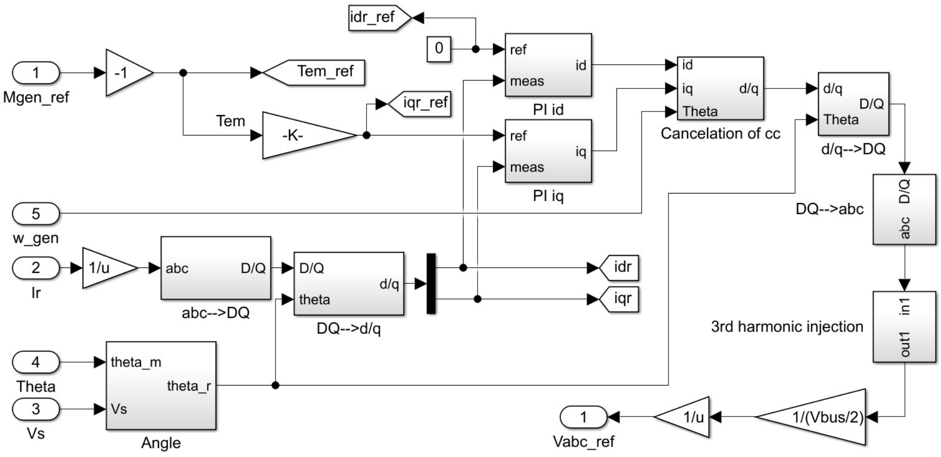

Figure 4.35. DFIM rotor vector control Simulink flow chart

4.3.5. DFIG grid side controller

The grid side converter controls part of the power flow of the DFIM. Part of the power generated by the wind turbine is delivered through the rotor of the DFIM. This power flow that goes through the rotor flows also through the DC link and finally is transmitted by the grid side converter to the grid [87]. In Figure. 4.36, is presented a simplified block diagram of the grid side system including a schematic of its control block diagram [87]:

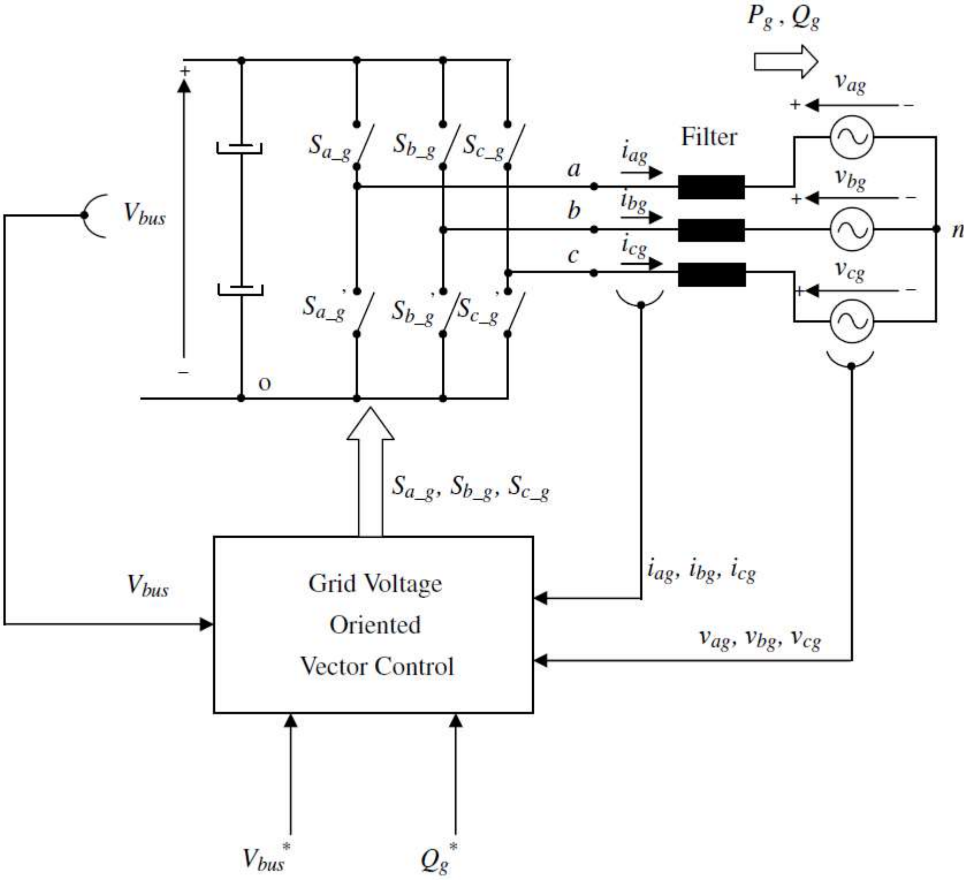

Figure 4.36. Grid side controller schematic [87]

Because the DC link is mainly formed by a capacitor, it is necessary to control the DC bus voltage (*Vbus*) The active power flow through the rotor crosses the DC link and then it is transmitted to the grid. Therefore, by only controlling the *Vbus* variable to a constant value, this active power flow through the converters is ensured, together with a guarantee that both grid and rotor side converters have available the required DC voltage to work properly [87].

In figure 4.37, is presented the grid voltage oriented vector control (GVOVC) block diagram. From the *Vbus* (DC bus voltage) and *Qg* (grid reactive power) references, it creates pulses for the controlled switches Sa_g, Sb_g, and Sc_g, from the abc voltage references for the grid side converter: $v_{af}*$, $v_{bf}*$, and $v_{cf}*$. The abc voltage references are created in dq coordinates ($v_{df}*$, $v_{af}*$), and then transformed to $\alpha\beta$ coordinates ($v_{af}*$, $v_{bf}*$), and finally the abc voltage references are obtained. The dq voltage references ($v_{df}*$, $v_{af}*$) are independently created by the dq current ($i_{dg}*$, $i_{qg}*$) controllers [87]. Meaning, that by modifying v_{df}, i_{dg} is mainly modified, while by modifying v_{qf}, i_{qg} is mainly modified. For better performance in the dynamic responses, in each equation, there is one coupling term considered in the control as a feed-forward term e_{df}, and e_{qf} from the following equations [87]:

$$\begin{aligned} e_{df} &= -\omega_{ss}\cdot L_f\cdot i_{qg} \\ e_{qf} &= -\omega_{ss}\cdot L_f\cdot i_{dg} \end{aligned} \tag{4.156}$$

where:
L_f [H] is the grid side inductive filter;
i_{dg} [A] is the grid current vector d component;
i_{qg} [A] is the grid current vector q component;
ω_{ss}=104.72 [rad/s] is the generator stator synchronous speed.

Note that under ideal conditions, vdg is constant and equal to the grid voltage amplitude.

Because of the alignment between the grid voltage pace vector and the d axis of the rotating reference frame, the current references ($i_{dg}*$, $i_{qg}*$) are totally decoupled from the active and reactive powers. The reason why $i_{dg}*$ control implies Pg control, and $i_{qg}*$ control implies *Qg* control. The constant terms *Pg* and *Qg*, are calculated according to the reference [87]:

$$\begin{aligned} P_g &= \tfrac{3}{2}\cdot v_{dg}\cdot i_{dg} = \tfrac{3}{2}\cdot\left|\overrightarrow{v_g}^{a}\right|\cdot i_{dg} & \qquad K_{Pg} &= \frac{1}{\frac{3}{2}\cdot v_{dg}} \\ Q_g &= -\tfrac{3}{2}\cdot v_{dg}\cdot i_{qg} = -\tfrac{3}{2}\cdot\left|\overrightarrow{v_g}^{a}\right|\cdot i_{qg} & \qquad K_{Qg} &= \frac{1}{-\frac{3}{2}\cdot v_{dg}} \end{aligned} \tag{4.157}$$

where:
i_{dg} [A] is the grid current vector d component;
i_{qg} [A] is the grid current vector q component;
v_{dg} [V] is the grid voltage vector d component;
v_g [V] is the grid voltage;
P_g [-] is the grid power;
Q_g [-] is the grid reactive power;
K_{Pg} [-] is the grid power control constant term;
K_{Qg} [-] is the grid reactive power control constant term;

The power *Pg* reference is created by the *Vbus* regulator. Indirectly, by this loop, the back-to-back converter ensures the active power flow.
For the voltage and the current coordinate transformations, the angle of the grid voltage is needed θ_g. This angle is estimated by a phase locked loop (PLL) as in reference [40][87] (Figure 4.38).

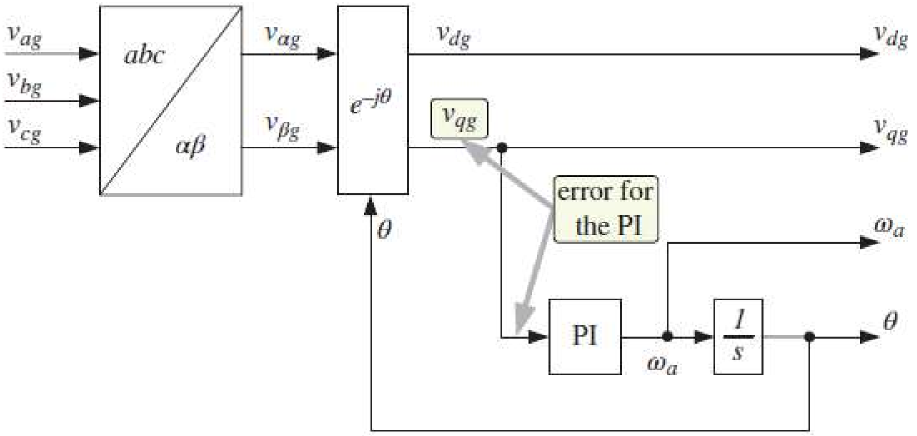

Figure 4.37. Classic PLL structure block diagram [40]

The gains for the proportional-integral (PI) regulators for the current loops are calculated according to the closed-loop current expressions, from reference [40, 48, 89].

$$s^2 \cdot (L_f) + s \cdot (R_f + k_p) + k_i = s^2 + 2 \cdot \xi \cdot \omega_n \cdot s + (\omega_n)^2$$
$$k_{pg} = 2 \cdot L_f \cdot \xi \cdot \omega_n - R_f \tag{4.158}$$
$$k_{ig} = L_f \cdot (\omega_n)^2$$

with

$$\omega_n = 2 \cdot 60 \cdot \pi \tag{4.159}$$

where:
L_f [H] is the grid side filter inductance;
R_f [Ω] is the grid side filter resistance;
ω_n [Hz] system first natural frequency.

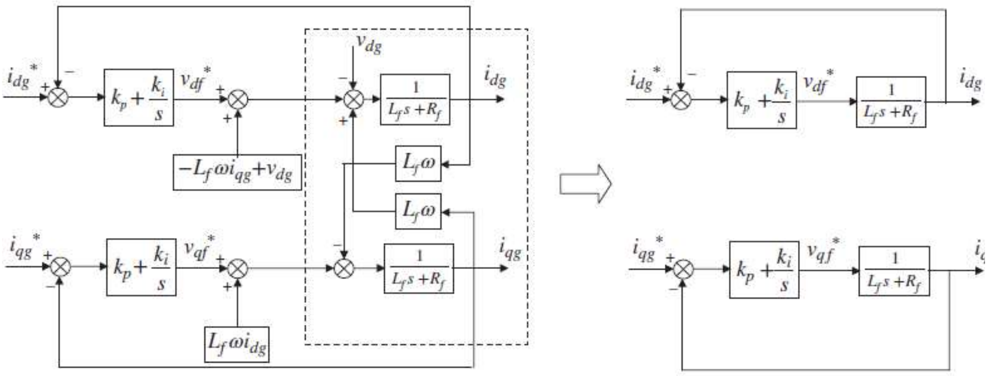

Figure 4.38. Current loops simplified structure for the L filter [40]

Finally, the presented VOVGC presented is designed to control the dc bus voltage and Reactive grid power (*Vbus, Qg*), providing also good dynamic response performance due to its vector control structure [87].

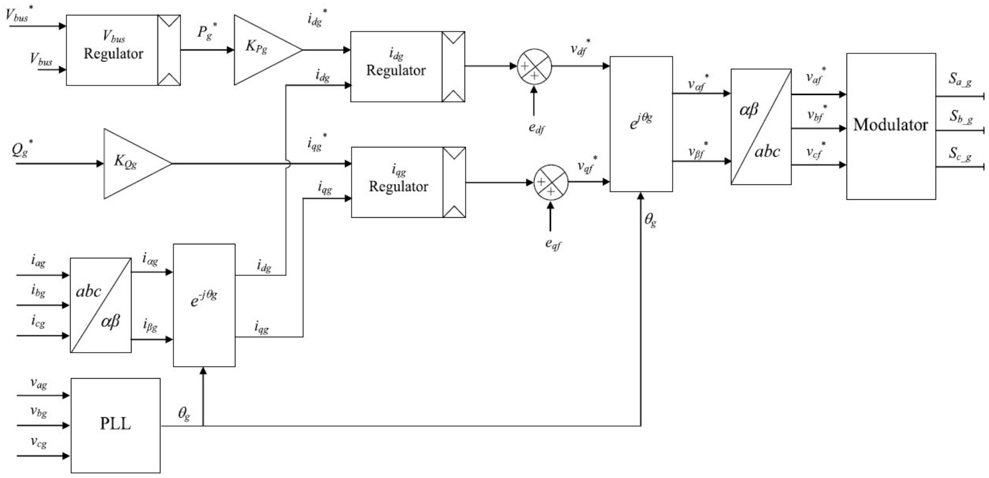

Figure 4.39. Grid voltage-oriented vector control block diagram [87]

In Figure 4.40., it can be seen the grid voltage oriented vector control (GVOVC), implementation in Simulink [43]:

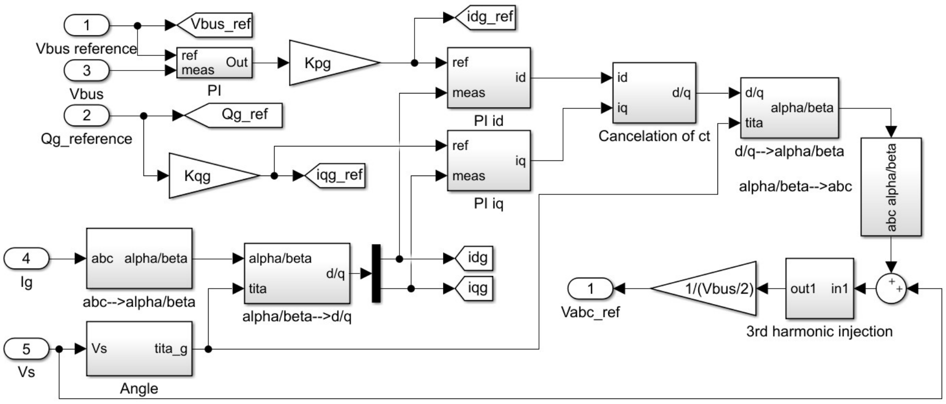

Figure 4.40. Grid voltage-oriented vector control (GVOVC) Simulink flow chart

4.3.6. WECS controller summary

Finally, by combining the generator torque controller, Equation 4.139 and the blade-pitch controller, Equation 4.151 together, is obtained the wind turbine control strategy (control level II) [48, 89]:

$$\begin{matrix} M_{gen.ctr}(\omega_f) \\ \beta_{ref} \end{matrix} = \begin{cases} \begin{cases} M_{gen.ctr}(\omega_f) = \begin{cases} 0, & \omega_f \le \omega_{cut.in} \ \ or\ v_{rot} > v_{cutout} \\ a_{1.1/2} \cdot \omega_f + b_{1.1/2}\,, & \omega_{cut.in} < \omega_f < \omega_{optimal} \\ k \cdot (\omega_f)^2, & \omega_{optimal} \le \omega_f \le \omega_{ms} \\ a_{2.1/2} \cdot \omega_f + b_{2.1/2}, & \omega_{ms} < \omega_f < \omega_{rated} \end{cases} \\ \beta_{ref} = 0° \end{cases} & \begin{matrix} P_{dem} \ge P_{gen.rated} \\ AND \\ \omega_f < \omega_{rated} \end{matrix} \\ \begin{cases} M_{gen.ctr}(\omega_f) = \dfrac{P_{gen.rated}}{\omega_f \cdot \eta_{gen}}, \\ \beta_{ref} = \dfrac{\beta_k}{\beta_k + \beta_{ref}} \cdot Kp_{rated} \cdot \omega_{err} + \dfrac{\beta_k}{\beta_k + \beta_{ref}} \cdot Ki_{rated} \cdot \displaystyle\int \omega_{err}\,, \end{cases} & \begin{matrix} P_{dem} \le P_{gen.rated} \\ OR \\ \omega_f \ge \omega_{rated} \end{matrix} \end{cases} \tag{4.160}$$

where:
v_{rot} [m/s] is the average wind speed over the rotor;
v_{cutout}=25 [m/s] is the cutout wind speed over the rotor;
$M_{gen.ctr}$ [Nm] is the controller desired generator torque;
ω_f [rad/s] is the filtered generator speed;
$a_{1.1/2}$=948.488 [-] is the slope for region 1½ linear equation;
$b_{1.1/2}$=-66478.5 [-] is the y-intercept for region 1½ linear equation.
k= 2.402242643637481 [s^2/rad^2] is the optimal constant;
$a_{2.1/2}$=1728.818 [-] is the slope for region 2½ linear equation;
$b_{2.1/2}$=-167269.89 [-] is the y-intercept for region 2½ linear equation;
$P_{gen.rated}$= 5 [MW] is the rated generator power;
P_{dem} [MW] is the demanded power;
η_{gen}=94.4 [%] is the rated generator efficiency;
$\omega_{cut.in}$=70.089 [rad/s] is the generator angular velocity at cut-in wind speed;
$\omega_{optimal}$=91.116 [rad/s] is the generator angular velocity at optimal tip speed ratio.
ω_{rated}=122.91 [rad/s] is the rated generator angular velocity.
β_{ref} [°] is the reference pitch angle;
β_k=0.2056 [rad] is the pitch angle where the pitch sensitivity has doubled;
Kp_{rated} [-]is the pitch controller proportional gain at rated operation point;
Ki_{rated} [-]is the pitch controller integral time constant at rated operation point;
ω_{ms}=115.192 [rad/s] is the generator rotor mechanical speed at synchronous stator speed;
ω_{err}= ω_{rated}-ω_f [rad/s] is the difference between rated and actual generator angular velocity.

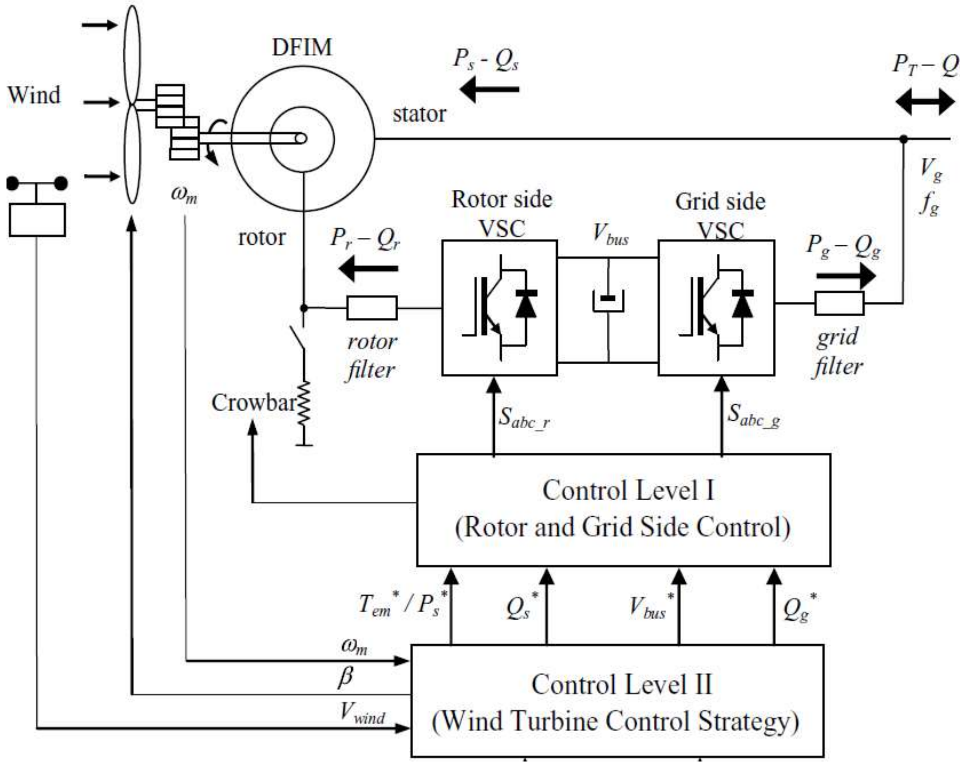

Figure 4.41. WECS controller scheme [87]

In Figure 4.42., it can be seen the full controller, rotor and gride side controller (control level I) and the wind turbine control strategy (control level II) developed in Simulink [43]:

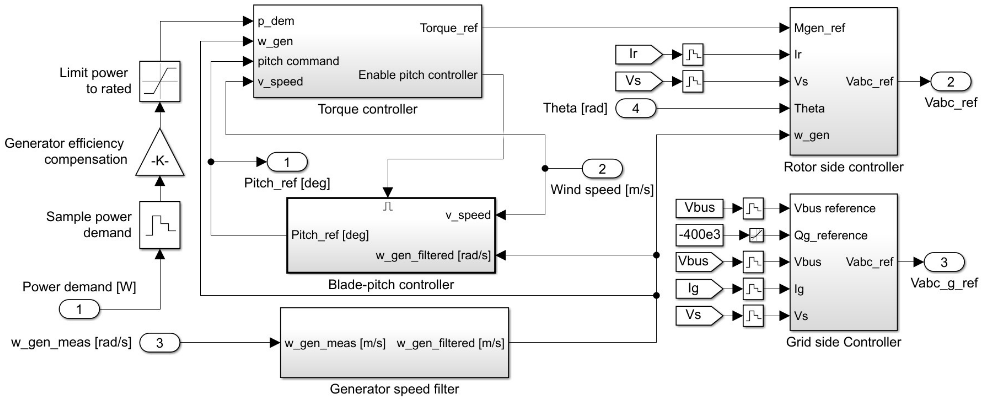

Figure 4.42. WECS controller flow chart in Simulink

In Table 4.2, it can be seen the main parameters of the proposed control strategy, calculated for the 5 MW NREL WECS:

Table 4.2. 5 MW NREL WECS controller main parameters

The corner frequency of the generator angular velocity filter	0.25 Hz
Peak power coefficient	0.4851
Tip-speed ratio at peak power coefficient	7.5
Blade-pitch angle at peak power coefficient	0°
Generator-torque optimal constant	2.402 s2/rad2
Rated generator power	5 MW
Rated generator torque	43095.552 Nm
Cut in generator angular velocity	70.089 rad/s
Optimal generator angular velocity	91.116 rad/s
Generator rotor mechanical speed at synchronous stator speed	115.192 rad/s
rated generator angular velocity.	122.91 rad/s
Generator slip at synchronous stator speed	10%
Minimum Blade-pitch angle for region 3	1°
Maximum generator torque	47402.91 Nm
Maximum generator torque rate	15000 Nm/s
Blade-pitch angle where the pitch sensitivity has doubled	0.2056 rad/s
Proportional gain at 0º blade-pitch angle	-1.474 s
Integral time constant at 0º blade-pitch angle	-0.026
Lower blade-pitch angle limit	0°
Upper blade-pitch angle limit	90°
Maximum blade-pitch angle rate	8°/s
Generator torque reference coefficient K_t	-0.1306
Rotor vector control id currents proportional (P) gain	0.2786
Rotor vector control id currents integral (I) gain	84.5216
Rotor vector control iq currents proportional (P) gain	0.2786
Rotor vector control iq currents integral (I) gain	84.5216
GVOVC DC bus voltage reference coefficient	0.0012
GVOVC reactive power reference coefficient	-0.0012
GVOVC id currents proportional (P) gain	0.3016
GVOVC id currents integral (I) gain	56.8489
GVOVC iq currents proportional (P) gain	0.3016
GVOVC iq currents integral (I) gain	56.8489

4.4. WECS simulations

Combining the WECS controller presented in the third subchapter (***4.3. Controlling a WECS***), with the nonlinear model of the NREL 5 MW wind turbine presented in the second subchapter (***4.2. WECS modelling***), a simulator was developed in Simulink [43].

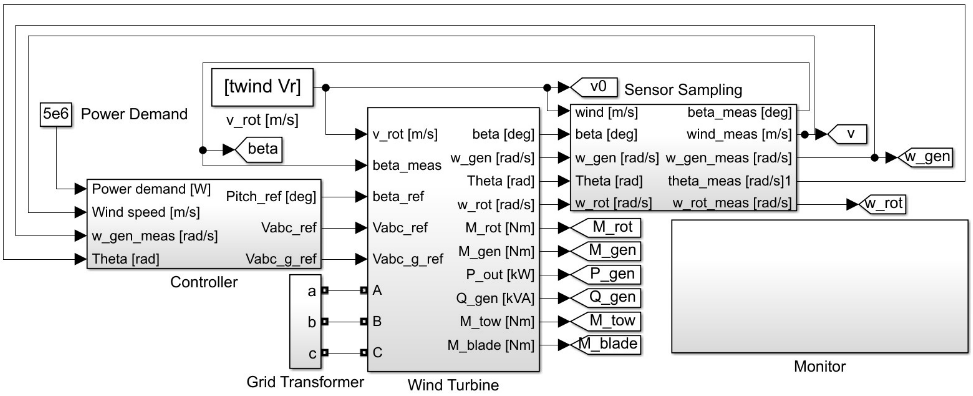

Figure 4.43. WECS simulator flow chart in Simulink

Using the developed WECS simulator, four simulations were executed in order to analyze and evaluate the response of the controller developed in the third subchapter (4.3. Controlling a WECS) to different scenarios: the response of the rated and derated WECS to a wind speed data covering all the operating range (from 0 to 30 m/s), and to a real turbulent wind speed time series covering the operation at full load (11 to 20 m/s) in one simulation, and covering the operation at partial load (region 1, 1 ½, 2, 2 ½) in another simulation.

4.4.1. *Response of rated WECS*

In the first simulation, is presented the response of the WECS to a wind speed ramp from 0 to 30 m/s in 3 minutes (180 seconds). This simulation was executed in order to see the response of the WECS at each wind speed of its operating range when the requested power is the rated power.

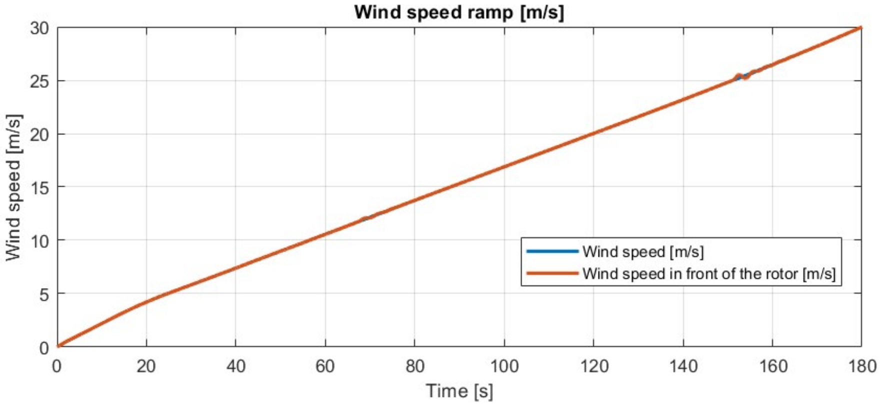

Figure 4.44. Wind time series covering all the operating range

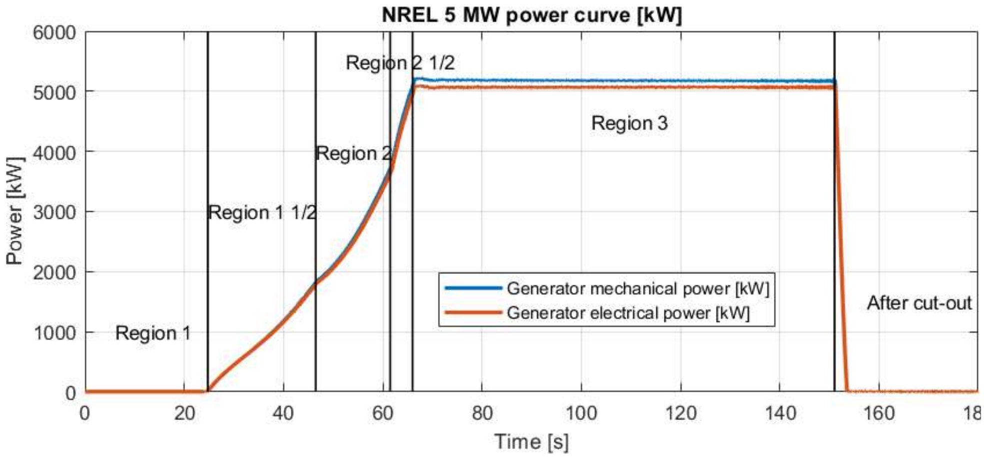

Figure 4.45. Power curve during operating range of rated 5 MW NREL

In Figure 4.45, it can be seen that in region 1, until the cut-in wind speed of 5 m/s (3 m/s in front of the rotor), the wind turbine does not produce any power and all the energy extracted from the wind is used just for rotating the rotor. Region 1 ½, starts at cut-in wind speed of 5 m/s (3 m/s in front of the rotor) and represents the startup region when the WECS starts to produce electric power. Region 2 starts when region 1 ½ ends and is the region where the WECS extracts the maximum power from the power available in the wind (maximum power point tracking). Region 2 ½ is a linear transition between region 2 and region 3. Region 3 starts at a wind speed of 11.4 m/s in front of the rotor and represents the rated power region because in this region the WECS starts adjusting the blade-pitch angle in order to maintain constant the produced power to the rated one. At 25 m/s starts the cut-off region, where the WECS stops producing power by pitching its blades to maximum and braking the rotor angular velocity.

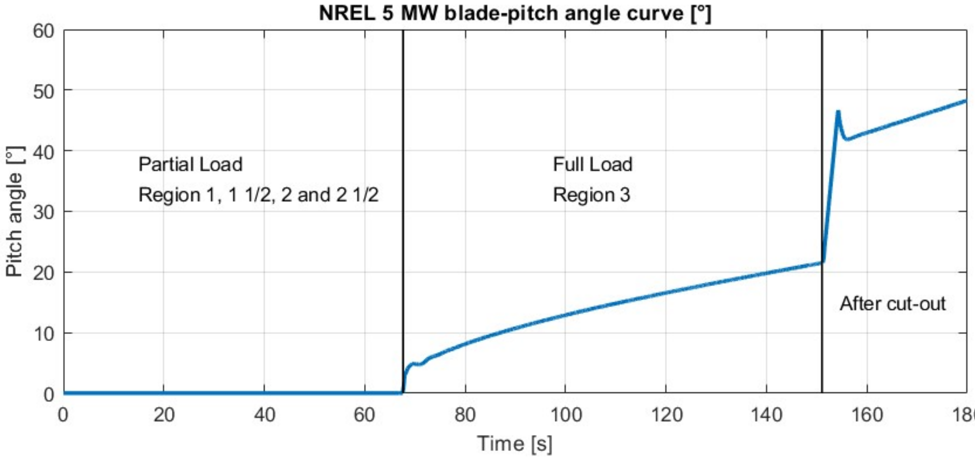

Figure 4.46. Blade-pitch angle curve during operating range of rated 5 MW NREL

In Figure 4.46, it can be seen that the blade-pitch angle is held constant at 0º (in regions 1, 1 ½, 2 and 2 ½) until the WECS reaches the rated power (region 3 starts at 11.4 m/s wind speed in front of the rotor). In region 3 the WECS starts pitching its blade in order to extract from the wind, only the rated power. At 25 m/s wind speed, the WECS cuts off by starting pitching its blades to maximum (tendency to pitch the blades to 90º) in order to reduce to the minimum the power extraction from the wind.

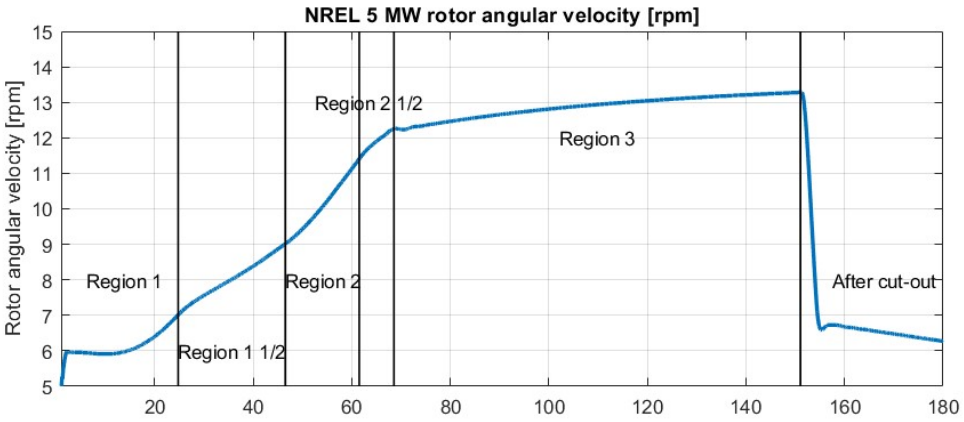

Figure 4.47. Rotor angular velocity curve during operating range of 5 MW NREL

In Figure 4.47, it can be seen that in region 1, until region 1 ½ (3 m/s wind speed in front of the rotor), all the extracted power from the wind is used just for starting to rotate the rotor. In the startup region (1 ½), it can be seen that the slope of the rotor angular velocity is reduced, because the WECS couples the drive train, and part of the power extracted from the wind it is converted into torque by the generator. In region 3, the rotor angular velocity reaches the rated velocity and the WECS controller tries to keep it constant to its rated value. At cut-off, the rotor angular velocity is quickly braked to almost 0, when the blades pitch angle reaches 90º, the moment when the braking system starts acting.

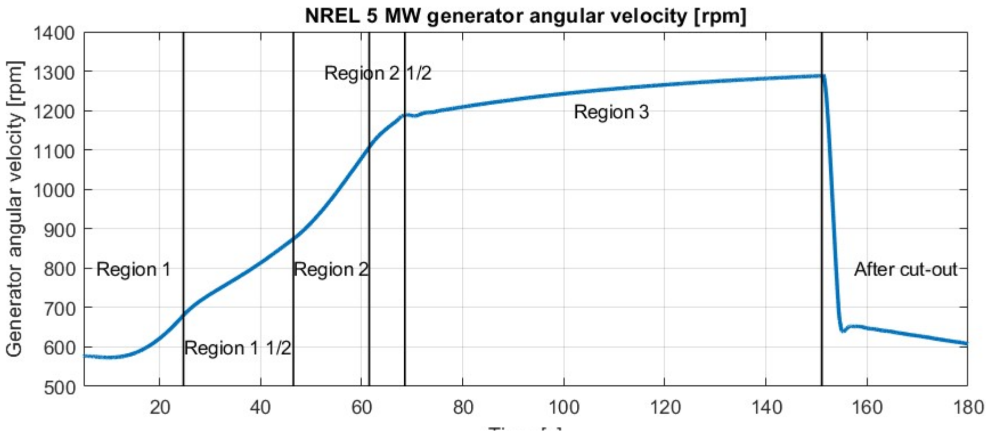

Figure 4.48. Generator angular velocity curve during operating range of 5 MW NREL

In Figure 4.48, it can be seen that region 1 stands until the cut-in wind speed when the generator speed reaches 669.3 rpm (70.089 rad/s). The startup region (1 ½) stands for 30% region above region 1, from 669.3 rpm (70.089 rad/s) to 870.09 rpm (91.116 rad/s). Region 2 is the region between the startup region and the generator machine's synchronous speed (1100 rpm -115.1917 rad/s). Region 3 starts at 99% (1173.7 rpm -122.9096 rad/s) of the generator rated angular velocity. At cut-off wind speed (25 m/s) the generator angular velocity is reduced to almost 0 and then held there by the braking system, the same as the rotor angular velocity. By comparing the figure above with Figure 4.48, it can be observed that the generator angular velocity follows the rotor angular velocity multiplying it with the drive train gear ratio (1:97).

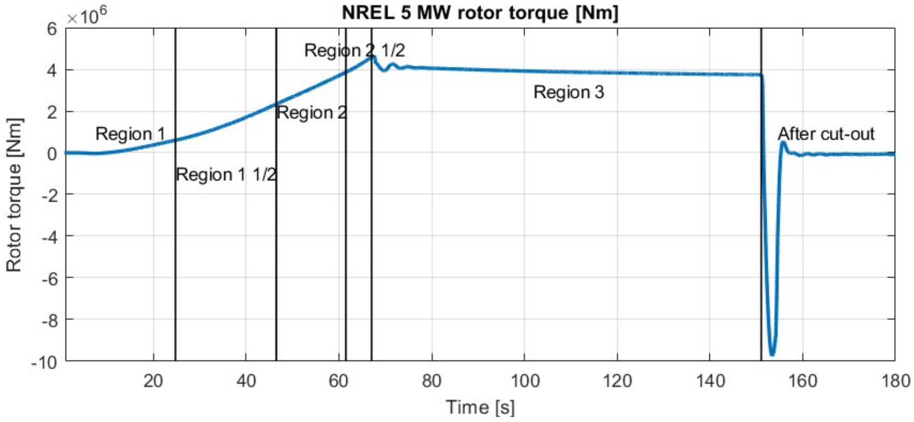

Figure 4.49. Rotor torque curve during operating range of rated 5 MW NREL

In the diagram from Figure 4.49, it can be seen the rotor torque. At the beginning of region 3, it can be seen the fluctuations created in rotor torque showing how sensitive is the rotor torque to the blade-pitching angle. At cut-off (25 m/s wind speed) it can be observed a huge increase in torque magnitude, given by the sum of the torque created by the rotor braking with the torque of the generator which tries to keep its direction.

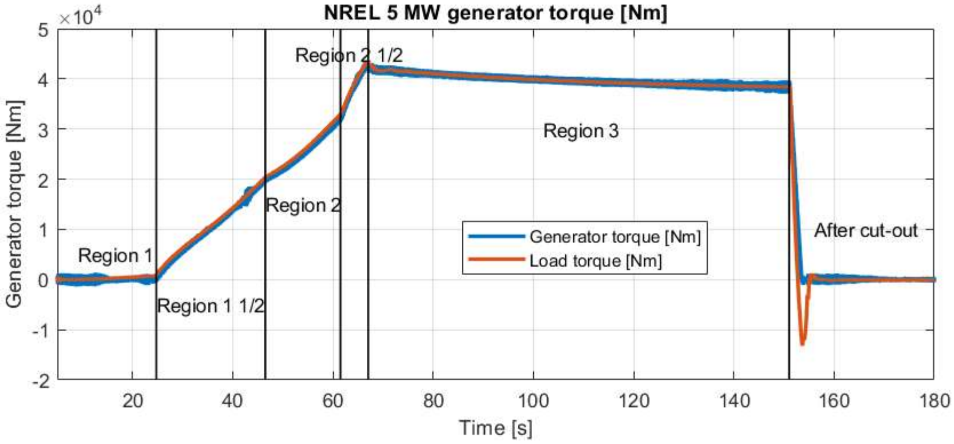

Figure 4.50. Generator torque curve during operating range of rated 5 MW NREL

In diagram (Figure 4.50), it can be seen that in region 1 the generator torque is 0 Nm, and the generator torque starts to couple to the drive train in startup region. In region 3 the generator reaches rated torque and tries to maintain constant torque during the entire region 3. At cut-out, the generator torque is reduced to 0 Nm.

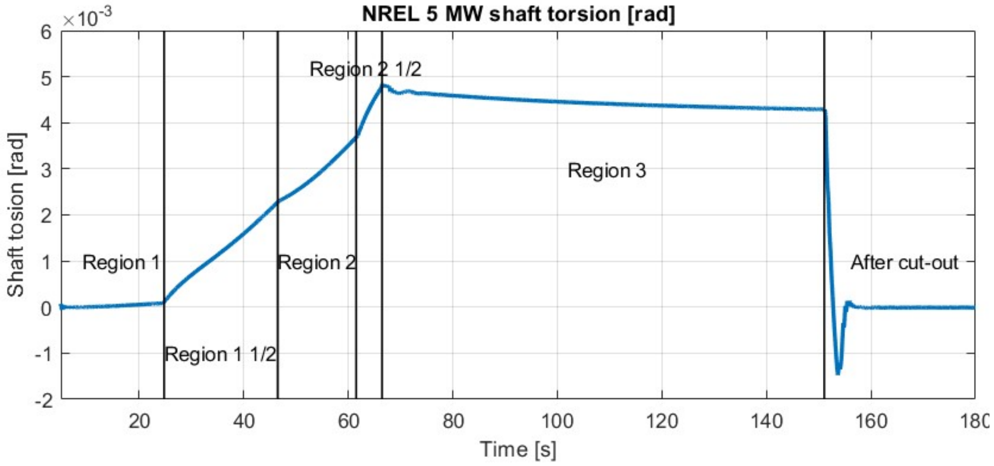

Figure 4.51. Shaft torsion curve during operating range of rated 5 MW NREL

In Figure 4.51, is presented the torsion momentum. In region 1 the torsion created by the rotor torque on the shaft is 0 rad/s. In region 3 because the rotor and generator torque are almost constant, the shaft torsion is also almost constant. At cut-off, the change in direction of the shaft torsion is due to the difference in rotor and generator torque direction during the time until the generator torque is disconnected. When the generator torque gets disconnected, the shaft torsion becomes 0.

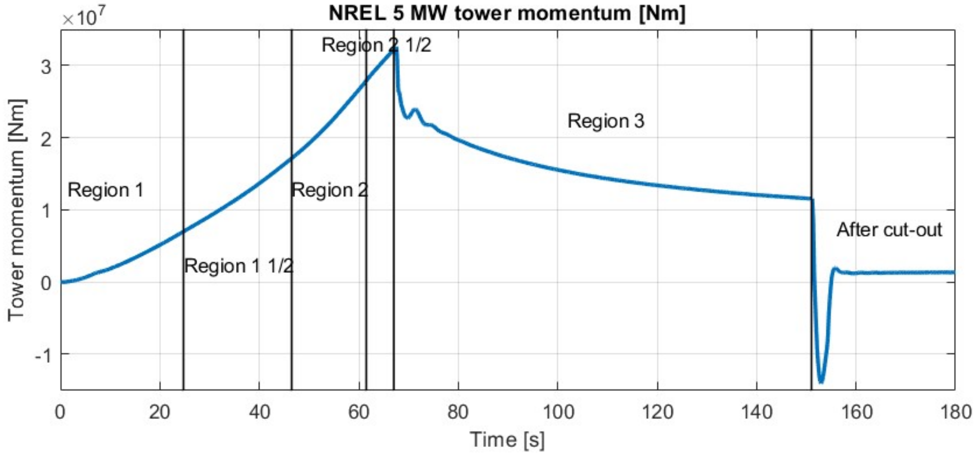

Figure 4.52. Tower momentum curve during operating range of rated 5 MW NREL

In diagram-Figure 4.52, it is presented the tower momentum during the WECS operation. In this diagram, it can be seen the correlation between the tower momentum variation and the blade-pitch angle variation. At a blade-pitch angle of 0º (in regions 1, 1 ½, 2 and 2 ½) the tower momentum increases direct proportional with the rotor torque, but in region 3, when the pitch actuator increases the blade pitch angle, the tower momentum starts decreasing. At WECS cut-off a significant increase in tower momentum occurs due to the braking torque of the rotor. After the cut-off, it can be seen that all the power created by the wind on the rotor, nacelle and tower is transmitted to the foundation by the tower.

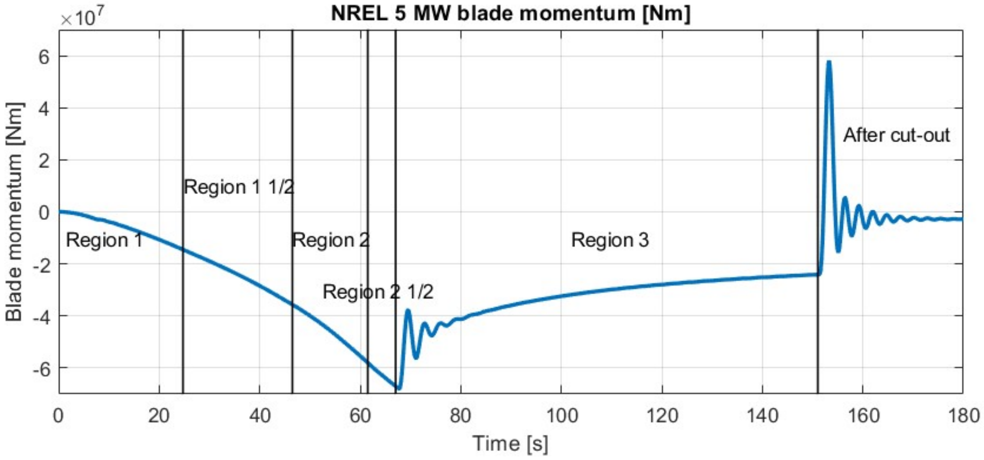

Figure 4.53. Blade momentum curve during operating range of rated 5 MW NREL

In Figure 4.53, it can be seen the blade momentum which until cut off variates proportional to the proportion of the power extracted from the wind power by the WECS. At cut-out wind speed, an increase in blade momentum occurs due to the inertia of the rotor.

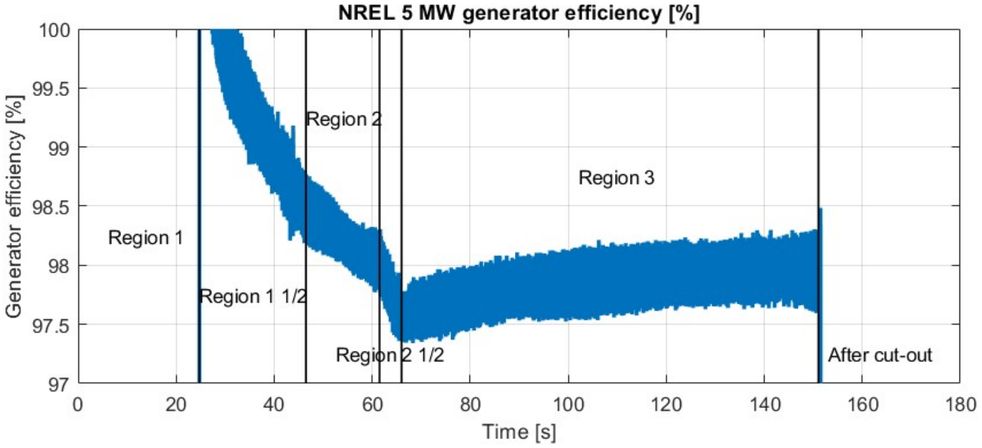

Figure 4.54. Generator efficiency curve during operating range of rated 5 MW NREL

In Figure 4.55, it can be seen the variation of the 3 phases of the generator stator voltage during each region.

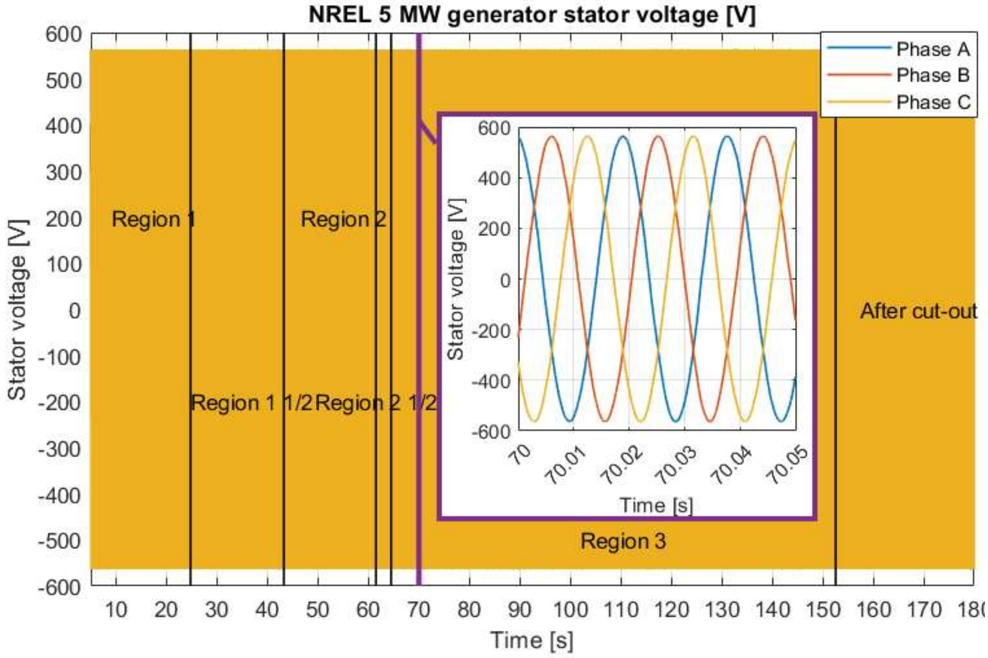

Figure 4.55. Generator stator voltage during operating range of rated 5 MW NREL

In Figure 4.56, it can be seen the variation of the 3 phases of the generator stator voltage during each region.

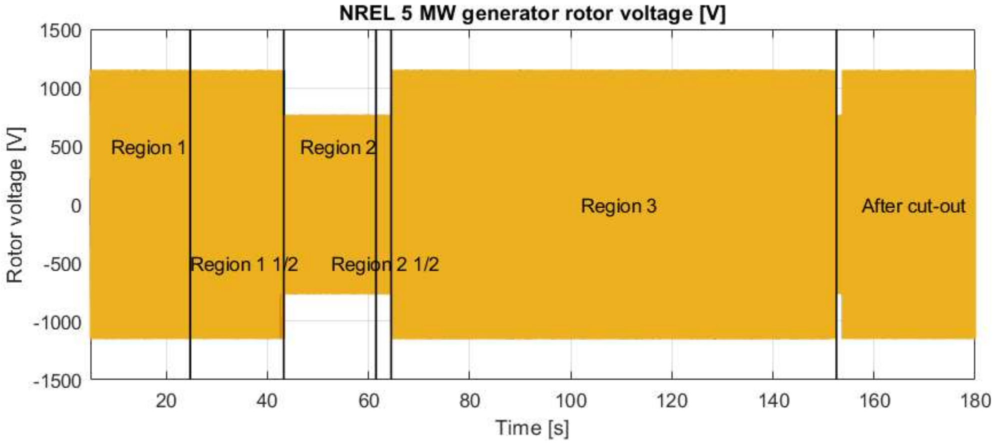

Figure 4.56. Generator rotor voltage during operating range of rated 5 MW NREL

In Figure 4.57, it can be seen the variation of the 3 phases of the generator stator currents during each region.

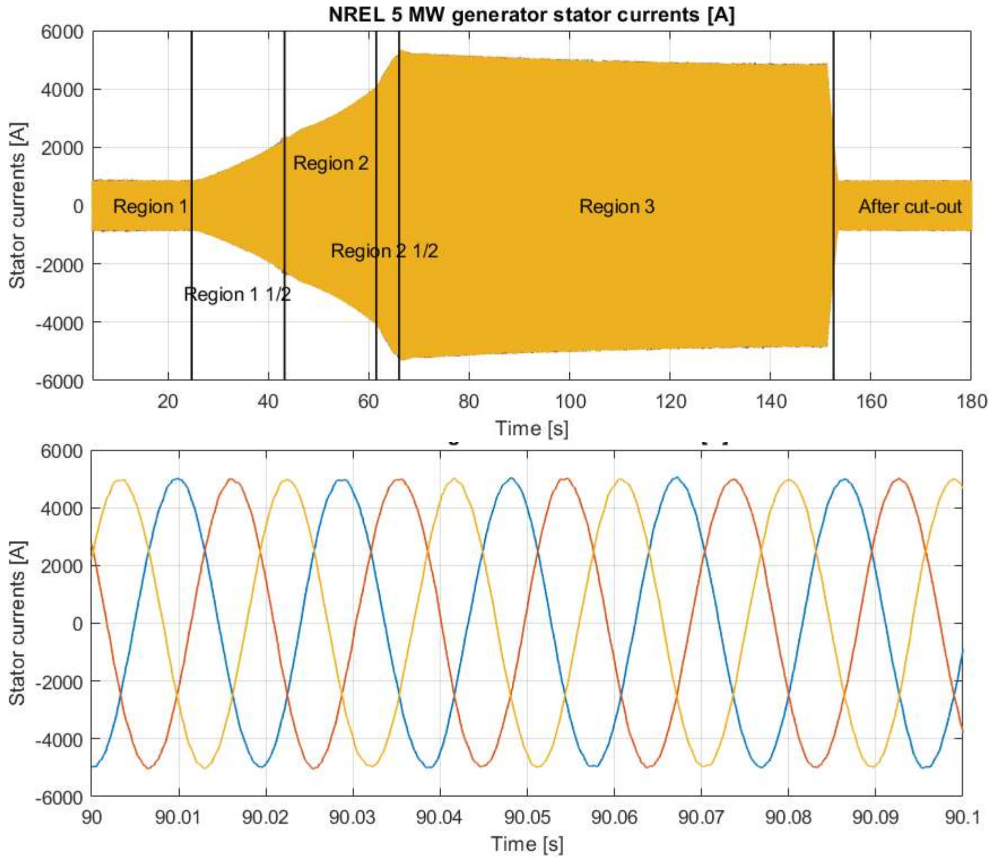

Figure 4.57. Grid currents curve during operating range of rated 5 MW NREL

In Figure 4.58, it can be seen the variation of the 3 phases of the generator rotor currents during each region. Between the time interval of 54 s and 57 s, it can be seen the response of the rotor currents at synchronous speed.

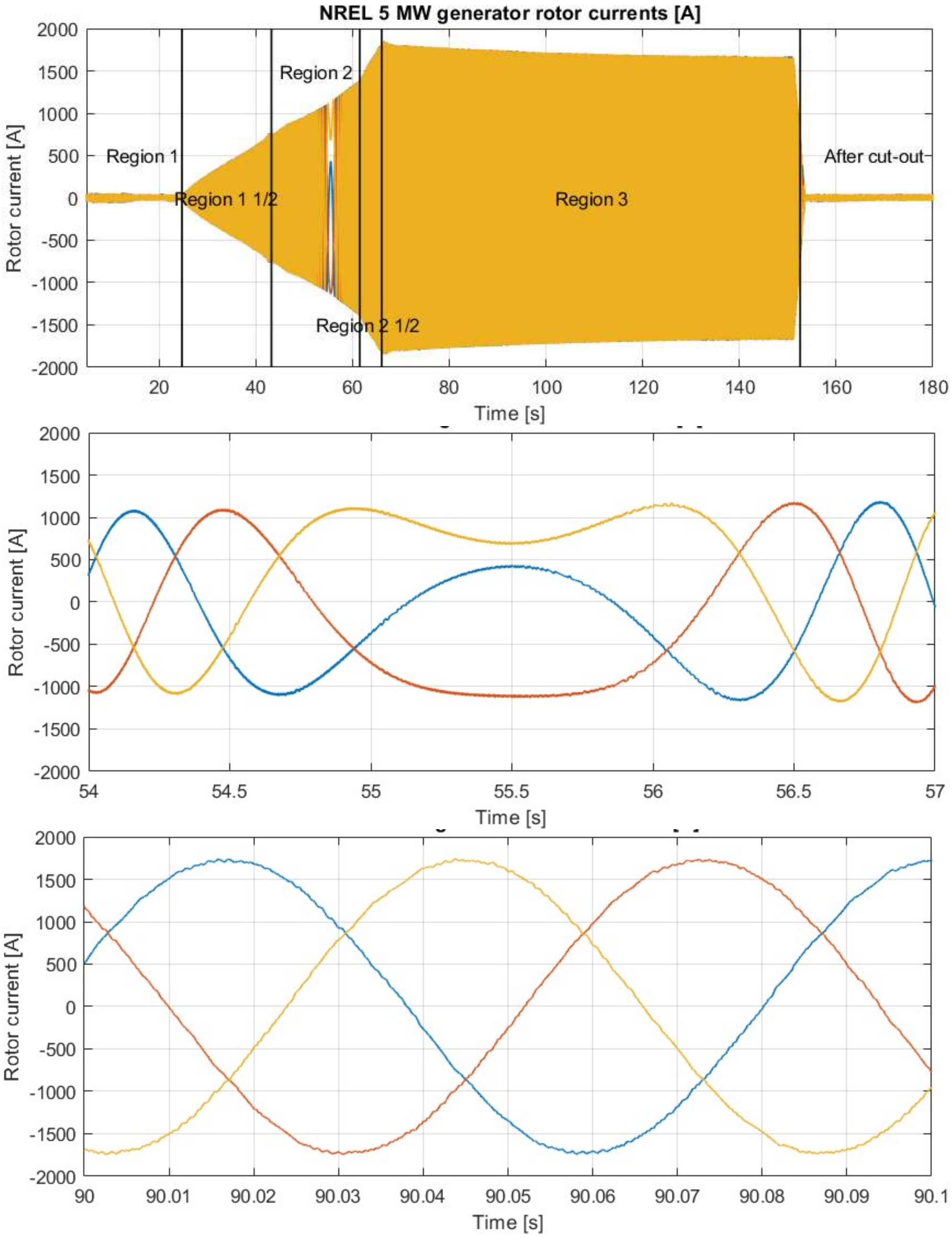

Figure 4.58. Generator rotor currents during operating range of rated 5 MW NREL

In Figure 4.59, it can be seen the variation of the grid currents in amplitude during each region.

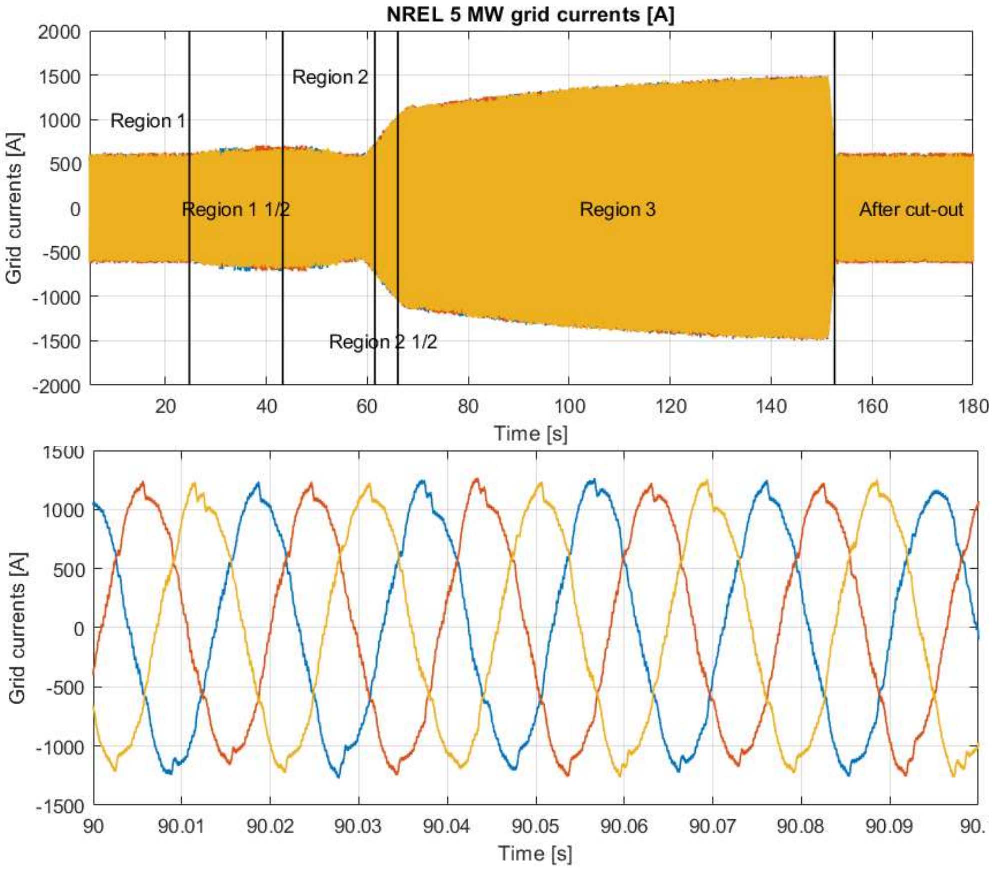

Figure 4.59. Grid currents curve during operating range of rated 5 MW NREL

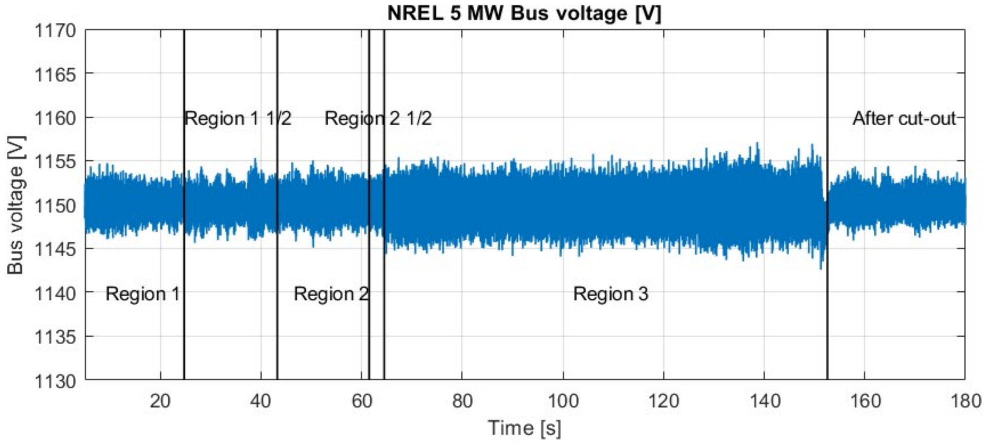

Figure 4.60. DC bus voltage during operating range of rated 5 MW NREL

In Figure 4.60, it can be seen the response of the grid voltage-oriented vector control (GVOVC) controlling the DC bus voltage (Vbus) during each region.

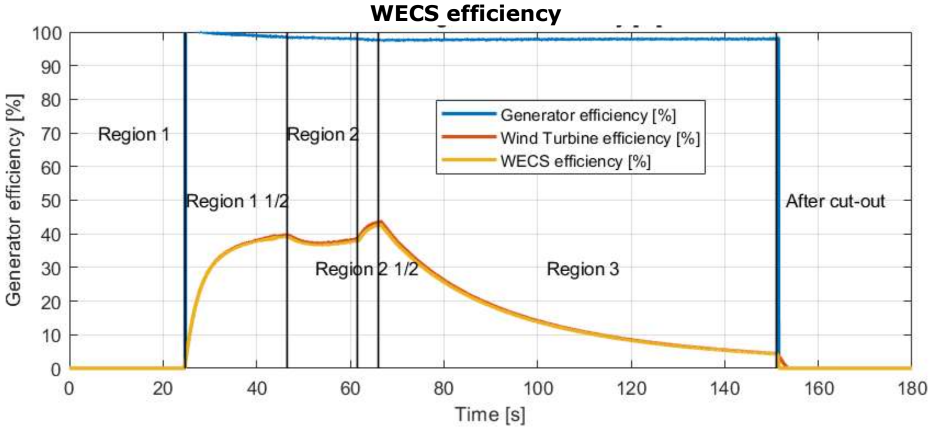

Figure 4.61. WECS efficiency during operating range of rated 5 MW NREL

In Figure 4.61, it can be seen the WECS efficiency during the entire operation range.

4.4.2. Response of derated WECS

In the second simulation, is presented the response of the derated WECS to a wind speed data covering all the operating range (from 0 to 30 m/s) (Figure 4.44). This simulation was executed in order to see the comparison between the response of the WECS at each wind speed of its operating range when the requested power is below rated power.

Figure 4.62 it can be seen that the WECS maintains its rated power curve (Figure 4.45) until it reaches the requested power, where it saturates. At cut-out wind speed (25 m/s) it can be observed that as lower is the requested power, as quicker is the cut-out.

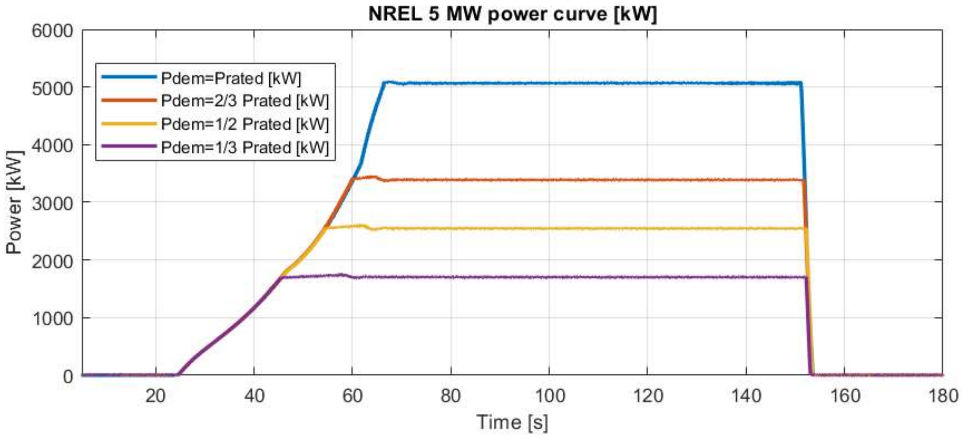

Figure 4.62. Power curve during operating range of derated 5 MW NREL

In the diagram from Figure 4.63, it can be seen that the blade pitch controller starts pitching depending on the demanded power. The lower the demanded power, the faster the blade starts being pitched.

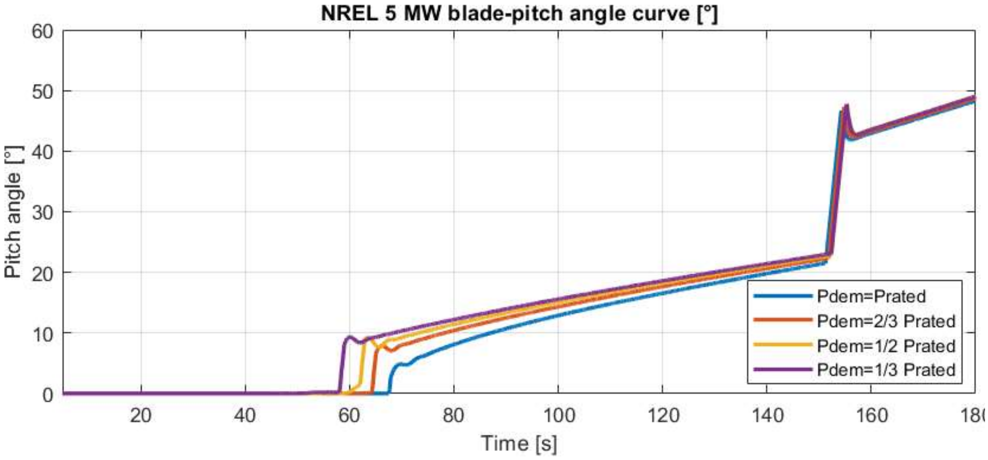

Figure 4.63. Blade-pitch angle curve during operating range of derated 5 MW NREL

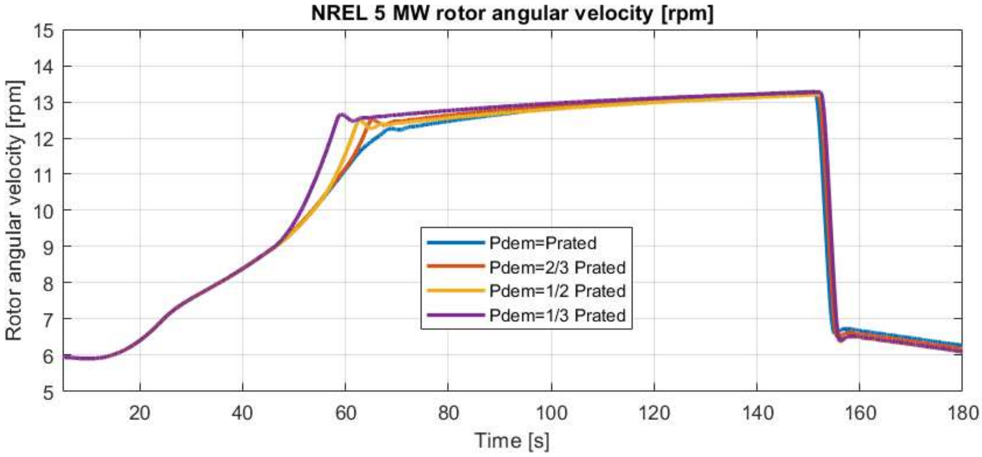

Figure 4.64. Rotor angular velocity during operating range of derated 5 MW NREL

In diagram-Figure 4.64, it can be seen that the rotor reaches its rated angular velocity depending on the demanded power. The lower the demanded power, the faster the rotor reaches the rated angular velocity. Once the rated angular velocity its reached, the WECS controller tries to maintain the rotor angular velocity constant, independent of the demanded power.

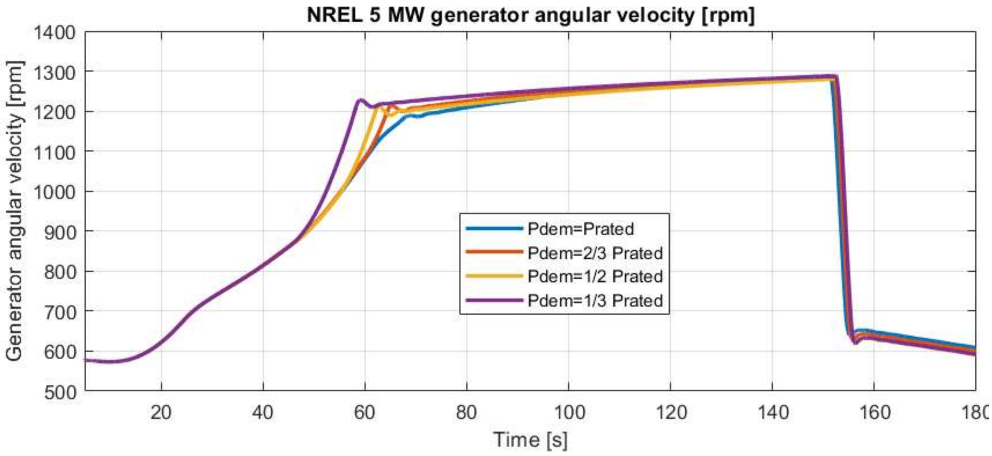

Figure 4.65. Generator angular velocity during operating range of derated 5 MW NREL

In Figure 4.65, it can be seen that, similar to the rotor, the generator reaches its rated angular velocity depending on the demanded power. The lower the demanded power, the faster the generator reaches its rated angular velocity. Once the rated angular velocity is reached, the WECS controller tries to maintain the generator angular velocity constant, independent of the demanded power.

In Figure 4.66, it can be seen that as higher the demanded power, as higher the rotor torque during operation because the power extracted from the wind is higher.

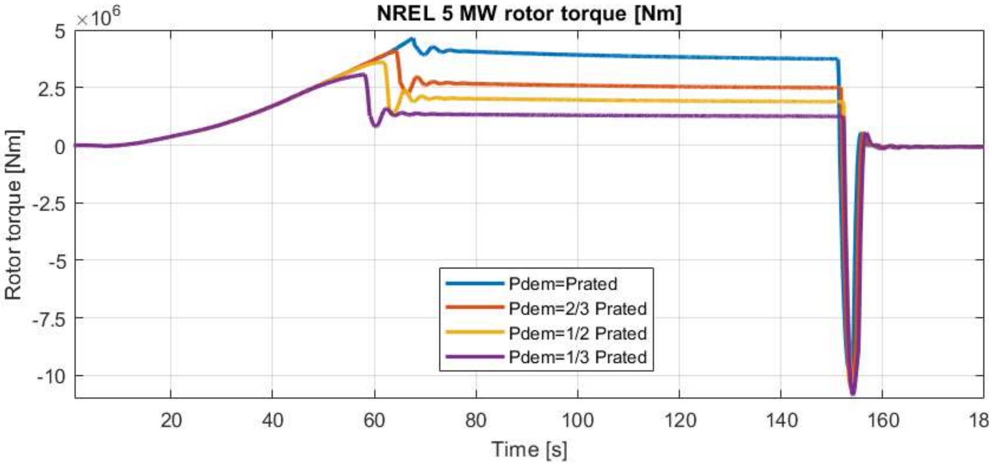

Figure 4.66. Rotor torque curve during operating range of derated 5 MW NREL

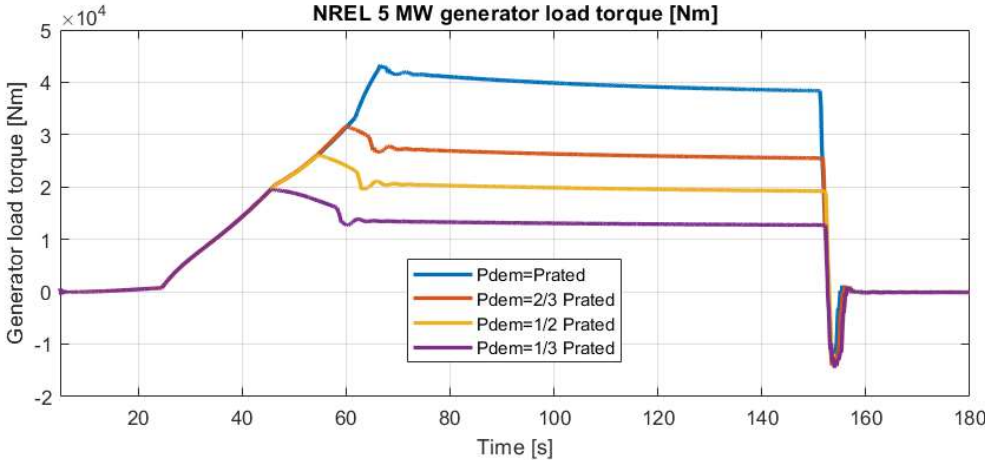

Figure 4.67. Generator load curve during operating range of derated 5 MW NREL

In Figure 4.67, similar to rotor torque, the higher the demanded power, the higher the generator load torque is during operation.

In Figure 4.68, similar to rotor torque, the higher the demanded power, the higher the electromechanical generator torque is during operation. At cut-out wind speed (25 m/s) it can be observed that the lower the demanded power, the quicker the cut-out.

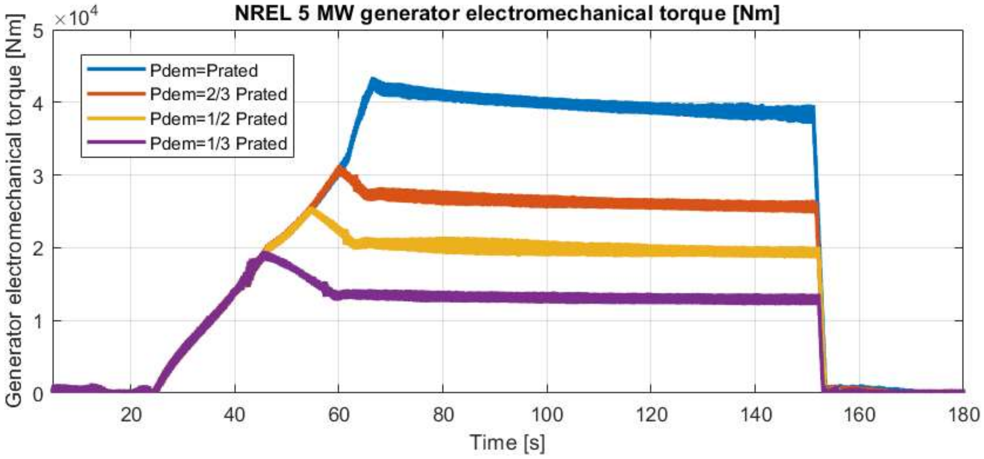

Figure 4.68. Generator torque curve during operating range of derated 5 MW NREL

In Figure 4.69, similar to rotor and generator torque, the higher the demanded power, the higher the shaft moment is during operation. At cut-out wind speed (25 m/s) it can be observed that the lower the demanded power, the quicker the cut-out.

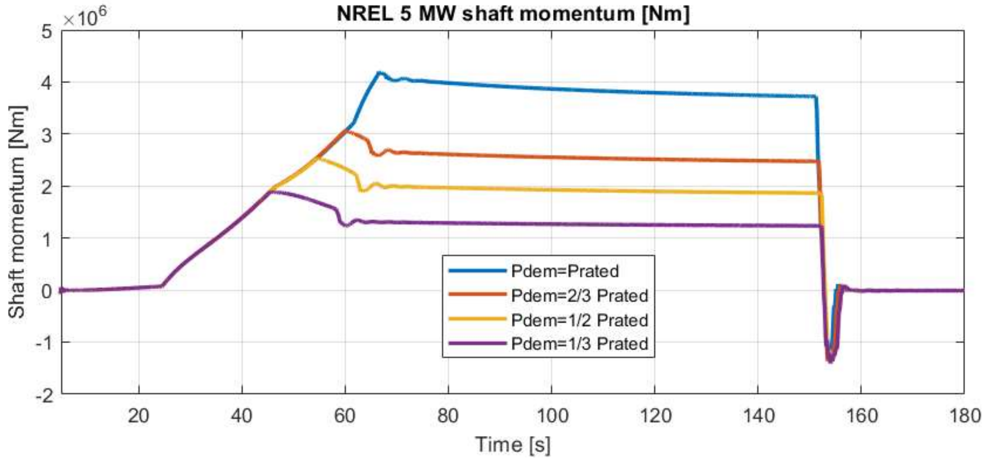

Figure 4.69. Shaft momentum curve during operating range of derated 5 MW NREL

In Figure 4.70, it can be seen the generator efficiency during the operating range. As lower the requested power, as higher the generator efficiency.

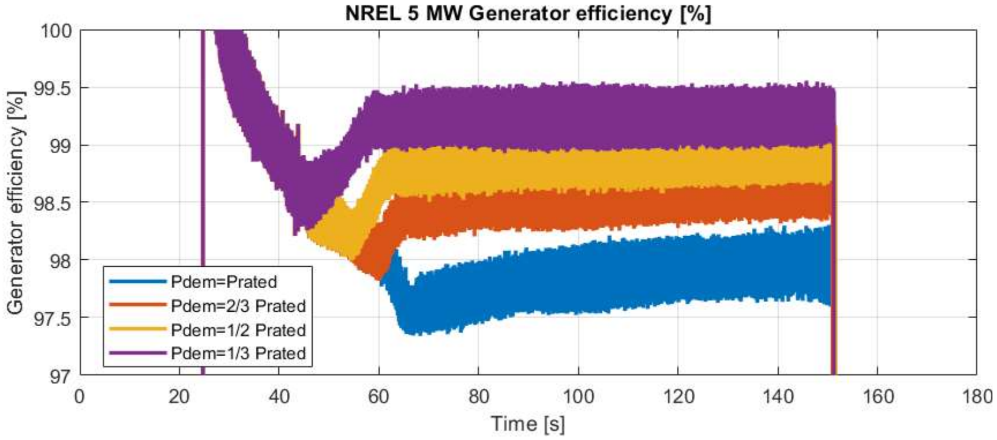

Figure 4.70. Generated efficiency during operating range of derated 5 MW NREL

In Figure 4.71, it can be seen that the voltage is maintained constant independently of the requested power from the WECS.

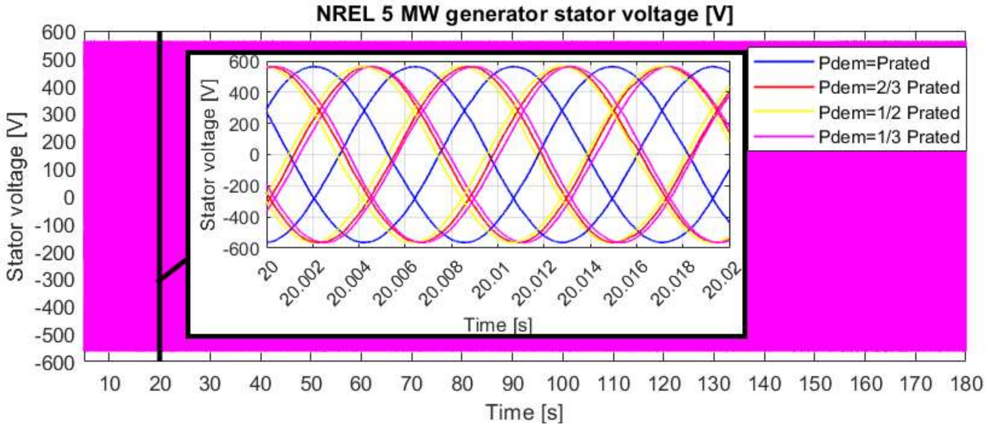

Figure 4.71. Generated stator voltage during operating range of derated 5 MW NREL

In Figure 4.72, it can be seen that the voltage is maintained constant independently of the requested power from the WECS.

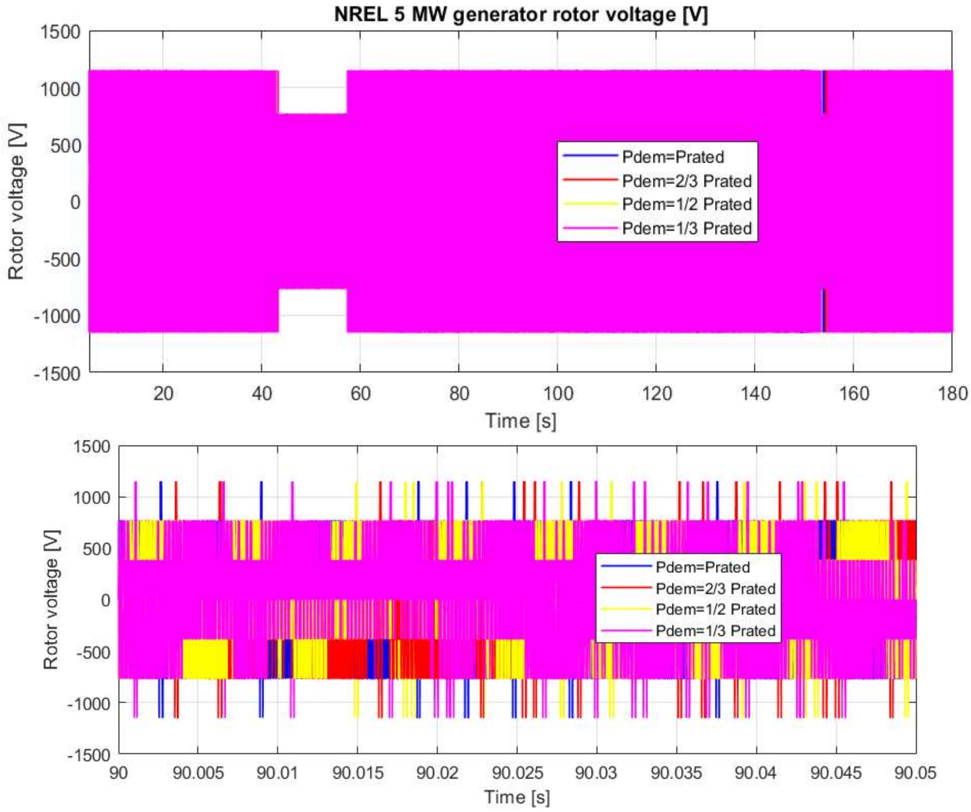

Figure 4.72. Generated rotor voltage during operating range of derated 5 MW NREL

In Figure 4.73, it can be seen how the generator stator currents decrease proportionally with the power produced by the WECS during the operation range.

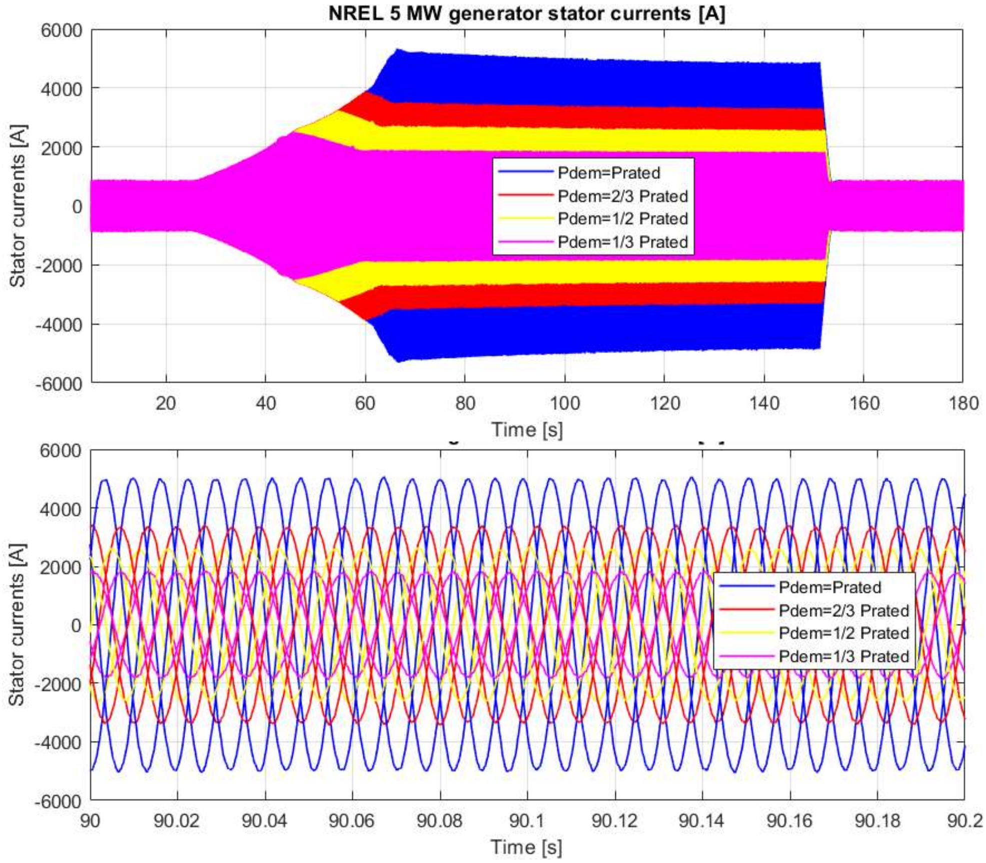

Figure 4.73. Generator stator currents during operating range of derated 5 MW NREL

In Figure 4.74, it can be seen how the generator rotor currents decrease proportionally with the power produced by the WECS during the operation range. Between the time interval of 52 s and 56 s, it can be seen the response of the rotor currents at synchronous speed.

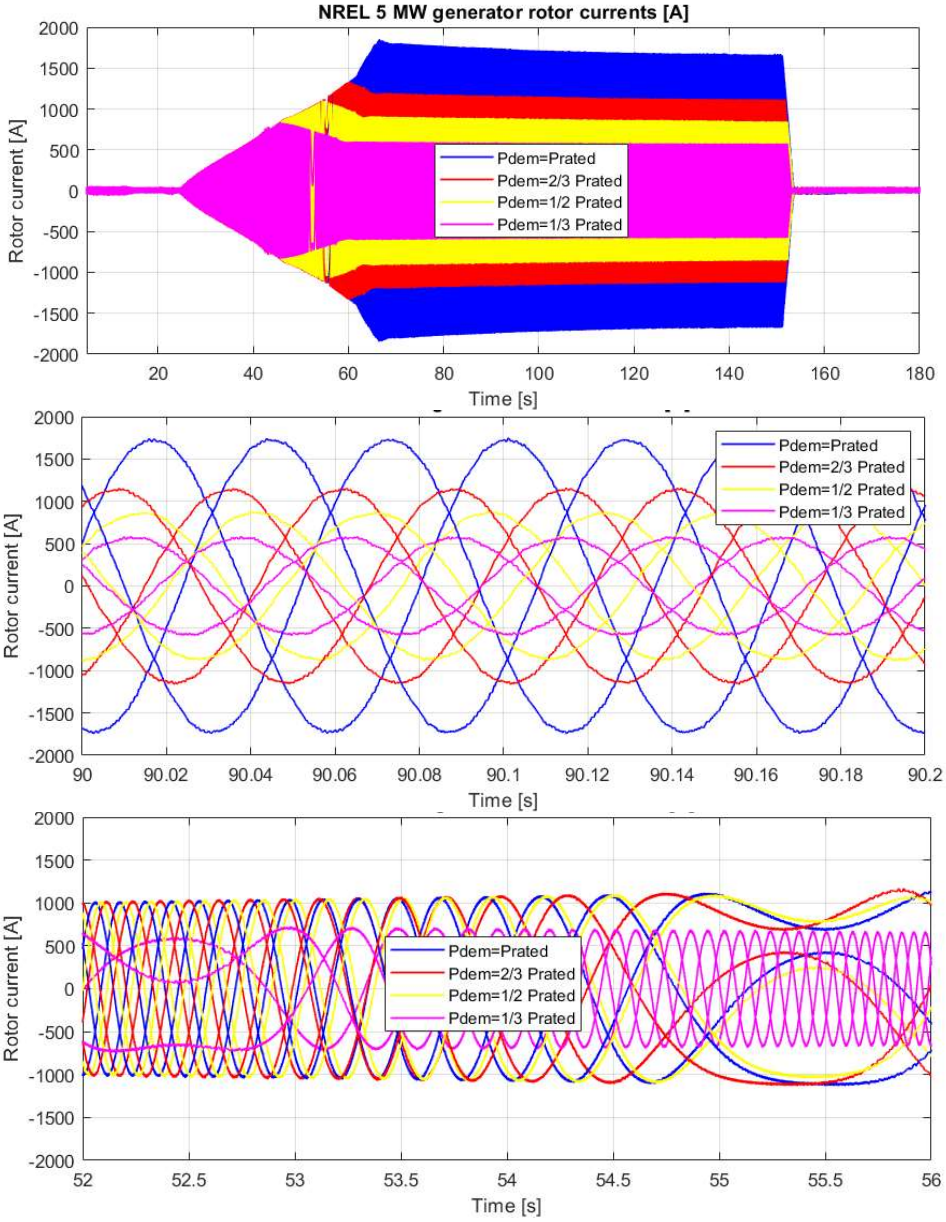

Figure 4.74. Generator rotor currents during operating range of derated 5 MW NREL

In Figure 4.75, it can be seen how the grid currents decrease proportional with the power produced by the WECS during the operation range.

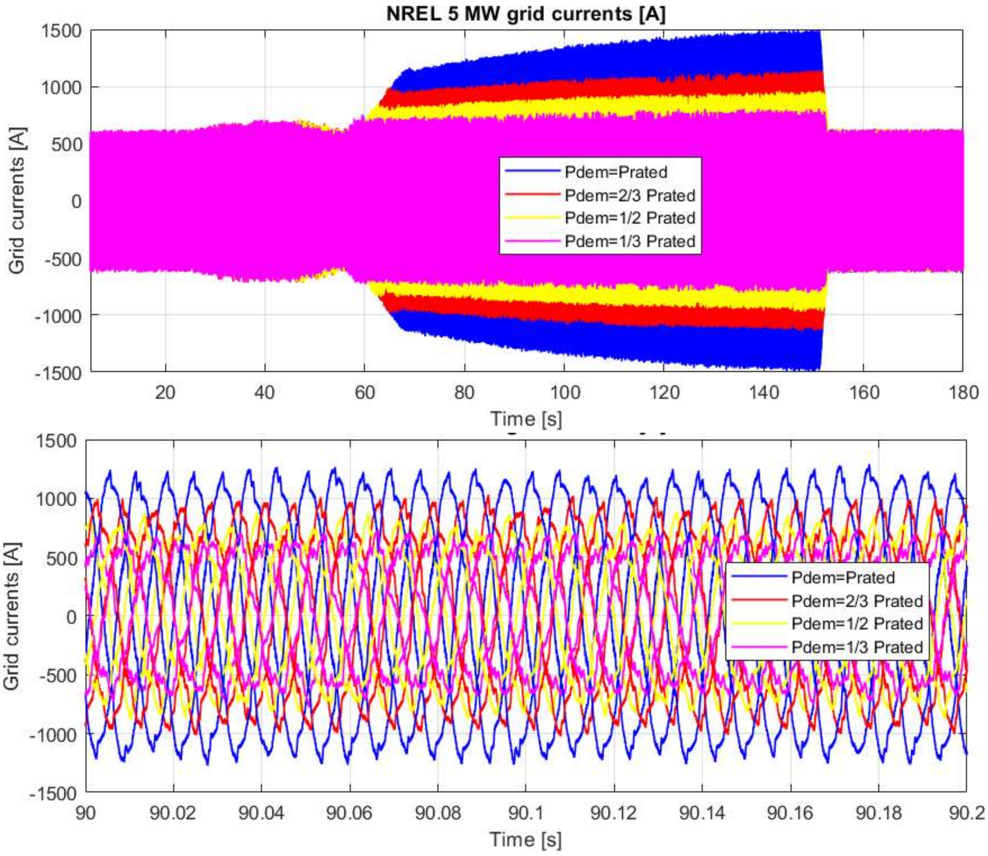

Figure 4.75. Grid currents during operating range of derated 5 MW NREL

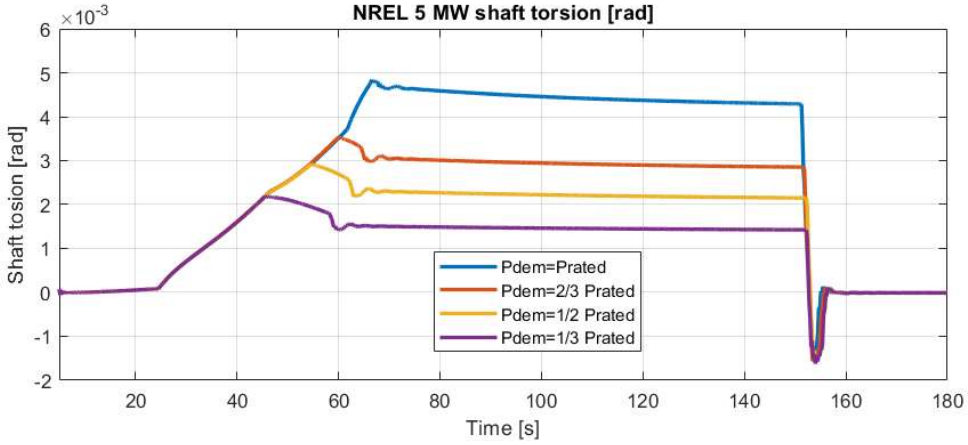

Figure 4.76. Shaft torsion during operating range of derated 5 MW NREL

In Figure 4.76, it can be seen the variation of the shaft torsion during the operation range when the requested power is lower than the rated power.

In Figure 4.77, it can be seen the response of the grid voltage-oriented vector control (GVOVC) controlling the DC bus voltage (Vbus) during each region.

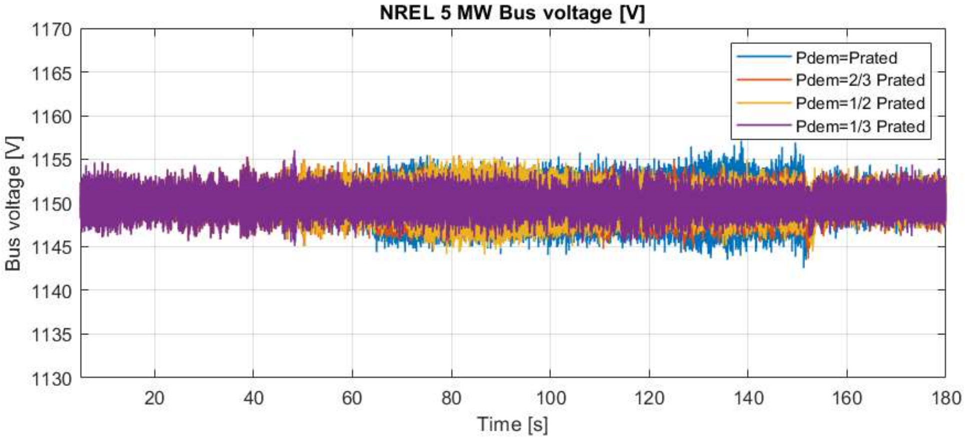

Figure 4.77. DC Bus voltage during operating range of derated 5 MW NREL

In Figure 4.78, it can be seen the variation of the WECS efficiency during the operation range when the requested power is lower than the rated power.

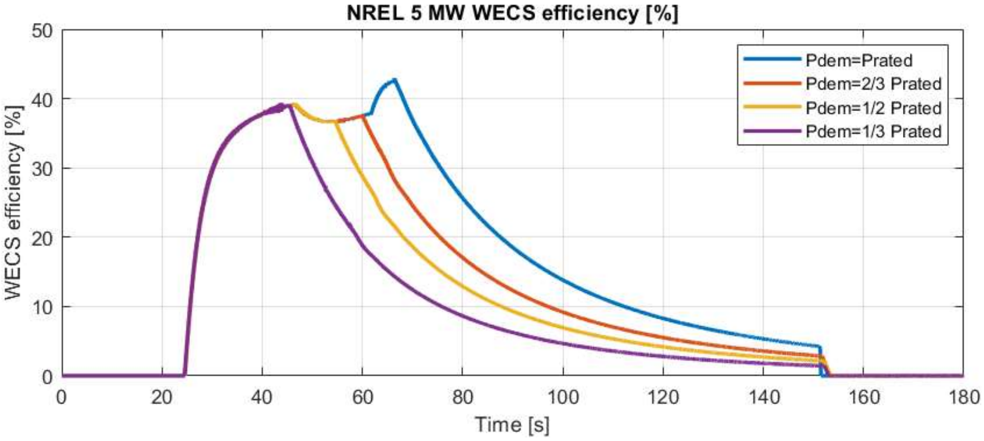

Figure 4.78. WECS efficiency during operating range of derated 5 MW NREL

4.4.3. Response of the WECS at full load

The current simulation represents the response of the WECS to a very turbulent wind speed time series, with wind speed variating between 12 and 20 m/s, during 2 minutes (Figure 4.79). This simulation was executed in order to see the response of the WECS operating at full load (with torque controller and blade-pitch controller) when the requested power is the rated power:

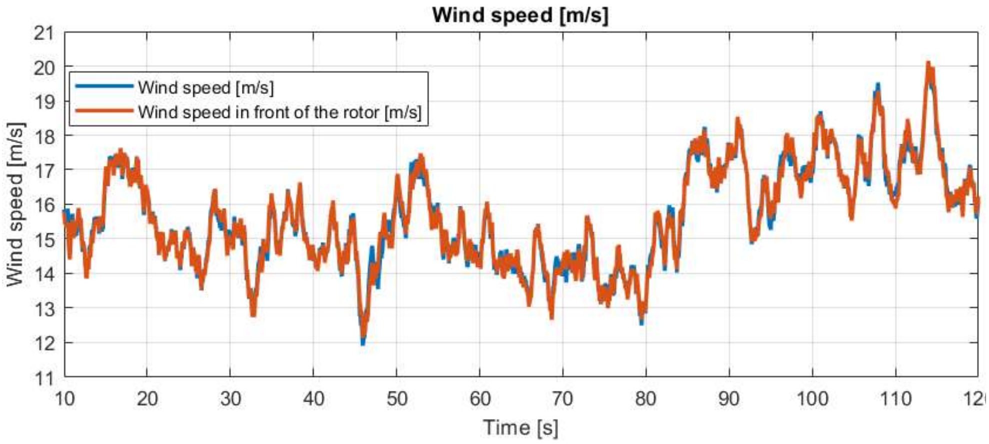

Figure 4.79. Wind speed time series corresponding to operation at full load

In the diagram (Figure 4.80), it can be seen the response of the WECS when the demanded power is equal or below the rated one. From the graph it can be seen the effectiveness of the gain schedule PI controller in adjusting the blade-pitch angle in order to maintain constant the demanded power, with minimum fluctuations in turbulent wind and without any power losses.

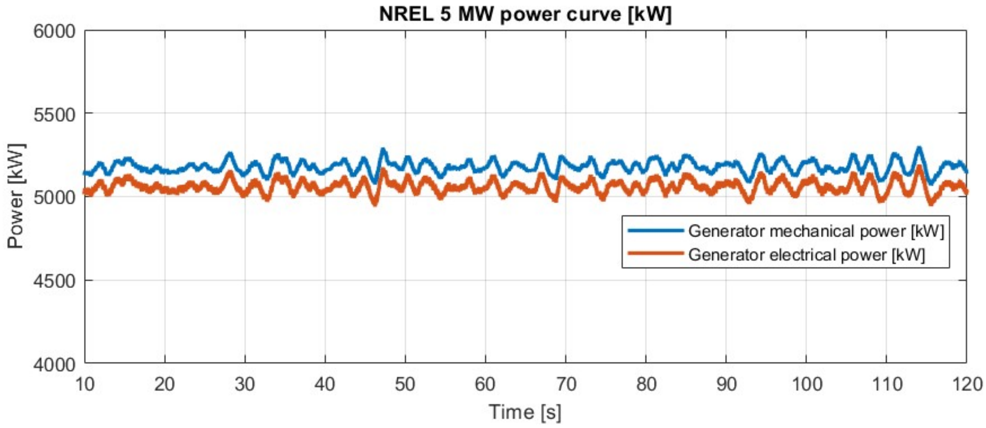

Figure 4.80. Power variation during operation at full load of derated 5 MW NREL

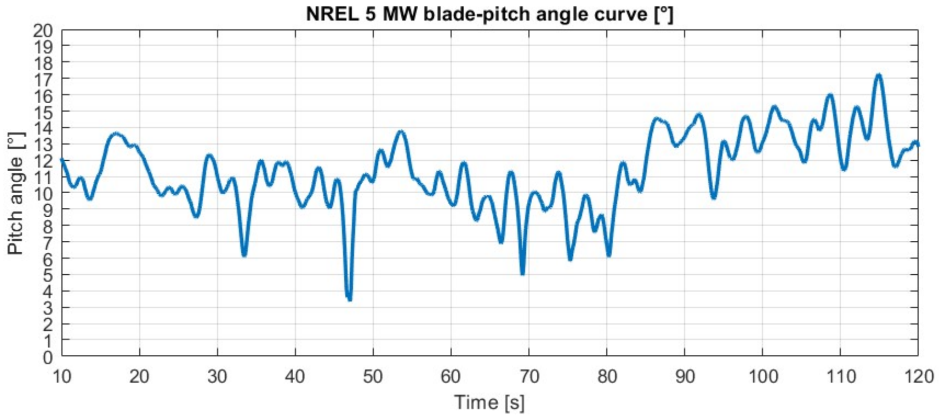

Figure 4.81. Blade pitch angle during operation at full load of derated 5 MW NREL

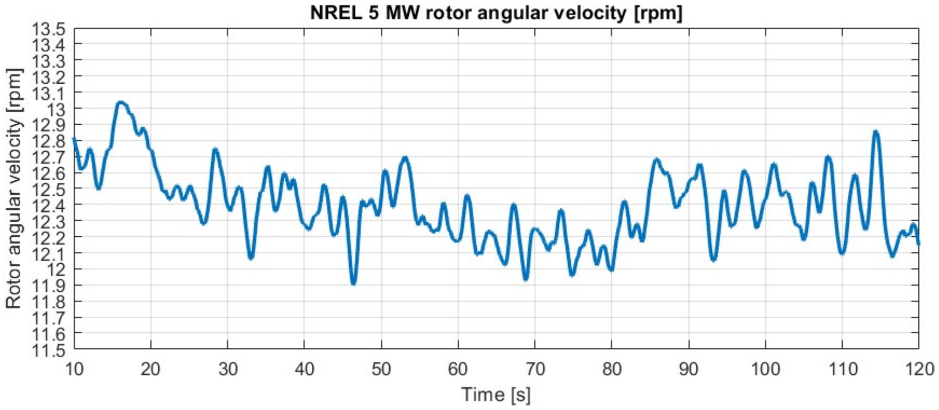

Figure 4.82. Rotor speed during operation at full load of derated 5 MW NREL

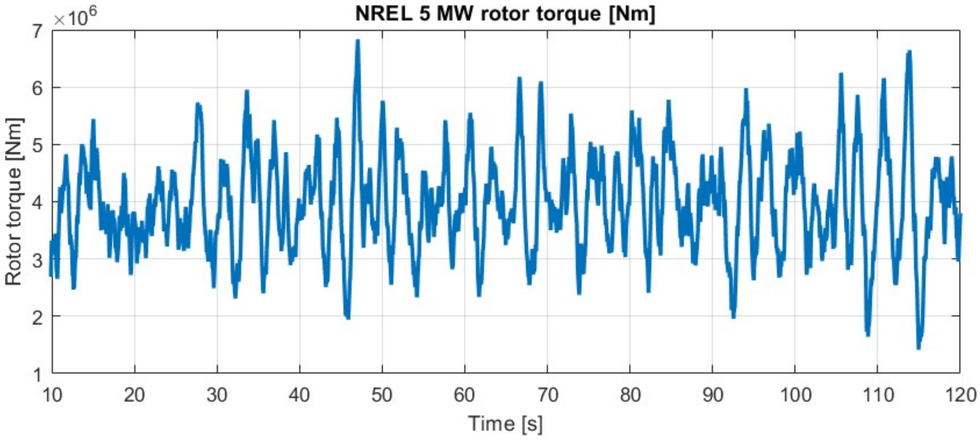

Figure 4.83. Rotor torque during operation at full load of derated 5 MW NREL

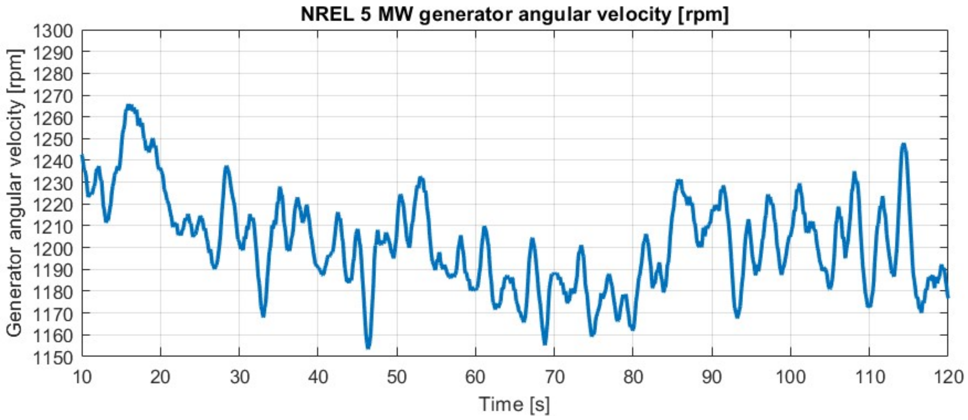

Figure 4.84. Generator speed during operation at full load of derated 5 MW NREL

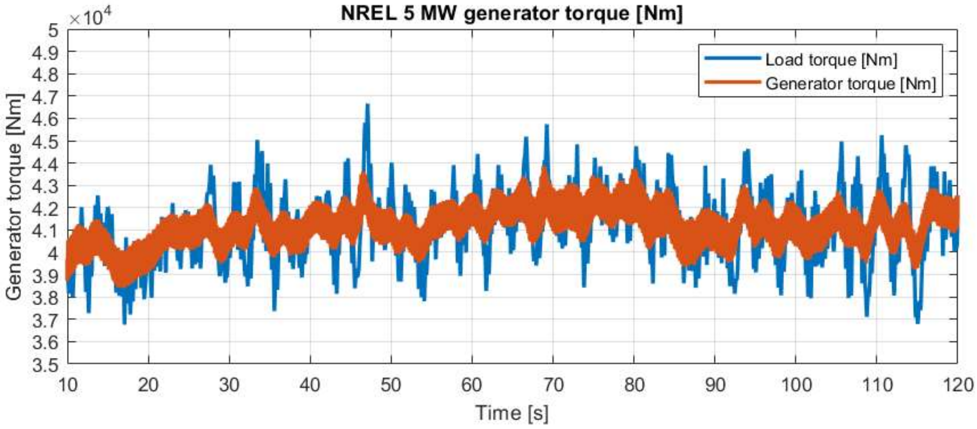

Figure 4.85. Generator torque during operation at full load of derated 5 MW NREL

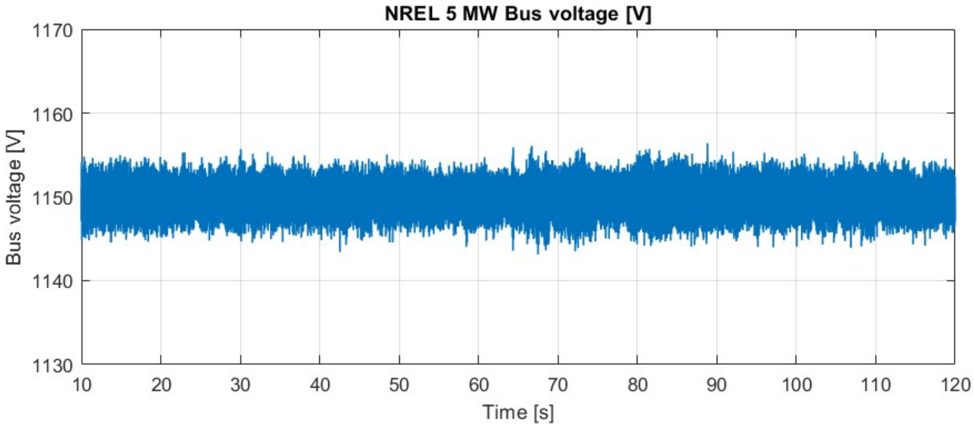

Figure 4.86. DC Bus voltage during operation at full load of derated 5 MW NREL

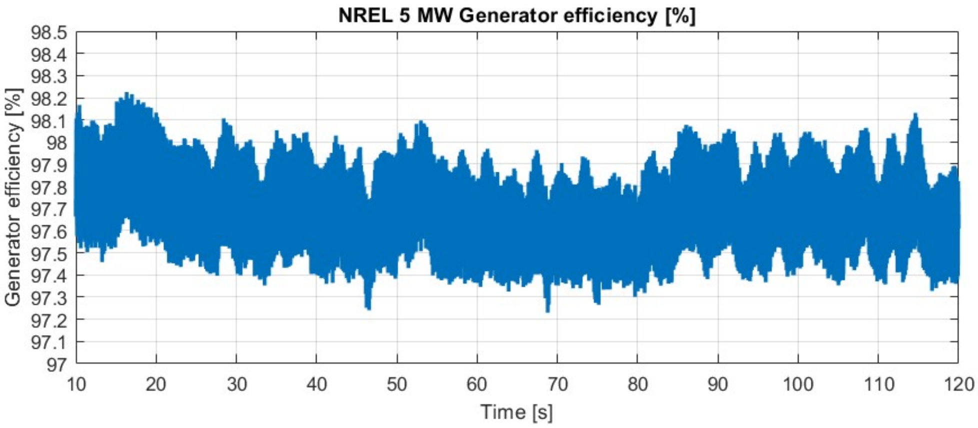

Figure 4.87. Generator efficiency during operation at full load of derated 5 MW NREL

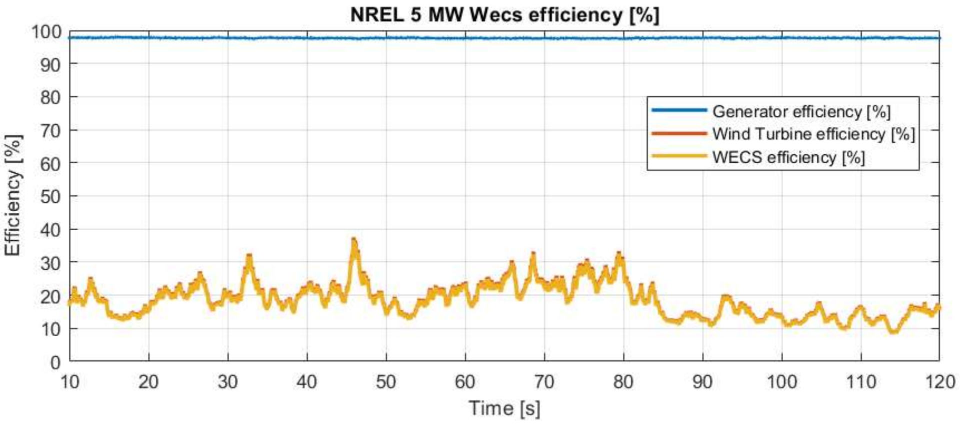

Figure 4.88. WECS efficiency during operation at full load of derated 5 MW NREL

BUPT

4.4.4. Response of the WECS at partial load

In the current simulation, is presented the response of the WECS to a very turbulent wind speed time series, with wind speed variating between 4 and 12 m/s, during 2 minutes (Figure 4.89). This simulation was executed in order to see the response of the WECS operating at partial load when the demanded power is the rated power.

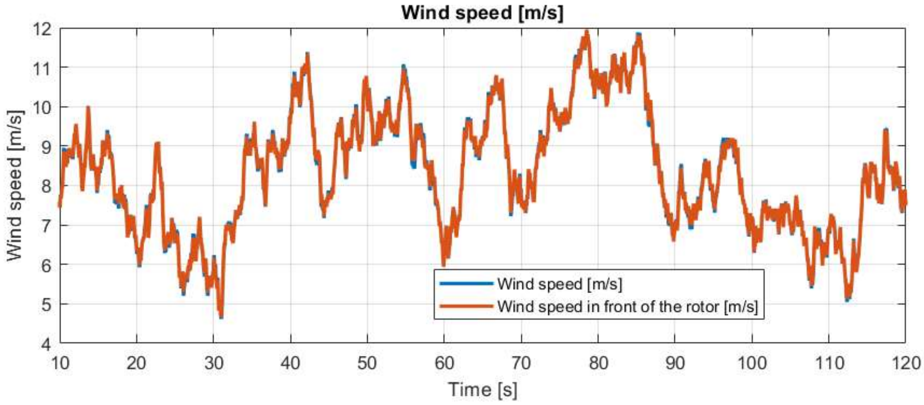

Figure 4.89. Wind speed time series corresponding to operation at partial load

In the diagram (Figure 4.90), similar as in the simulation with the response of the WECS at full load (the blade-pitch controller adjusts the blade pitch angle in order to maintain constant the power demand), at partial load, the controller also saturates the power production of the WECS to demanded power by enabling the blade pitch controller when the produced power reaches demanded power.

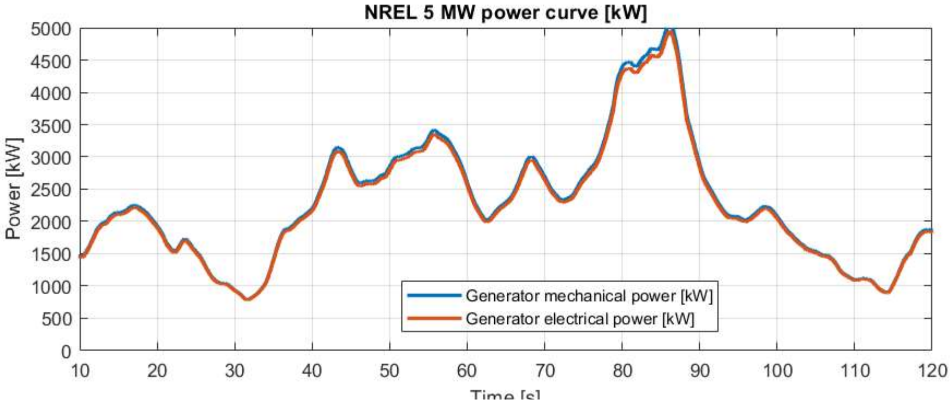

Figure 4.90. Power variation during operation at partial load of derated 5 MW NREL

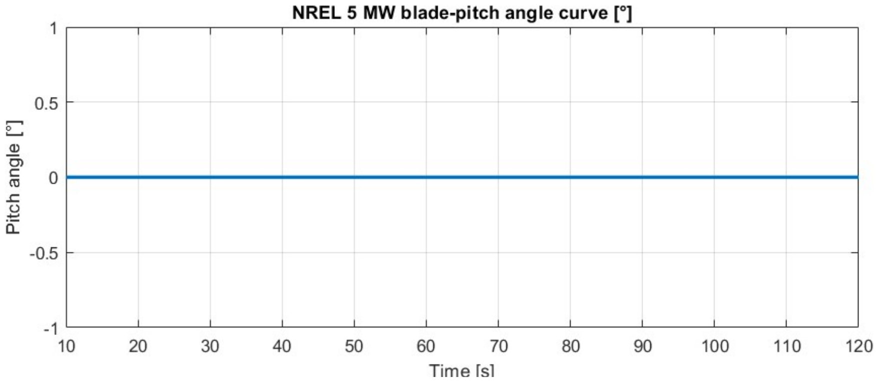

Figure 4.91. Pitch angle during operation at partial load of derated 5 MW NREL

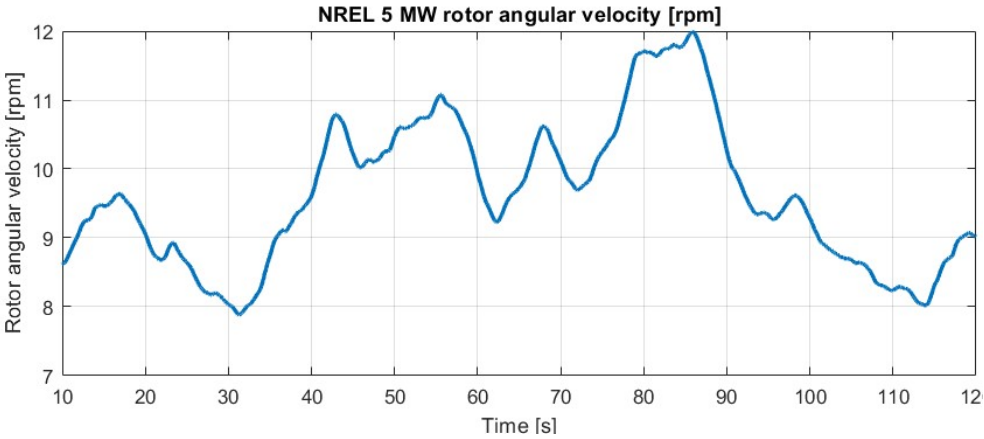

Figure 4.92. Rotor speed during operation at partial load of derated 5 MW NREL

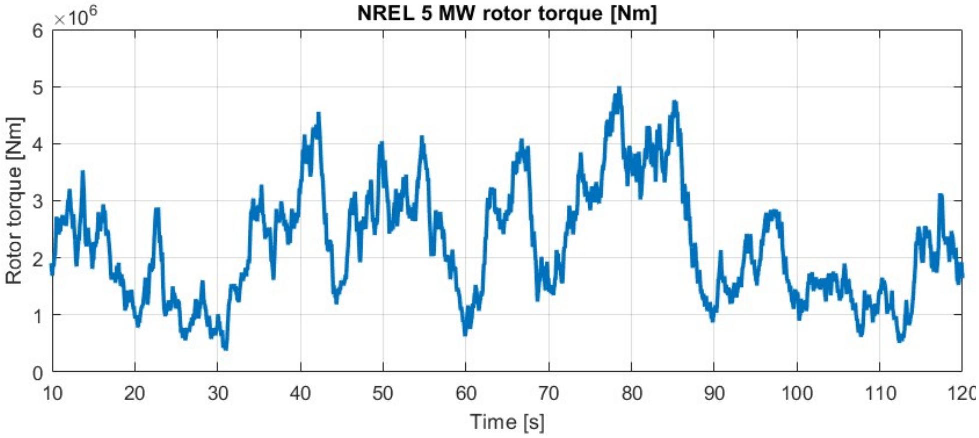

Figure 4.93. Rotor torque during operation at partial load of derated 5 MW NREL

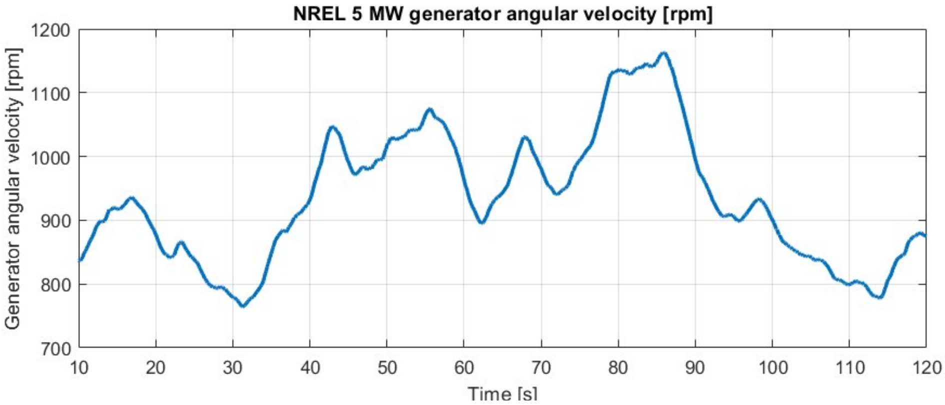

Figure 4.94. Generator speed during operation at partial load of derated 5 MW NREL

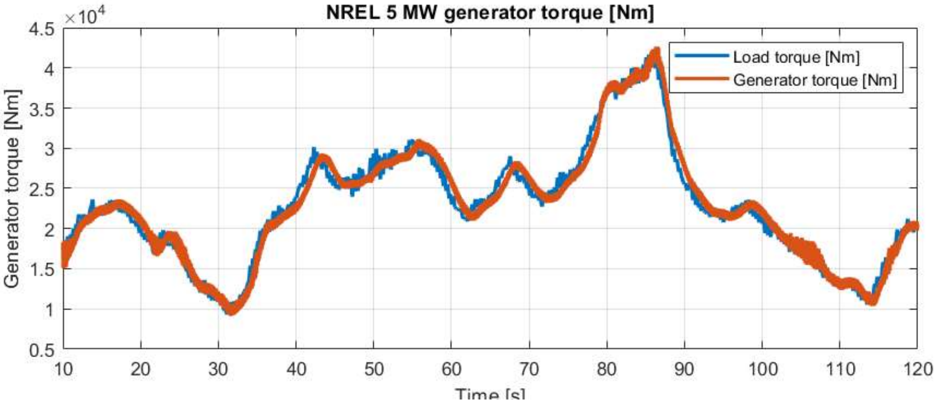

Figure 4.95. Generator torque during operation at partial load of derated 5 MW NREL

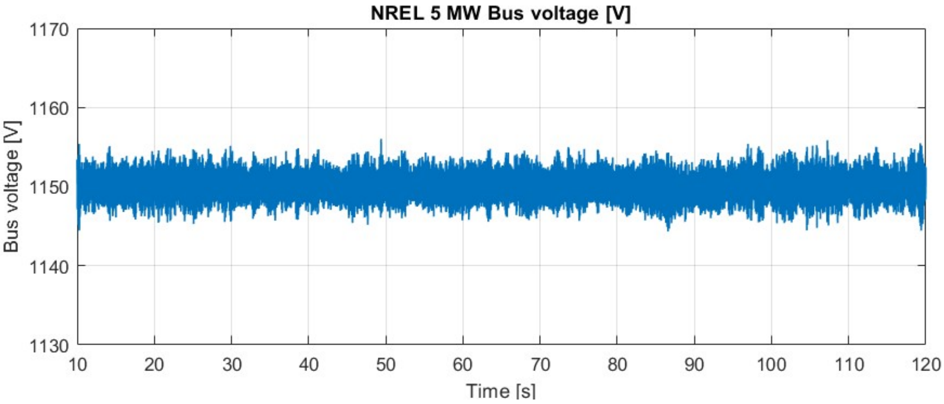

Figure 4.96. DC Bus voltage during operation at partial load of derated 5 MW NREL

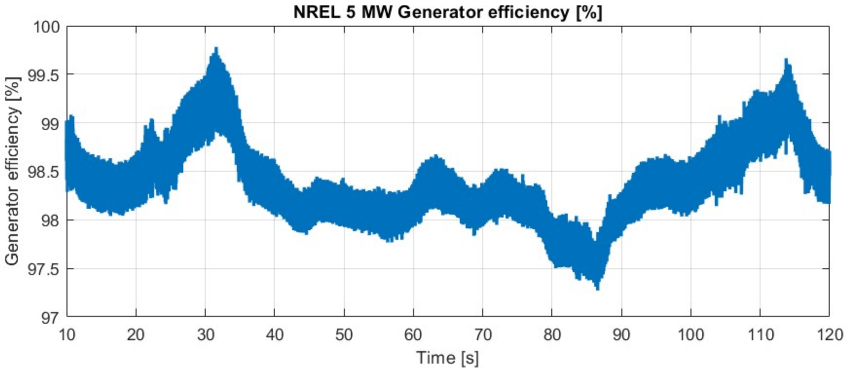

Figure 4.97. Generator efficiency variation during operation at partial load of derated 5 MW NREL

4.4.5. Comparison between baseline and proposed control strategy

In the following simulations, a comparison between the response of the baseline (from reference [86]) and proposed control strategies [89] to a wind speed data covering all the operating range (from 0 to 30 m/s), is presented. The difference between the 2 controllers consists in:

1. The proposed control strategy can be derated.
2. In the presented controller, decuples the rotor of the WECS when the cut-off wind speed is reached.
3. The controller design is based on the linearized model from the second subchapter (4.2. WECS modelling), while the controller developed in reference [86] is based on a first order WECS model.
4. The maximum power point tracking was determined based on the maximum value of the CP table, while in the controller developed in reference [86] was determined by using an external software where the WECS had already implanted a controller.
5. The gain schedule for the PI controller is determined based on the linearization of the rotor torque sensitivity to the blade-pitching angle, while in the reference [86], was determined by performing a linearization analysis of the aerodynamic power sensitivity in a third-party software where the WECS had already implemented a gain schedule PI controller.

Table 4.3. Controller parameter differences with 5 MW NREL baseline controller [85]

Controller parameter	**Baseline**	**Proposed**
Proportional gain at 0º blade-pitch angle	-0.0188 s	-1.474 s
Integral time constant at 0º blade-pitch angle	-0.008	-0.026
Blade-pitch angle where the pitch sensitivity has doubled	6.3 º	11.78 º

2.1.1.7. During the entire operation range

In the following simulation, a comparison between the response of the WECS with baseline and proposed control strategies to a wind speed data covering all the operating range (from 0 to 30 m/s).

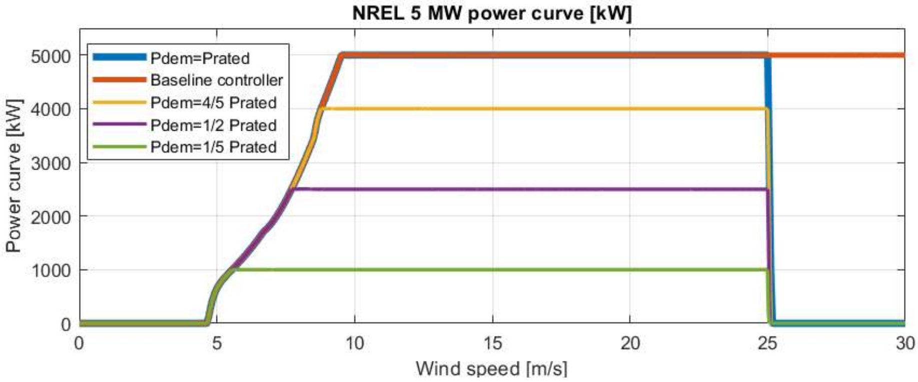

Figure 4.98. Power curve during operating range Baseline vs. Proposed control strategy

In the graph (Figure 4.98), it can be seen that the proposed control strategy at rated demanded power responds as the baseline controller. At cut-off (25 m/s) wind speed, it can be seen that the proposed control strategies stop the power production, while the baseline controller keeps holding the power production at rated output power of the WECS.

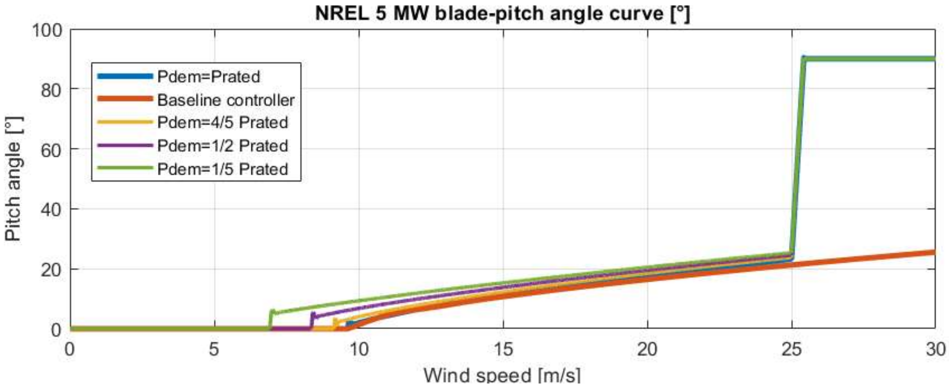

Figure 4.99. Blade-pitch angle during operating range Baseline vs. Proposed control strategy

In diagram-Figure 4.99, it seems that the response of the blade-pitch angle of the proposed control strategy is a little bit underdamped, while the one of the baseline controller seems to have a critical (even a little bit overdamped) response. The proposed blade-pitch angle controller was designed for a quick rise time response in turbulent wind. At cut-off (25 m/s) wind speed, it can be seen that the proposed control strategy pitches the blades to the upper limit (90º) in order to reduce to maximum, the aerodynamic power acting on the rotor, while the baseline controller keeps pitching the blades for rated power production.

2.1.1.8. During operation at full load

In this simulation is presented a comparison between the responses of baseline and proposed control strategies at partial load. The simulated response at partial load consists in the response of the WECS to the turbulent wind speed time series from the diagram (Figure 4.79).

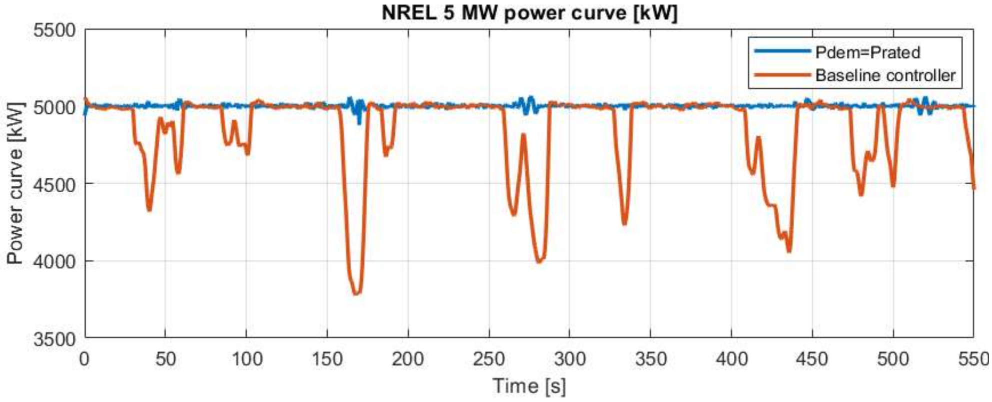

Figure 4.100. Power variation during operation at full load Baseline vs. Proposed control strategy

From Figure 4.100, it can be seen that the purposed controller has a smaller error band with fewer power losses compared to the baseline controller. The reason for this difference in the power response of the controllers is explained in Figure 4.101 Where it can be seen that the proposed blade-pitch controller, responds faster to a turbulent wind speed variation compared to the baseline controller.

The influence of the faster response to a turbulent wind speed variation of the proposed blade-pitch controller, compared to the baseline controller can be seen also in Figure 4.101 In this diagram, the proposed control strategy operates with a smaller error band compare to the baseline controller due to faster response in blades pitching.

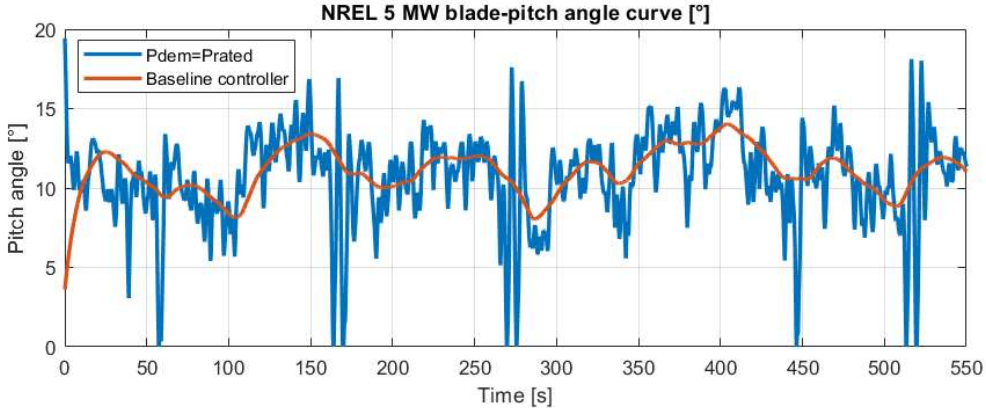

Figure 4.101. Blade-pitch angle variation during operation at full load Baseline vs. Proposed control strategy

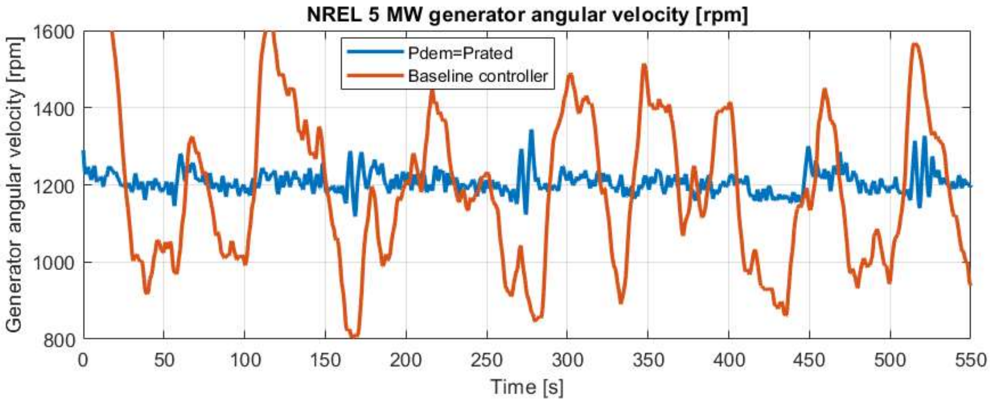

Figure 4.102. Generator angular velocity variation during operation at full load Baseline vs. Proposed control strategy

Because the proposed control strategy operates with a smaller error band in generator angular velocity control compared to the baseline controller, the applied generator torque by the purposed controller presents also a smaller error band compared to the baseline controller.

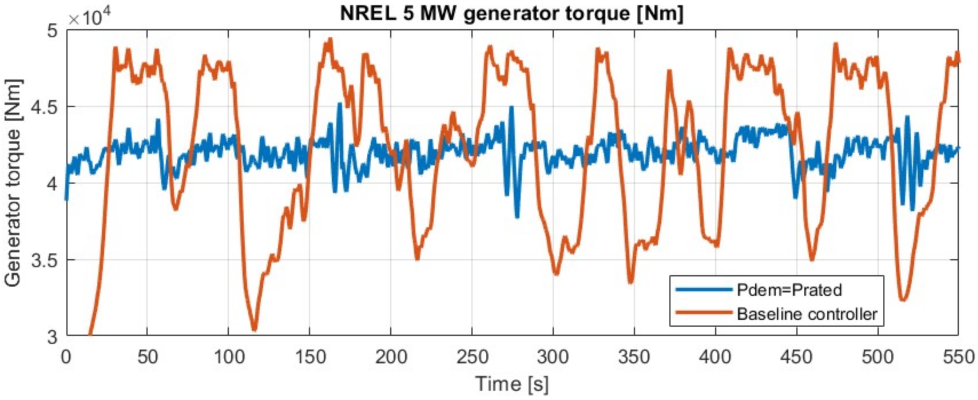

Figure 4.103. Generator torque variation during operation at full load Baseline vs. Proposed control strategy

2.1.1.9. During operation at partial load

In this simulation is presented a comparison between the responses of baseline and proposed control strategies at partial load. The wind speed time series used in this simulation is presented in Figure 4.89.

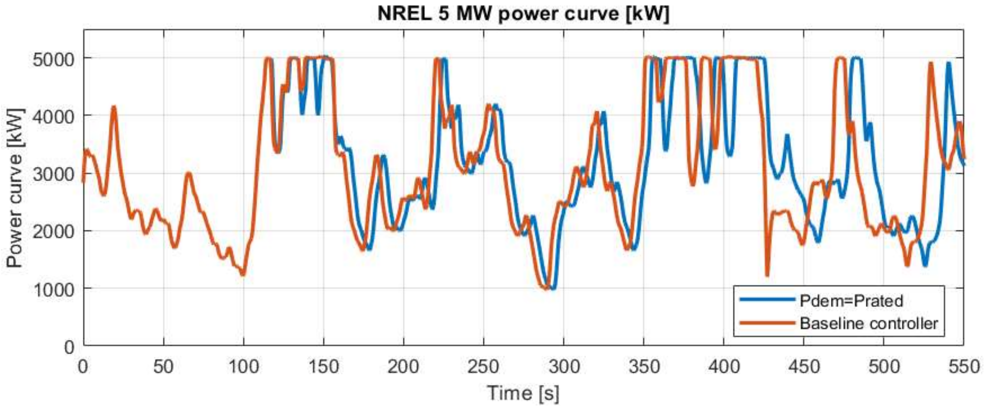

Figure 4.104. Power variation during operation at partial load Baseline vs. Proposed control strategy

From the comparison of the responses of the baseline and proposed control strategies at partial load from Figure 4.104, it can be seen that both controllers respond the same in the first 100 seconds. After the first 100 seconds, the proposed control strategy presents a time response delay compared to the baseline controller. This time delay occurs at the time that the blades start being pitched (Figure 4.105), and can be explained by the fact that by pitching more and faster the blades, larger and faster displacements of the rotor in the wind speed direction are created influencing the wind speed in front of the rotor.

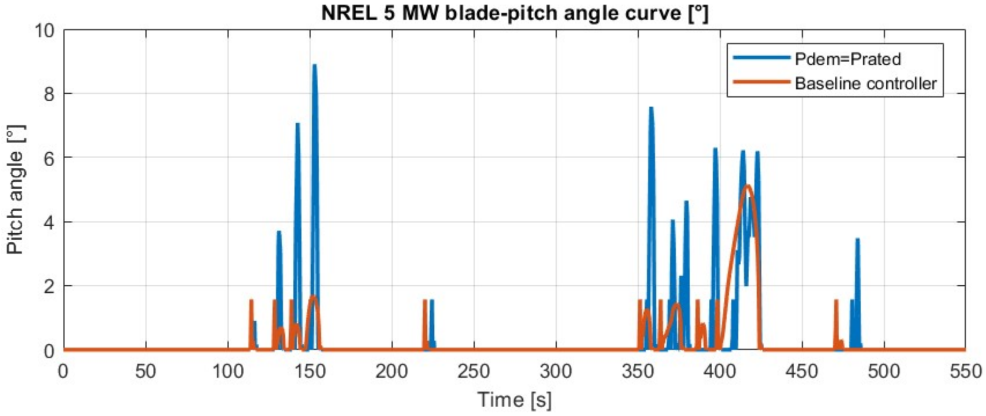

Figure 4.105. Blade-pitch angle variation during operation at partial load Baseline vs. Proposed control strategy

In order to confirm that the time delay between the proposed and baseline controllers doesn't occur when the blades are not pitched. A new simulation is executed for comparing the responses of the proposed control strategy to the baseline controller, where the blade pitch actuator is not enabled. By ensuring that the blade pitch actuator is disabled, the simulation was executed with a real wind speed time series, where the wind speed variates between 2 and 10 m/s, during 9 minutes (Figure 4.106).

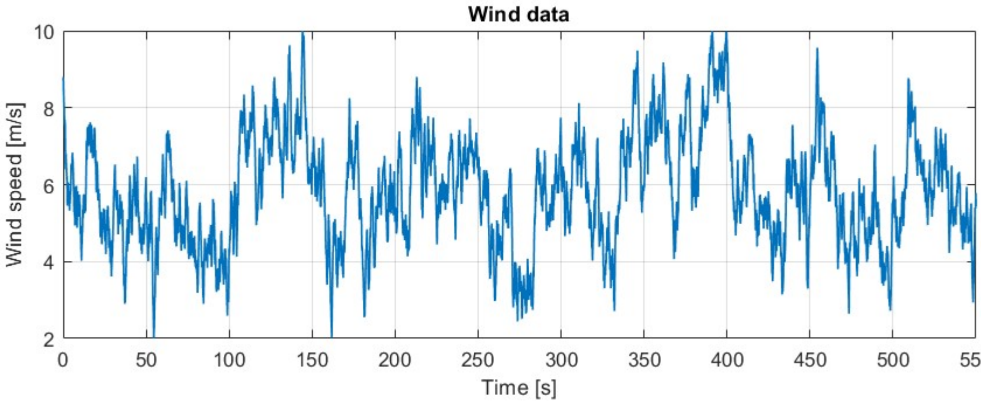

Figure 4.106. Wind speed time series corresponding to operation at partial load ensuring blade pitch actuator to be disable

In the diagram from Figure 4.107, it can be seen that without pitching the blade there is no time delay between the proposed and baseline controllers.

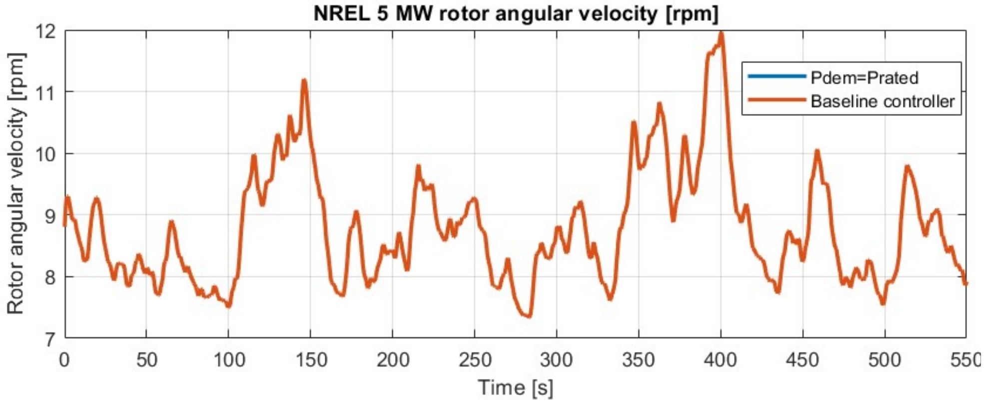

Figure 4.107. Generator angular velocity variation during operation at partial load Baseline vs. Proposed control strategy ensuring blade pitch actuator to be disable

4.4.6. Summary of the WECS simulations

After analyzing the simulations, it can be concluded, that according to the executed simulations, the presented controller responds as expected in calm or extreme wind conditions. Until the cut-in wind speed in front of the rotor, the WECS controller uses the power extracted from to wind only for starting and speeding the rotor. In the startup region (the region from the cut-in wind speed until the generator angular velocity reaches 669.3 rpm), the controller connects the generator load and starts the power production. In region 2, the controller tracks the optimal power production by extracting the maximum power (allowed by its rotor aerodynamics) from the wind. Between partial and full load regions, there is a linear transition given by region 2 ½ in the torque controller design, that allows switching smoothly between the torque and blade-pitch controllers. The blade-pitch controller takes over every time the produced power reaches the demanded power. Finally, by comparing the proposed control strategy to the baseline controller, the power production of the purposed controller settles faster, closer and with a smaller error band compare to the baseline controller, due to faster response in blade pitching angle. The faster response in blade pitching angle produces less power production fluctuations and losses during operation at full load in high turbulent wind. The proposed control strategy decouples the rotor of the WECS at cut-off (25 m/s) wind speed and reduces to 0 the power production.

4.5. WECS chapter conclusion

Finally, from chapter ***4. WECS***, it can be concluded, that by combining the nonlinear model of the WECS resulted from the combination of the nonlinear models of the WECS components from reference [84] (aerodynamics, tower and blade) and [88] (Drive train, generator and blade pitch actuator), a nonlinear model (subchapter ***4.2. WECS modelling***) capable to simulate a WECS, including the cut-off, was developed.

In ***4.3 WECS control strategy***, it is developed a control system that combines a first control level (DFIG rotor and grid side controllers, [87]) with a second control level (generator-torque and blade-pitch controllers [88]). The first control level (called the DFIG controller) controls two pulse modulation bandwidths (the DFIG rotor and grid side) that regulate the convertors switch pulses. The second control level, called the wind turbine (WT) controller, consists of two controllers (the generator-torque controller and the blade-pitch controller) that regulate the rotor and generator torque and speed. A torque controller has been developed, based on the one from [86], which has been improved through its ability to adapt power production to power demand (derating the WECS power when the power demand is lower than the rated power). Through the proposed solution, the generator torque is reduced when the wind reaches the cut-off speed or when the generated power reaches demanded power. Simultaneously, the blade pitching actuator is enabled.

According to the personal methodology for developing the proposed gain scheduled PI controller for controlling the blade-pitch angle, an improvement compares to the baseline blade-pitch angle controller from reference [86], was obtained. The improvement was obtained by scheduling the proportionality constant (K_p) and integration time (K_i) of the PI blade-pitch controller; the scheduled K_p and K_i values were obtained based on the linearization of the WECS model, by using the Taylor series approximation and by determining a mathematical equation that allows the calculation of the gains scheduling according to the current value of the WT blade-pitch angle (β) and the value of the WT blade-pitch angle for which the WT rotor torque has doubled (βk).

The improvements in the blade-pitch controller are confirmed by the analysis of the simulations results from subchapter ***4.4. WECS simulations***, where it can be clearly seen that the power production of the purposed controller settles faster, closer and with a smaller error band and produces less power production fluctuations and losses during operation at full load in high turbulent wind, due to faster response in blade pitching angle.

As personal contribution to the controller presented in reference [86], it can be considered also the methodology for developing the WECS controller, a mathematical methodology that does not require the help of any external instrument for control development or parameters identification and can be developed for any WECS that presents the required parameters from Table 4.1.

5. PUMPING SYSTEMS POWERED BY A PHOTOVOLTAIC ENERGY CONVERSION SYSTEM (PSPPECS)

The current chapter presents the modelling and simulation of a pumping system powered by a photovoltaic energy conversion system (PSPPECS). The first subchapter (***5.1. PSPPECS description***) presents a short description of a general PSPPECS and its components. The second subchapter (***5.2. PSPPECS modelling***) consists of a nonlinear mathematical model of the described PSPPECS, and the third subchapter (***5.3. PSPPECS control strategy***) presents the proposed control strategy. The fourth subchapter (***5.4. Monitoring system***) presents the development and implementation of a proposed non-intrusive monitoring system for determining the performance of an existing isolated high-power photovoltaic pumping system. In the fifth subchapter (***5.5. PSPPECS simulations***), the performance of the proposed control strategy is determined by analyzing several performance indicators during four simulations. A simulation for each type o day: a clear sky day, one day with one big cloud, one day with many small and quick clouds and one fully cloudy day. Finally, in the last subchapter (***5.6. Conclusions***) are presented the chapter conclusions.

5.1. PSPPECS description

In the last decade, more and more irrigation systems have been upgraded with sprinklers, or drip irrigation systems, for increasing water usage efficiency. Due to this reason, the energy consumption by the irrigation systems increased drastically leading to such a cost of the energy consumption, that nowadays, represents the highest cost in operating an irrigation system. Currently, the PSs, especially the ones used in agricultural irrigation, are powered by the national power grid or by diesel or gasoline generators, where the national power grid is missing (remote areas). Because most of these systems are used during the summer, with maximum demand on the hottest and sunniest days of the year, the solution for powering an irrigation PS with PVGs (Photovoltaic generators) leads to an excellent integration of the PVGs into such systems.

The continuing rise of the electricity, together with a favorable legislation and a reasonable stable low price the photovoltaic panels, is making the industrial and agricultural sector consider installing pumping systems powered by photovoltaic generators. However, despite the economic profitability and the independence from the fluctuations of the electricity prices, offered by photovoltaic power pumping systems and the fact that their market demand is constantly growing, those systems still need technological maturation in order to become robust, durable, reliable and efficient.

Given the above, the current chapter proposes a control strategy that through proper tuning, ensures higher efficiency, robustness, durability, and reliability. In this chapter, it is also presented a non-intrusive methodology for monitoring, the performance of an isolated high-power photovoltaic pumping system through sensor measurements.

Figure 5.1. Existing PSPPECS in Aragon, Spain

The existing isolated high-power photovoltaic pumping system, considered in this work and used in model and control strategy validation, is located in the Aragon region in Spain [54, 94], and it is used for direct irrigation of tree fruit orchards. In Figure 5.1, it can be seen the photo of the real system and in Figure 5.2 its layout and the main components: PECS, submersible pump, induction motor, hydraulic (irrigation) network, variable frequency drive (VFD) and the system controller.

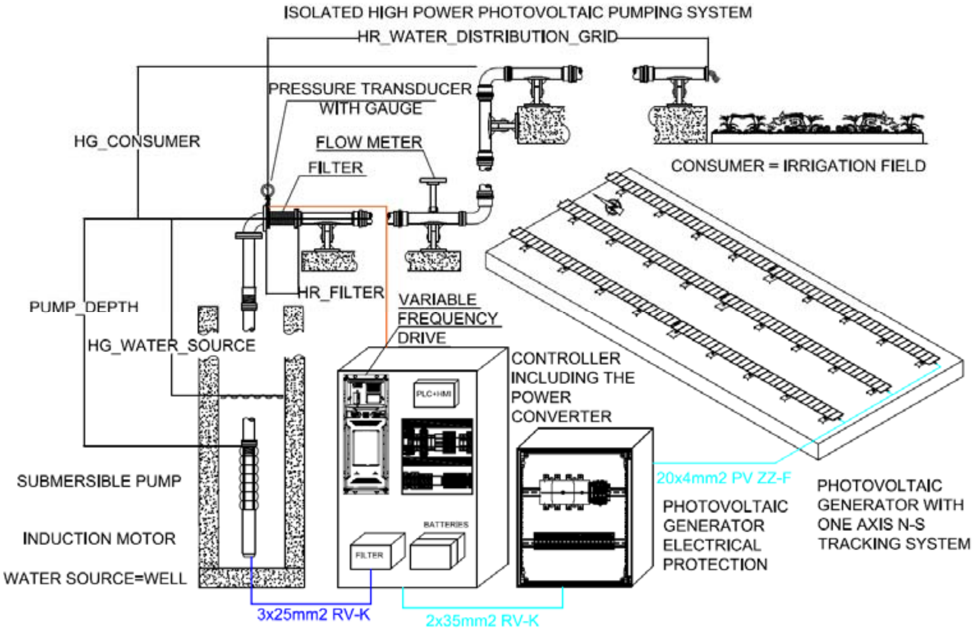

Figure 5.2. PSPPECS layout [54]

5.1.1. PECS

The PECS considered in this chapter, is the same as the one described in chapter 3. The 56.95 kW PECS powering the pumping system, consists of 170 photovoltaic panels of 335 W [58] (its technical specifications can be seen in Table 3.1) combined in 10 strings of 17 photovoltaic panels in series (series of 5.695 kW). Another photovoltaic panel of 335 W [58] is used for powering the control unit. The 171 photovoltaic panels are distributed on 3 decentralized self-operated horizontal single-axis trackers (HSAT) [61] (57 on each tracker). The trackers have N-S (north-south) orientation and a 110º range of motion around their axis. The trackers' technical specifications can be seen in Table 3.2.

5.1.2. Submersible pump

The same submersible pump [44], as the one described in chapter 2, is considered also in this chapter for water collection from a well and distributing it into an irrigation hydraulic network. The submersible pump's technical specifications can be seen in Table 2.3. Even though the pump is installed at a depth of 40 m (PUMP_DEPTH≈ 40 m below the ground level in Figure 5.2), the water is extracted from a depth of 30.5 m (HG_WATER_SOURCE≈ 30.5 m dynamic level in Figure 5.2). The maximum extractable flow from the well is 91.85 m^3/h.

5.1.3. Hydraulic network

The same hydraulic network described in chapter 2, is considered also in the current chapter. The considered pumping system irrigates 5 sectors. In Table 2.5 are presented the nominal values of the key parameters for each sector (operating points), obtained by analyzing the collected data collected with the monitoring system.

5.1.4. Induction motor

The pump is powered by a 50 Hz, 3 phase (400V) induction motor [44] of 30 kW. The induction motor has 2 poles leading to an angular velocity of 2870 rpms. The current consumption by the motor is 101 A considering a 0.85 power factor, and an efficiency of 84%. In Table 5.1 it can be seen the technical specifications of the induction motor.

Table 5.1. Induction motor technical specifications

Properties	Value	Symbol	Unit
Induction motor nominal power	30	P_{IM}	kw
Induction motor efficiency	84	η_{IM}	%
Induction motor rated frequency	50	f_{IM}	Hz
Induction motor rated voltage	400	v_{IM}	V
Induction motor rated current	101	i_{IM}	A
Induction motor number of poles	2	p_{motor}	-
Induction motor nominal speed	2870	ω_{ps}	rpm
Induction power factor (cos φ)	0.85	pf_{IM}	-

5.1.5. Variable frequency drive

The AC induction motor is powered driven by a 45 kW variable frequency drive [37] working at a voltage of 400 V with a maximum continuous current of 94 A. The variable frequency drive has 2 analog inputs, 2 analog outputs, 3 digital inputs, 3 configurable digital outputs; 2 relay outputs, one safe torque off input, 2 Modbus RS485 communication ports and an on-board PLC (Programmable Logic Controller). The onboard PLC includes besides the programming functions, two PID controllers with anti-windup and user scaling to provide flow-specific functionality, a water hammer control with S-ramp decelerations and low load condition monitoring and hysteresis for dry pump detection [37]. In Table 5.2 it can be seen the technical specifications of the variable frequency drive.

Table 5.2. Variable frequency drive technical specifications

Properties	Value	Symbol	Unit
Variable frequency drive rated power	45	P_{vfd}	kW
Variable frequency drive rated voltage	400	V_{vfd}	V_{ac}
Variable frequency drive maximum continuous current	94	I_{vfd}	A
Analog inputs	2		-
Analog outputs	2		-
Digital inputs	2		-
Digital outputs	2		-
Relay outputs	2		-
Safe torque inputs	1		-
Communication protocols	2 x Modbus RS485		

5.1.6. Programmable logic controller (PLC)

Even though the variable frequency drive has already integrated an on-board PLC (Programmable logic controller), the partial load controller (MPPT controller) and the full load controller (pressure controller) are programmed into a separate PLC [95] that communicates with the variable frequency drive through Modbus RS485 communication. The PLC has integrated a Multi-touch HMI (Human Machine Interface), used by the user for operating the entire system [95]. In Table 5.3 it can be seen the technical specifications of the PLC.

Table 5.3. PLC technical specifications

Properties	Parameter value or description
Touch sensor	Multi-touch panel
Touch technology	Projective Capacitive Touch (PCT)
Processor	ARM Cortex-A9 800 MHz
Memory	DRAM: 512 MB RAM, Flash: 1GB SLC, NVRAM: 128kB Retain
Removable memory	SD-card type: SDSC, SDHC
Cooling	Fanless CPU and system cooling, natural convection-based passive cooling
Interfaces	2 x Ethernet 10/100 Mbps; 1 x USB host 2.0, 1 x USB device 1 x RS232, 1 x RS485, 1 x CAN
Operating system	Windows Embedded Compact 7 Pro
Degree of protection	IP65 at the front, IP20 at the rear
Operating temperature	0 °C - +50 °C

5.2. PSPPECS modelling

The typology of the considered PSPPECS is presented in Figure 5.3, and contains a submersible centrifugal pump powered by a PECS, and delivers water from a well directly into a hydraulic distribution network at different operating points.

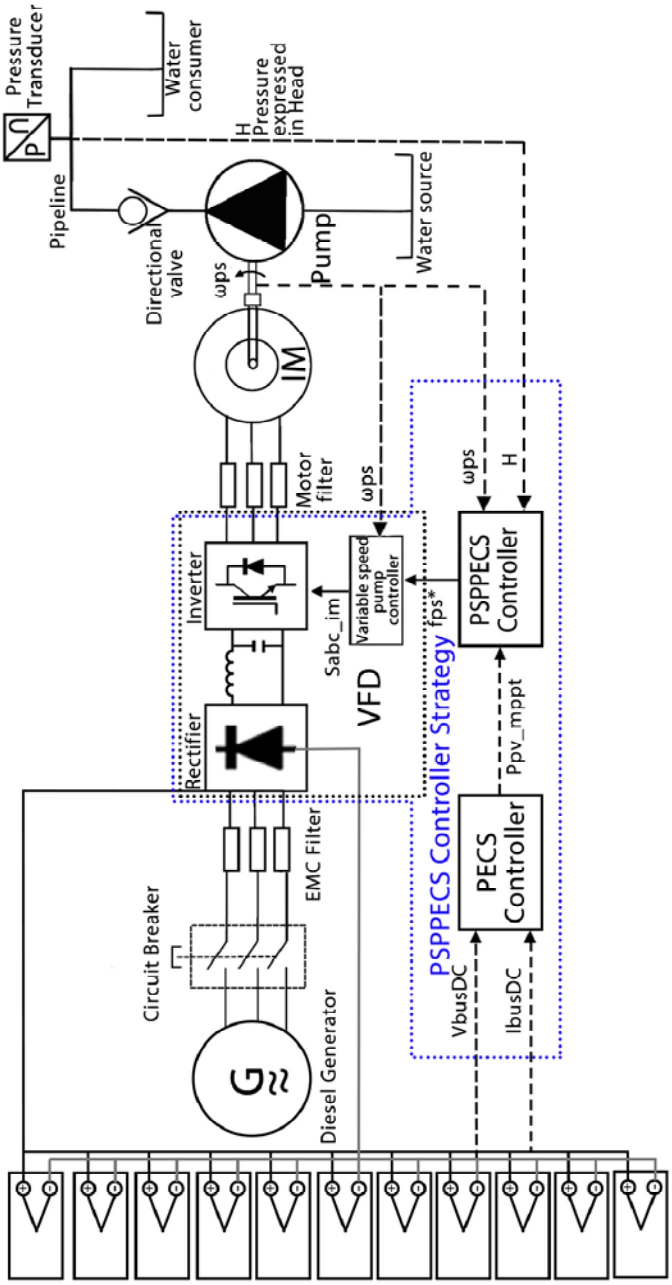

Figure 5.3. Structure of the PSPPECS control system

The PSPPECS nonlinear model is developed by combining the pumping system model developed in section ***2.2. Pumping system modelling*** with the PECS model developed in section ***3.2. PECS modelling***. The current produced at a certain voltage by the dynamic PECS model (Equation 3.36), powers the VFD (induction motor driver) model (Equation 2.3). The VFD drives the induction motor, which makes the pump discharge water into the hydraulic network.

5.3. PSPPECS control strategy

The PSPPECS proposed control strategy is made of 3 control structures in cascade, as presented in Figure 5.3. To the variable speed pump controller (developed in section ***2.3. Pumping system control strategy***), a PSPPECS controller has been added, to which the PECS Controller (developed in section ***3.3. PECS controller***) has been added.

The variable speed pump controller is necessary to drive the pump induction motor through a VFD at different reference speeds. It contains two PI regulators, one for the speed and one for the flux connected in cascade with two equally tuned PI current regulators, one to control the "*d*"-axis (real components) currents and one for the "*q*"-axis (imaginary components) currents. The electrical frequency error $\Delta f=(fm^*-fm)$ (the difference between the reference and current pump frequency) is provided by the PSPPECS controller (Equation 5.1) to the PI speed controller from the variable speed pump controller:

$$\Delta f=\begin{cases}\dfrac{-p_{motor}\cdot\omega_{pss}}{2\cdot\pi} & P_{PECS}<P_{psmin} & \multirow{2}{*}{$H<H^*$}\\ \dfrac{p_{motor}\cdot fm^*}{6\cdot\pi\cdot\left(P_{pump}\right)^*}\cdot\left(P_{PECS}-P_{pump}\right) & P_{PECS}\geq P_{psmin} & \\ \dfrac{p_{motor}\cdot fm^*}{4\cdot\pi\cdot H^*}\cdot\Delta H & & H\geq H^*\end{cases} \tag{5.1}$$

where:

P_{psmin} represents the power required by the pump motor to start its proper operation (the power required for pumping the flow necessary for the motor cooling);
P_{PECS} is the power generated by the PECS, P_{pump} is the current power of the pump;
fm and fm^* are the induction motor current and reference electrical frequencies;
p_{motor} is the induction motor's pairs of poles;
ω_{pss} is the current speed of the pump;
and $\Delta H=(H^*-H)$ the head (pressure) error (the difference between the reference and current pump head).

The PSPPECS controller ensures the control in 3 specific cases:

1. when the pumping head is higher than its reference ($H\geq H^*$), the PSPPECS controller executes a pumping head control;
2. when the pumping head is lower than its reference ($H<H^*$), and the power produced by the PECS it is lower than the minimum power required to operate the pump ($P_{PECS}<P_{psmin}$), the PSPPECS controller decelerates the PS;
3. when the pumping head is lower than its reference ($H<H^*$), and the power produced by the PECS it is higher than the minimum power required for the pump operation ($P_{PECS}\geq P_{psmin}$), the PSPPECS controller drives the PS so that its absorbed power tracks the PECS produced power;

The PECS controller is necessary for operating the PECS at its maximum power point (MPP) and passing it as a reference to the PSPPEC controller.

5.4. Monitoring system

A monitoring system has been developed and implemented to determine the performance of the photovoltaic pumping system, a system more precise than the current ones (using the methodology proposed by IEC 62253 [96]), due to its ability to evaluate transitory regimes and detect electric and hydraulic shocks. The proposed monitoring system uses a non-intrusive monitoring data logging and acquisition (whose layout is presented in Figure 5.4) that measures and stores the transducers values each second. The transducers used by the monitoring system are: a calibrated photovoltaic cell [97] for measuring the irradiance and cell temperature, a DC voltage transducer [98], a pressure transducer [99], a volume flow transducer [100] and a temperature sensor [101] for measuring the water temperature.

5.4.1. Calibrated photovoltaic cell

The calibrated photovoltaic cell [97], is used for measuring the solar radiation, the photovoltaic cell's temperature and the ambient temperature. The measured data is sent through Modbus Rs485 communication to the data logger [102]. In Table 5.4 it can be seen the technical specifications of the calibrated photovoltaic cell.

Table 5.4. Calibrated photovoltaic cell technical specifications

Properties	Value	Unit
Nominal supply voltage	12	
Supply voltage range	6 to 28	V_{DC}
Maximum consumption	90	mW
Operating temperature range	-20 to + 50	ºC
Degree of protection	IP54	
Communications protocol, Mode	Modbus RTU Rs485 Slave	
Transmission speed	9600 / 38400	bps
Maximum distance	500	m

5.4.2. DC Voltage transducer

A DC voltage transducer [98], is used as a configurable and universal galvanic isolator (DC) that measures the DC voltage of the photovoltaic generator. The measured data (0-1000 V DC) is sent as analog signal (0-10 V DC) to the data logger. In Table 5.5 it can be seen the technical specifications of the voltage transducer.

Table 5.5. Voltage transducer technical specifications

Properties	Value	Unit
Nominal supply voltage	24	V_{DC}
Supply voltage range	20 to 30	V_{DC}
Voltage Input	0 to 1000	V_{DC}
Isolation Input/Output	1500	V
Isolation Input/ Supply	1500	V
Output 1	0/20 or 4/20 or 0/5	mA
Output 2	0/10 or 0/5 or 0/±10	V
Maximum global error	0.05	%
Linear error	0.03	%
Operating temperature	-25 to 70	ºC

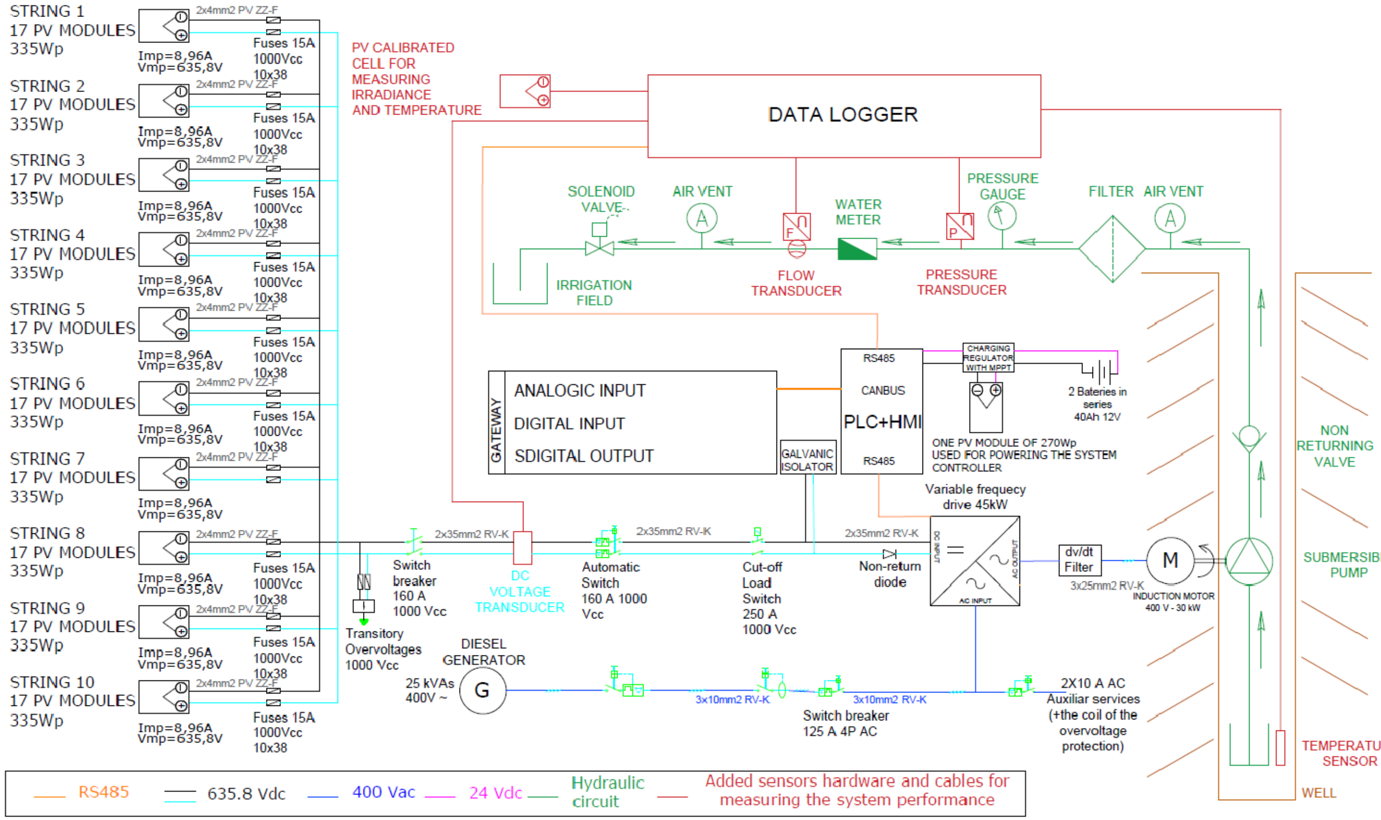

Figure 5.4. The monitoring system proposed for determining the PSPPECS performance

5.4.3. Pressure transducer

The pressure transducer [99], is used for measuring the relative pressure within a range of -1 to 10 bars. The measured pressure data is sent as an analog signal (4-20 mA) to the data logger [102]. In Table 5.6 it can be seen the technical specifications of the pressure transducer.

Table 5.6. Pressure transducer technical specifications

Properties	Value	Unit
Pressure Measuring range	-1 to 10	bar
Pressure resistance	25	bar
Bursting pressure	300	bar
Operating voltage	-20 to + 50	ºC
Medium temperature	-40 to 90	°C
Ambient temperature	-40 to 90	°C
Storage temperature	-40 to 100	°C
Pressure cycles (min.) across lifetime	60 million times for 1.2 x nominal pressure	
Shock resistance	50 g (DIN EN 60068-2-27, 11 ms)	
Vibration resistance	20 g (DIN EN 60068-2-6, 10...2000 Hz)	

5.4.4. Volume flow transducer

The volume flow transducer [100], is used for measuring the pumped volume flow. The measured flow data is sent as frequency signal through impulses to the data logger [102] (each impulse represents 100 l). In Table 5.7 it can be seen the technical specifications of the volume flow transducer.

Table 5.7. Volume flow transducer technical specifications

Properties	Value	Unit
Nominal flow	60	m^3/h
Nominal Diameter	100	mm
Maximum flow (short duration)	250	m^3/h
Maximum flow (permanent duration)	125	m^3/h
Minimum flow	1.5	m^3/h
Pressure loss at maximum permanent flow	0.2	bar
Maximum operating temperature	50	°C
Maximum admissible pressure	16	bar

5.4.5. Temperature sensor

The temperature sensor PT100 [101], is a temperature dependent component and its resistance rises linearly with the temperature (within a precision of ±0.5°C), and in the current work is used for measuring the water temperature from the well. The measured temperature data is sent as an analog signal (4-20 mA) to the data logger [102]. In Table 5.8 it can be seen the technical specifications of the temperature sensor.

Table 5.8. Temperature sensor technical specifications

Properties	Value	Unit
Temperature measuring range	-50 to +230	°C
Temperature measuring resolution	±0.5	°C
Measuring current	max. 1mA (no self-heating)	

5.4.6. Data logger

The data logger [102], is used for storing the collected data each second. The stored data is collected from the analog sensors measurements (temperature sensor, voltage and pressure transducer), frequency sensor measurements (flow transducer), measured data from the photovoltaic calibrated cell (solar irradiation and photovoltaic cell's temperature) and from the Variable frequency drive (Induction motor frequency, angular velocity, voltage, power and current consumption) trough Modbus RTU RS 485 communication. In Table 5.9 it can be seen the technical specifications of the data logger.

Table 5.9. Data logger technical specifications

Properties	Value	Unit
Supply voltage range	5 to 30 V DC	V_{DC}
Frequency channels (pulse counters)	Up to 16 (10 physical plus 6 extra)	
Analog channels (voltage)	Up to 23 (15 physical plus 8 extra)	
5V outputs	10 (1 for every physical frequency channel)	
Modbus RS485 (Data Logger as Master)	3	-
Modbus RS485 (Data Logger as Slave)	1	-
Modbus TCP (Data Logger as Slave)	1	-
Ethernet port	1	-
Collected data	1 second data storage Averaging each 1, 5 and 10 minutes	
Connectivity	Global remote access - 2G/3G/4G Modem	

5.4.7. Monitoring system collected data

The monitored isolated high-power photovoltaic pumping system irrigates 5 sectors whose pressure reference was preset. In Table 5.10 are presented the nominal values of the key parameters for each sector (operating points), obtained by analyzing of the collected data during the monitoring campaign.

Table 5.10. Monitoring system collected data

Sector	**Htotal (mca)**	**Q (m3/h)**	**Pressure (bar)**	**Pressure Reference (bar)**	**V bus DC (V)**	**Isc (A)**	**Voc (°C)**	**Power (kW)**	**Freq. (Hz)**
1	68	54	3.4812354	3.5	681.520	8.005	38.647	12.029	33.0518
2	76	84	4.1882240	4.2	644.28	8.44	34.961	22.319	39.0077
3	76	91.5	4.4208378	4.4	624.023	8.049	32.532	25.301	40.3471
4	76	90	4.168346	4.2	653.076	7.783	37.744	24.676	40.0732
5	72	85.5	3.7906919	3.8	652.832	7.576	38.416	21.890	38.6260

From the entire measurement campaign, 4 types of representative days were selected, based on which the further discussions in this paper will be held:

a) A clear sky day, without any clouds;
b) A day where a large and dense cloud passed slowly over the PV generator;
c) A day with many small clouds that passed quickly and sequentially over the PV generator;
d) A fully cloudy day.

5.5. PSPPECS simulations

Combining the PSPPECS control strategy presented in the third subchapter (5.3. PSPPECS control strategy), with the dynamic model of the PSPPECS presented in the second subchapter (5.2. PSPPECS modelling), a simulator was developed in Simulink [43].

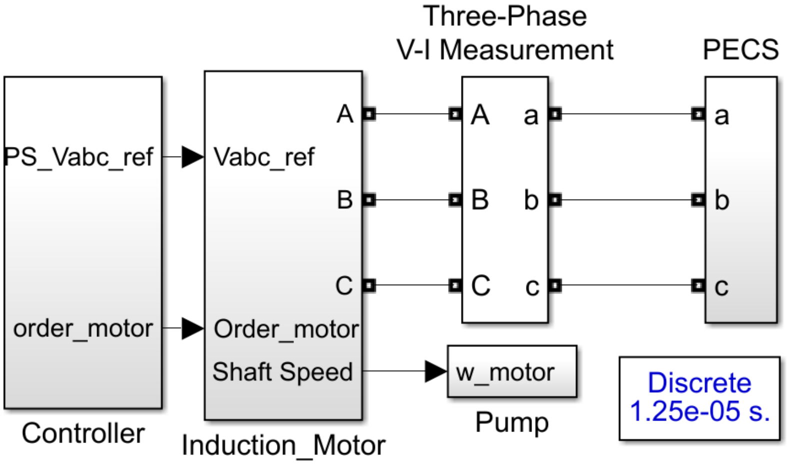

Figure 5.5. PSPPECS flow chart in Simulink

Using the developed PSPPECS simulator, four simulations were executed in order to analyze, evaluate and compare the PSPPECS simulation response with the PSPPECS real response (from the monitoring campaign) during a clear sky day, a day with a big cloud, a day with many small clouds and a fully cloudy day.

It has to be mentioned that due to the reason that the monitoring campaign was executed before developing the PSPPECS simulator, the PI controller in the real system was tuned by trial-and-error tuning method, and the proportional and integral gains are not the same as the ones utilized in the simulator.

5.5.1. Clear sky day

In the first simulation, the PSPPECS simulator performance is compared with the real PSPPECS performance, during a clear sky day. The simulator inputs, the global irradiance reaching the PV generator plane and the PV cell temperature, can be seen in Figure 3.14 and Figure 3.15.

In Figure 5.6, it can be seen a comparison between the power responses of the PSPPECS simulator and real installation. At the beginning of the day, the real system starts its operation with several failed attempts and an overshoot. This can be explained by the reason that the PI gains are not the same for the simulator and real installation, as they were identified differently, for the simulator they were identified considering an equivalent 2nd order system, and for the real installation they were identified using trial and error method. During the transitions through different operating points, the simulator's dynamical response matches the real system response. At the end of the day, when the power produced by the PECS decreases, the simulator tracks perfectly the PECS produced power, while the real system presents huge oscilations, due to the poor capabilities of the controller or improper tuning method.

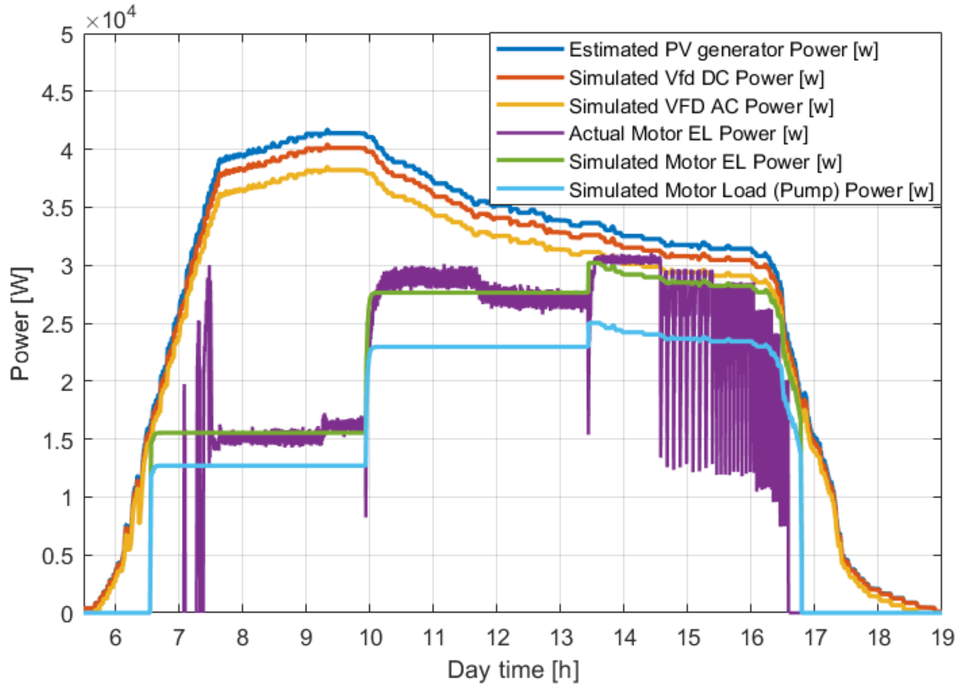

Figure 5.6. PSPPECS power response during a clear sky day

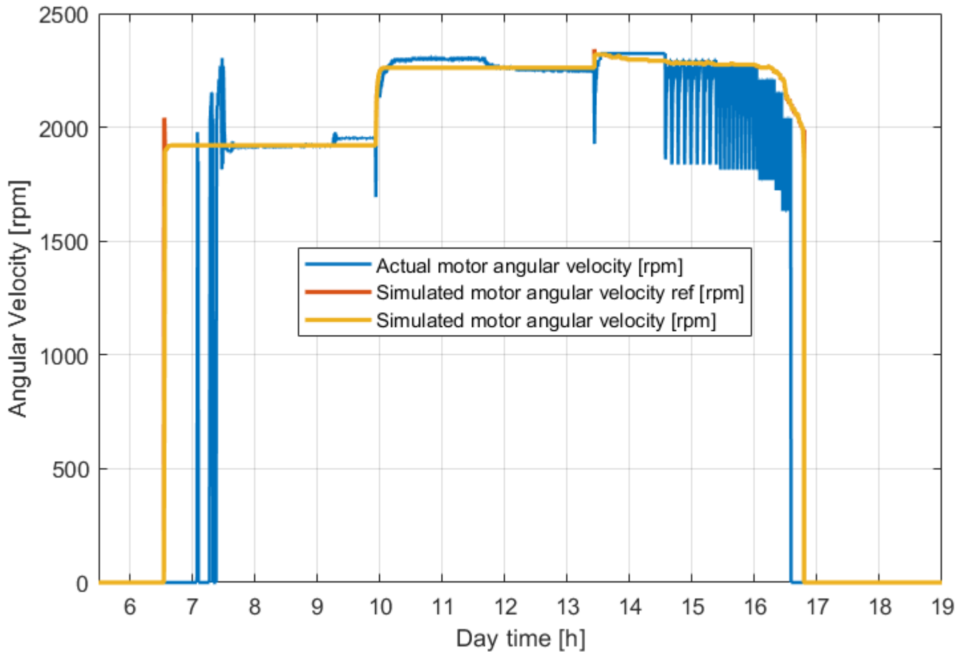

Figure 5.7. PSPPECS induction motor angular velocity response during a clear sky day

In Figure 5.7, it can be seen a comparison between the induction motor's angular velocity of the PSPPECS simulator and real installation. Same as in Figure 5.6, at the beginning of the day, the real system starts its operation with several failed attempts and an overshoot and at the end of the day, the speed controller of the real system presents many huge oscillations, due to the poor capabilities of the controller or improper tuning method. Overall, Figure 5.7 shows that the real system operates a bit over 9 hours during a clear sky day, while the simulator claimed a 10 hours of operation considering the same conditions.

In Figure 5.8 is depicted the comparison between the induction motor torque of the considered PSPPECS during the monitored and simulated clear sky day. In Figure 5.8 the same dynamic response behavior as in Figure 5.7 and Figure 5.6 can be seen: an overshoot when the real system starts its operation and many huge oscillations when the pumping system should track PECS MPP.

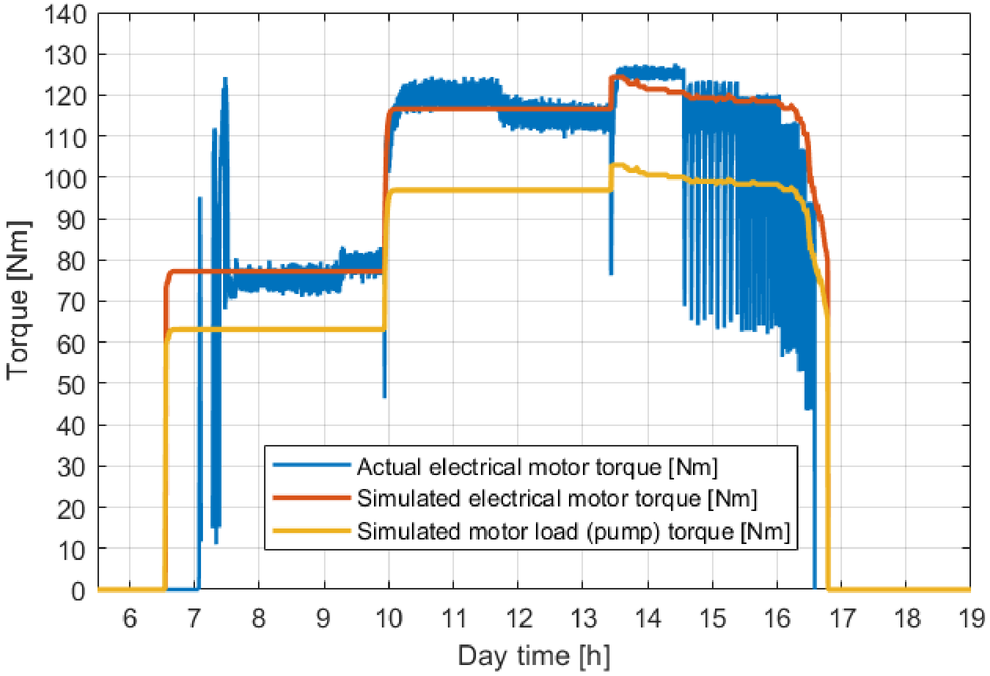

Figure 5.8. PSPPECS induction motor torque response during a clear sky

Figure 5.9 depicts the comparison between the actual (real system) and simulated pump head variation during the considered clear sky day. Due to the limited range (-1 bar to 10 bar) of the pressure transducer [100] and its conversion to head (m), it cannot be confirmed, but it is suspected that cavitation (recorded pressure can be below atmospheric pressure) occurred when the real system started its operation after the failed attempts, and that water hammer (occurred due to overpressure) occurred at the end of the operation when the pumping system stopped. While changing the sectors (transitioning to different pressure points) the simulated response matches the real one.

In Figure 5.10, is presented a comparison between the simulated and real pump's discharged flow. A 7% difference can be seen between the total real (708.0538 m^3) and simulated flow 758.5974 m^3 of the considered pump during a clear sky day.

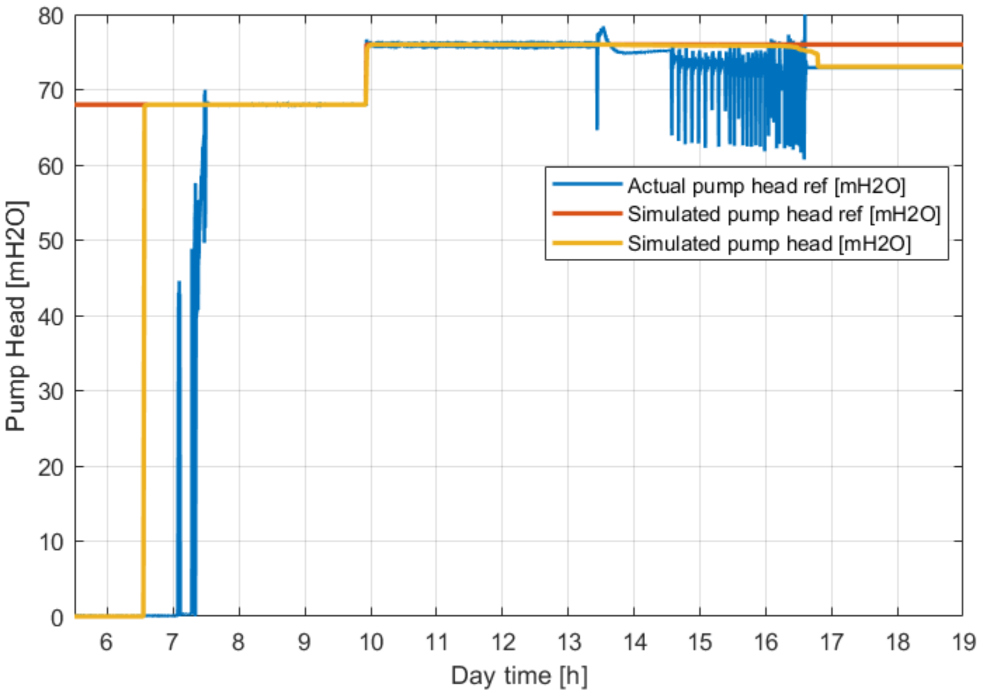

Figure 5.9. PSPPECS pump head response during a clear sky

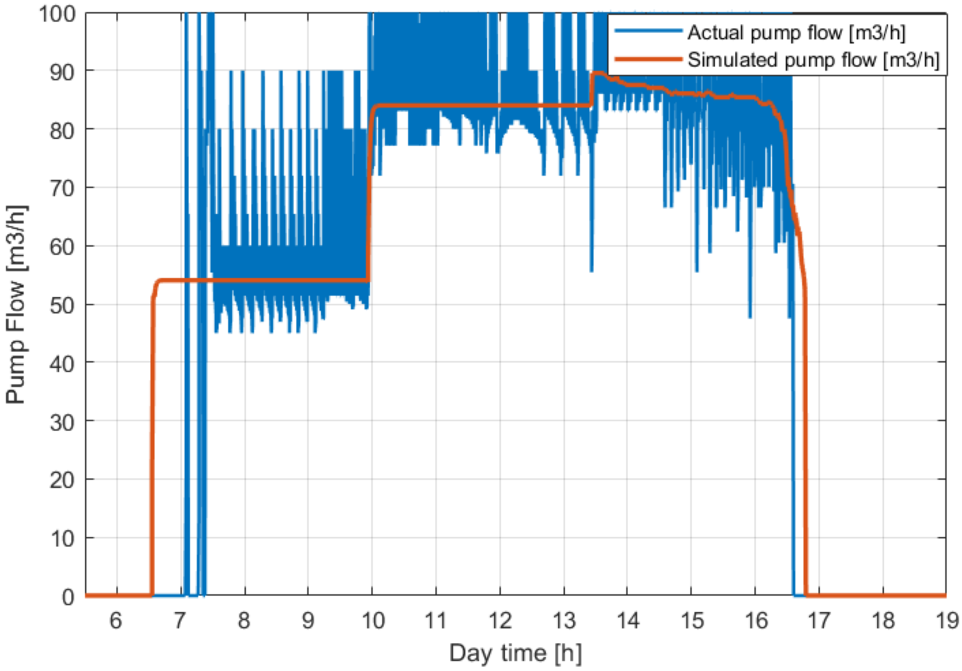

Figure 5.10. PSPPECS pump discharge response during a clear sky

5.5.2. Big cloud day

In the second simulation, the PSPPECS simulator performance is compared with the real PSPPECS performance, during a day with one big cloud. The simulator inputs, the global irradiance reaching the PV generator plane and the PV cell temperature, can be seen in Figure 3.14 and Figure 3.15.

In Figure 5.11, it can be seen a comparison between the power responses of the PSPPECS simulator and real installation. At the beginning of the day, the simulated system starts one hour earlier than the real system, and this fact can be explained by the higher threshold of the required power to start the pumping system in the real system compared to the simulator (where the power threshold to start the system it is exactly calculated). During the transitions through different operating points, the simulator's dynamic response matches quite well with the real system response. In Figure 5.11, it can be seen the control strategy of the real system, has implemented a safety measure that is missing in the Simulink simulator, that after two unsuccessful attempts to start the pumping system executes a delay of 10 minutes until the next attempt. At the end of the day, only the simulator stops the operation of the pumping system by tracking the last usable produced power by the PECS, while the real system stops its operation by powerlessness.

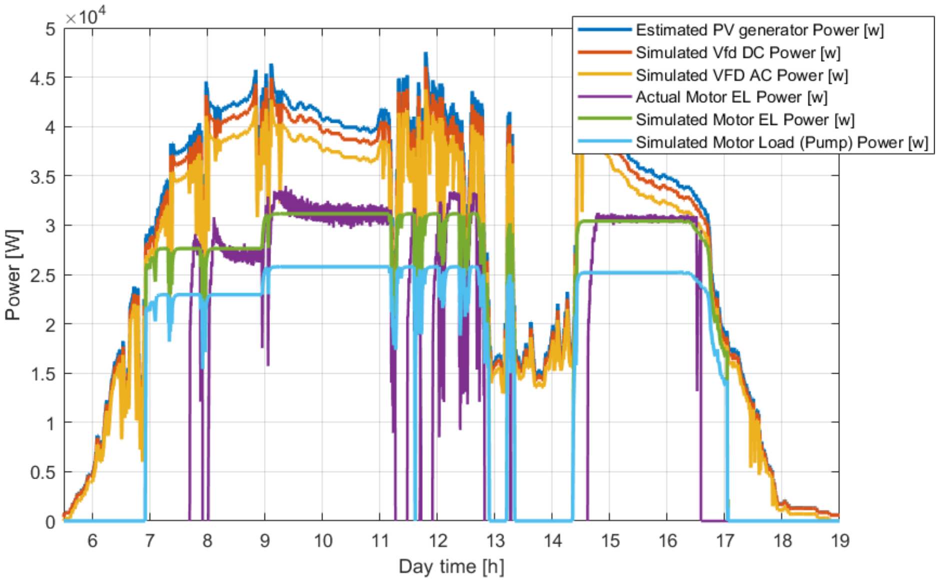

Figure 5.11. PSPPECS power response during a day with a big cloud

In Figure 5.12, it can be seen a comparison between the induction motor’s angular velocity of the PSPPECS simulator and real installation. Same as in Figure 5.11, the simulated system starts one hour earlier than the real system, as a result of the different starting power thresholds. The real system safety measure that is missing in the Simulink simulator, where after two unsuccessful attempts to start the pumping system, the controller executes a delay of 10 minutes until the next attempt it is confirmed also by angular velocity variation from Figure 5.12. At the end of the day, only the simulator stops the operation of the pumping system by deceleration, while the real system stops its operation by falling. Overall, Figure 5.12 shows that the real system operates for around 6 and a half hours, while the simulator claims almost 9 hours of operation during the considered day with a big cloud.

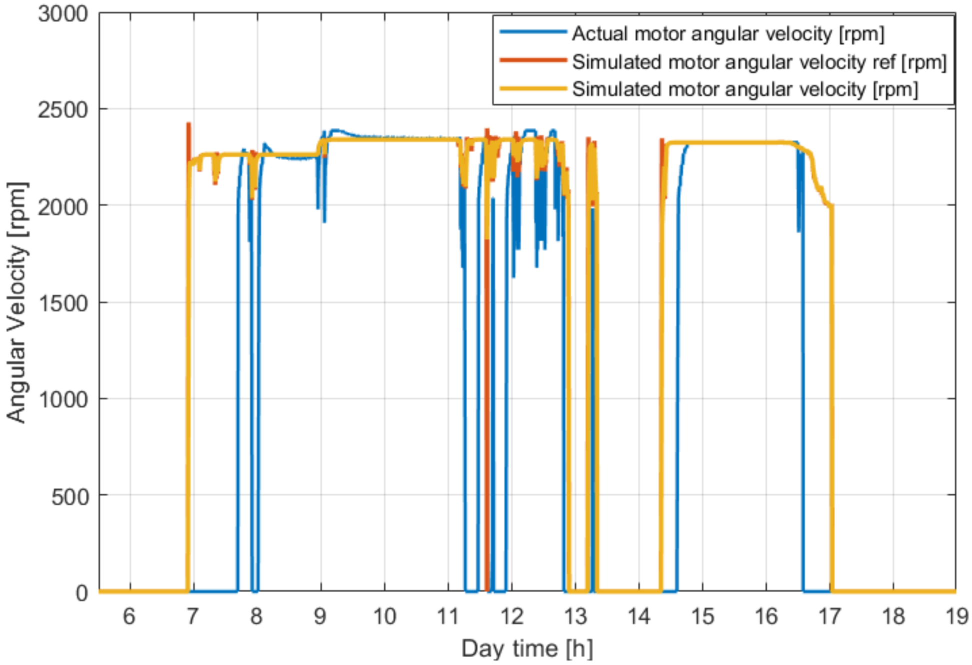

Figure 5.12. PSPPECS induction motor angular velocity response during a day with a big cloud

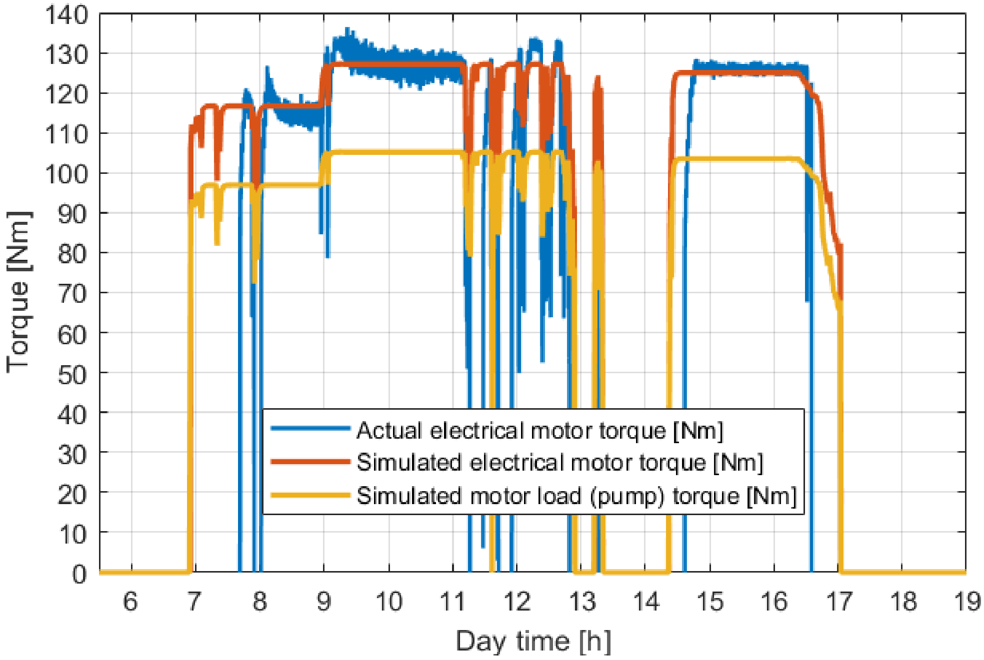

Figure 5.13. PSPPECS induction motor torque response during a day with a big cloud

In Figure 5.13 is depicted the comparison between the induction motor torque of the considered PSPPECS during the monitored and simulated day with a big cloud, where it can be seen that during the torque transitions the simulated dynamic response matches the real one. Regarding the starting and stopping of the pumping system operation, the same behavior can be seen as in Figure 5.11 and Figure 5.12.

Figure 5.14 depicts the comparison between the actual (real system) and simulated pump head variation during the considered day with a big cloud. From the logged data of the real system, it can be seen, that the control strategy of the real system increases the pump's head in small steps until it reaches the reference head, while the proposed control strategy in the developed simulator, tries to reach the head reference in one big step. This strategy confirms the poor capabilities of the controller or improper tuning method, being unable to make the pump reach its referenced head in one go.

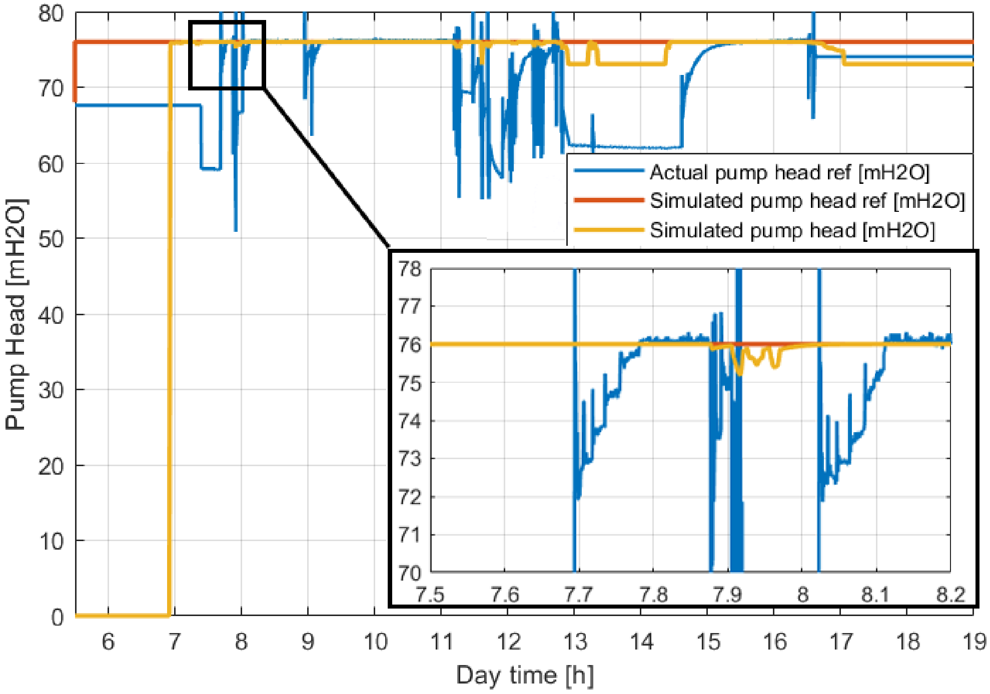

Figure 5.14. PSPPECS pump head response during a day with a big cloud

In Figure 5.15, is presented a comparison between the simulated and real pump's discharged flow. The real pump's discharged flow it has been recorded as a frequency of flow meter impulse given at every 100 liters discharged by the pump. A 30% difference can be seen between the total real (582.7366 m^3)and simulated flow 762.2874 m^3 of the considered pump during a clear sky day.

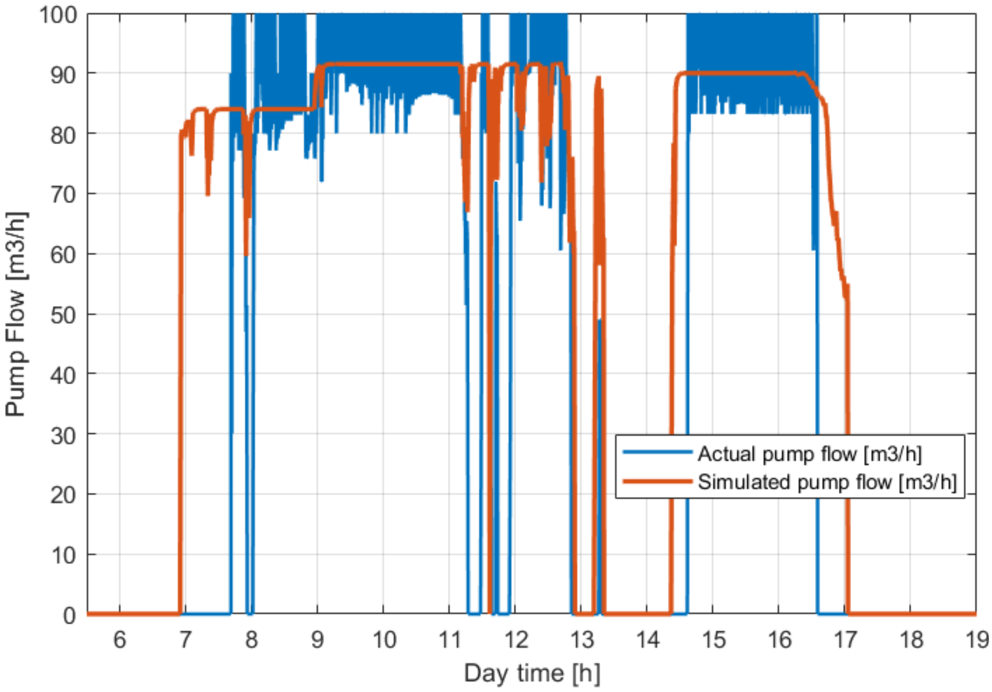

Figure 5.15. PSPPECS pump discharge response during a day with a big cloud

5.5.3. Many small clouds day

In the third simulation, the PSPPECS simulator performance is compared with the real PSPPECS performance, during a day with many small clouds. The simulator inputs, the global irradiance reaching the PV generator plane and the PV cell temperature, can be seen in Figure 3.14 and Figure 3.15.

In Figure 5.16, it can be seen a comparison between the power responses of the PSPPECS simulator and real installation. In the beginning of the day, the real system starts almost one hour later with a significant overshoot, and this fact can be explained by the higher threshold of the required power to start the pumping system in the real system compared to the simulator, and the overshoot can be happening to the low accuracy of the trial and tuning method (as the tunning occurred during one day with a specific global irradiation and a different PV generator average cell temperature). During the transitions through different operating points, the simulator's dynamic response matches quite well with the real system response. Figure 5.16, confirms the safety measure implemented in the control strategy of the real system (missing in the proposed control strategy), that after two unsuccessful attempts to start the pumping system executes a delay of 10 minutes until the next attempt.

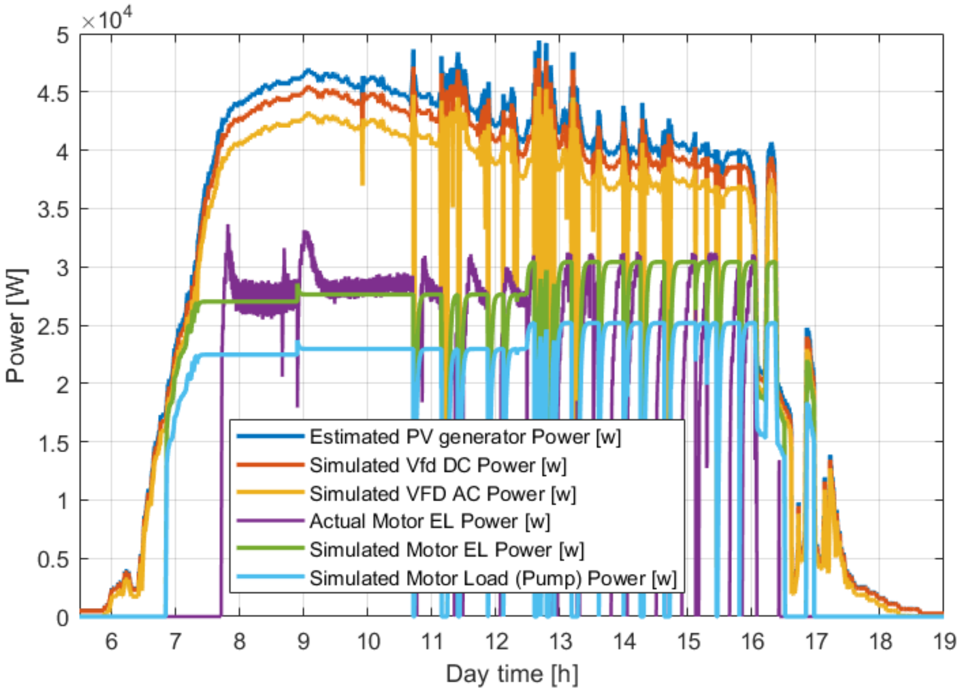

Figure 5.16. PSPPECS power response during a day with many small clouds

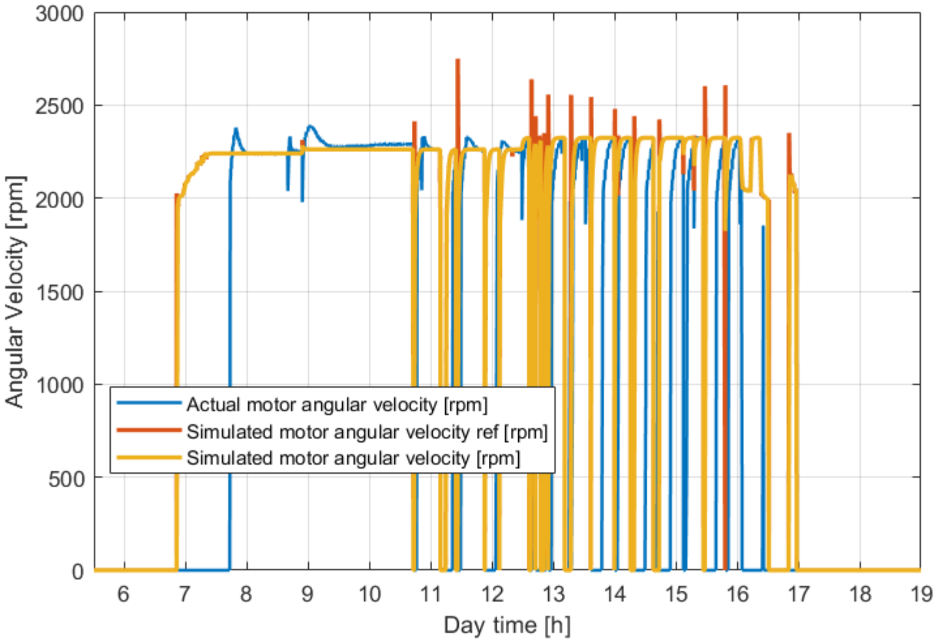

Figure 5.17. PSPPECS induction motor angular velocity response during a day with many small clouds

In Figure 5.17, it can be seen a comparison between the induction motor's angular velocity of the PSPPECS simulator and real installation. Same as in Figure 5.16, the real system starts almost one hour later and with a significant overshoot. The real system safety measure that is missing in the Simulink simulator, where after two unsuccessful attempts to start the pumping system, the controller executes a delay of 10 minutes until the next attempt it is confirmed also by the angular velocity variation from Figure 5.17. Overall, Figure 5.17 shows that the real system operates around 6 hours and 20 minutes, while the simulator claims 9 hours and 15 minutes of operation during the considered day with a big cloud.

In Figure 5.18 is depicted the comparison between the induction motor torque of the considered PSPPECS during the monitored and simulated day with many small clouds, where it can be seen that during the torque transitions the simulated dynamic response matches the real one.

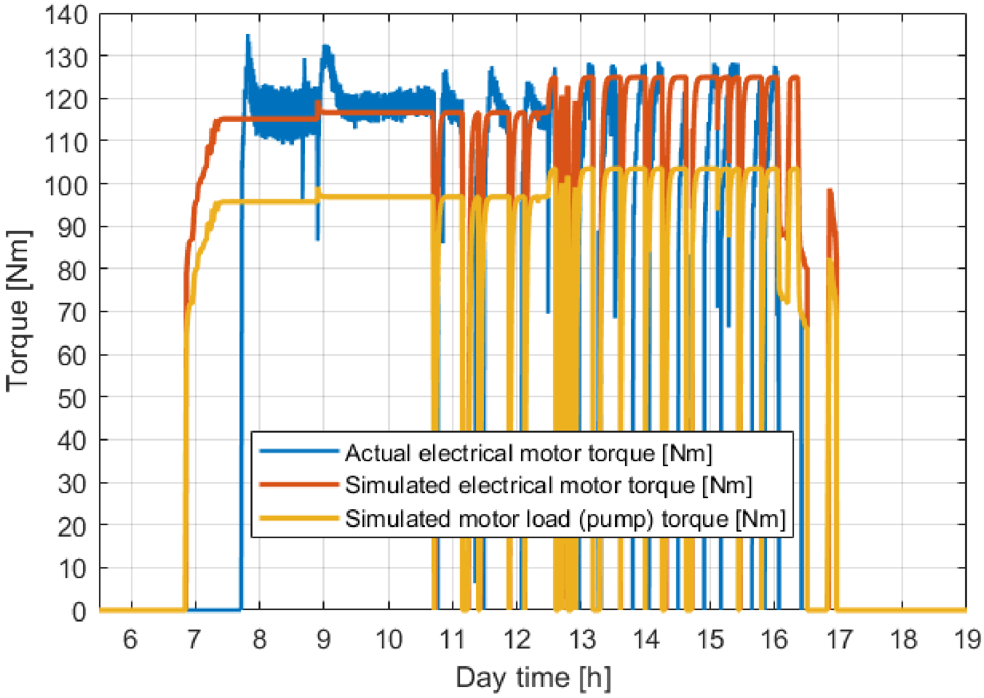

Figure 5.18. PSPPECS induction motor torque response during a day with many small clouds

Figure 5.19 depicts the comparison between the actual (real system) and simulated pump head variation during the considered day with many small clouds. Similar to Figure 5.14, Figure 5.19 confirms that the control strategy of the real system increases the pump's head in small steps until it reaches the reference head, while the proposed control strategy in the developed simulator makes the pump to reach the head reference in one big step.

In Figure 5.20, is presented a comparison between the simulated and real pump's discharged flow. The discharged flow pumped by the PSPPECS simulator during the day with many small clouds reached 758.7423 m^3, while the real PSPPECS system discharged only 571.0960 m^3 (almost 33% higher).

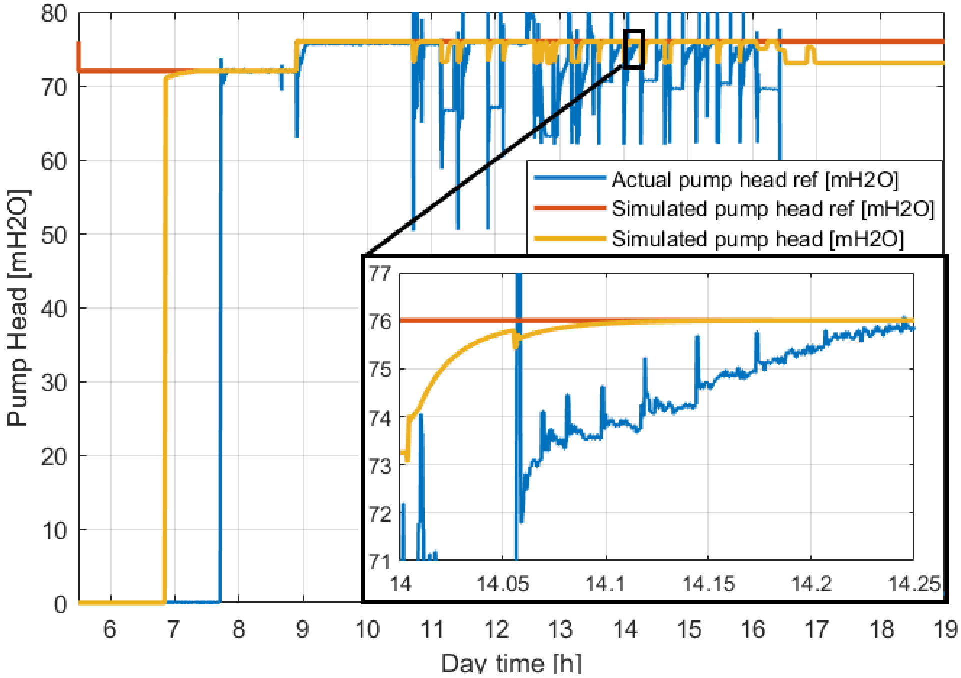

Figure 5.19. PSPPECS pump head response during a day with many small clouds

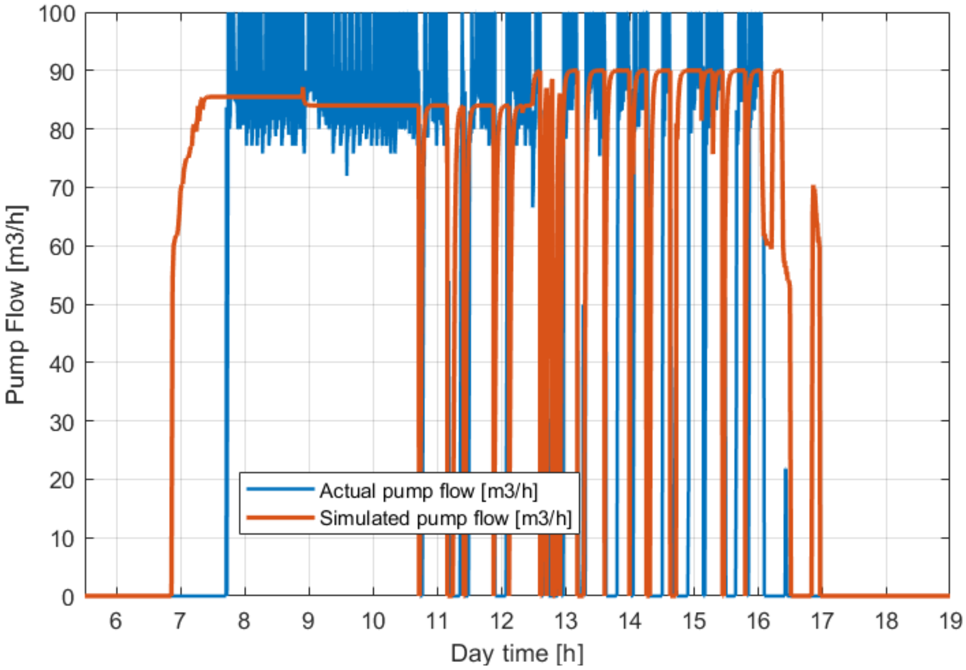

Figure 5.20. PSPPECS pump discharge response during a day with many small clouds

5.5.4. Fully cloudy day

In the last simulation, the PSPPECS simulator performance is compared with the real PSPPECS performance, during a fully cloudy day. The simulator inputs, the global irradiance reaching the PV generator plane and the PV cell temperature, can be seen in Figure 3.14 and Figure 3.15.

Figure 5.21 presents a comparison between the power responses of the PSPPECS simulator and real installation during a fully cloudy day. Both control strategies, the simulated proposed one and the one implemented in the real system started and stopped the pumping system continuously all day. The control strategy implemented in the real PSPPECS, consists in the safety measure that is missing in the Simulink simulator, after two unsuccessful attempts to start the pumping system executes a delay of 10 minutes until the next attempt.

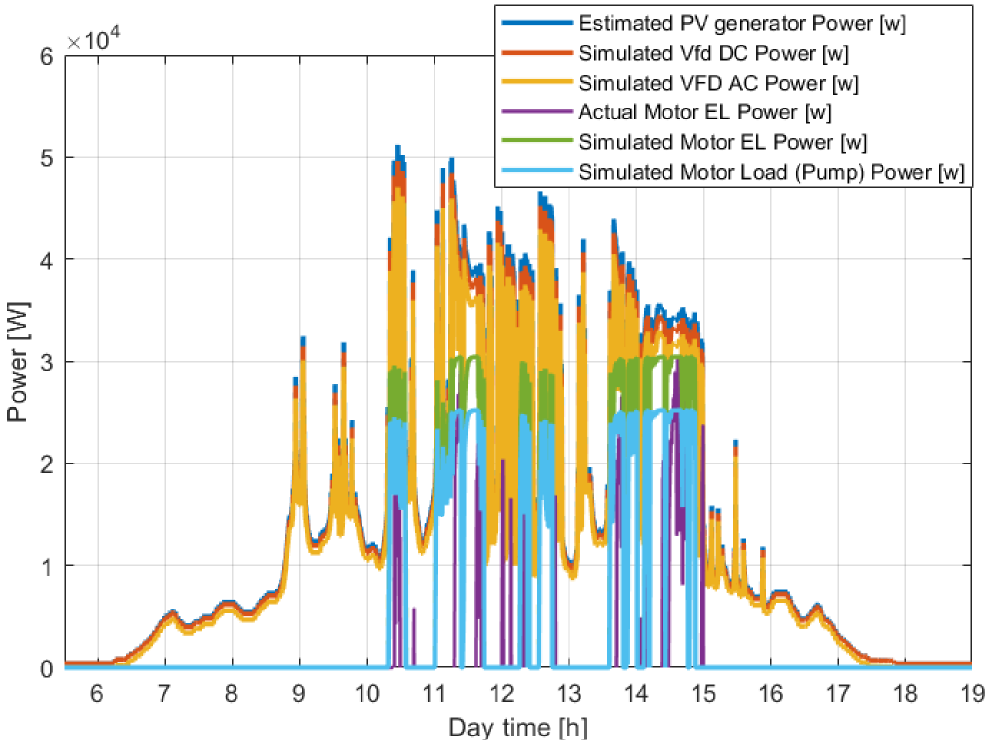

Figure 5.21. PSPPECS power response during a fully cloudy day

Figure 5.22 presents a comparison between the induction motor's angular velocity of the PSPPECS simulator and real installation. Overall, Figure 5.22 shows that the real system operates for almost 50 minutes, while the simulator claims 2 hours and 20 minutes of operation during the considered day with a big cloud, but with more starting attempts, leading to shortcircuiting the induction motor of the pump.

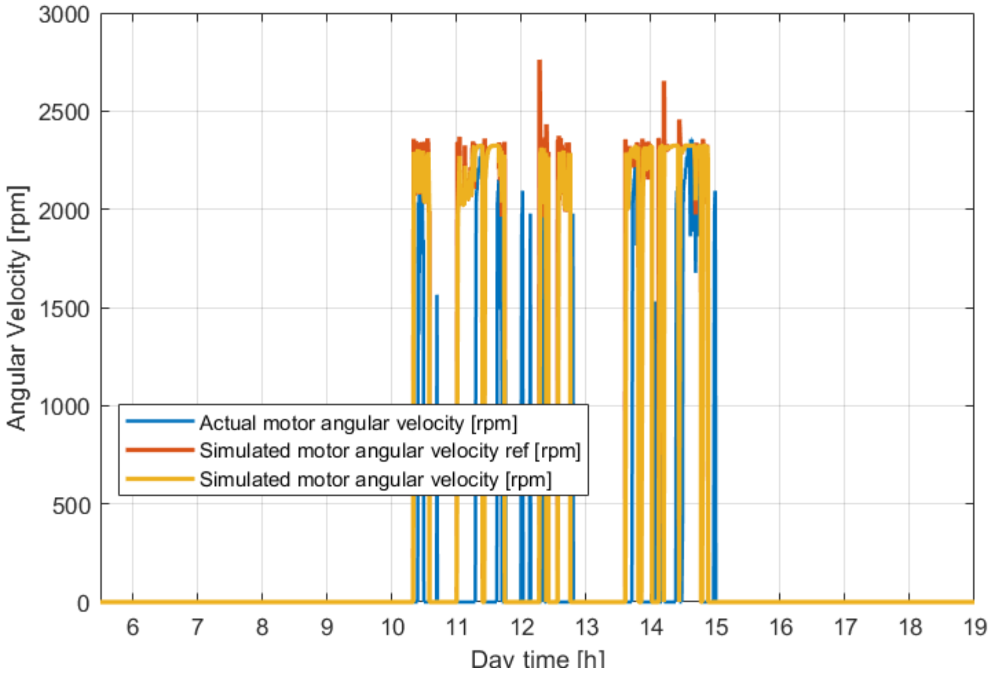

Figure 5.22. PSPPECS induction motor angular velocity response during a fully cloudy day

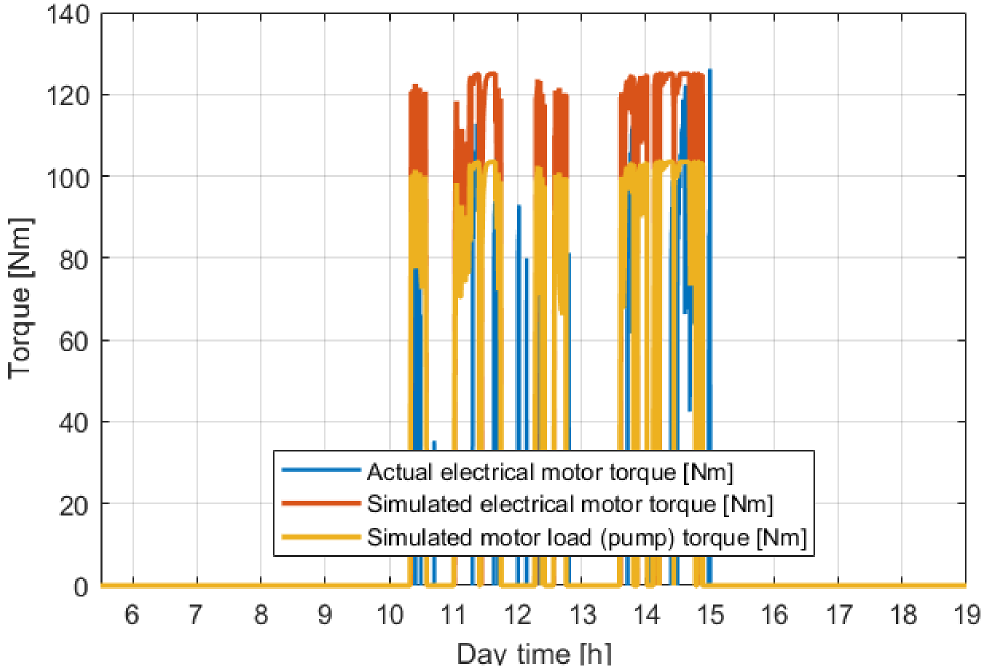

Figure 5.23. PSPPECS induction motor torque response during a fully cloudy day

In Figure 5.23 is depicted a comparison between the real and simulated induction motor torque response of the considered PSPPECS during a fully cloudy day.

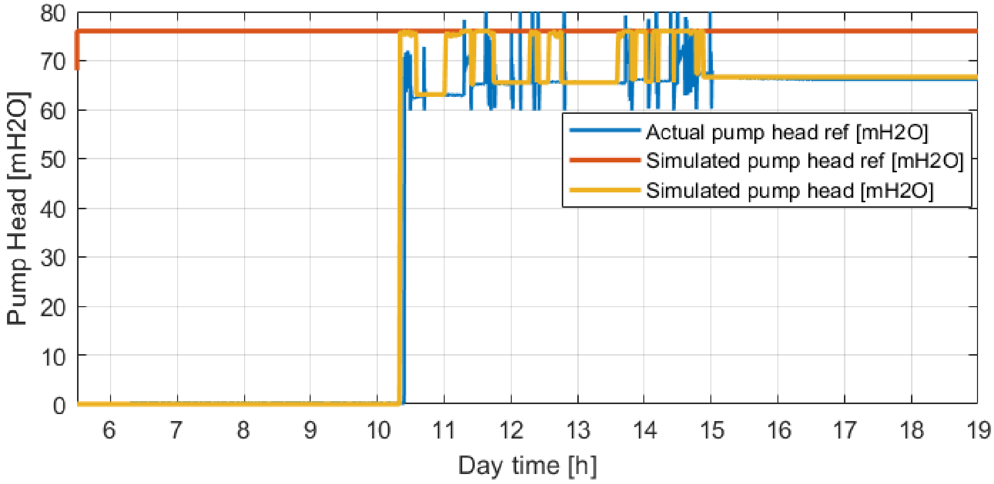

Figure 5.24. PSPPECS pump head response during a fully cloudy day

Figure 5.24 depicts the comparison between the actual (real system) and simulated pump head variation during the considered fully cloudy day. This diagram confirms that the control strategy of the real system increases the pump's head in small steps until it reaches the reference head, while the proposed control strategy is trying to reach the head reference in one big step.

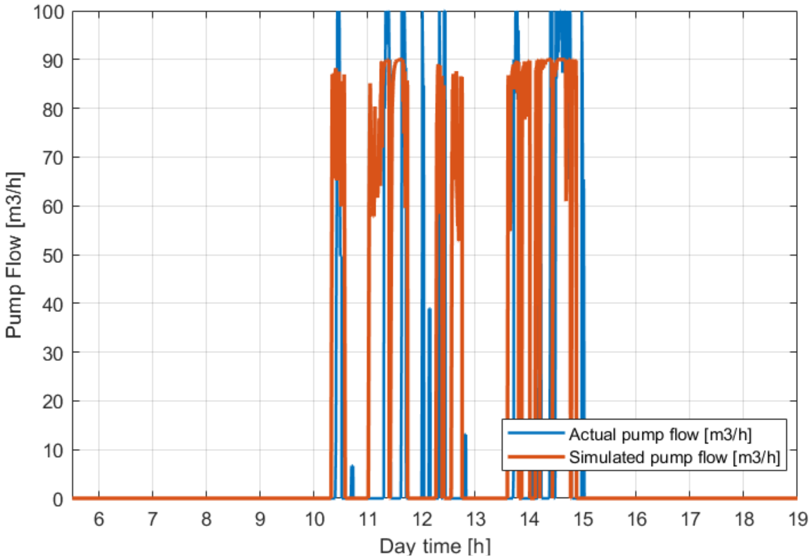

Figure 5.25. PSPPECS pump discharge response during a fully cloudy day

In Figure 5.25, is presented a comparison between the simulated and real pump's discharged flow. The discharged flow pumped by the PSPPECS simulator during the day with many small clouds reached 192.5603 m^3, while the real PSPPECS system discharged only half, 89.9913 m^3.

5.6. PSPPECS chapter conclusions

According to chapter ***5. PSPPECS***, it can be concluded, that the advanced model of the PSPPECS in subchapter ***5.2 PSPPECS modelling*** can be used for both dimensioning and simulating nominal and transitory regimes. The personal contribution to pumping system modelling consists in developing a model capable of simulating also transitory regimes through all the subsystems (centrifugal pump, induction motor, motor drive and PECS) involved in the entire PSPPECS, not only nominal regimes as the ones presented in the specialized literature [103-113].

In subchapter ***5.3 PSPPECS control strategy*** it is developed a strategy for controlling a PSPPECS made out of 3 controllers in cascade. To the variable speed pump controller, it has been added in cascade a PSPPEC controller, to which it has been added in cascade a PECS Controller. The PSPPECS controller was addressed for 3 distinct cases: when the control system executes a pressure control (the case when the pumping head is higher than its reference), when the control system decelerates the operation of the PS (the case when the pumping head is lower than its reference and the power produced by the PECS is lower than the minimum power required for operating the pump) and when the control system drives the PS so that its absorbed power tracks the PECS produced power (the case when the pumping head is lower than its reference and the power produced by the PECS is higher than the minimum power required for operating the pump).

In the fourth subchapter ***(5.4. Monitoring system***) a monitoring system was developed and implemented for determining the performance of an existing isolated high-power photovoltaic pumping system. The major contribution of this subchapter consists in performing a monitoring campaign much deeper and more precise than the one proposed by IEC 62253 [96]. The proposed monitoring system uses a non-intrusive monitoring data logging and acquisition) that measures and stores the transducers values each second. The transducers used by the monitoring system are: a calibrated photovoltaic cell (used for measuring the irradiance temperature), a direct current (DC) voltage transducer (necessary for measuring the DC bus voltage, capable of detecting electric shocks), a pressure transducer (for measuring the hydraulic network pressure, capable of detecting hydraulic shocks), a volume flow transducer (for measuring the discharged flow rate by the pump into the hydraulic network), and a temperature transducer (for measuring the pumping liquid temperature).

Finally, in the fifth subchapter (***5.5. PSPPECS simulations***), the accuracy of the PSPPECS model and the performance of the proposed control strategy are validated by a comparison between the simulated results in Matlab/Simulink (PECS produced power, power absorbed by the VFD, induction motor and pump, the speed and torque of the induction motor and pump, and the pumping head and flow) with those obtained using the proposed monitoring system, on the existing PSPPECS in Aragon, Spain for five representative days (a clear sky day, a day with a big cloud covering the sky during a period of the day, a day with many small clouds and a fully cloudy day).

6. PUMPING SYSTEMS POWERED BY A WIND ENERGY CONVERSION SYSTEM

The current chapter presents the modelling and simulation of a pumping system powered by a wind energy conversion system (PSPWECS). The first subchapter (***6.1. PSPWECS description***) presents a short description of a general pumping system and its components. The second subchapter (***6.2. PSPWECS modelling***) consists of a nonlinear mathematical model of the described system, and the third subchapter (***6.3. PSPWECS control strategy***) presents the proposed control strategy. In the fourth subchapter (***6.4. PSPWECS simulations***), the performance of the proposed control strategy is determined by analyzing several performance indicators of the system's simulated response to a wind speed ramp. Finally, in the last subchapter (***6.5. Conclusions***) are presented the chapter conclusions.

6.1. PSPWECS description

The pumping systems (PS), especially the ones used in irrigation installations, have evolved significantly in recent decades in order to reach a greater efficiency of water exploitation and usage. This has been achieved by integrating various modern solutions that have replaced the traditional ones, for example, gravity irrigation has been replaced by sprinkler or drip irrigation systems. The payback of those methods represents the drastic increase in energy consumption. Due to this reason, currently, the energy consumption of a pumping unit represents the highest cost in operating a PS (water supply systems or irrigation systems). Currently, the PSs, are powered by the national power grid or by diesel or gasoline generators, where the national power grid is missing (remote areas). Few PS are powered by renewable energy sources (RES), most of which are powered by PECS [114] as there is an excellent integration of the PECS into such systems, because they are used during the summer, with maximum demand on the hottest and sunniest days of the year [5]. Another solution for powering the PSs represents the wind energy conversion systems (WECS) for windy periods and areas. This solution, depending on the characteristics of the wind, can ensure, at the pumping site, the availability of energy also during the night and on cloudy days, when the efficiency of the PVG is very low.

Due to the current favorable legislation, coupled with the continuing decline in wind energy prices, the agricultural sector is considering the installation of PS powered by a WECS. Despite the economic profitability offered by wind-powered pumping installations and the fact that their market demand is constantly increasing [114, 115], there is still no industrial/ commercial solution designed for irrigation purposes (pumping water at constant pressure). Most of the PS powered by a WECS [45, 116, 117] are designed only for energy storage (pumping water at variable flow and pressure in a water storage).

In consequence to the above, the current chapter proposes a reliable and robust solution for modelling and controlling a high-power PSPWECS. Most of the WECS manufacturers are not open to changing/adjusting their current control strategies, for a full integration within an irrigation PS, because of the high-cost of such a change/adjustment which the manufacturers believe that the potential market cannot pay it. Due to this reason, the current work has more industrial applicability compared to other related work [118–122], because it consists of integrating a commercial WECS, without altering its hardware or controller, into an existing PS.

6.2. PSPWECS modelling

The PSPWECS modelling consists in the pumping system (PS) model, developed in section ***2.2 Pumping system modelling***, combined together with the wind energy conversion system (WECS) model developed in section ***4.2. WECS modelling***. The PS model contains the variable frequency drive, the induction motor (IM), the centrifugal pump and the water distribution together with the irrigation systems. The WECS model contains an aeroelastic model of a three-blade horizontal axis wind turbine based on lookup tables for the aerodynamics (power and thrust coefficients, CP and CT) [84]; a 3^{rd}-order drive train model; an alpha-beta (α-β) representation of the doubly-fed induction generator (DFIG) together with the back-to-back converter; a 1st-order pitch actuator; and a 2nd order tower model). The dynamics of the other systems were either ignored or in-directly transferred to the already modeled systems. The current produced at a certain voltage by the dynamic WECS model (Equation 4.73), powers the VFD (induction motor driver) model (Equation 2.3). In Figure 6.1 it can be seen the layout of the PSPWECS.

6.3. PSPWECS control strategy

The PSPWECS control strategy (Figure 6.1) contains three levels of controllers: three first-level controllers (two necessary for the power converters of the WECS generator stator and rotor, and one for the pump motor), three second-level controllers (two necessary for the WECS and the one for the PS) and one third-level controller (necessary for the control of the entire PSPWECS system).

The first-level controllers regulate the voltage and current wave forms produced by the WECS (the DFIG stator and rotor controllers proposed in sections ***4.3.4. DFIG rotor side controller*** and ***4.3.5***. ***DFIG grid side controller***), respectively, the ones absorbed by the induction motor of the pump (the controller proposed in section ***2.3.1***. ***Fixed speed pump controller***).

The second-level controllers contain two controllers that regulate both the torque and speed of the WT rotor and WECS generator (the generator-torque controller and the blade-pitch controller, from sections ***4.3.2. Generator-torque controller*** and ***4.3.3. Blade-pitch controller***), respectively, the speed controller of the pump's induction motor (the flux and variable speed pump controller, from section ***2.3.2. Variable speed pump controller***).

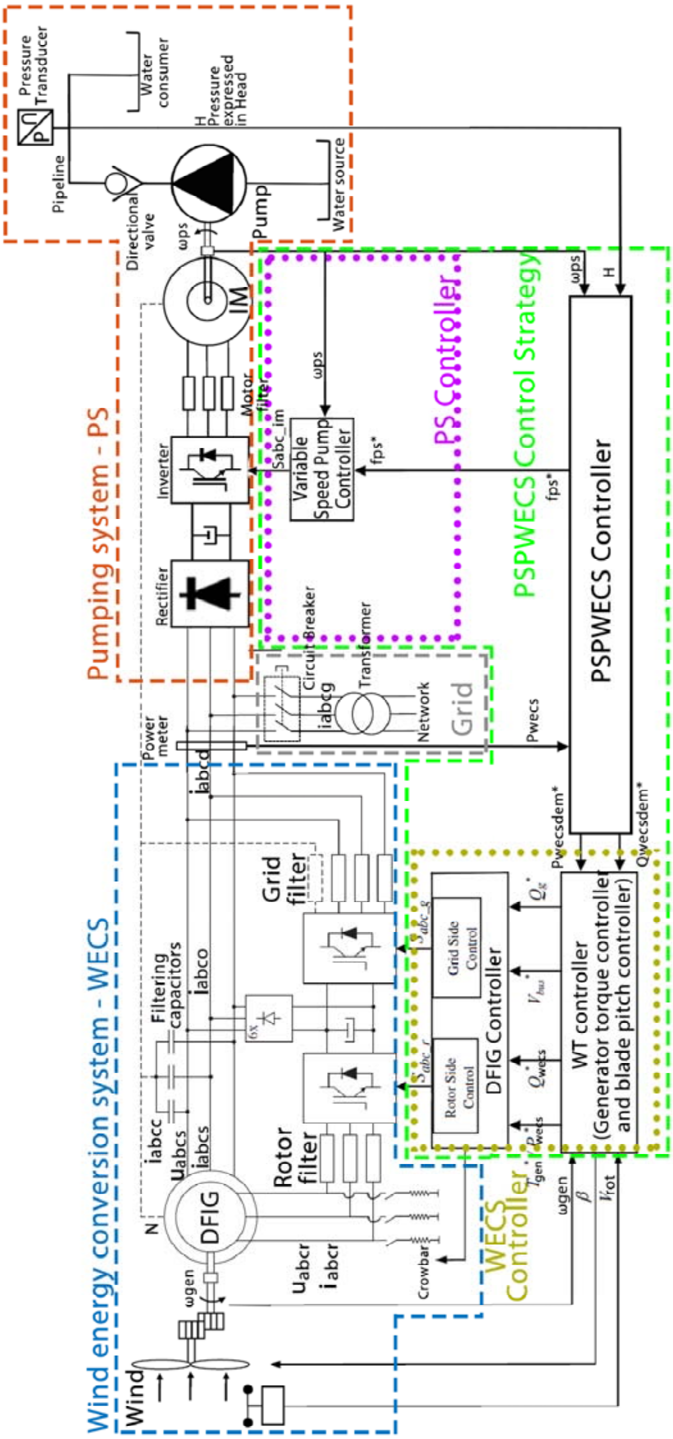

Figure 6.1. Structure of the PSPWECS control system [48]

The third level contains the PSPWECS controller (Figure 6.1), which generates the reference of the WECS power ($P_{WECSdem}$*) according to the pumping pressure reference (expressed in the pump head *H*) and its reference, as in Equation 6.1 [48]:

$$P_{wecsdem} = \begin{cases} P_{ps0} \cdot \eta_0 & H < H^* \\ \left(\frac{3 \cdot P_{ps0}}{2 \cdot H_0} \cdot \Delta H + P_{ps0}\right) \cdot \eta_s & H \geq H^* \end{cases} \qquad (6.1)$$

and calculates frequency error *Δf=(fm*-fm)* (the difference between the reference and current frequency of the motor) of the variable speed pump controller according to power produced by the WECS (P_{WECS}) as in Equation (6.2) [48]:

$$\Delta f = \begin{cases} \frac{-p_{motor} \cdot \omega_{pss}}{2 \cdot \pi} & P_{wecs} < P_{psmin} \\ \frac{p_{motor} \cdot fm^*}{6 \cdot \pi \cdot (P_{pump})^*} \cdot (P_{wecs} - P_{pump}) & P_{wecs} \geq P_{psmin} \end{cases} \qquad (6.2)$$

where P_{psmin} represents the minimum power required by the pump motor (to ensure the pumping of the minimum flow required for the pump motor cooling).

The PSPWECS controller ensures the control in 4 specific cases:

1. when the power produced by the WECS is lower than the minimum power required to operate the pump ($P_{WECS}<P_{psmin}$), the PSPWECS controller decelerates the PS;
2. when the power produced by the WECS is greater than the minimum power required for operating the pump ($P_{WECS} \geq P_{psmin}$), the PSPWECS controller drives the PS, so that its absorbed power tracks the PECS produced power;
3. when the pumping head is lower than its reference ($H<H^*$), the PSPWECS controller demands the WECS to produce only the necessary power for the nominal operation of the PS;
4. when the pumping head is higher than its reference ($H \geq H^*$), the PSPWECS controller regulates the power produced by the WECS according to the PS power demand so that the pressure it is equal to its reference.

6.4. PSPWECS simulations

Combining the PSPWECS control strategy presented in the third subchapter (6.3. PSPWECS control strategy), with the dynamic model of the PSWPECS presented in the second subchapter (6.2. PSPWECS modelling), a simulator was developed in Simulink [43].

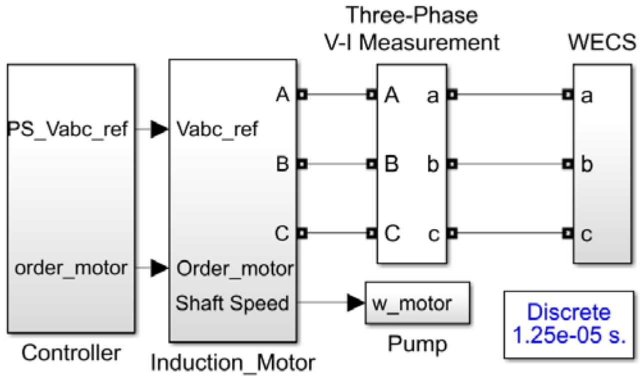

Figure 6.2. PSPWECS flow chart in Simulink

The performance of the proposed PSPWECS control strategy is determined by the analysis of several performance indicators (WECS power production, efficiency and components loading and PS power consumption, efficiency, discharge and pumping head) during a simulation to a wind speed ramp from 4 to 26 m/s. The considered WECS operates under normal conditions in a wind speed ranging from 5 to 25 m/s and when the demanded power equals the rated power. The input parameters necessary for modelling, defining the controller, and running the simulation are the same as the ones considered in section ***2.4. Pumping system simulations***, and in ***section 4.4 WECS simulations***. The scenario depicted in this subchapter illustrates how the PS responds with an available power produced by a WECS during

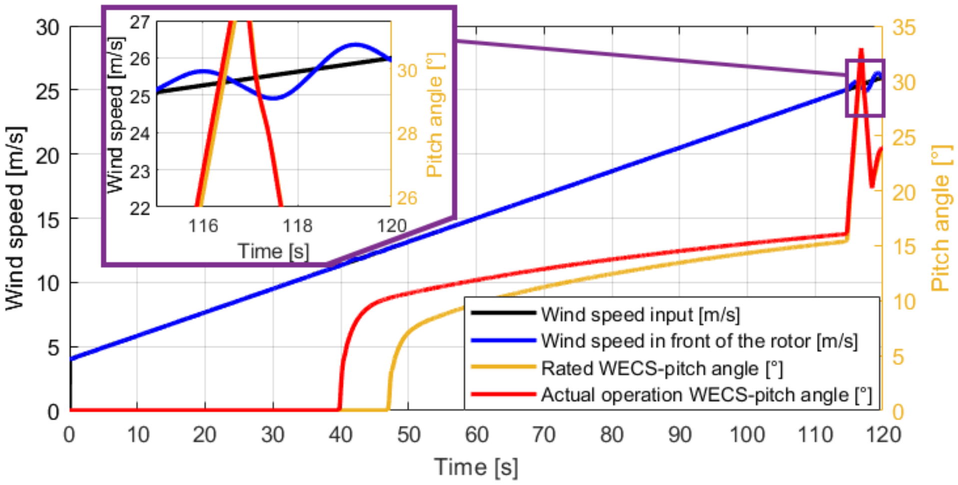

Figure 6.3. Pitch angle variation during the wind speed ramp [48]

Figure 6.3 shows the blade-pitching angle operation of the WECS, when the demanded power equals the WECS rated power, and when the demanded power equals the actual power necessary for operating the pumping system at its rated).

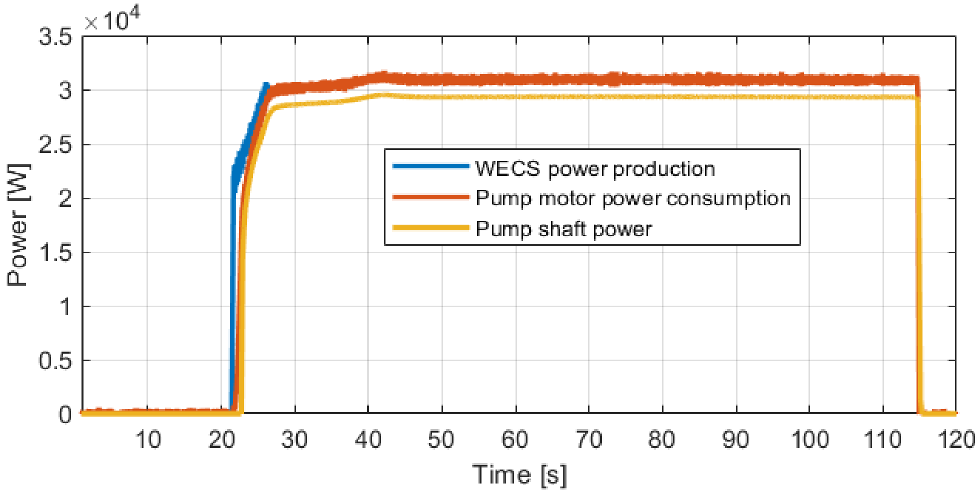

Figure 6.4. WECS power production and PS power consumption [48]

Figure 6.4 present the WECS produced power (blue), the pump, and motor power (red and yellow). In this figure, it can be seen that the power consumption of the PS motor tracks the WECS produced power at partial-load (time from 20 to 40 s), and how the WECS demanded power is regulated by the PI controller according to the pumping pressure reference at full-load (time from 40 to 115 s);

Figure 6.5 shows the efficiencies of each subsystem integrated into the PSPWECS (blue—wind turbine, red—WECS generator, yellow—pump motor efficiency, purple—pump efficiency, green—the entire system efficiency).

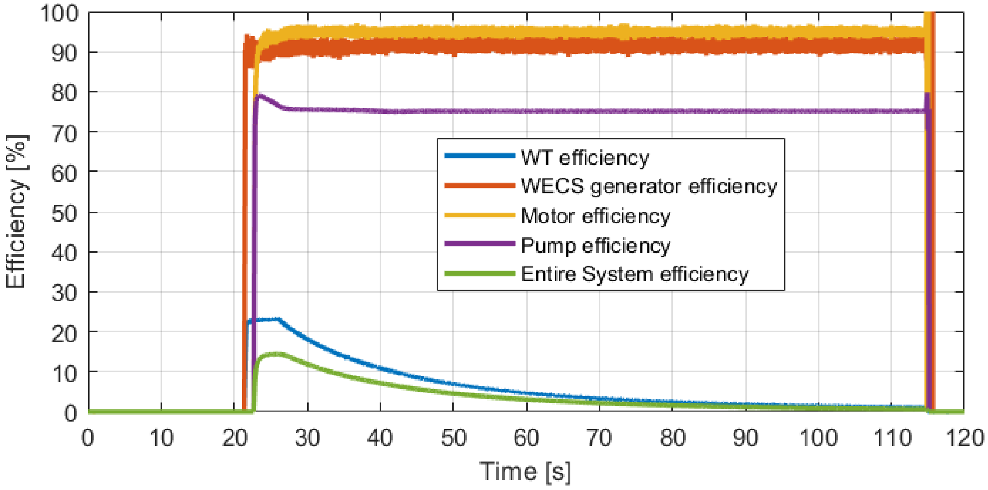

Figure 6.5. Efficiency of each subsystem in the PSPWECS [48]

In Figure 6.6, is presented the flow pumped by the pump into the irrigation network utilizing the power produced by the WECS.

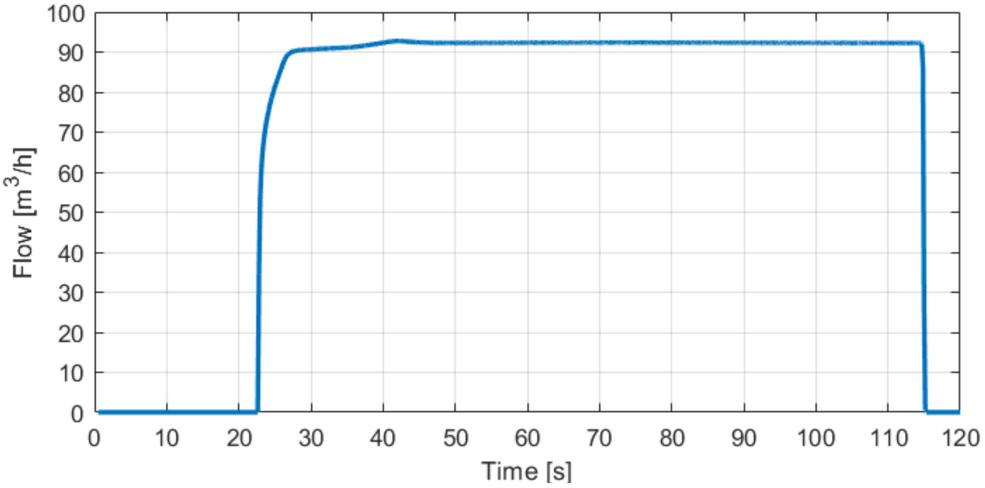

Figure 6.6. Water discharged by the PS into the irrigation network [48]

Figure 6.7 is illustrated the head variation of the centrifugal pump together with the irrigation network pressure reference expressed in the pump head.

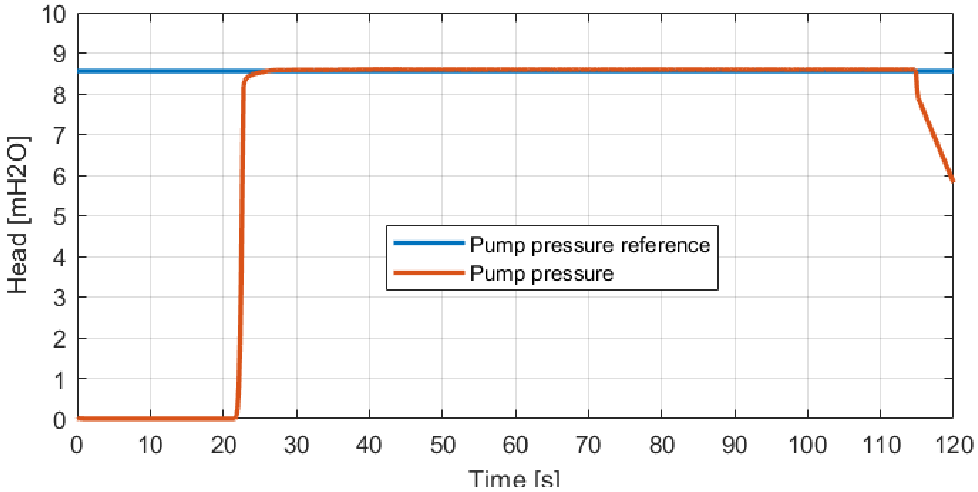

Figure 6.7. PS head variation [48]

Figures 6.8 depicts a comparison between the power produced by the same WECS (more details can be found in reference [92]), ~~with red~~ when it's demanded power is requested by the PS controller for the rated operation of the PS (possible only when the rated power of the pump is below the rated power of the WECS) and ~~with blue~~ when the WECS demanded power is equal to it's ratend (the case when the WECS operats with the purpose of injecting all the energy, for example in a wind farm that exports all the energy to the grid or).

In the diagrams form Figures 6.8-6.13, the WECS response is ilustrated with blune when the WECS rated power is demanded, and with red when the rated power of the PS is demanded.

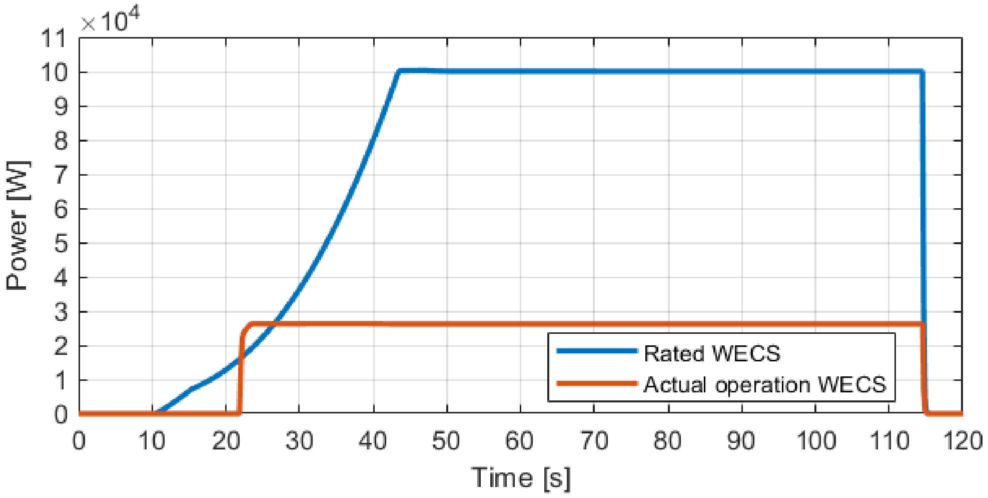

Figure 6.8. Rated vs actual power production of the WECS [48]

Figure 6.9 shows the WECS generator angular velocity during the operation when the demanded power is equal to the rated power (blue) and when the demanded power is the power required by the pump for its rated operation (red).

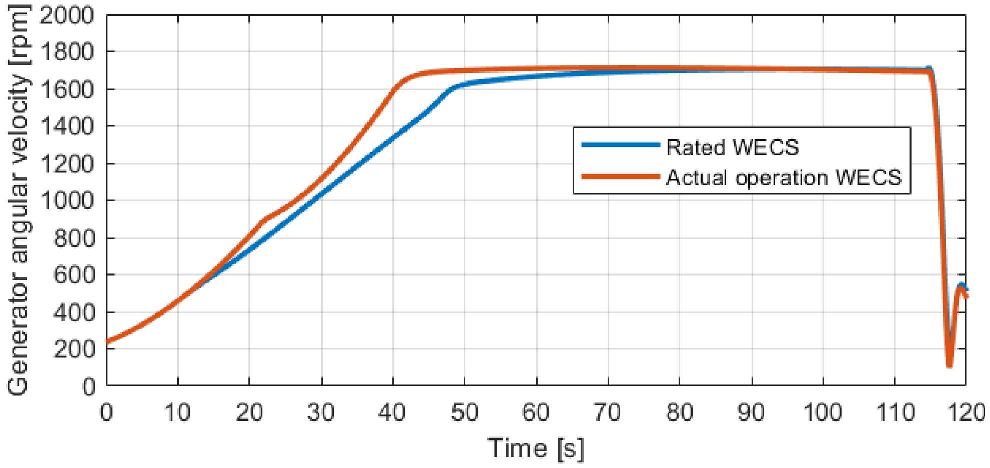

Figure 6.9. Rated vs actual generator angular velocity of the WECS [48]

Figure 6.10, presents how the WECS power is derated mainly by derating the WT and generator torque in order to reduce the loads taken by the drive train (WT and WECS generator torques are adapted to the requested power by the PS). The same case can be seen also in Figure 6.11, where it can be seen that the torsion of the drive shaft is reduced proportionally to the derated power.

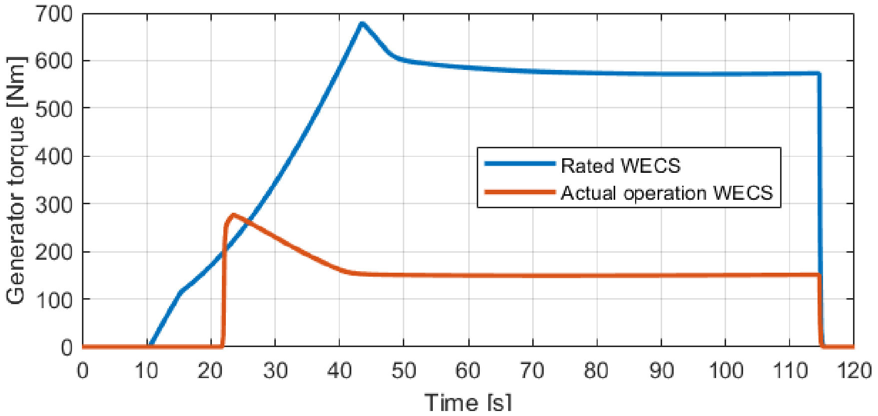

Figure 6.10. Rated vs actual generator torque of the WECS [48]

Figure 6.11 ilustrates how the proposed control strategy for the PSPWECS reduces the tower bending moment proportionally to the WECS power derated to the necessary power required by the PS for its rated operation.

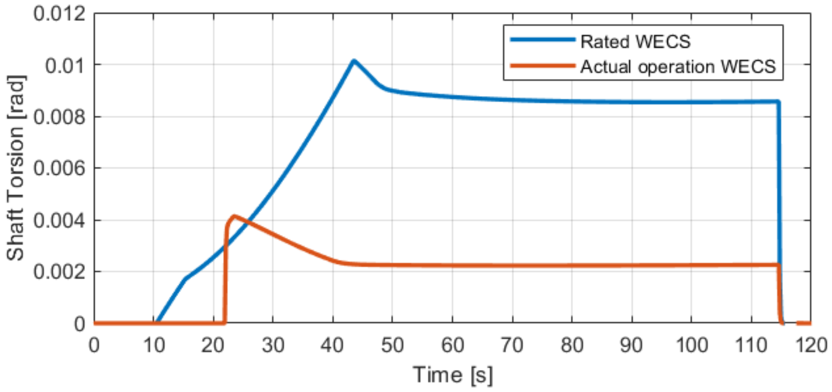

Figure 6.11. Rated vs actual drive train torsion of the WECS [48]

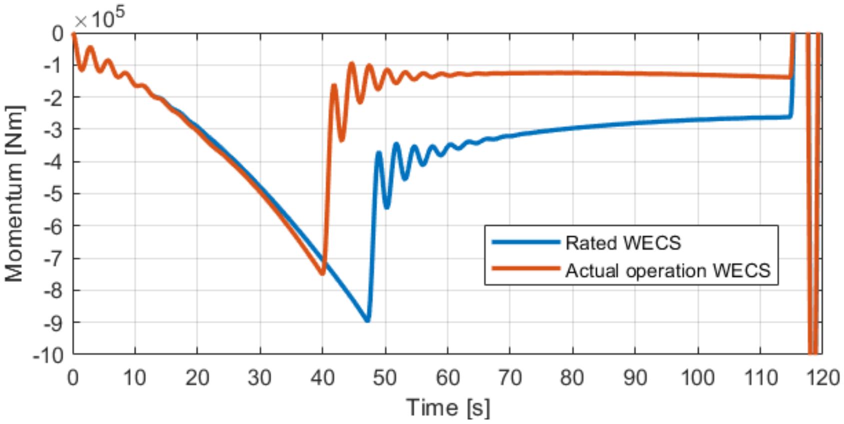

Figure 6.12. Rated vs actual tower momentum of the WECS [48]

Similar to Figure 6.12, Figure 6.13 illustrates how the proposed control strategy for the PSPWECS reduces the blades bending moment proportionally to the WECS power derated to the necessary power required by the PS for its rated operation.

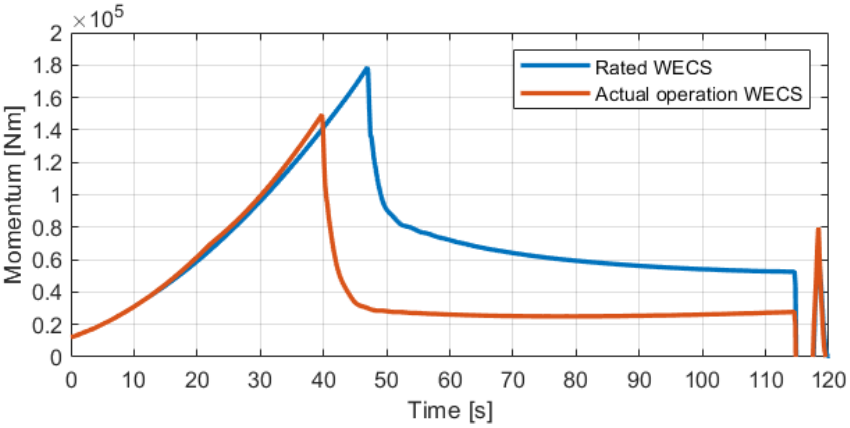

Figure 6.13. Rated vs actual blade momentum of the WECS [48]

6.5. PSPWECS chapter conclusions

This chapter shows the application of leading-edge technology within the area of PSPWECS. The PSPWECS adequate dynamic model developed in section ***6.2 PSPWECS modelling***, consists in integrating the WECS model from ***4.2. WECS modelling*** into the PS from ***2.2. Pumping system modelling***.

The proposed control strategy (***6.3. PSPWECS control strategy***) is based on a PSPWECS controller that was addressed for 4 distinct cases: (i) the control system decelerates the PS (when the power produced by the WECS is lower than the minimum power required for operating the pump); (ii) the control system drives the PS so that its absorbed power tracks the WECS produced power (when the power produced by the WECS is higher than the minimum power required for operating the pump); (iii) the control system demands the WECS to produce only the necessary power for the nominal operation of the PS (when the pumping head is lower than its reference); (iv) the control system regulates the power produced by the WECS according to the PS power demand so that the pressure it is equal to its reference (when the pumping head is higher than its reference).

The simulation results depicted in section ***6.4 PSPWECS simulations*** cover the transition through the entire operation range considered representative for the PWPWECS. The simulation results validate the correctness, performance and effectiveness of the proposed control strategy.

The performance indicators from Figures 6.4 to 6.13 confirm the contribution of the current work in controlling a PSPWECS, that controls the pump speed so that the PS consumption power tracks the WECS produced power at partial load, and the controls of the WECS power production according to the necessary power of the PS to reach the pumping head reference at full load. The performance indicators from Figures 6.8 to 6.13 show that, at full load operation, the WECS produces only the power necessary for the rated operation of the PS, in order to avoid unnecessary loading [123] of the WECS components.

Finally, the main contribution of the work presented in the current chapter compared to other related work [118–122] consists of integrating a commercial WECS, without altering its hardware or controller, into an existing pumping system. The main reason why most of the WECS manufacturers are not open to changing/adjusting their current control strategies, for a full integration within an irrigation PS, is because of the high cost of such a change/adjustment which the manufacturers believe that the potential market cannot pay it. Nevertheless, the unintrusive proposed control strategy system and the promising simulations results indicate the possibility for the application of the proposed scheme to be set up for implementation without additional cost.

7. GENERAL CONCLUSIONS, PERSONAL CONTRIBUTIONS AND FUTURE RESEARCH

7.1 General conclusions

In the present work, a great relevance field is addressed, that of pumping systems powered by renewable energy sources, with a special focus on the modelling and control strategies development for PS powered by RES such as PECS or WECS.

The work is designed as a progressive development of solutions to the main problems related to the considered pumping systems that are continuously supplemented, the end of each chapter highlights the particularities, recommendations and conclusions usable in the following chapters.

The major objectives achieved in the Phd thesis are: the development and validation of models that describe precisely the operation of a high-power PS, of a PECS or WECS; as well as the use of the developed models for the synthesis, implementation and validation of control strategies of an isolated high-power PS powered by a fluctuating and intermittent energy source (photovoltaic or wind energy source). These objectives lines up with the European Union 2030 target in terms of reduction of greenhouse gas emissions, increasing the share of renewable energy consumption and increasing the energy efficiency.

Solving the problems raised in the PhD thesis, the following main conclusions can be drawn.

The analysis through simulation of a PS operating in various specific regimes (fixed speed, variable speed, variable flow, variable pressure and variable available power) requires the development of MM for the main components (subsystems) of these types of system: the motor driver, the induction motor, the centrifugal pump and the hydraulic network. The developed and proposed dynamic MM of the PS has been implemented and validated both using Matlab/Simulink simulation software and experimentally on an existing PS. The proposed MM can be used for dimensioning and simulation or in the synthesis and development of various PS control strategies.

The PS control strategy has been addressed for two types of induction motor drivers of high-power pumps (commercially available): the soft starter for driving the induction motor at a fixed speed and the VFD with at least one PI controller integrated for driving the induction motor at variable speed, variable flow, variable pressure or variable available power.

The case studies carried out through simulation and experimentally on an industrial high-power PS led to the conclusion that by using the MM developed for the PS components, the proposed control strategies ensure good performance, being recommended for PS configurations with induction motors driven by soft starters or by VFD with at least one integrated PI controller.

A static model was developed for the dimensioning and simulation of the nominal operation of the SCEF, and a single-diode dynamic model was considered for simulating transitory regimes and the synthesis and development of control strategies.

To control the PECS, a control structure was developed for the MPPT of a PECS based on the P&O algorithm and adapted for its further integration into the control strategy of a PS.

The case studies, performed by simulation and experiment, on an existing PECS, confirm that by using the developed MM of the conversion system subsystems, the control strategy provides good performance, and it is recommended for PECS configurations powering high-power PS.

In the current work, a nonlinear dynamic MM was developed, used in the simulation of the transient regimes of a WECS and its linearized version, used in the synthesis of the control strategy.

The variable pitch and speed WECS control strategy was developed on two control levels: the controllers of the DFIG rotor and stator converters on the first level, and the controller of the generator-torque and blade-pitch angle on the second level. To adapt the produced power to a variable reference power by enabling the WT blade-pitch actuator and to decouple the WT rotor when the wind reaches the cut-off speed, changes in the generator-torque controller were required. In addition, significant improvements were made by scheduling the proportionality constant (Kp) and integration time (Ki) of the PI blade-pitch controller; the scheduled Kp and Ki values were obtained based on the linearization of the WECS model, by using the Taylor series approximation and by determining a mathematical equation that allows the calculation of the gains scheduling according to the current value of the WT blade-pitch angle (β) and the value of the WT blade-pitch angle for which the WT rotor torque has doubled (βk).

The case studies, carried out by simulation in Matlab/Simulink, confirm that, using the WECS nonlinear dynamic model, the developed and proposed control strategy provides good performance, being recommended for WECS configurations powering high-power PS.

The PSPPECS dynamic MM developed and proposed in the current work has been implemented and validated both in Matlab/Simulink software and experimentally and it can be used for dimensioning, simulation and in the synthesis and development of various control strategies.

The PSPPECS control strategy was addressed for 3 distinct cases: when the control system executes a pressure control (the case when the pumping head is higher than its reference), when the control system decelerates the operation of the PS (the case when the pumping head is lower than its reference and the power produced by the PECS is lower than the minimum power required for operating the pump) and when the control system drives the PS so that its absorbed power tracks the PECS produced power (the case when the pumping head is lower than its reference and the power produced by the PECS is higher than the minimum power required for operating the pump).

The case studies, carried out by simulation in Matlab/Simulink and experimentally on the existing PSPPECS, confirm that the MM developed for the PSPPECS components, as well as the proposed control strategy ensures good performance and an increase in robustness and reliability (by reducing the number of electric and hydraulic shocks in a PSPPECS).

The PSPWECS controller was addressed for 4 distinct cases: (i) the control system decelerates the PS (when the power produced by the WECS is lower than the minimum power required for operating the pump); (ii) the control system drives the PS so that its absorbed power tracks the WECS produced power (when the power produced by the WECS is higher than the minimum power required for operating the pump); (iii) the control system demands the WECS to produce only the necessary power for the nominal operation of the PS (when the pumping head is lower than its reference); (iv) the control system regulates the power produced by the WECS according to the PS power demand so that the pressure it is equal to its reference (when the pumping head is higher than its reference).

The case studies, carried out by simulation, confirm that by using the MM developed for the PSPWECS components, the proposed control strategy ensures good performance and reduces the load on the mechanical components of the SCEE, as well as the number of hydraulic and electrical shocks in a PSPWECS.

To elaborate the presented PhD thesis, it has been undertaken a bibliography containing **123** references from specialized literature, most of them very recent. Furthermore, the bibliography includes **13** references whose main author or coauthor is the author of the thesis: **1** scientific article published in a journal indexed **ISI Web of Science** (WoS) with **Q1** quartile and an **impact factor** (IF) equal to **2.592**; **1** scientific article published in a journal indexed **ISI WoS** with **Q3** quartile and an **IF** equal to **3.252**; **2** scientific articles published in journals indexed **ISI WoS** with **Q4** quartile, one with an **IF** equal to **0.782**, and one without an impact factor; **6** scientific papers published in international conference volumes indexed **ISI WoS**; **2** published in specialized journals indexed in **international data bases** (BDI) and **1** book as coauthor.

In conclusion, it can be stated that the new solutions proposed in the current work, are novel, efficient and adequate for operating a pumping system powered by renewable energy sources.

7.2 Personal contributions

The present thesis includes, from the author's point of view, the following significant contributions:

- development and experimental validation (on an existing PSPPECS from Aragon, Spain section ***3.5. PECS chapter conclusion***, ***5.1. PSPPECS description*** and ***5.5. PSPPECS simulations***) of a PS mathematical model that can be used for both dimensioning and simulation of a pumping systems (section ***2.2. Pumping system modelling***);
- development of the mathematical equations expressing: the electrical frequency error (the deviation of the current value from its reference) according to pump discharge (flow) error (***Equation 2.70***), the pumping head (pressure) error (***Equation 2.72***), respectively, the error of the power absorbed by the induction motor of the pump (***Equation 2.74***) The relations have been further used to develop the control strategy of the centrifugal pump via a VFD at the reference flow/pressure or to track the power produced by a fluctuating and intermittent power source (section ***2.3.2. Variable speed pump controller***);
- design and implementation of control strategies for operating a PS (based on the vector control of an induction machine, whose references for the current regulation are provided by two PI regulators in cascade, one for speed and one for flux) at: variable speed, variable flow rate, variable pressure or variable absorbed power (***section 2.3. Pumping system control strategy)***;
- carrying out a scenario consisting of five simulations in Matlab/Simulink that served to determine the performance of the dynamic MM proposed for the PS,

respectively, the performance of the control strategies developed for fixed speed, variable speed, variable flow rate, variable pressure and variable available power (section ***2.4. Pumping system simulations***);

- the development of a static model, respectively, a dynamic model usable for the simulation of the permanent regime and the transitory regimes in a PECS (section ***3.2. PECS modelling***);
- development of a control structure for the MPPT of a PECS based on the P&O algorithm that has been adapted for its further integration into a PS control strategy (section ***3.3. PECS controller***);
- implementing the proposed PECS model and control strategy, and validating them experimentally during four different scenarios: a day with a clear sky, a day with a single large and dense cloud covering the sky during a specific period of the day, a day with many small and fast clouds and a completely cloudy day (section ***3.4. PECS simulations***);
- development of a nonlinear dynamic model used in the simulation of the transient regimes of a WECS, and a linearized version, used in the synthesis of the control strategy (section ***4.2. WECS modelling***);
- analysis, synthesis and implementation of a WECS generator-torque controller capable of adapting the power production to a variable reference power by enabling the WT blade-pitch actuator and decupling the rotor when the wind reaches the cut-off speed (section ***4.3. WECS control strategy***);
- analysis and synthesis of a gain scheduling PI controller. The values of the gains scheduling (K_p and K_i) were obtained based on the linearization of the WECS nonlinear model using Tylor series approximation, and by developing the mathematical equations for calculating the gains scheduling based on the current value of the blade pitch angle (β) and the value of the blade pitch angle for which the WT rotor torque has doubled (βk) (***Equations 4.149*** and ***4.150***);
- implementing the nonlinear MM and the control strategy of a WECS and validating them by simulating four different scenarios: the operation at nominal and partial regime (the reference power being ⅓, ½ and ⅔ of the nominal power) to a wind speed covering the entire operating range (a ramp variation from 0 to 30 m/s) and to a time series of a very turbulent wind speed (section ***4.4. WECS simulations***);
- development and validation of a PSPPECS model capable of simulating transitory regimes through all the subsystems (centrifugal pump, induction motor, motor drive and PECS) in section ***5.2. PSPPECS modelling***;
- development, implementation and validation of a PSPPECS control strategy capable of ensuring the control in 3 distinct cases (section ***5.3. PSPPECS control strategy***):
  1. when the pumping head is higher than the reference, the control strategy regulates the pumping head;
  2. when the pumping head is lower than the reference and the power produced by the PECS is lower than the minimum power required for the PS operation, the control strategy decelerates the PS;
  3. when the pumping head is lower than the reference and the power produced by the PECS is higher than the minimum power required by the

PS operation, the control strategy operates the PS so that the power absorbed by it tracks the power produced by the PECS.

- developing and implementing a more accurate monitoring system than the existing ones (which uses the methodology proposed by IEC 62253 [96]), by using a non-intrusive data acquisition and logging system that measures and records the values of the transducers each second (section ***5.4. Monitoring system***);
- implementation, simulation and experimental validation of the proposed PSPPECS model and control strategy (section ***5.5. PSPPECS simulations***);
- development of a PSPWECS model capable of simulating transitory regimes through all the subsystems (centrifugal pump, induction motor, motor drive and WECS) in section ***6.2. PSPWECS modelling***;
- analysis, synthesis and implementation of a PSPWECS control strategy capable of ensuring the control in 4 distinct cases (section ***6.3. PSPWECS control strategy***):
    1. when the power produced by a WECS is lower than the minimum power required by the PS operation, the control strategy decelerates the PS;
    2. when the power produced by a WECS is higher than the minimum power required by the PS operation, the control strategy operates the PS so that its power absorbed tracks the power produced by the WECS;
    3. when the pumping head is lower than the reference, the control strategy demands the WECS, through a reference, to produce the power required for the PS nominal operation;
    4. when the pumping head is higher than the reference, the control strategy regulates the power produced by the WECS according to the PS power demand so that the pressure it is equal to its reference.
- implementing the PSPWECS model and control strategy in Matlab/Simulink and validating them by simulating the operation of the entire system at a wind speed covering the entire operating range (a ramp variation from 0 to 30 m/s) in section ***6.4. PSPWECS simulations***.

The presented issues, as well as the obtained results and solutions, shows the industrial applicability of the current work, opening new perspectives for future research on PS powered by RES.

7.3 Future research

As research directions that can continue the results obtained in this thesis, and that can be addressed in the future, are:

- development, implementation, simulation and experimental validation of a Pumping Systems Powered by a Wind-Photovoltaic Hybrid Energy Conversion System;
- analysis, synthesis and implementation of advanced control strategies such as robust control, model predictive control, fuzzy logic control or neural network-based control, etc.

REFERENCES

[1] I. Renewable Energy Agency, RENEWABLE ENERGY STATISTICS 2020 STATISTIQUES D'ÉNERGIE RENOUVELABLE 2020 ESTADÍSTICAS DE ENERGÍA RENOVABLE 2020 About IRENA. 2020.

[2] J. Lee and F. Zhao, "GWEC Global Wind Report," Wind energy Technol., p. 78, 2020, [Online]. Available: www.gwec.net.

[3] E. Sesto and N. H. Lipman, "Wind energy in Europe," 1992.

[4] European Commission, "2030_En @ Ec.Europa.Eu," 2030 Climate and Energy Framework. 2019, [Online]. Available: https://ec.europa.eu/clima/policies/strategies/2030_en.

[5] A. Ursachi and **D. Bordeasu**, "Smart Grid Simulator," no. 5, pp. 488–491, 2014.

[6] "kituri-solare-fotovoltaice-pentru-irigatii-in-agricultura @ www.esolar.ro." [Online]. Available: https://www.esolar.ro/tehnologie-solara-fotovoltaica/kituri-solare-fotovoltaice-si-eoliene-pentru-irigatii-in-agricultura/kituri-solare-fotovoltaice-pentru-irigatii-in-agricultura.html.

[7] "ada37d6277b8bc009e9f4dd45accbb7617df20ba @ profyheat.com." [Online]. Available: https://profyheat.com/produs/sistem-autonom-de-irigare/.

[8] "kit-fotovoltaic-pompa-fluid-solar-2-6-pedrollo @ www.ivp.ro." [Online]. Available: https://www.ivp.ro/kit-fotovoltaic-pompa-fluid-solar-2-6-pedrollo.

[9] "pompa+panou+solar @ www.emag.ro." [Online]. Available: https://www.emag.ro/search/pompa+panou+solar.

[10] T. D. Short and M. A. Mueller, "Solar powered water pumps: problems, pitfalls and potential," 2002 International Conference on Power Electronics, Machines and Drives (Conf. Publ. No. 487), Sante Fe, NM, USA, 2002, pp. 280-285, doi: 10.1049/cp:20020129.

[11] Short, Tim & Thompson, P.. (2003). Breaking the mould: Solar water pumping-the challenges and the reality.Solar Energy. 75.1-9. 10.1016/S0038- 92X(03)00233-0

[12] "f909e923a40bb36426edab047c44c9e6639cc20d @ www.riegosolar.net." [Online]. Available: http://www.riegosolar.net/es/riego-con-energia-solar/.

[13] L. Micu, **D. Bordeasu**, I. Bordeasu, M. Popescu, O. Oanca and S. Duma, "Influence of nitriding thermochemical treatments upon cavitation erosion resistance of duplex X2CrNiMoN22-5-3 stainless steels.", HIDRAULICA, no. 4, pp. 27-33, 2014.

[14] Bordeasu, I.; Micu, L.M.; Oanca, O.V.; Pugna, A.; Bordeasu, C.; Popoviciu, M.O.; **Bordeasu, D.** Laser beam treatment effect on AMPCO M4 bronze cavitation erosion resistance. IOP Conf. Ser. Mater. Sci. Eng. 2015, 85, 10. https://doi.org/101088/1757-899X/85/1/012005.

[15] Micu, L.M.; Bordeasu, I.; Popoviciu, M.O.; Popescu, M.; **Bordeasu, D.**; Salcianu, L.C. Influence of volumic heat treatments upon cavitation erosion resistance of duplex X2CrNiMoN 22-5-3 stainless steels. IOP Conf. Ser. Mater. Sci. Eng. 2015, 85, 012019.

[16] "63f666a45c138a95b4744f9962881673b5978304 @ solenersa.com." [Online]. Available: https://solenersa.com/en/.

[17] "solar-water-solutions @ www.grundfos.com." [Online]. Available: https://www.grundfos.com/market-areas/water/solar-water-solutions.html.

[18] "d34f82d829466f6b5e4577c114fb328f8f538830 @ www.frutaslarinconada.com." [Online]. Available: http://www.frutaslarinconada.com/en/.

[19] "6a33de1ee36ff8a790f74581c2c3a067ee19c085 @ www.se.com." [Online]. Available: https://www.se.com/ro/ro/product/VW3A5306/filtru-iesire-dv-dt-pentru-variator-de-viteza---ip00/.

[20] "global-photovoltaic-pv-pumping-systems-for-irrigation-market-research-report @ www.themarketreports.com." [Online]. Available: https://www.themarketreports.com/report/global-photovoltaic-pv-pumping-systems-for-irrigation-market-research-report.

[21] MASLOWATEN, Technical Specifications for PV irrigation systems, 2007. [Online]. Available: http://maslowaten.eu/?page_id=57&lang=es.

[22] "default @ www.sisifo.info." [Online]. Available: https://www.sisifo.info/en/default.

[23] Conroy, Niamh & Deane, J.P. & O Gallachoir, Brian. (2011). Wind turbine availability: Should it be time or energy based? – A case study in Ireland. Renewable Energy. 36. 2967-2971. 10.1016/j.renene.2011.03.044.

[24] "manufacturer_en_71_goldwind @ www.thewindpower.net." [Online]. Available: https://www.thewindpower.net/manufacturer_en_71_goldwind.php.

[25] Srikanth D, K. Himaja, Ch. Swasthik, and P. Uday Kumar, "Water Pumping System using Solar and Wind Power," Int. J. Eng. Res., vol. V9, no. 05, pp. 613–615, 2020, doi: 10.17577/ijertv9is050462.

[26] Bordeașu, I, Păcurar, C, **Bordeașu, D** Hidraulica Aplicată –Hidrostatica-Noțiuni Teoretice și Aplicații- (Ediție revizuită și completată), Editura Politehnica, Timisoara/2017, ISBN 978-606-35-10166-1, pp.156

[27] F. M. White, "Fluid mechanics," Seventh Ed., University of Rhode Island: McGraw-Hill, 2009.

[28] M. H. Rashid, POWER ELECTRONICS HANDBOOK, Third edit. Oxford, UK: Elsevier Ltd, 2011.

[29] Andrzej Trzynadlowski, Control of Induction Motors, Academic Press, 2001, ISBN 0127015108, 9780127015101

[30] Austin Hughes, Bill Drury, Electric Motors and Drives: Fundamentals, Types and Applications, Newnes, 2013, 0080993680, 9780080993683

[31] [Industrial Motion control Motor selection, drives, control tuning, applications Hakan Gurocak pag 132]

[32] Muhammad H. Rashid, Power Electronics Handbook (Third Edition), Butterworth-Heinemann, 2011, ISBN 9780123820365.

[33] L. W. Mays, Hydraulic Design Handbook. McGraw-Hill Education, 1999.

[34] B. E. Larock, R. W. Jeppson, and G. Z. Watters, Hydraulics of Pipeline Systems. Boca Raton, Florida: CRC Press LLC, 2000. doi: 10.1201/9780367802431.

[35] **Bordeasu, D.**; Prostean, O.; Filip, I.; Dragan, F.; Vasar, C. Modelling, Simulation and Controlling of a Multi-Pump System with Water Storage Powered by a Fluctuating and Intermittent Power Source. Mathematics 2022, 10(21), 4019. https://doi.org/10.3390/math10214019

[36] Nidec Control Techniques, "Digistart D3 23 A-1600A 200 V-690 V," 2017.

[37] Nidec, “Powerdrive F300.” Nidec Control Techniques Ltd, The Gro Newtown Powys SY16 3BE UK, p. 324, 2017.

[38] G. Janevska and R. M. Bitola, “Mathematical Modeling of Pump System,” EIIC, pp. 455–458, 2013.

[39] Muñoz, J., Martínez-Moreno, F. and Lorenzo, E. (2011), On-site characterisation and energy efficiency of grid-connected PV inverters. Prog. Photovolt: Res. Appl., 19: 192–201.

[40] G. Abad, Power Electronics and Electric Drives for Traction Applications. Chichester, West Sussex, United Kingdom: John Wiley & Sons, Ltd., 2016. doi: 10.1002/9781118954454.

[41] H. Abu-Rub, M. Malinowski, and K. Al-Haddad, POWER ELECTRONICS FOR RENEWABLE ENERGY SYSTEMS, TRANSPORTATION AND INDUSTRIAL APPLICATIONS. West Sussex,United Kingdom: IEEE Press and John Wiley & Sons Ltd, 2014.

[42] C. Haţiegan, C. Chioncel, E. Răduca, C. Popescu, I. Pădureanu, M. Jurcu, **D. Bordeaşu**, S. Trocaru, F. Dilertea, O. Bădescu, I. Terfăloagă, A. Băra and L. (Barboni) Haţiegan, "Determining the operating performance through electrical measurements of a hydro generator", IOP Conference Series: Materials Science and Engineering, vol. 163, p. 012031, 2017.

[43] Mathworks, “Matlab and Simulink,” 2016. http://www.mathworks.com/products/matlab/ (accessed Feb. 08, 2021).

[44] Caprari, Submersible Electric Pump E8P95/7ZC+MAC870-8V Technical Data Sheet. 2019. Available online: https://ipump.caprarinet.net/ (accessed on 9 October 2021).

[45] Sarasúa, J.I.; Martínez-Lucas, G.; Platero, C.A.; Sánchez-Fernández, J.Á. Dual Frequency Regulation in Pumping Mode in a Wind–Hydro Isolated System. Energies 2018, 11, 2865. [CrossRef]

[46] Yang, Z.; Soleiman, K.; Løhndorf, B. Energy Efficient Pump Control for an Offshore Oil Processing System. IFAC Proc. Vol. 2012, 45, 257–262. [CrossRef]

[47] Sârbu, I.; Borza, I. Energetic optimization of water pumping in distribution systems. Period. Polytech. Ser. Mech. Eng. 1998, 42, 141–152.

[48] **Bordeașu, D.**; Proștean, O.; Hatiegan, C. Contributions to Modeling, Simulation and Controlling of a Pumping System Powered by a Wind Energy Conversion System, Energies 2021 14, 7696. https://doi.org/10.3390/en14227696

[49] Predescu, A.; Truică, C.-O.; Apostol, E.-S.; Mocanu, M.; Lupu, C. An Advanced Learning-Based Multiple Model Control Su-pervisor for Pumping Stations in a Smart Water Distribution System. Mathematics 2020, 8, 887. https://doi.org/10.3390/math8060887

[50] Oshurbekov, S.; Kazakbaev, V.; Prakht, V.; Dmitrievskii, V. Improving Reliability and Energy Efficiency of Three Parallel Pumps by Selecting Trade-Off Operating Points. Mathematics 2021, 9, 1297. https://doi.org/10.3390/math9111297

[51] Thorley, A.R.D. (1991). Fluid Transients in Pipeline Systems. D. & L. George Ltd Publ., Herts, UK.

[52] Li, W.; Ji, L.; Shi, W.; Zhou, L.; Chang, H.; Agarwal, R.K. Expansion of High Efficiency Region of Wind Energy Centrifugal Pump Based on Factorial Experiment Design and Computational Fluid Dynamics. Energies 2020, 13, 483.

[53] Sul, S. Control of Electric Machine Drive Systems; John Wiley & Sons: Hoboken, NJ, USA, 2011; pp. 291–294.

[54] **Bordeașu, D.** Study on the implementation of an alternative solution to the current irrigation system. In Proceedings of the ErgoWork 2022 International Conference on Ergonomics and Workplace Management, Timișoara, Romania, 16 June 2022, that will be published in special issue of ACTA TECHNICA NAPOCENSIS SERIES-APPLIED MATHEMATICS, MECHANICS AND ENGINEERING journal.

[55] S. Khadidja, M. Mountassar, and B. Mohamed, "Comparative study of incremental conductance and perturb & observe MPPT methods for photovoltaic system," IEEE, vol. pp. 1-6, 2017, doi: 10.1109/GECS.2017.8066230.

[56] C. H. Lin, C. H. Huang, Y. C. Du, and J. L. Chen, "Maximum photovoltaic power tracking for the PV array using the fractional-order incremental conductance method," Applied Energy, vol. 88, no. 12, pp. 4840–4847, 2011, doi: 10.1016/j.apenergy.2011.06.024.

[57] A. Belkaid, I. Colak, and O. Isik, "Photovoltaic maximum power point tracking under fast varying of solar radiation," Applied Energy, vol. 179, pp. 523–530, Oct. 2016, doi: 10.1016/j.apenergy.2016.07.034.

[58] Trina Solar, 144 cell multicrystalline photovoltaic module 335–345w power available online at: www.trinasolar.com, 2017.

[59] K. Ishaque, Z. Salam, A. Shamsudin, and M. Amjad, "A direct control based maximum power point tracking method for photovoltaic system under partial shading conditions using particle swarm optimization algorithm," Applied Energy, vol. 99, pp. 414–422, 2012, doi: 10.1016/j.apenergy.2012.05.026.

[60] Mathworks, "PV Array," https://www.mathworks.com/help/physmod/sps/powersys/ref/pvarray.html, 2015.

[61] STI Norland, STI-H250 Horizontal Single Axis Tracker – Technical Data https://www.stinorland.com/es, 2017

[62] EN 1991-1-1: Eurocode 1: Actions on structures - Part 1-1: General actions - Densities, self-weight, imposed loads for buildings

[63] EN 1991-1-4:2005 Wind actions - Eurocodes

[64] ISO 9223:2012 Corrosion of metals and alloys — Corrosivity of atmospheres

[65] EN IEC 61000-6-2:2019 Electromagnetic compatibility (EMC) - Part 6-2: Generic standards - Immunity standard for industrial environments

[66] EN IEC 61000-6-4: 2019 Electromagnetic compatibility (EMC) - Part 6-4: Generic standards - Emission standard for industrial environments

[67] EN 50178 Electronic equipment for use in power installations - European Standard

[68] European Comission, PVGIS 5.2 PHOTOVOLTAIC GEOGRAPHICAL INFORMATION SYSTEM, available online at: https://re.jrc.ec.europa.eu/pvg_tools/en/

[69] Narvarte, L. & Pigueiras, Eduardo. (2008). Tracking and Ground Cover Ratio. Progress in Photovoltaics: Research and Applications. 16. 703 - 714. 10.1002/pip.847.

[70] Pigueiras, Eduardo & Narvarte, L. & Munoz, J.. (2011). Tracking and back-tracking. Progress in Photovoltaics: Research and Applications. 19. 747–753. 10.1002/pip.1085

[71] A. Fatah et al., “A Modified Perturbe and Observe MPPT Technique for Standalone Hybrid PV-Wind with Power Management,” 2021. doi: 10.1109/ICCAD52417.2021.9638740.

[72] T. H. Kwan and X. Wu, “The Lock-On Mechanism MPPT algorithm as applied to the hybrid photovoltaic cell and thermoelectric generator system,” Applied Energy, vol. 204, pp. 873–886, 2017, doi: 10.1016/j.apenergy.2017.03.036.

[73] J. Prasanth Ram and N. Rajasekar, “A new robust, mutated and fast tracking LPSO method for solar PV maximum power point tracking under partial shaded conditions,” Applied Energy, vol. 201, pp. 45–59, 2017, doi: 10.1016/j.apenergy.2017.05.102.

[74] J. Ahmed and Z. Salam, “A Maximum Power Point Tracking (MPPT) for PV system using Cuckoo Search with partial shading capability,” Applied Energy, vol. 119, pp. 118–130, Apr. 2014, doi: 10.1016/j.apenergy.2013.12.062.

[75] Ishaque K, Salam Z, Taheri H. Simple, fast and accurate two-diode model for photovoltaic modules. Sol Energy Mater Sol Cells 2011;95:586–94.

[76] Ishaque K, Salam Z, Taheri H, Syafaruddin. Modeling and simulation of photovoltaic (PV) system during partial shading based on a two-diode model. Simul Model Pract Theory 2011;19:1613–26.

[77] J. Riedemann, W. Jara, C. Pesce and R. Peña, "Predictive Current Control of an Induction Machine for Solar Pumping Application," 2018 IEEE International Conference on Automation/XXIII Congress of the Chilean Association of Automatic Control (ICA-ACCA), 2018, pp. 1-5, doi: 10.1109/ICA-ACCA.2018.8609791.

[78] W. Said, H. A. Gaber and A. Mami, "Sizing and Simulation of an Energy Sufficient Stand-alone PV Pumping System," 2017 International Conference on Promising Electronic Technologies (ICPET), 2017, pp. 8-13, doi: 10.1109/ICPET.2017.8.

[79] S. Shukla and B. Singh, "Solar PV array fed speed sensorless vector control of induction motor drive for water pumping," 2016 7th India International Conference on Power Electronics (IICPE), 2016, pp. 1-6, doi: 10.1109/IICPE.2016.8079443.

[80] R. A. Santos, DAMAGE MITIGATING CONTROL FOR WIND TURBINES, no. December. The University of Colorado, 2006.

[81] **Bordeasu, D.**, Pulido, T. V., & Nielsen, C. (2016). Pellet plant energy simulator: IOP Conference Series: Materials Science and Engineering. In International Conference on Applied Sciences 2015, ICAS 2015 IOP Publishing. IOP Conference Series: materials Science and Engineering Vol. 106 No. 1 https://doi.org/10.1088/1757-899X/106/1/012002.

[82] T. Milos, M. Popoviciu, I. Bordeasu, R. Badarau, A. Bej and **D. Bordeasu**, "The 3D blade surface generation for Kaplan turbines using analytical methods and CAD techniques", HIDRAULICA, vol. 2, no. 2, pp. 65-74, 2013.

[83] O. W. Collaborative, OFFSHORE WIND TECHNOLOGY OVERVIEW. Long Island - New York City, 2009.

[84] K. Hammerum, P. Brath, and N. K. Poulsen, “A fatigue approach to wind turbine control,” J. Phys. Conf. Ser., vol. 75, no. 1, p. 012081, Jul. 2007, doi: 10.1088/1742-6596/75/1/012081.

[85] A. Debes and **D. Bordeasu,** “H ∞ ROBUST CONTROLLER FOR WIND TURBINE POWER BOOSTING,” Aalborg University, 2017.

[86] J. Jonkman, S. Butterfield, W. Musial, and G. Scott, Definition of a 5-MW Reference Wind Turbine for Offshore System Development. Golden, Colorado: National Renewable Energy Laboratory, 2009.

[87] G. Abad, J. López, M. A. Rodríguez, L. Marroyo, and G. Iwanski, Doubly Fed Induction Machine: Modeling and Control for Wind Energy Generation. 2011.

[88] J. D. Grunnet, M. Soltani, T. Knudsen, M. Kragelund, and T. Bak, “Aeolus toolbox for dynamics wind farm model, simulation and control,” Eur. Wind Energy Conf. Exhib. 2010, EWEC 2010, vol. 4, pp. 3119–3129, 2010.

[89] **Bordeașu, D.**; Proștean, O.; Vașar, C.; Debeș, A. Load Comparison Between Two Controlling Strategies for Wind Energy Conversion System Power-Boosting. In Proceedings of the IEEE 16th International Symposium on Applied Computational Intelligence and Informatics (SACI 2022), Timișoara, Romania, 25 May 2022.

[90] S. W. Smith, The Scientist and Engineer’s Guide to Digital Signal Processing. San Diego: CA: California Technical Publishing, 2006.

[91] R. D. Strum and D. E. Kirk, Contemporary Linear Systems Using MATLAB. Pacific Grove, California, USA: Brooks/Cole, 2000.

[92] Fuhrländer FL. Fuhrländer FL 100 kW Wind Turbine Technical Data Sheet. 2021. Available online: https://en.wind-turbinemodels.com/turbines/279-fuhrlaender-fl-100-astos/ (accessed on 9 October 2021).

[93] M. H. Hansen, A. Hansen, T. J. Larsen, S. Øye, P. Sørensen, and P. Fuglsang, Control design for a pitch-regulated, variable speed wind turbine, vol. 1500, no. January. 2005.

[94] Direct solar irrigation in an orchard. Available online: https://bombeatec.com/en/casos-de-exito/direct-solar-irrigation-in-an-orchard/ (accessed on 5 June 2022).

[95] B. U. I. A. Eaton Electrical Sector, XV300 Manual, 3rd ed. Hein-Moeller-Straße 7-11, D-53115 Bonn: Eaton Industries GmbH, 2019.

[96] IEC. IEC 62253 International Standard Photovoltaic pumping systems – Design qualification and performance, 2011 measurements (Edition 1.0, 2011-07). Geneva, Switzerland: IEC Central Office.

[97] Atersa, “Datasol MET Adquisiciòn de Radiaciòn, Temperaturas y Velocidad del Viento Manual de Operaciòn y de instalaciòn,” 2008.

[98] Remberg, “ISO2 Plus Aislador Universal ±v-i(dc) con alimentación 24vdc,” no. dc. Remberg, pp. 0–3.

[99] ifm, “Operating instructions Electronic pressure sensor for industrial applications PT54xx/PU54xx,” 2020.

[100] Calor, “Contor apa rece WOLTMAN WPD R100 DN100 se poate echipa cu releu REED,” Calor Design, 2021. http://www.calorserv.ro/produse/contor-apa-rece-woltman-wph-zf-n-ZENWPHZFN100

[101] REISSMANN, “Winding temperature monitoring and surface temperature - Pt100 Sensor,” vol. 10, no. 0. REISSMANN Sensortechnik GmbH, D-74538 Rosengarten-Uttenhofen, pp. 1–9.

[102] K. Engineering, “USER GUIDE ORBIT 360,” 2021.

[103] R. K. Pachauri and Y. K. Chauhan, "Fuzzy logic controlled MPPT assisted PV-FC power generation for motor driven water pumping system," 2014 IEEE Students' Conference on Electrical, Electronics and Computer Science, 2014, pp. 1-6, doi: 10.1109/SCEECS.2014.6804485.

[104] M. Zigliotto, M. Carraro, R. Antonello and A. Costabeber, "A fast-MPPT low-complexity autonomous PV water pumping scheme for PMSM," 3rd Renewable Power Generation Conference (RPG 2014), 2014, pp. 1-6, doi: 10.1049/cp.2014.0834.

[105] M. Dubey, S. Sharma and R. Saxena, "Single stage PV system based Direct Torque Controlled PMSM drive for pump load application," 2016 IEEE International Conference on Power Electronics, Drives and Energy Systems (PEDES), 2016, pp. 1-5, doi: 10.1109/PEDES.2016.7914518.

[106] S. Shukla and B. Singh, "Solar PV array fed speed sensorless vector control of induction motor drive for water pumping," 2016 7th India International Conference on Power Electronics (IICPE), 2016, pp. 1-6, doi: 10.1109/IICPE.2016.8079443

[107] N. Pushpraj, N. Gupta, V. Gupta and M. A. Mulla, "Solar energy harvesting for irrigation water pumping system," 2017 IEEE International Conference on Power, Control, Signals and Instrumentation Engineering (ICPCSI), 2017, pp. 1398-1402, doi: 10.1109/ICPCSI.2017.8391941.

[108] W. Said, H. A. Gaber and A. Mami, "Sizing and Simulation of an Energy Sufficient Stand-alone PV Pumping System," 2017 International Conference on Promising Electronic Technologies (ICPET), 2017, pp. 8-13, doi: 10.1109/ICPET.2017.8.

[109] J. Riedemann, W. Jara, C. Pesce and R. Peña, "Predictive Current Control of an Induction Machine for Solar Pumping Application," 2018 IEEE International Conference on Automation/XXIII Congress of the Chilean Association of Automatic Control (ICA-ACCA), 2018, pp. 1-5, doi: 10.1109/ICA-ACCA.2018.8609791.

[110] R. Kumari and R. Dahiya, "Speed control of solar water pumping with indirect vector control technique," 2018 2nd International Conference on Inventive Systems and Control (ICISC), 2018, pp. 1401-1406, doi: 10.1109/ICISC.2018.8399039.

[111] B. Said, T. Mohamed and B. Belkacem, "On Robust Control of Induction Motor with Multicell Inverter for PV Pumping Applications," 2019 International Conference on Applied Automation and Industrial Diagnostics (ICAAID), 2019, pp. 1-6, doi: 10.1109/ICAAID.2019.8934968.

[112] F. Mehazzem and A. Reama, "Integral Backstepping Control for Water Pumping System FED by MPPT Fuzzy-Logic PV Source," 2020 2nd International Conference on Smart Power & Internet Energy Systems (SPIES), 2020, pp. 111-115, doi: 10.1109/SPIES48661.2020.9243002.

[113] B. N. Kar, P. Samuel and A. Naik, "Solar PV Array Fed Fuzzy Logic Controlled PMSM Drive for Water Pumping System," 2021 International Conference in Advances in Power, Signal, and Information Technology (APSIT), 2021, pp. 1-5, doi: 10.1109/APSIT52773.2021.9641332.

[114] Stoyanov, L.; Bachev, I.; Zarkov, Z.; Lazarov, V.; Notton, G. Multivariate Analysis of a Wind–PV-Based Water Pumping Hybrid System for Irrigation Purposes. Energies 2021, 14, 3231. https://doi.org/10.3390/en14113231.

[115] Ronad, B.F.; Jangamshetti, S.H. Optimal cost analysis of wind-solar hybrid system powered AC and DC irrigation pumps using HOMER. In Proceedings of the 2015 International Conference on Renewable Energy Research and Applications (ICRERA), Palermo, Italy, 22–25 November 2015; Volume 5, pp. 1038–1042. https://doi.org/10.1109/ICRERA.2015.7418568.

[116] Jamii, J.; Mimouni, F. Model of wind turbine-pumped storage hydro plant. In Proceedings of the 2018 9th International Renewable Energy Congress (IREC), Hammamet, Tunisia, 20–22 March 2018; pp. 1–6. https://doi.org/10.1109/IREC.2018.8362478.

[117] Li, H.; Zheng, C.; Lv, S.; Liu, S.; Huo, C. Research on optimal capacity of wind power based on coordination with pumped storage power. In Proceedings of the 2016 IEEE PES Asia-Pacific Power and Energy Engineering Conference (APPEEC), Xi'an, China, 25–28 October 2016; pp. 1214–1218. https://doi.org/10.1109/APPEEC.2016.7779685.

[118] Ouchbel, T.; Zouggar, S.;Elhafyani, M.L.; Seddik, M.; Oukili, M.; Aziz, A.; Kadda, F.Z. Power maximization of an asynchronous wind turbine with a variable speed feeding a centrifugal pump. Energy Convers. Manag. 2014, 78, 976–984.

[119] Barara, M.; Bennassar, A.; Abbou, A.; Akherraz, M.; Bossoufi, B. Advanced Control of Wind Electric Pumping System for Isolated Areas Application. Int. J. Power Electron. Drive Syst. 2014, 4, 567–577.

[120] Zeddini, M.A.; Pusca, R.; Sakly, A.; Mimouni, M.F. MPPT control of Wind Pumping Plant Using Induction Generator. In Proceedings of the 14th International conference on Sciences and Techniques of Automatic Control & Computer Engineering STA, Sousse, Tunisia, 20–22 December 2013; pp. 438–442.

[121] Harrouz, A.; Dahbi, A.; Harrouz, O.; Benatiallah, A. Control of wind turbine based of PMSG connected to water pumping system in South of Algeria. In Proceedings of the 3rd International Symposium on Environmental Friendly Energies and Ap-plications (EFEA), Paris, France, 19–21 November 2014; pp. 22–25. https://doi.org/10.1109/EFEA.2014.7059951.

[122] Zhang, C.; Wang, L.; Li, H. Experiments and Simulation on a Late-Model Wind-Motor Hybrid Pumping Unit. Energies 2020, 13, 994. https://doi.org/10.3390/en13040994.

[123] T. Milos, I. Bordeasu, R. Badarau, A. Bej and **D. Bordeasu**, "Failure Cause Analysis of a 5 KW Wind Turbine Blade in Extreme Wind Conditions", MATERIALE PLASTICE, vol. 50, no. 4, pp. 279-284, 2013.